THÈSE DE DOCTORAT DE L'UNIVERSITÉ DE LILLE

EGENGSYS

LABORATOIRE DE GÉNIE CIVIL ET GÉO-ENVIRONNEMENT

Présentée Par

Hualin ZHANG

pour obtenir le grade de

DOCTEUR DE L'UNIVERSITÉ DE LILLE

Domaine

GÉNIE CIVIL

Sujet de la thèse

Approche numérique du comportement mécanique des sédiments maritimes contenant des hydrates de méthane

Soutenue le 28 mars 2025

Ali ZAOUI	**Professeur**	Université de Lille	*Président du jury*
Kun SU	**Expert-HDR**	TotalEnergies	*Rapporteur*
Frédéric COLLIN	**Professeur**	Université de Liège	*Rapporteur*
Mahdia HATTAB	**Professeur**	Université de Lorrain	*Examinateur*
Ling ZENG	**Professeur**	Changsha University of Science and Technology	*Invité*
Assef MOHAMAD-HUSSEIN	**Ingénieur**	SLB	*Invité*
Hanbing BIAN	**MCF-HDR**	Université de Lille	*Directeur*
Yun JIA	**MCF-HDR**	Université de Lille	*Co-directrice*

LGCgE-UNIVERSITÉ DE LILLE

DOCTORAL THESIS

FROM THE UNIVERSITY OF LILLE

EGENGSYS

LABORATORY OF CIVIL ENGINEERING AND GEO-ENVIRONMENT

By

Hualin ZHANG

to obtain the degree of

DOCTOR OF UNIVERSITY OF LILLE

Domain

CIVIL ENGINEERING

Thesis subject

The numerical approach of mechanical behavior of gas hydrate bearing sediments

Defended 28 March 2025

Ali ZAOUI	**Professor**	University of Lille	*President of the jury*
Kun SU	**Expert-HDR**	TotalEnergies	*Rapporteur*
Frédéric COLLIN	**Professor**	University of Liège	*Rapporteur*
Mahdia HATTAB	**Professor**	University of Lorraine	*Examiner*
Ling ZENG	**Professor**	Changsha University of Science and Technology	*Invited member*
Assef MOHAMAD-HUSSEIN	**Engineer**	SLB	*Invited member*
Hanbing BIAN	**MCF-HDR**	University of Lille	*Supervisor*
Yun JIA	**MCF-HDR**	University of Lille	*Co-supervisor*

LGCgE-UNIVERSITY OF LILLE

Résumé

Les hydrates de gaz naturel (NGH) sont des structures cristallines où les molécules de gaz sont piégées dans des cages constituées par les molécules d'eau sous des conditions de basse température et de haute pression. Ils se trouvent largement dans les sédiments marins et les régions de pergélisol. En raison de leur haute densité énergétique et de leurs vastes réserves, les NGH sont considérés comme une ressource énergétique durable prometteuse. Cependant, les NGH sont des substances métastables qui ne sont stables que dans des conditions spécifiques d'équilibre de phase, leur décomposition étant susceptible de se produire dès qu'ils subissent une perturbation. L'instabilité potentielle des réservoirs sédimentaires exposés lors de la récupération des NGH, accompagnée par la décomposition des hydrates, peut déclencher des catastrophes géologiques sous-marines. De plus, les produits dissociés des NGH sont des sources de gaz à effet de serre. Par conséquent, la récupération sûre et efficace des NGH nécessite une compréhension approfondie de la manière dont leur présence affecte les propriétés géomécaniques des sédiments hôtes.

Les études en laboratoire sont une condition préalable à la compréhension du milieu multiphasique composé d'hydrate-sédiment-fluide, qui implique les tests physico-mécaniques des carottes ou des sédiments contenant des hydrates de gaz naturels (GHBS) synthétisés artificiellement. Par conséquent, en se basant sur la littérature existante sur les propriétés thermiques, hydrauliques et mécaniques des GHBS, ce travail décrit systématiquement les caractéristiques physico-mécaniques des GHBS et analyse leurs réponses mécaniques sous divers facteurs en extrayant des données pertinentes, en mettant l'accent sur la manière dont les hydrates contribuent au comportement mécanique des sédiments hôtes et les mécanismes sous-jacents qui les animent (saturation en hydrate, morphologie des hydrates, distribution des hydrates, dissociation des hydrates). Les recherches actuelles sur la modélisation constitutive simulent le comportement géomécanique des GHBS via des équations mathématiques, incluant le renforcement de la résistance et de la rigidité par les hydrates, la dégradation des liaisons, la dilatation, la cohésion, le ramollissement par déformation, le changement de volume et la dissociation des hydrates, avec peu d'entre elles impliquant l'effet thermique, la forme de la surface de rupture et l'anisotropie des matériaux. À travers l'analyse de différents cadres théoriques, ce

travail catégorise les modèles constitutifs existants pour les GHBS en cinq catégories: modèle basé sur le critère de Mohr-Coulomb, modèle basé sur le critère de Drucker-Prager, modèle de Duncan-Chang, modèle d'état critique et modèle de fluage. Les avantages, les limitations et les domaines de recherche future de chaque modèle sont évalués de manière critique, en mettant particulièrement l'accent sur le modèle d'état critique, qui offre une caractérisation relativement complète des GHBS. Cette discussion révèle que les modèles existants ne parviennent pas à aborder de manière adéquate la caractéristique anisotrope.

Cependant, en raison de la structure en couches, de l'arrangement des particules et de la distribution diversifiée du contenu en hydrate dans les environnements naturels, les propriétés mécaniques des GHBS présentent souvent une anisotropie significative. De plus, la plupart des modèles supposent une seule forme de surface de rupture, limitant leur application à des conditions de rupture plus complexes. Compte tenu de ces lacunes, ce travail propose un nouveau modèle constitutif élasto-plastique basé sur la théorie HISS dans le cadre de l'état critique, qui peut ajuster la forme de la surface de rupture grâce à des modifications de paramètres, lui permettant de prendre en compte les changements de volume et les effets anisotropes lors de la dissociation des hydrates. La comparaison entre les calculs numériques et les données expérimentales valide l'efficacité et l'exactitude du modèle à reproduire le comportement mécanique des GHBS, offrant ainsi des perspectives pour l'exploitation future et les méthodologies de recherche.

Mots clés: Hydrates de gaz naturel; Sédiments contenant des hydrates de gaz; Propriétés mécaniques; Modèle constitutif; Théorie HISS; Cadre de l'état critique

Abstract

Natural gas hydrates (NGH) are crystalline structures where gas molecules are trapped within water molecules under low temperatures and high pressures. They are widely found in marine sediments and permafrost regions. Due to their high energy density and vast reserves, NGH are considered a promising sustainable energy resource. However, NGH are metastable substances that are stable under specific phase equilibrium conditions, with the decomposition of which once suffer from any disruptions. The potential instability of sediment reservoirs exposed during the recovery of NGH induced by hydrate decomposition due to this inherent property, which triggers submarine geological disasters. Also, the dissociated products of NGH are the sources of greenhouse gases. Therefore, the safe and effective recovery of NGH necessitates a deep understanding of how their presence affects the geo-mechanical properties of host sediments.

Laboratory studies are the prerequisite for understanding the multiphase medium of hydrate-sediment-fluid, which involve the physical-mechanical testing of cores or artificially synthesized gas hydrate-bearing sediments (GHBS). Hence, building upon the literature on thermal-hydraulic-mechanical properties of GHBS, this work systematically describes the physical-mechanical characteristics of GHBS and analyzes their mechanical responses under various factors through extracting relevant data, with an emphasis on how hydrates contribute to the mechanical behavior of host sediments and the driven underlying mechanisms (hydrate saturation, hydrate morphology, hydrate distribution, hydrate dissociation). Current constitutive modelling researches simulate the geo-mechanical behavior of GHBS via mathematical equations, including the enhancement of strength and stiffness by hydrates, bonding degradation, dilation, cohesion, strain softening, volume change, and hydrate dissociation, with few involving thermal effect, yield surface shape, and material anisotropy. Through the analysis of different theoretical frameworks, this work categorizes the existing constitutive models for GHBS into five types: Mohr-Coulomb criterion-based model, Drucker-Prager criterion-based model, Duncan-Chang model, critical state model, and creep model. Each model's strengths, limitations, and areas for future research are critically evaluated, with a particular focus on the critical state model, which provides a relatively

comprehensive characterization of GHBS. The above discussion reveals that existing models fail to adequately address the anisotropic characteristic.

However, due to the layered structure, particle arrangement, and diverse hydrate content distribution in natural settings, the mechanical properties of GHBS often exhibit obvious inherent anisotropy. Furthermore, most models assume a single yield surface shape, limiting their application to more complex yield conditions. Given these shortcomings, this work proposes a new elastoplastic constitutive model based on HISS theory within the critical state framework, which can adjust the yield surface shape through parameter modifications, allowing it to account for volumetric changes and anisotropic effects during hydrate dissociation. The comparison between the numerical calculations and experimental data validates the model's effectiveness and accuracy in reproduce the mechanical behavior of GHBS, offering insights for future exploitation and research methodologies.

Key words: Natural gas hydrates; Gas hydrate-bearing sediments; Mechanical properties; Constitutive model; Hiss theory; Critical state framework

Contents

Résumé iii

Abstract v

Contents vii

List of Figures xiii

List of Tables xviii

Nomenclature xx

List of Abbreviations xxii

Acknowledgements xxiii

Objectives and structure of the PhD thesis 1

Chapter 1. Introduction 6

1.1 Natural gas hydrate 6

1.1.1 Historical process of research on NGH 6

1.1.2 Hydrate structure 7

1.1.3 Hydrate nucleation hypothesis 10

1.1.4 Hydrate formation and stability conditions 11

1.1.5 Hydrate distribution and advantages 16

1.2 Gas hydrate-bearing sediments 19
1.2.1 Overview 19
1.2.2 Hydrate morphologies in coarse-grained sediments 21
1.2.3 Hydrate morphologies in fine-grained sediments 22
1.3 Gas hydrate application and extraction 24
1.3.1 Hydrate reservoir classification 24
1.3.2 Methods for gas hydrate recovery 26
1.3.3 Field trials for hydrate production 29
1.3.4 Climate changes induced by gas hydrate recovery 30
1.3.5 Geological disasters caused by gas hydrate recovery 31
1.4 Significance 33
1.4.1 The importance of exploring the geo-mechanical behavior of GHBS 33
1.4.2 The importance of the constitutive modeling for GHBS 33
1.5 Conclusions 34
Chapter 2. Fundamental physical-mechanical characteristics of GHBS 36
2.1 Thermal property 37
2.1.1 Thermal conductivity 38
2.1.2 Specific heat 40
2.1.3 Thermal diffusivity 41
2.1.4 Enthalpy of reaction 42

2.2 Fluid flow property and compressibility 43
2.2.1 Porosity 44
2.2.2 Permeability 45
2.2.3 Compressibility 50
2.3 GHBS remolding methods and experimental techniques 53
2.3.1 Methods for specimen preparation in the laboratory 54
2.3.2 Test apparatuses 57
2.3.3 Initial conditions 60
2.4 Influence of hydrate saturation on the mechanical responses of GHBS 61
2.4.1 Measurement methods for hydrate saturation 61
2.4.2 Stress-strain behavior of sediments in the presence of hydrates 62
2.4.3 Mechanisms of volumetric deformation and strength failure in GHBS 66
2.4.4 Analysis of the variation in mechanical parameters related to hydrate saturation 68
2.4.5 Influence of hydrate dissociation on mechanical behavior of GHBS 76
2.5 Influence of other factors on the mechanical responses of GHBS 81
2.5.1 Analysis of the variation in mechanical parameters related to effective confining stress 81
2.5.2 Analysis of the variation in mechanical parameters related to temperature 85
2.5.3 Influence of sediment composition, strain rate, and porosity on mechanical behavior of GHBS 88
2.6 Time-dependent deformation characteristics in GHBS 91

2.7 Conclusions.....93

Chapter 3. Recent developments in the constitutive models for GHBS 96

3.1 Constitutive model with Mohr-Coulomb criterion 96

3.1.1 Extended on Mohr-Coulomb strength theory 97

3.1.2 Extended on Mohr-Coulomb failure criterion.....97

3.1.3 Features and limitations 99

3.2 Constitutive model based on Drucker-Prager criterion 101

3.2.1 Drucker-Prager criterion 101

3.2.2 Extended Drucker-Prager model.....101

3.2.3 Features and limitations 104

3.3 Non-linear elastic model based on Duncan-Chang model.....105

3.3.1 Duncan-Chang model.....105

3.3.2 Extended Duncan-Chang model 106

3.3.3 Features and limitations 108

3.4 Critical state model 110

3.4.1 Extended on modified Cam-clay model.....110

3.4.2 Extended on state-dependent model.....117

3.4.3 Features and limitations 119

3.5 Creep constitutive model 122

3.5.1 Fitted model through experiment.....123

3.5.2 Extended visco-elastic-plastic model 124

3.5.3 Limitations and prospects 127

3.6 Insights and evaluation on constitutive equations of GHBS 128

3.6.1 Evaluation of strength equations 128

3.6.2 Evaluation of stiffness equations 130

3.6.3 Evaluation of bonding degradation equations 132

3.7 Conclusions 135

Chapter 4. The proposed constitutive model for GHBS 137

4.1 Introduction of modified Cam-clay model 138

4.1.1 Basic stress-strain equation 138

4.1.2 Elastic behavior 139

4.1.3 Hardening parameter and yield function 140

4.1.4 Flow rule and consistency condition 142

4.1.5 Numerical applications 143

4.2 Model theory 145

4.2.1 Hierarchical single surface theory 145

4.2.2 Subloading surface theory 147

4.3 Proposed elastoplastic constitutive model 148

4.3.1 Yield function 148

4.3.2 Hardening law 151

4.3.3 Cross-anisotropy in elastic phase 154

4.3.4 Flow rule and consistency function 162

4.3.5 Model parameters 166

4.4 Numerical analysis 168

4.4.1 Program implementation 168

4.4.2 Triaxial test using synthetic GHBS 171

4.4.3 Triaxial test using natural GHBS 177

4.4.4 Simulation for hydrate recovery using depressurization 183

4.5 Conclusions 185

Chapter 5. Conclusions and perspectives 187

5.1 Conclusions 187

5.2 Perspectives 189

References 191

List of Figures

Figure 1.1: The development history of NGH 7

Figure 1.2: Various hydrate structures and their constituted cavities (Sloan, 1998) 8

Figure 1.3: Mechanism diagram of hydrate nucleation (LCH) 11

Figure 1.4: The phase equilibrium stability zone of NGH (Xie et al., 2020) 13

Figure 1.5: The phase equilibrium curve of hydrates with various gas compositions 14

Figure 1.6: Effect of inhibitors on hydrate formation 15

Figure 1.7: Phase equilibrium curve for hydrate formation in the presence of various promoters 16

Figure 1.8: The distribution of NGH around the world (modified by Ruppel and Kessler (2017)) 18

Figure 1.9: Carbon reserve of global energy resource (modified by Makogon et al. (2007)) 18

Figure 1.10: The multiphase system of GHBS 20

Figure 1.11: Schematic of different HM in coarse-grained sediments 22

Figure 1.12: Schematic of different HM in fine-grained sediments 23

Figure 1.13: Resource pyramid for NGH (modified by Collett et al. (2009)) 25

Figure 1.14: Classification of hydrate deposits 26

Figure 1.15: Methods for recovery hydrates in sediment deposits 27

Figure 1.16: Several issues induced by hydrate decomposition (modified by Sultan et al. (2004)) 32

Figure 1.17: Schematic diagram of strength and deformation issues due to hydrate decomposition 32

Figure 2.1: The change law of thermal conductivity under various effect factors (Cortes et al., 2009) 40

Figure 2.2: The impacts of S_h and HM on permeability of GHBS 50

Figure 2.3: Schematic of the volumetric response of GHBS under isotropic compression 51

Figure 2.4: One-dimensional consolidation characteristics of sediments in the presence of hydrates (Kim et al., 2019; Nakashima et al., 2021; Tan 2004; Yoneda et al., 2019) 53

Figure 2.5: The general method for preparing HBS 54

Figure 2.6: Diagram of various methods for indoor specimens' preparation: (a) DGM; (b) EDM; (c) ISM; (d) HPM..... 55

Figure 2.7: GHBS triaxial apparatuses: (a) Masui et al., (2008); (b) Miyazaki et al., (2011); (c) Hyodo et al., (2013a); (d) Luo et al., (2018)..... 59

Figure 2.8: The relationship among stress, strain, and volume for bonded soil (modified by Uchida et al. (2012))..... 64

Figure 2.9: Schematic of stress-strain behavior of GHBS: (a) Comparison of mechanical behavior between GHBS and HFS; (b) Impacts of HM and S_h on mechanical responses of GHBS66

Figure 2.10: Mechanisms controlling the strength and dilation failure for sediments in the presence of hydrates..... 68

Figure 2.11: Mechanical responses of host sediments in the presence of hydrates..... 69

Figure 2.12: Change of c with varying S_h..... 71

Figure 2.13: Change of φ with varying S_h..... 71

Figure 2.14: Hydrates contribution to the peak strength..... 74

Figure 2.15: Hydrates contribution to the stiffness..... 74

Figure 2.16: Change of ν with varying S_h..... 75

Figure 2.17: Change of ψ with varying S_h..... 76

Figure 2.18: The dependency of effective parameters on S_h under thermal stimulation 77

Figure 2.19: The dependency of peak strength on dissociation ratio under depressurization and CO2 replacement 78

Figure 2.20: The variation in effective parameters under various dissociation methods 79

Figure 2.21: Mechanical responses of GHBS with respect to $\sigma_c^{'}$ 82

Figure 2.22: Change of σ_s with varying $\sigma_c^{'}$ 84

Figure 2.23: Change of E_{50} with varying $\sigma_c^{'}$ 84

Figure 2.24: Change of v with varying $\sigma_c^{'}$ 85

Figure 2.25: Mechanical responses of GHBS with respect to T 86

Figure 2.26: Change of σ_s with varying T 87

Figure 2.27: Change of c and φ with varying T 88

Figure 2.28: Mechanical responses of GHBS with respect to sediment composition 89

Figure 2.29: Peak strength versus strain ratio 90

Figure 2.30: Peak strength versus porosity 91

Figure 2.31: Schematic of the creep behavior of sediments without and with hydrate presence: (a) Creep test; (b) Creep curves of GHBS under various factors; (c) Comparison between HFS and GHBS 93

Figure 3.1: Schematic of yield surfaces for critical state model extended on modified CCM ... 117

Figure 3.2: Schematic diagram of the components of Nishihara creep model 125

Figure 4.1: Schematic diagram of consolidation line (V - Inp) 140

Figure 4.2: Diagram of the yield surface for modified CCM 141

Figure 4.3: Numerical results for normal consolidated soil (OCR=1) 144

Figure 4.4: Numerical results for over consolidated soil (OCR=2) 144

Figure 4.5: Numerical results for over consolidated soil (OCR=5) 145

Figure 4.6: The change of yield surface induced by shape parameters 147

Figure 4.7: Schematic diagram of subloading surface relative to normal yield surface 147

Figure 4.8: Schematic diagram of various shapes of yield surface in *p*-*q* space 150

Figure 4.9: Schematic diagram of subloading yield surface 151

Figure 4.10: The relationship between *U* and *R* 153

Figure 4.11: Elastic modulus versus hydrate saturation (Masui et al. 2005) 155

Figure 4.12: General representation of the anisotropic sediments 157

Figure 4.13: Procedures for the program implementation 170

Figure 4.14: Simulations for the stress paths and yield surfaces with various hydrate morphologies 172

Figure 4.15: Numerical modeling for the mechanical response of GHBS through the comparison between experimental results obtained from Masui et al. (2005) 173

Figure 4.16: Visualization of predicted yield surface with stress path in *p*-*q* space (S1 and S4 model) 175

Figure 4.17: Comparative analysis of stress-strain and volumetric behavior of GHBS using S1 and S4 model 176

Figure 4.18: Simulations for the stress paths and yield surfaces under various S_h 176

Figure 4.19: Numerical modeling for the mechanical response of GHBS through the comparison between experimental results obtained from Hyodo et al. (2013b) 177

Figure 4.20: Simulations for the stress paths and yield surfaces in natural GHBS 179

Figure 4.21: Numerical modeling for the mechanical response of GHBS through the comparison between experimental results obtained from Masui et al. (2008) 179

Figure 4.22: The impact of parameter μ on stress responses 180

Figure 4.23: The impact of parameter α_* on volume change 180

Figure 4.24: Simulations for the stress paths and yield surfaces in core specimens 182

Figure 4.25: Numerical modeling for the mechanical response of GHBS through the comparison between experimental results obtained from Yoneda et al. (2015b) 183

Figure 4.26: Simulation for hydrate recovery using depressurization 185

List of Tables

Table 1.1: Properties of hydrate crystal structure (Koh, 2002).....8

Table 1.2: Comparison of properties of ice, sI and sII hydrate structures (Jr and Koh, 2007).....9

Table 1.3: Description of three strategies for NGH recovery.....28

Table 2.1: Comparison of the thermal-related parameters of different specimen components (Aromada et al., 2019; Hu and Xiao, 2023; Waite et al., 2009).....37

Table 2.2: Summary of the existing permeability model for GHBS.....47

Table 2.3: A summary of methods for hydrate formation in the laboratory.....56

Table 2.4: Basic parameters for typical triaxial apparatuses.....58

Table 2.5: Summary of the mechanical tests related to c and φ (Effected by S_h).....70

Table 2.6: Summary of mechanical tests on HBS related to peak strength and stiffness (Effected by S_h).....73

Table 2.7: Summary of mechanical tests on HBS related to hydrate dissociation.....79

Table 2.8: Summary of mechanical tests on methane HBS related to strength and stiffness (Effected by $\sigma_c^{'}$).....82

Table 2.9: Summary of mechanical tests on HBS related to mechanical parameters (Effected by T).....86

Table 3.1: Characteristics of constitutive model with M-C criterion for GHBS reported in the existing literature.....100

Table 3.2: Characteristics of constitutive model based on D-P criterion for GHBS reported in the existing literature.....104

Table 3.3: Characteristics of nonlinear elastic model for GHBS reported in the existing literature 109

Table 3.4: Characteristics of critical state models for GHBS reported in the existing literature.120

Table 3.5: Summary of strength equations for GHBS in the existing literature.....129

Table 3.6: Summary of stiffness equations for GHBS in the existing literature 131

Table 3.7: Summary of degradation equations for GHBS in the existing literature.....134

Table 4.1: Model parameters for modified Cam-clay model.....143

Table 4.2: Parameters related to controlling the shape of yield surface 149

Table 4.3: Detailed explanation for the model parameters 166

Table 4.4: Detailed experimental conditions (Masui et al. (2005)) 171

Table 4.5: Numerical modelling parameters (Masui et al. (2005)).....171

Table 4.6: Detailed experimental conditions (Hyodo et al. (2013b)) 174

Table 4.8: Detailed experimental conditions (Masui et al. (2008)) 178

Table 4.9: Numerical modelling parameters (Masui et al. (2008)).....178

Table 4.10: Detailed experimental conditions (Yoneda et al. (2015b)).....181

Table 4.11: Numerical modelling parameters (Yoneda et al. (2015b)) 182

Nomenclature

Latin alphabet

c	Cohesion	MPa
c^s	Specific heat	J / (kg·K)
C_c	The compression index	-
C^e_{ijkl}	Elastic matrix	-
C^{ep}_{ijkl}	Elastoplastic matrix	-
e	Void ratio	-
E	Elastic modulus	GPa
G	Shear modulus	GPa
h	Seabed depth	m
K	Bulk modulus	GPa
K_1	Effective permeability	D, mD
M	Critical stress ratio	-
p_a	Atmosphere pressure	Pa
p'	Mean effective stress	MPa, kPa
p_{cs}	Pre-consolidation stress	MPa, kPa
p_{cc}, p_{cd}	Strength enhancement by hydrates	MPa, kPa
P	Pressure	MPa, kPa
q	Deviatoric stress	MPa, kPa
R	Subloading surface ratio	-
R_f	Failure ratio	-
R_g	Gas constant	J/ mol • K
S_h	Hydrate saturation	%
t	Time	h, min
T	Temperature	℃, K
u	Pore water pressure	MPa, kPa
v	Poisson's ratio	-
V	Specific volume	-

Greek alphabet and other symbols

α_*	Anisotropy factor	-
λ	Slope of swelling line	-
λ_T	Thermal conductivity	W / (m · K)
κ	Slope of normal compression line	-
κ_T	Thermal diffusivity	m^2 / s
ΔH	Reaction enthalpy	kJ / mol
ϕ	Porosity	%
ρ	Density	kg / m^3
ρ'	Mean shift stress	MPa, kPa
ψ	Dilatancy angle	°
φ	Internal friction angle	°
φ_0	State-dependent parameter	-
ω	Damage factor	-
χ	Degradation factor	-
$\sigma_c^{'}$	Effective confining stress	MPa, kPa
$\sigma_v^{'}$	Vertical effective stress	MPa, kPa
σ_{cs}	Creep stress	MPa, kPa
σ_s	Peak strength	MPa, kPa
σ_r	Residual strength	MPa, kPa
ε	Strain	-
$\dot{\varepsilon}$	Strain rate	mm / min
τ_f	Shear strength	MPa, kPa
η	Current stress ratio	-

List of Abbreviations

AMHCS : Anisotropic methane hydrate critical state

BSR : Bottom simulating reflector

CCM : Cam-clay model

CD : Consolidated drained

CSM : Critical state model

CT : Computed Tomography

CU : Consolidated undrained

D-C : Duncan-Chang

D-P : Drucker-Prager

DGM : Dissolved gas method

EDM : Excess-driven method

GHBS : Gas hydrate-bearing sediments

HBS : Hydrate-bearing sediments

HFS : Hydrate-free sediments

HISS : Hierarchical Single Surface

HM : Hydrate morphology

HPM : Hydrate premixing method

ISM : Ice seeding method

KGM : Kozeny Grain Model

LBNL : Lawrence Berkley National Laboratory

LCH : Labile cluster hypothesis

LSNM : Local Structure Nucleation Mechanism

M-C : Mohr-Coulomb

MHCS : Methane hydrate critical state

NGH : Natural gas hydrates

PCM : Parallel Capillary Model

RSM : Reservoir Simulator Model

Acknowledgements

Time flies, and in the blink of an eye, I find myself approaching the threshold of thirty. Throughout my PhD journey, I have been super lucky to meet so many people who were willing to help and care about me. Their support has given me the courage and perseverance to face numerous scientific challenges and fulfill my personal ambitions. I would like to take this opportunity to express my gratitude to them.

At first, I am sincerely grateful to my supervisors, Professor Hanbing Bian and Professor Yun Jia, for their meticulous guidance and support throughout my academic career. From the prospective of the research, they helped me overcome numerous challenges with their profound knowledge and attentive care, and made me move forward progressively. In addition, they not only supported me in my scientific endeavors but also in my personal life, especially when I first arrived in France, unable to speak French and faced with unfamiliar environment and language barriers. They patiently taught me how to handle various practical matters and often shared the pleasure of life and experience together, making me feel comfortable in a foreign land. In addition, I would like to thank Professor Mroueh and Professor Lancelot for their guidance on my research project. They provided the solutions to the problems that I raised at each group meeting, allowing me to continue my work smoothly.

I feel truly honored and grateful to the amazing members of my PhD defense jury for their time, effort, and invaluable support. It means a lot to me that they took the time to be part of my defense, and I sincerely appreciate their effort. First and foremost, I would like to express my gratitude to Dr. Ali Zaoui, my jury president and also the director of our laboratory, for his strong support of my defense. Under his leadership, the defense committee ensured a fair and rigorous evaluation. His profound academic insights and guidance have been truly enlightening, and I am very lucky to get his guidance throughout this journey. I am also extremely thankful to my rapporteurs, Dr. Frédéric Collin and Dr. Kun Su, for their detailed and thoughtful review of my dissertation. Their valuable feedback and suggestions helped me improve my work significantly, allowing me to refine my ideas and arguments to make my research even stronger. A big thanks also goes to my examiner, Dr. Mahdia Hattab, whose expertise and encouragement made my defense a truly enriching experience. Her insightful questions pushed me to think deeper and

improve my research in ways I hadn't ever expected. I am deeply grateful to Dr. Ling Zeng, my master's supervisor and invited jury member, for his continuous support throughout my academic journey. He was the one who first introduced me to the world of research, equipping me with the fundamental skills of academic writing and scientific exploration. Without his recommendation, I would not have had the opportunity to pursue my PhD studies in France, and for that, I am forever indebted to him. Finally, I extend my sincere thanks to Dr. Assef Mohamad-Hussein, my invited jury member, for his valuable insights and contributions to my defense discussion. His broader perspective added depth to my research and provided me with new directions to explore in the future. I am truly grateful for the collective expertise, dedication, and generosity of my jury members. Their feedback and guidance have played a huge role in shaping my final dissertation, and I will always appreciate their time and support as I move forward in my academic and professional journey.

I am also grateful to the China Scholarship Council for their financial support, which allowed me to focus on my research without financial concerns. Furthermore, I must thank my parents for their unconditional love and support throughout my pursuit of academic dreams. They have been my solid back, giving me the courage to explore the world. Additionally, I wish to thank my girlfriend, Xinyi Wang, whose companionship and love are important to me. She has provided immense emotional and practical support in my life, and her excellent cooking has brought the warmth of home to my life. The completion of my final thesis would not have been possible without the strong support from my institution, LGCgE. I extend my sincere thanks to Director Ali and all the members who warmly welcomed me. I also thank my colleagues and friends at LGCgE—Wantian Zhou, Huicong Yu, Shanshan He, Zhenning Shi, Hui Dong, Nan Hou, Ugo, Lionel, Lilan Zhang, Xiaodong Zhu, Zhu Yan, Pengchang Wei, Jianhong Wan, Jiwei Jia and Hanna—with whom I have spent unforgettable and enjoyable life in Lille.

Objectives and structure of the PhD thesis

With the rapid development of the world, the escalating demand for energy coexists with the stark reality of diminishing fossil fuel reserves. Currently, traditional fossil energies still constitute nearly 90% of global energy consumption (Yu et al., 2021). While reserves were once considered abundant, the tremendous demand for fossil fuels in rapidly industrializing countries remains intense, particularly in fields such as electricity, transportation, and petrochemicals. By 2040, it is predicted that oil demand will increase by 7%, and natural gas demand by 25% (İncekara, 2021). Oil and gas fields are increasingly approaching their production peaks, which poses the risk of depletion. Additionally, the combustion of fossil fuels, which releases carbon dioxide (CO_2) and other greenhouse gases, has a profound impact on climate change, prompting a global re-evaluation of energy production and consumption patterns (Quadrelli and Peterson, 2007). In response to these energy crises and environmental challenges, several international environmental agreements have been enacted such as the Kyoto Protocol of 1997 and the Paris Agreement of 2016, the objective of which is to foster the development of clean energy solutions and reduce greenhouse gas emissions. The issue of carbon neutrality has become a focal point in global political and economic development to date. Natural gas hydrates (NGH), with their potential for reduced carbon emissions, stand out from traditional hydrocarbons. NGH are viewed as viable transitional clean energy sources that could help in achieving peak carbon and neutrality goals (Englezos and Lee, 2005; Makogon, 2010; Yin and Linga, 2019). The recovery of NGH offers a promising avenue for supplementing traditional energy sources while mitigating environmental impacts, thus aligning with global strategies for sustainable development.

NGH are crystalline compounds formed by water and natural gas molecules under low temperature and high pressure, where gas molecules are encapsulated by water molecules (Demirbas et al., 2016). It is easy to burn when exposed to fire, which can be referred to "combustible ice". NGH remains stable under certain phase equilibrium conditions, dissociating

once these conditions are disrupted. Current surveys have revealed that NGH are extensively distributed in loose marine sediments and within the fractures of rocks in permafrost regions, exhibiting heterogeneous distribution patterns (Li et al., 2016). It is reported that the carbon content in NGH exceed twice than that of traditional energy sources, and the energy density released upon combustion is evidently higher than that of conventional natural gas. Hence, NGH can be considered a promising energy resource in the 21st century (Cui et al., 2018).

NGH are extensively located in deepwater regions of the worldwide ocean and permafrost (Chong et al., 2016). According to the hydrate resource pyramid, which outlines the relative abundance of NGH and the feasibility of its extraction, hydrates deposited in coarse-grained sedimentary layers beneath the seabed are deemed the most valuable for extraction purposes (Collett et al., 2009). As a result, a larger proportion of research is directed towards investigating submarine coarse-grained hydrate-bearing sediments. Gas hydrate-bearing sediments (GHBS) are composed of a multiphase composite geomaterial that includes the soil skeleton, hydrates, and pore fluids (gas and water). Within this structural framework, hydrates serve as a cementing agent, which adhere to the host sediments in various occurrence forms. Notably, this cementation imparts a range of physical and mechanical properties to the host sediments, influencing their structural stability subjected to various environmental conditions (Jiang et al., 2014).

The potential for NGH recovery has garnered global interest, with common extraction methods involving drilling into sediment layers and applying techniques like thermal injection, depressurization, or replacement to recover hydrates (Yang et al., 2019). However, during the recovery process (e.g., drilling friction, fluctuations in drilling pressure), the thermodynamic equilibrium of hydrates is easily disrupted, leading to dissociation into water and gas (Liu et al., 2019). On the one hand, this result will provoke changes in cementation strength and dilation of sedimentary layers, triggering a series of geological disasters including wellbore instability, platform settlement, and even submarine landslides. On the other hand, the inadvertent release of greenhouse gases poses an environmental concern by accelerating the thawing of permafrost and intensifying the greenhouse effect (Li et al., 2023; Yan et al., 2020). Thus, safe and effective extraction of NGH focuses on understanding the mechanical behavior of GHBS and the mechanical responses induced by hydrate dissociation. Current literature on GHBS centers on two main domains: laboratory experimental research and constitutive modeling. Laboratory studies serve as a prerequisite for a better understanding of the multiphase medium of hydrate-sediment-

fluid, which involves the performance of mechanical tests on core samples or artificially synthetic GHBS (Santamarina et al., 2012; Yoneda et al., 2013, 2015a). It exhibits a variation in experimental results due to differences in initial control conditions, there remains a gap in the comparative analysis of experimental data obtained considering the same factors (Liang et al., 2020). Consequently, this study meticulously compiles and evaluates existing research on GHBS, providing a comprehensive summary of the physical-mechanical properties of GHBS and analyzing the corresponding data to assess their mechanical responses under different influence factors. Constitutive modeling research endeavors to describe the stress-strain relationships of GHBS under diverse environmental conditions by simulating their geo-mechanical behavior through mathematical models (Wang et al., 2021). Most researches are based on theoretical frameworks such as Mohr-Coulomb, Duncan-Chang, Drucker-Prager, Cam-clay, and state-dependent models, incorporating specific parameters to reflect the contributions of hydrates to sediment strength and stiffness, degradation of hydrate bonds upon shearing, dilation, cohesion, effective confining pressure, strain softening, volumetric deformation, and hydrate dissociation characteristics. Additionally, some studies involve considerations of the thermodynamic properties of hydrates, the shape of the yield surface, and material anisotropy (Kong et al., 2023; Li et al., 2018; Miyazaki et al., 2012; Zhang et al., 2018). This study organizes and reviews existing reports on constitutive models for GHBS, and then evaluates the advantages, limitations, and recommendations for each type of model. Among these models, this study emphasizes the uniqueness of the critical state model and comprehensively summarizes the strength equations, stiffness equations, and bond degradation equations involved in the constitutive models. Discussions reveal that existing models rarely address sediment anisotropy, yet in natural setting, GHBS often exhibit variations in physical-mechanical properties along different directions due to the diversity in their layered structure, particle arrangement, and hydrate concentration distribution. In light of this, this study proposes a new elastoplastic constitutive model that can describe the volumetric changes during hydrate dissociation and anisotropic effects in GHBS. Validated through numerical calculations and corroborated with experimental data, this model demonstrates its effectiveness and accuracy in predicting the mechanical responses of GHBS, offering insights for future extraction and research methodologies.

The objective of our study is to perform a comprehensive review and synthesis of the geo-physical-mechanical behavior of GHBS. It seeks to propose new constitutive model and numerical

analysis method that will enrich the theoretical foundations in the geotechnical and geological fields, and to support the risk assessments and energy development decisions for hydrate reservoirs. Accordingly, this manuscript is structured into five chapters, each organized adhering to the work structure framework, as depicted in Fig. 0:

Chapter 1 Provides an overview of NGH and GHBS, introduces the structure, formation, and stability conditions of NGH and their advantages as a promising energy resource, explores the various morphologies in which hydrates occur within host sediments, discusses the application value and recovery methods of NGH, as well as the geological and environmental issues that may arise during the recovery process, and finally leads to the importance of the research on the geo-mechanical behavior and constitutive modeling for GHBS.

Chapter 2 Systematically compiles the geo-mechanical performance of GHBS as reported in the literature, describes the thermal properties, fluid dynamics, and compressibility of sediments in the presence of hydrate, summarizes the methods used for synthesizing GHBS in the laboratory associated with mechanical testing equipment, provides a comprehensive discussion on the mechanical responses of sediments contributed by hydrates and elucidates the underlying mechanisms, analyzes how various factors such as effective confining pressure, temperature, porosity, strain rate, sediment composition, hydrate dissociation, and time-dependency impact the mechanical properties of GHBS.

Chapter 3 Consolidates the current advancements in the constitutive modeling of GHBS, categorizes the constitutive models into those established based on the Mohr-Coulomb criterion and Drucker-Prager criterion, extended Duncan-Chang models, critical state models, and creep models based on the diversity of theoretical frameworks, focuses on the applicability, limitations, and areas worthy of further investigation for each model type, with particular emphasis on the uniqueness of critical state model, provides a comprehensive summary and evaluation of the strength equations, stiffness equations, and bond degradation equations involved in these constitutive models.

Chapter 4 Introduces the Modified Cam-clay model and verifies the reliability of corresponding simulation results across various consolidation ratios, discusses the feasibility of adjusting yield surface shapes using Hierarchical Single Surface (HISS) theory and the effectiveness of the subloading surface theory in facilitating a smooth transition in elastoplastic processes, proposes an elastoplastic constitutive model for GHBS using HISS yield surface

incorporating the cementation effects of hydrates associated with subloading surface coefficient while considering cross-anisotropy, captures model parameters from the literature for numerical analysis and validates through comparison with experimental results varying in hydrate saturation and hydrate occurrence forms.

Chapter 5 Summarizes the main conclusions, proposes the direction for further research.

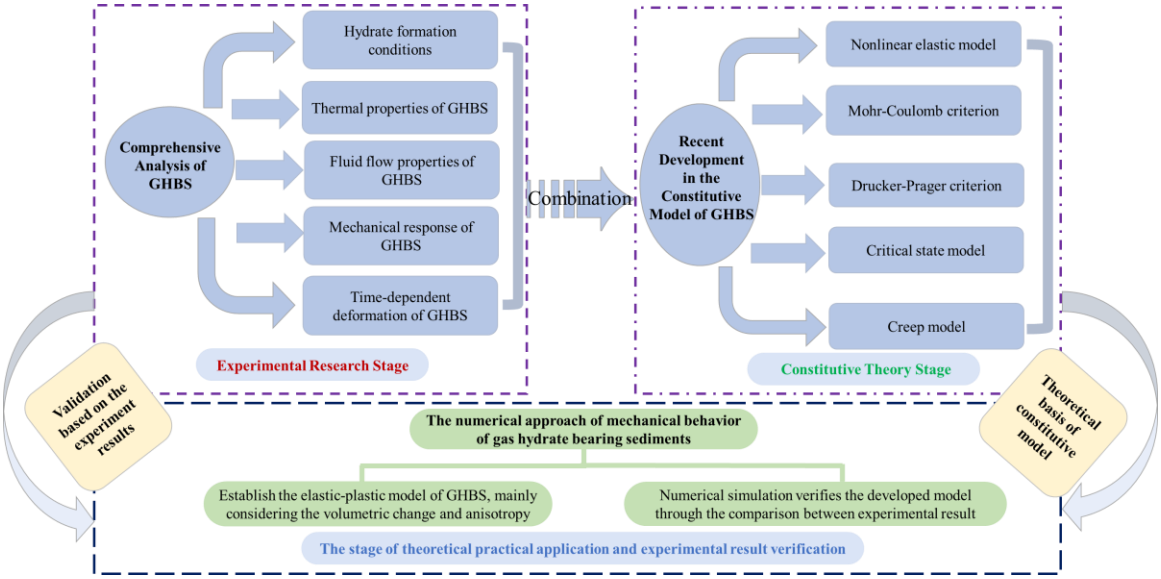

Figure 0: The structure framework of PhD thesis

Chapter 1. Introduction

Chapter 1 offers an extensive introduction to the subject of this thesis, encompassing the object of study, its background, structure, and practical significance. Initially, section 1.1 begins with the definition and historical origins of NGH, outlining how researchers discovered this compound and progressively explored its attributes, structure, and formation mechanisms, alongside their applications in society. Subsequently, according to the three main hypotheses of hydrate nucleation, the environmental and phase equilibrium conditions essential for hydrate formation are discussed and how temperature, pressure, gas composition, inhibitors, and promoters affect hydrate formation is elaborated. This chapter also describes the global distribution of hydrates and their potential as an energy resource, with a particular focus on their prevalence in marine sediments. Section 1.2 provides an overview of GHBS and the various morphologies in which hydrates manifest in both coarse-grained and fine-grained sediments. Considering the potential of NGH in the fields of environment and energy, the narrative shifts to hydrate extraction. Section 1.3 assesses the feasibility of hydrate recovery through the classification of hydrate reservoirs, and provides a detailed discussion of the advantages and disadvantages of three recovery methods, supplemented by case studies from field trials. Given the challenges associated with hydrate recovery, this section also contemplates the potential problems during the recovery process, particularly focusing on the impacts of hydrate decomposition on climate change and geological hazards. Finally, the importance of studying the geo-mechanical behavior of GHBS and corresponding constitutive modeling is highlighted.

1.1 Natural gas hydrate

1.1.1 Historical process of research on NGH

NGH are solid, ice-like compounds in which gas molecules are encapsulated in a cage-like lattice formed by water molecules through hydrogen bonding (Hassanpouryouzband et al., 2020; Yu et al., 2019). Research on NGH can be divided into three phases: laboratory research, resource investigation, and recovery. The initial laboratory research began in 1778 when Joseph Priestley

obtained crystals by introducing sulfur dioxide into water at lower temperatures, although he did not identify these as hydrates (Tse, 2015). In the early 19th century, Sir Humphry Davy synthesized chlorine hydrates in the laboratory, which he was the first to term as hydrates (Davy, 1800). Further interest in the structure and thermodynamic properties of hydrates emerged in 1934 when Hammerschmidt reported an ice-like substance obstructing natural gas pipelines, which remained stable at temperatures above the freezing point of water (Hammerschmidt, 2002). In the 1930s, Soviet researchers discovered the presence of natural methane hydrates in Siberia, followed by similar findings in Alaska and the Mackenzie Delta in the United States and Canada (Beauchamp, 2004). With the implementation of deep-sea drilling programs in the 1980s, hydrate specimens were discovered worldwide. The turn of the 21st century saw notable advancements, with the Mallik project in the permafrost region of Canada's Mackenzie Delta marking the first commercial extraction of hydrates (Sahu et al., 2020). In 2013, Japan pioneered the extraction of hydrates from marine deposits, and in 2017, China achieved successful drilling and recovery of hydrates in the South China Sea, with prospects for commercial utilization by around 2050 (Feng et al., 2019; Yiallourides and Partain, 2019). The evolution of the research on NGH are illustrated in Fig. 1.1.

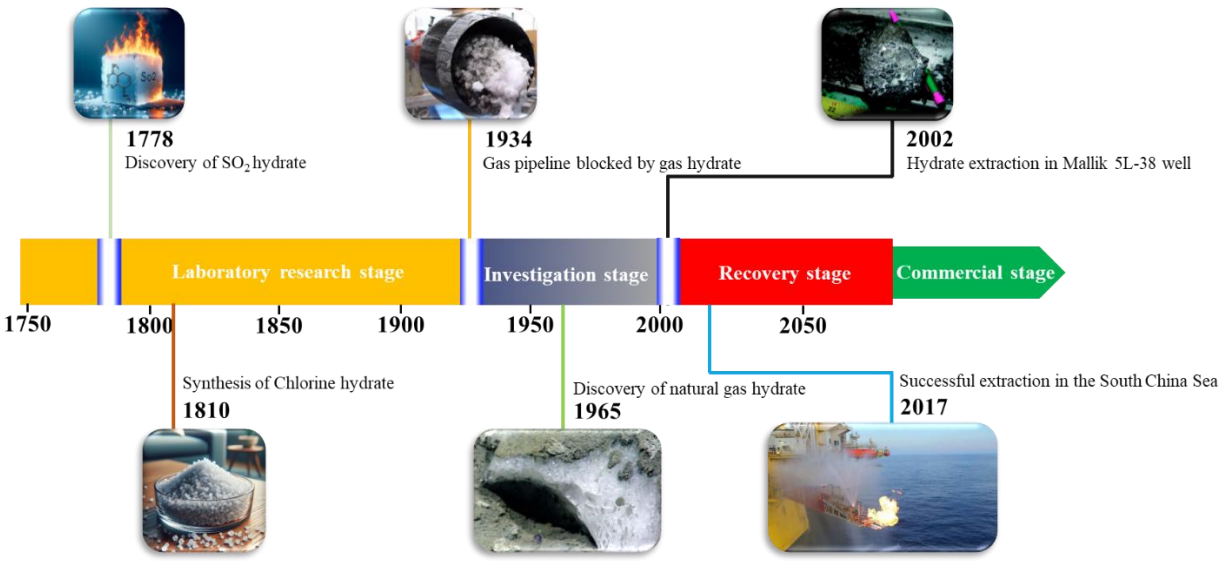

Figure 1.1: The development history of NGH

1.1.2 Hydrate structure

The molecular formula for NGH is typically denoted as M_nH_2O where M represents the type of encapsulated gas and n is the number of gas molecules. In 1940, the first structure of NGH was

identified through X-ray diffraction (Ripmeester, 2000). Over subsequent decades, techniques such as neutron diffraction and nuclear magnetic resonance were successively applied to the structural study of hydrates (Broseta et al., 2017; Mao et al., 2002). To date, the structures of NGH have been classified into three types based on the arrangement of water and gas molecules: Structure I (sI), Structure II (sII), and Structure H (sH) (Koh, 2002; Sloan, 1998) (Fig. 1.2). Each type of structures includes cage-like structural units such as the pentagonal dodecahedron (5^{12}), tetrakaidecahedron ($5^{12}6^2$), hexakaidecahedron ($5^{12}6^4$), pentakaidecahedron ($4^35^66^3$), and irregular icosahedron ($5^{12}6^8$) (Jin et al., 2013). Structure I hydrates are the most prevalent, typically encapsulating small molecular gases such as methane and carbon dioxide, with each cage structure consisting of 46 water molecules to form cages of 5^{12} and $5^{12}6^2$, yielding an ideal molecular formula of $8M{\cdot}46H_2O$. Structure II hydrates accommodate the gases larger than ethane and smaller than pentane, which consist of 136 water molecules that form 5^{12} and $5^{12}6^4$ cages, with an ideal molecular formula of $24M{\cdot}136H_2O$. Structure H hydrates involve larger molecules such as volatile oils, which consist of 5^{12}, $5^{12}6^8$, and $4^35^66^3$ cages, incorporating 34 water molecules to form an ideal formula of $6M{\cdot}34H_2O$ (Sloan, 2003; v. Stackelberg and Müller, 1954). The crystalline properties of these three types of hydrates are documented in Table 1.1,

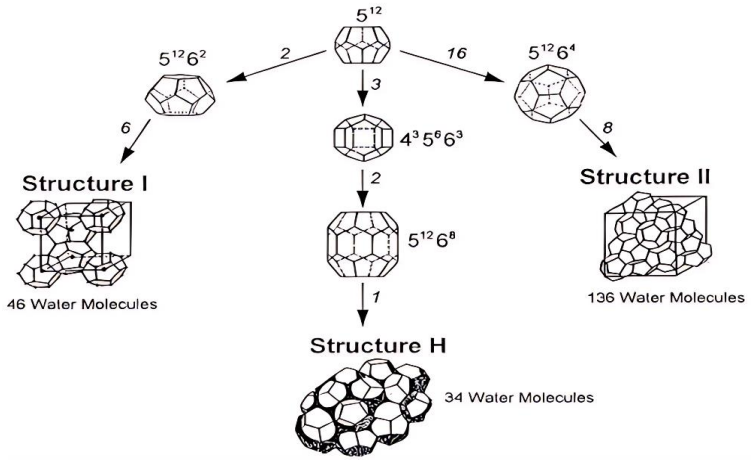

Figure 1.2: Various hydrate structures and their constituted cavities (Sloan, 1998)

Table 1.1: Properties of hydrate crystal structure (Koh, 2002)

Structure property	sI		sII		sH		
Structure units	5^{12}	$5^{12}6^2$	5^{12}	$5^{12}6^4$	5^{12}	$4^35^66^3$	$5^{12}6^8$

Cavity number	2	6	16	8	3	2	1
Number of water molecules	46		136		34		
Cavity radius (%)	3.4	14.4	5.5	1.73	-		
Density (kg/cm^3)	912		940		1952		
Lattice type	Cubic		Face-centered cubic		Hexagonal		

According to Sloan (1998), if the cavities within hydrate structure are completely filled, each guest molecule will be enveloped by the minimum number of water molecules, which results in a composition of approximately 85% water and 15% gas across all three hydrate structures. Given this high water content, it is postulated that the mechanical properties of hydrate structures should be similar to those of ice (Stern et al., 1998). Table 1.2 presents detailed characteristics of hydrate crystals alongside a comparison with ice. As shown in this table, some thermodynamic parameters differ, but Sloan's hypothesis is essentially correct.

Table 1.2: Comparison of properties of ice, sI and sII hydrate structures (Jr and Koh, 2007)

Property	Ice	sI	sII
Water molecule number	4	46	136
Lattice parameters at 273 K	a=4.52, c=7.36	12	17.3
Dielectric constant at 273 K	94	~58	58
Young's modulus (*GPa*)	9.5	8.4^{est}	8.2^{est}
Poisson's ratio	0.33	~0.33	~0.33
Bulk modulus (*GPa*)	8.8	5.6	8.482
Shear modulus (*GPa*)	3.9	2.4	3.6663
Compressional velocity (*m/s*)	3870.1	3778	3821.8
Shear velocity (*m/s*)	1949	1963.6	2001.14
Velocity ratio (comp/shear)	1.99	1.92	1.91
Linear thermal expansion at 200 K (K^{-1})	56×10^{-6}	77×10^{-6}	52×10^{-6}
Adiabatic bulk compression at 273 K (*GPa*)	12	14^{est}	14^{est}
Heat capacity ($J \cdot kg^{-1}K^{-1}$)	3800	3300	3600

Thermal conductivity ($W \cdot m^{-1}K^{-1}$)	2.23	0.49±0.02	0.51±0.02
Refractive index	1.3082	1.346	1.350
Density (kg/cm^3)	916	912	940

1.1.3 Hydrate nucleation hypothesis

In nature, the hydrate formation is a time-dependent crystallization process, in which gas sources are provided by microbial degradation and are diffused through liquid water (You et al., 2019). From a microscopic perspective, independent guest molecules undergo physical processes such as aggregation growth or separation, termed nucleation. Upon reaching a critical size, components from the bulk solution migrate to the hydrate particle-liquid interface, followed by reactions at the crystal surface, leading to continuous growth. Currently, there are three main hypotheses pertaining to the nucleation mechanism, which underpin the theoretical understanding of hydrate phase equilibrium (Warrier et al., 2016).

Labile Cluster Hypothesis (LCH) is widely applied regarding hydrate nucleation, which was proposed by Sloan and his coworkers (Christiansen and Sloan Jr., 1994) (Fig. 1.3). This hypothesis suggests that hydrate nucleation is triggered under low *T* and high *P*, where gas molecules are encapsulated in cages formed by water molecules through hydrogen bonding. As the reaction proceeds, water molecules self-assemble to form a complex lattice and create "cages" around gas molecules. The cage structure varies depended on gas type, manifesting as sI, sII, or sH. CH_4 and CO_2 form sI while larger or smaller gas molecules result in sII, and sH necessitates the combination of two gas molecules (Sloan, 2003). Gas molecules continuously flow into the newly formed cages with a certain rate affected by gas solubility. Hydrate crystals expand with increasing molecules, followed by agglomeration, ultimately resulting in the accumulation of hydrates (Jr and Koh, 2007; Wang et al., 2021). The higher the gas concentration, the faster the expansion of hydrate crystals and the shorter the nucleation time. Permafrost regions exhibiting excellent gas impermeability, and the deep sea characterized by high pressure and low temperature, are ideal environments for hydrate nucleation subjected to LCH (Schicks, 2022).

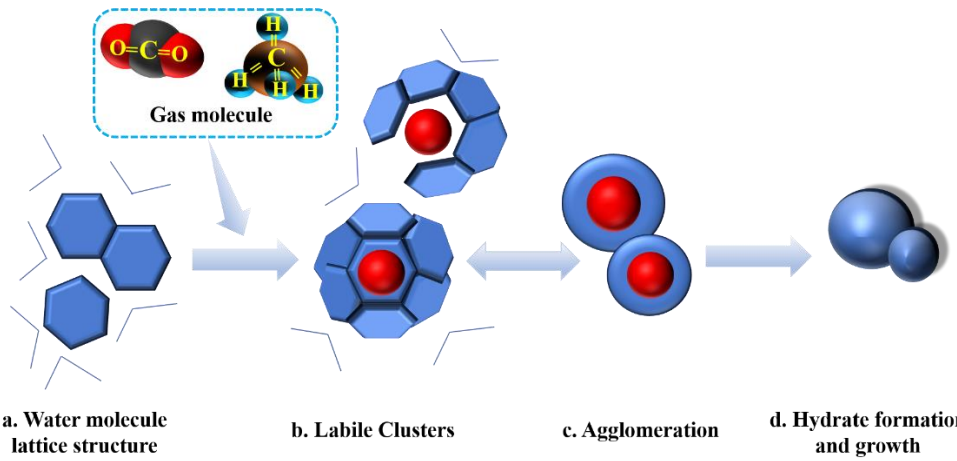

Figure 1.3: Mechanism diagram of hydrate nucleation (LCH)

However, this standpoint contrasts with the view of Radhakrishnan and Trout (Radhakrishnan and Trout, 2002), who argue that hydrate crystals should be separate rather than agglomerating. After that, they proposed the Local Structure Nucleation Mechanism (LSNM), asserting that gas molecules dissolve in mesh-like structures formed by water molecules to produce transient water clusters. Stable hydrate crystals formed by the clusters under *T-P* condition. This hypothesis explains why hydrate can form in the absence of nucleation conditions (Schicks and Luzi-Helbing, 2015). Nevertheless, given the reliance on localized structures, extensive experiments are required to verify its validation.

Blob Hypothesis is established by combining unstable cluster nucleation hypothesis with the local structure nucleation hypothesis (Jacobson et al., 2010). This hypothesis posits that heterogeneous liquid regions emerge termed "Blob" when gas dissolves in liquid water, which act as precursors to hydrate. Under specific *T-P* conditions, Blob structure undergoes disintegrating and reforming, transitioning from a heterogeneous liquid phase to a stable structure of NGH (Khurana et al., 2017).

1.1.4 Hydrate formation and stability conditions

The formation and stability of NGH are determined by their structures, thermodynamic factors, and gas composition. In seabed environment, overlying water column can exert pressure exceeding 10MPa, which is essential for hydrate formation. The elevated pressure augments gas solubility, enhancing hydrogen bonding and van der Waals interactions among gas and water molecules. This facilitates the diffusion and wrapping of gas molecules in water phase, promoting

hydrate nucleation (Tanaka et al., 2020). In natural settings, temperature ranging within 0-15°C is vital for hydrate formation, with variations dependent on deposit depth (Sahoo and Best, 2021). Lower *T* reduces the thermal movement between molecules and promotes the formation of hydrogen bonds and van der Waals attraction between water and gas molecules, which results in a stable hydrate crystal structure (Wang et al., 2022). With advancements in thermodynamic theory and the consolidation of foundational research, researchers have proposed to use phase equilibrium relationships to assess the stability of NGH. These relationships elucidate the interconnections among state variables such as temperature, pressure, and composition for different phases within a multi-phase system at equilibrium. Fig. 1.4 presents the phase equilibrium curves for NGH in marine and permafrost regions, clearly delineating their respective stability zones (Xie et al., 2020). The yellow dashed box in the figure marks the stability region for methane hydrates, while the white dashed line indicates the stability region for the hydrate structures containing larger molecules. The corresponding phase equilibrium boundaries are depicted with solid yellow and white lines, respectively. In the natural setting, most hydrates are sI methane hydrates, while larger molecular gas forms of sII or sH hydrates demonstrate greater stability and thicker phase equilibrium boundaries. Additionally, the red curve in the figure illustrates the geothermal gradient, showing an increase in formation temperature with greater depth below the Earth's surface, alongside a corresponding pressure increase of approximately 1 MPa per 100 m of descent (Lerche and Bagirov, 1998). In marine settings, the thickness of the hydrate boundary typically ranges from 300 to 500 m; however, in deeper regions, this boundary can exceed 1000 m, and in regions with lower geothermal gradients, the phase equilibrium boundary tends to be thicker (Booth et al., 1998; Max, 2003).

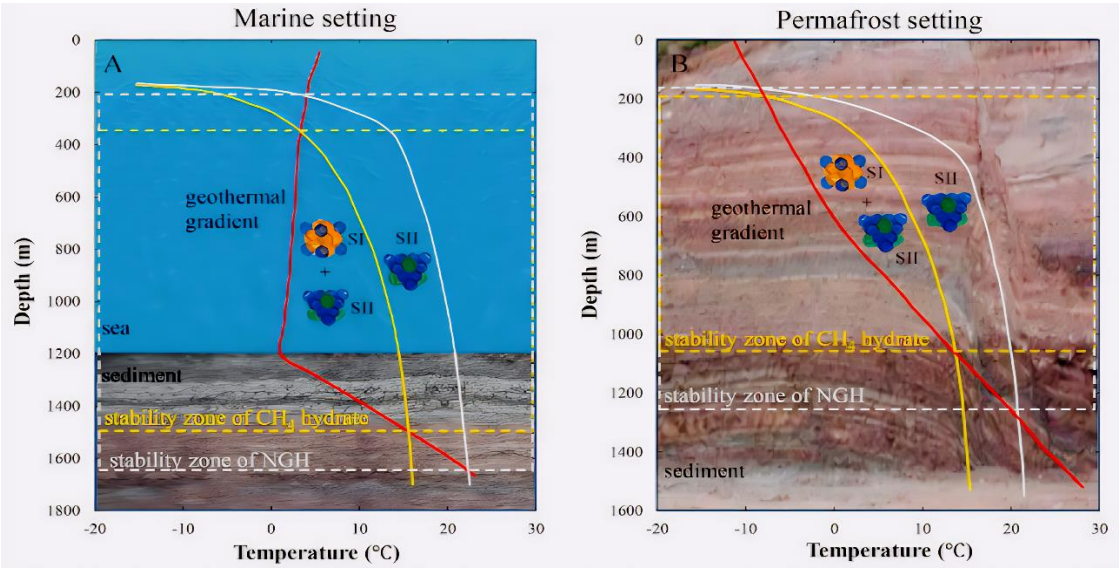

(a) Marine environment (b) Permafrost region

Figure 1.4: The phase equilibrium stability zone of NGH (Xie et al., 2020)

In addition to *T*-*P* conditions previously mentioned, there are other elements that influence hydrate formation and stability including gas composition, inhibitors, and promoters (Shahnazar and Hasan, 2014). Diverse gas compositions demonstrate distinct propensities for hydrate formation due to the variation in molecular size, polarity, and interaction forces between gas and water molecules. According to phase equilibrium curve, CH_4 hydrates as the primary component of NGH form under approximately 2.9MPa at 1.4°C, with increasing *P* requirements at higher *T*, meanwhile cutting down the formation time (Chong et al., 2016). In contrast, hydrates containing Ethane and Propane form at comparatively lower *P*. Also. it is observed that a decline in *P* that required for CO_2 hydrate formation. Hydrogen Sulfide (H_2S) alters the solubility dynamics induced by varying *P*, thus inhibiting hydrate formation under high *P* (Liu et al., 2013; Yang et al., 2015; Kvamme et al., 2014). For the mixed NGH, form conditions of which is more complex such as CO_2-CH_4 mixtures, the presence of CO_2 can significantly decrease *P* required for hydrate formation (Gupta et al., 2018). The phase equilibrium curves of hydrates consisting of different gas compositions are shown in Fig. 1.5.

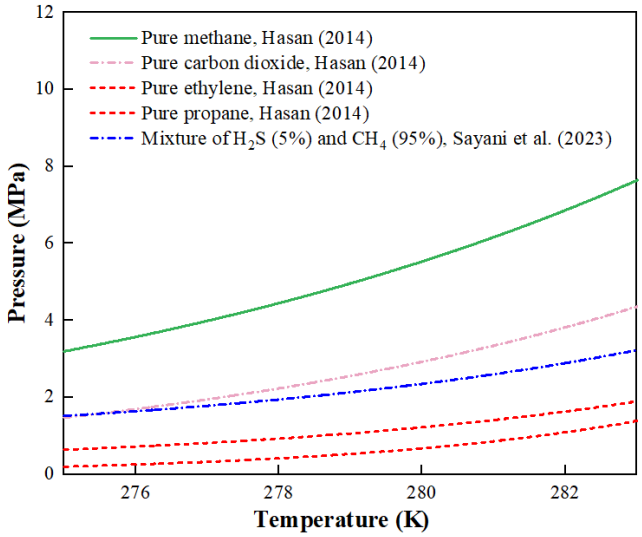

Figure 1.5: The phase equilibrium curve of hydrates with various gas compositions

The principal function of inhibitors lies in impeding the formation of hydrates. The compounds vie with gas molecules for water molecule interactions, consequently diminishing the probability for hydrate nucleation. In initial research, alcohols specifically methanol and ethanol have been identified as potent inhibitors, acting thermodynamically by shifting the hydrate equilibrium curve to lower *T* and higher *P* (Antunes et al., 2018; Kvamme et al., 2022). Kim et al. (2010) provided a comprehensive overview of hydrate inhibitors and examined that thermodynamic inhibitors were used at higher concentrations to shift hydrate equilibrium conditions, while kinetic inhibitors and anti-agglomerants were used at lower concentrations to deter the agglomeration of hydrate crystals. Moreover, Zhang et al. (2017) emphasized the potential of polyvinyl caprolactam as a low-dosage hydrate inhibitor, demonstrating the capability to prevent hydrate formation under flow assurance conditions. Richard and Adidharma (2013) investigated a novel ionic liquid inhibitor termed 1-ethyl-3-methylimidazolium chloride (EMIM-Cl), revealing that the effectiveness of inhibitors containing EMIM-Cl increases with *P*. Fig. 1.6a summarizes the research findings on phase equilibrium curve for hydrate formation in the presence of various inhibitors (Bavoh et al., 2018; Kim et al., 2011; Lee et al., 2016; Long et al., 2018, 2015), where the green curve represents the fitted phase equilibrium data for pure CH_4 hydrates, sourced from Deaton (1946). It is evident that the phase equilibrium curve incorporating inhibitors is positioned above the baseline green curve, indicating a higher *P* required for hydrate formation compared to CH_4 hydrates.

Inhibitors function by altering the thermodynamic equilibrium conditions, the mechanism of which stems from the destruction of water molecule structure induced by inhibitors (Fig. 1.6b). The elevation in *P* at which hydrates form is dependent on the concentration and type of inhibitor, and the suppression effect can be quantified by the relative shift of equilibrium curves in *T*-*P* space (Nasir et al., 2020).

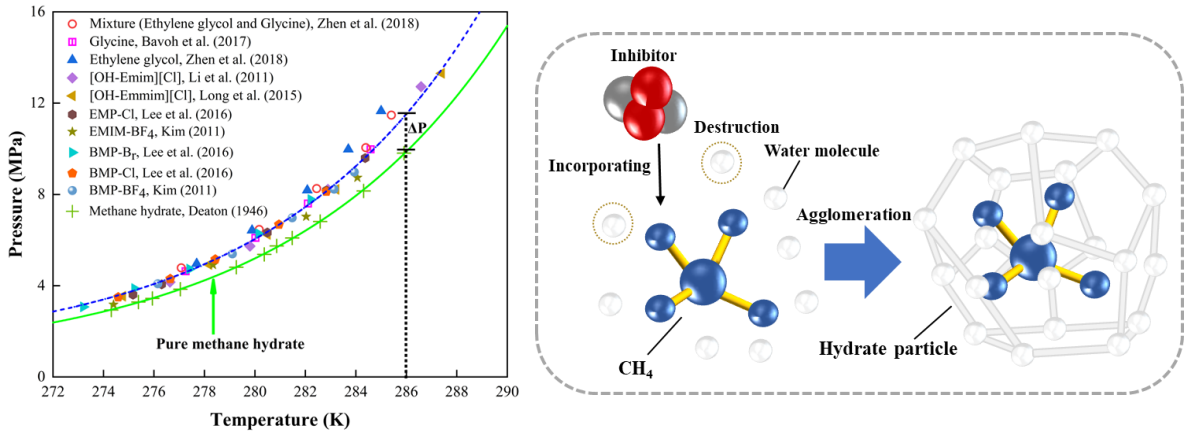

(a) Phase equilibrium curve (b) Mechanism of incorporating inhibitors

Figure 1.6: Effect of inhibitors on hydrate formation

Conversely, promoters modify the kinetic behavior of water molecules, which facilitates the interaction with gas molecules, thus augmenting the efficiency and stability of hydrate formation. Ghaedi et al. (2016) posited that salts can improve the ionic strength of solution, which lowers the freezing point of water and allows hydrate formation under higher *T*. Yet, excessive salt could inhibit hydrate formation due to the "salting out" effect. Sun et al. (2022) elucidated that short-chain alcohols can accelerate hydrate nucleation. This arises from the interaction of alcohols with water molecules, which disrupts the hydrogen bonding, expanding the volume accessible to gas molecules. Tetrahydrofuran (THF) is a widely utilized promoter owing to the decreased pressure for hydrate formation (Inkong et al., 2019). In addition, surfactants encompassing anions, cations, and non-ions, which can dramatically alter the rate of hydrate formation. Notably, anions expedite methane hydrate formation with an induction time that is approximately 15 times shorter than other surfactant categories (Viriyakul et al., 2021). Sodium dodecyl sulfate (SDS) demonstrates marked efficacy in diminishing the surface tension between two phases. This is attributed to the enhancement in gas solubility facilitating the interactions between gas molecules and water, thereby elevating the likelihood of hydrate formation (Partoon et al., 2013). Fig. 1.7 summarizes

the research results related to phase equilibrium curve for hydrate formation in the presence of various promoters (Inkong et al., 2019; Joon Shin et al., 2009; Sun and Sun, 2010; Torré et al., 2015), where the purple fitting curve represents the pure CO_2 hydrates, as reported in Vlahakis, 1972. In contrary to inhibitors, the phase equilibrium points incorporating promoters are all located below the fitting curve of pure NGH, indicating that promoters expedite hydrate formation by reducing the pressure necessary to form hydrates. It is noted that the phase equilibrium curve for pure CO_2 hydrate is observed to be positioned beneath that of pure CH_4 hydrate, which confirms the higher propensity for CO_2 hydrate formation.

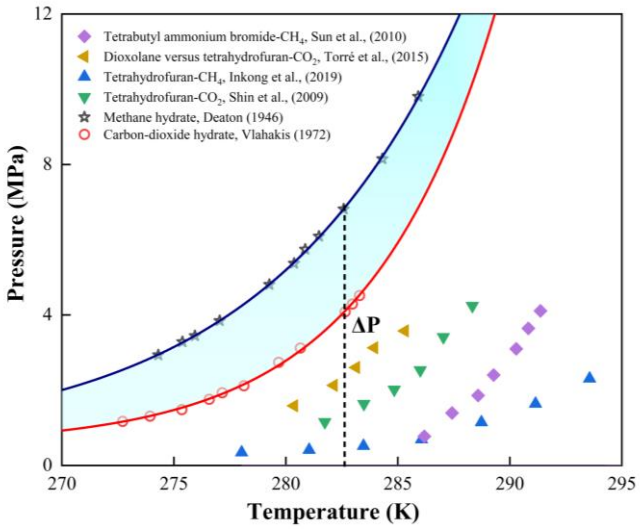

Figure 1.7: Phase equilibrium curve for hydrate formation in the presence of various promoters

Hydrate formation in porous media encompasses a multitude of factors, predominantly involving temperature and pressure modulation through incorporating specific inhibitors or promoters. Yet, the synergistic impact of combining chemical additives or additional liquid ionic concentrations has been insufficiently explored. It is appropriate to investigate the synergistic effects of multiple inhibitors and promoters to achieve optimal hydrate formation. Furthermore, the integration of nanoparticles holds the potential for enhancing the thermal stability of NGH.

1.1.5 Hydrate distribution and advantages

According to the stability conditions required for NGH, the ideal environments for the growth of NGH are characterized by high pressure and low temperature, thus hydrates are commonly found in permafrost regions and marine sediments (Chazallon et al., 2021; Demirbas, 2010). Such areas include continental margins, submarine highs, marginal seas, and deep-sea basins,

particularly at ocean depths ranging from 200 m to 600 m, which provide the stable environmental conditions necessary for hydrate stability (Mienert et al., 2005). Additionally, the geothermal gradient plays a critical role in hydrate stability by influencing the temperature at various depths (Kamath et al., 1987), which can exceed the equilibrium *T* for the corresponding in-situ *P*, thus fostering stable conditions for hydrate formation on continental shelves.

Globally, deposits of NGH have been identified in 116 regions, with terrestrial permafrost deposits primarily located in areas such as the U.S. Alaska, Canada's Mackenzie Delta, and Russia's Siberia, while marine deposits are mainly found in the Sea of Japan, the Indian Ocean, the South China Sea, the Gulf of Mexico, and the Caribbean Sea (Collett et al., 2011; Majorowicz and Osadetz, 2001; Milkov and Sassen, 2001; Yakushev and Chuvilin, 2000). Simulation studies suggest that approximately 27% of global terrestrial areas and about 90% of marine areas fall within potential hydrate growth zones (Makogon et al., 2007). Specifically, the areas conducive to natural gas accumulation in the global oceans cover about 189×10^6 km^2, of which about 30% may contain NGH (Milkov, 2004). A detailed map of the global distribution of NGH is displayed in Fig. 1.8.

Currently, coal, oil, and conventional natural gas are the primary constituents of the global energy supply. However, according to the estimates by the United States Geological Survey, the carbon storage capacity in NGH is expected to exceed twice that of conventional fossil fuels (Yu et al., 2021). Fig. 1.9 visually compares the reserves of hydrates with other conventional fuels, illustrating the significant potential of hydrate resources. The vast majority of NGH reserves are located in the oceanic deposits, with a relatively minor portion stored on land. Estimates suggest that the volume of methane hydrates in marine regions ranges from 3.1×10^{15} to 7.6×10^{18} m^3, while in permafrost regions, the reserves range from 1.4×10^{13} to 3.4×10^{16} m^3. Statistically, the global supply capacity of NGH is valued between 2.83×10^{13} to 8.5×10^{13} m^3 (Chibura et al., 2022; Judd, 2000). Additionally, NGH boast a high energy density; under standard conditions, the decomposition of one unit volume of hydrate releases 164 units of natural gas and 0.87 units of water, underscoring its potential as a sustainable energy resource (Moridis et al., 2011). Methane, the primary component of NGH, has a higher hydrogen-to-carbon ratio than other hydrocarbons, which results in lower carbon dioxide emissions upon combustion—approximately 50% less compared to other fossil fuels (Aregbe, 2017). This attribute makes methane a cleaner and more

environmentally friendly alternative, positioning NGH as a compelling option in the pursuit of reducing global carbon emissions.

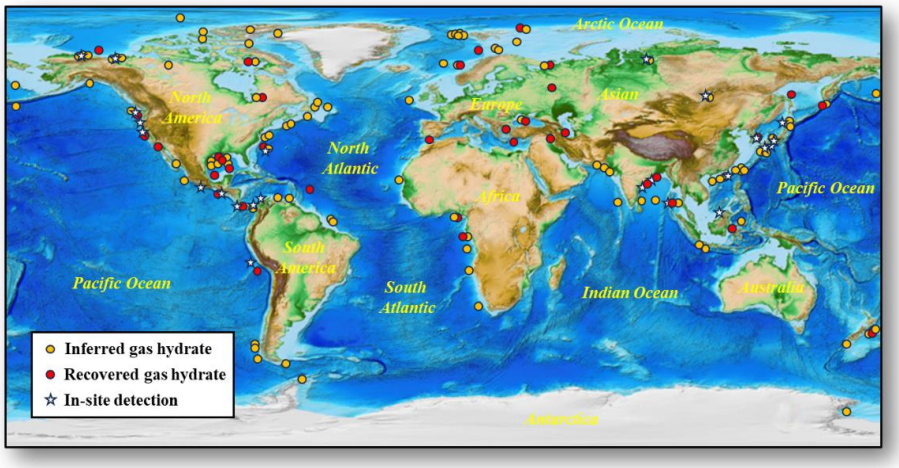

Figure 1.8: The distribution of NGH around the world (modified by Ruppel and Kessler (2017))

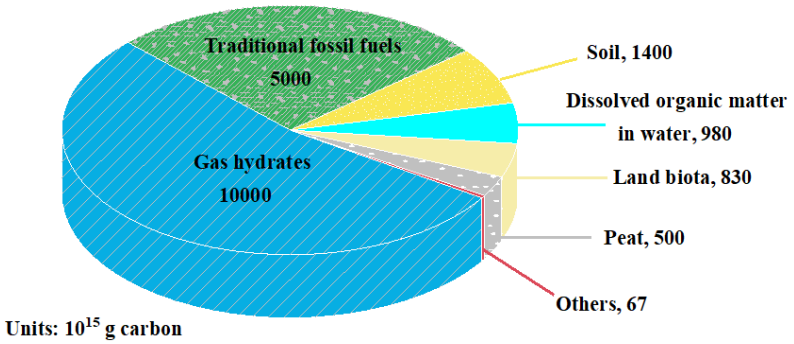

Figure 1.9: Carbon reserve of global energy resource (modified by Makogon et al. (2007))

Overall, with the rapid development of the world, the escalating demand for energy coexists with the stark reality of diminishing fossil fuel reserves. While traditional fossil fuels were once abundant, the usage of which has significantly impacted global emissions, resulting in environmental degradation and intensified greenhouse effect (Krey et al., 2009; Wei et al., 2021). Global energy crisis coupled with climate change demonstrates the urgent imperative for sustainable and environmentally-friendly energy sources (Misyura, 2020). NGH are considered to be the most promising energy resource in the 21st century due to their high energy storage, cleanliness, and abundant carbon reserves, which is also termed combustible ice (Huang et al., 2012).

1.2 Gas hydrate-bearing sediments

1.2.1 Overview

Seismic detection techniques play a pivotal role in assessing the distribution of NGH within continental margin storage zones in offshore areas (Pecher and Holbrook, 2003). Through the reflection of acoustic signals, seismic imaging enables the visualization of subsurface structures, where the presence of bottom simulating reflector (BSR) is commonly indicative of potential hydrate reservoirs (Hyndman and Spence, 1992). However, the absence or subtlety of BSR does not preclude the existence of NGH, as it primarily marks the base of stable hydrate formations and the top of free gas. It is noteworthy that seismic data have limitations in quantifying the volume fraction of shallow hydrates (Kumar et al., 2007). Seismic surveys involve the use of the air gun as a sound source and the deployment of multiple receivers, whose generated acoustic waves reflect the vertical motion characteristics of different materials. To enhance the accuracy of reservoir parameters, it is necessary to conduct multiple seismic surveys with varied operational parameters. Additionally, the differential deformation characteristics of shear waves (S-waves) and compressional waves (P-waves) are utilized to provide deeper insights into the distribution and quantity of NGH (Biswas, 2022). Marine electromagnetic methods, although still in the early stages of research, have demonstrated potential for effectively characterizing hydrate distributions (Schwalenberg et al., 2020). With the integration of these diverse methods, the detection and characterization of NGH deposits have made great advancements.

NGH are typically stored in the pore space of porous sediments. GHBS refer to the sedimentary materials that are mixtures of sand, clay, and soil containing hydrates, which can be conceptualized as granular skeletons with pores, partially filled with liquid, gas, hydrate, or ice (Dai and Santamarina, 2017) (Fig. 1.10). The occurrence of NGH in sediments reflects the interactions between hydrates and host sediments, significantly impacting the physical-mechanical properties of host sediments, with the extent of impact depending on the hydrate content and its distribution within the pore spaces. Initial studies have indicated that hydrates may manifest in dispersed, nodular, vein, and massive forms within sediments (Burger et al., 2003). With further research on the effects of capillary pressure and thermodynamics, scholars found that the hydrate morphology is controlled by the particle size of the sediment matrix. Host sediments can be

categorized into coarse-grained sediments and fine-grained sediments due to the difference in particle size, where coarse-grained sediments have a median grain size (d_{50}) larger than 75 μm while fine-grained sediments have a d_{50} smaller than 75 μm (Park et al., 2018). In coarse-grained sediments like gravels, the larger pore spaces coupled with lower capillary pressures contribute to higher permeability, facilitating the mobility and clustering of gas molecules within the hydrates, which result in the formation of fluids that fill the pores. Conversely, fine-grained sediments such as clays and mudstones exhibit low permeability due to smaller pore sizes and higher capillary pressures, which restrict the supply of gas molecules and inhibit fluid flow (Dai and Santamarina, 2017). Hydrate formation in coarse-grained sediments is invasive, where accumulated hydrates form cage-like clusters that extend into new pores; whereas in fine-grained sediments, hydrate growth is displacement-based (Terzariol et al., 2020); it occurs by displacing surrounding fine-grained sediments, with the reorganization of the spatial structure within the pores, potentially leading to the formation of isolated hydrate bodies such as lenses or nodules. Although over 90% of NGH are stored in fine-grained sediments (Li et al., 2021), research has predominantly concentrated on coarse-grained sediments, which is driven by: compared to the fine-grained sediments, the coarse-grained sediments exhibiting high permeability supports hydrate formation, the facilitation of the detection via seismic methods owing to the evident variations in acoustic impedance, the ease of gas production associated with their porous structure, and the ease of hydrate recovery because of the stable depositional environments such as river deltas and seabed deposits. Current research indicates that hydrate morphology is not only controlled by the properties of the host sediment (porosity, permeability, and grain size), but also is influenced by necessary chemical components and environmental conditions (Xie et al., 2020).

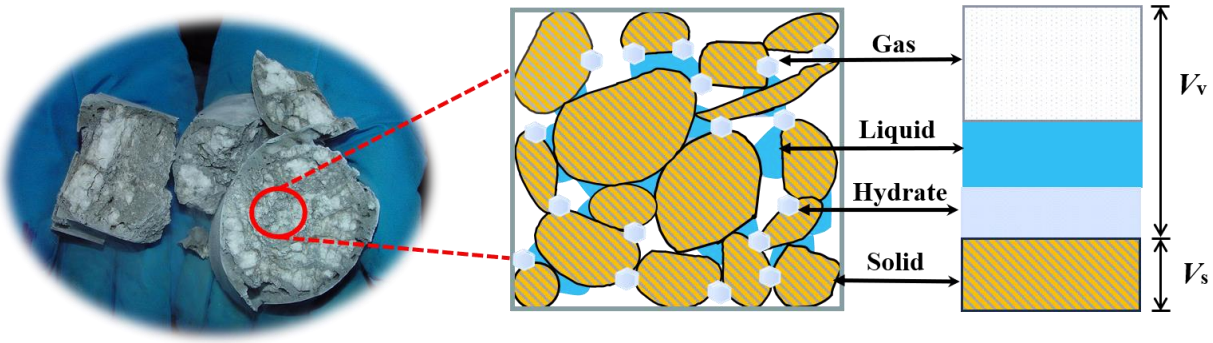

Figure 1.10: The multiphase system of GHBS

1.2.2 Hydrate morphologies in coarse-grained sediments

Hydrate morphology (HM) refers to the physical arrangement and distribution of hydrates within the pore space of sediments (Yang et al., 2015). Understanding HM could help in predicting the fundamental properties of host sediments. For the coarse-grained sediments, hydrate morphologies mainly include five types, with the dependent of hydrate content within pore space. In geological science, the content of hydrate crystals can be expressed as hydrate saturation. hydrate saturation (the volume fraction of hydrates within the pore space of sediments) is defined as the ratio of hydrate volume to the total pore volume, which can be expressed as (Zhang et al., 2015):

$$S_h = \frac{V_h}{V_v} \times 100\% \tag{1.1}$$

where V_h is the hydrate volume, V_v is the pore volume

The different pore habits of hydrates in coarse-grained sediments are shown in Fig. 1.11. At lower hydrate saturation (S_h < 25%), the predominant morphology observed is pore-filling where hydrates grow as part of pore fluid and occupy the pore space without contacting the particles. In this case, it exhibits an enhancement in the density and acoustic impedance of host sediments while impacting their permeability and bulk modulus (Guo et al., 2023). The kind of hydrates can be easily identified in seismic surveys, with a lower risk of gas leakage during the recovery. Successful detections of such hydrates have been reported in diverse regions, including Japan, the South China Sea, and the Gulf of Mexico. When S_h = 25~40%, it exhibits an improvement in bearing capacity, transitioning into the load-bearing morphology. Hydrate binds multiple sediment grains to support the weight of overburden, enhancing the mechanical properties of GHBS (Mahabadi et al., 2019). In an intermediary phase referred to as the patchy state (S_h = 0~100%), hydrates are unevenly distributed in sporadic clusters or fragments within host sediments, where variations in local S_h can induce notable local differences in the physical and chemical properties of sediments and also affect the stability of the reservoir and fluid flow behaviors (Bagherzadeh et al., 2011). The cementing type tends to appear at higher S_h (S_h > 40%) where hydrate acts as binders to connect with sediment grains, with the supplement of cementation effect, which displays enhanced mechanical properties and reduced compressibility in deposits (Wu et al., 2023). A distinct type is grain-coating where hydrates generate a thin “coat” on the grain surface, effectively encapsulating the particles. This coat serves as a barrier to impede the flow of gas and liquid,

exerting a substantial impact on fluid permeability (Li et al., 2021). Such hydrates have been discovered in the Mackenzie Delta and Blake Ridge.

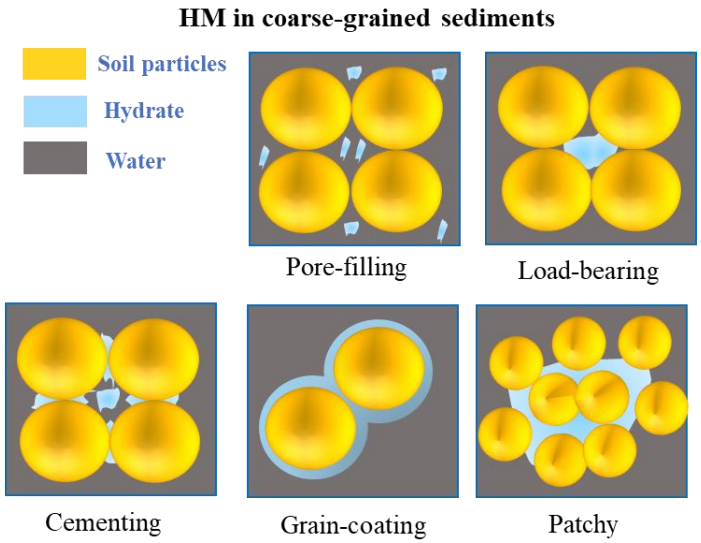

Figure 1.11: Schematic of different HM in coarse-grained sediments

In essence, for the coarse-grained sediments, HM can be broadly categorized into inter-granular and grain-boundary structures (Wu et al., 2015). For intergranular occurrences, hydrates nucleate and grow within the pore spaces of grains without altering the physical contact or configuration, encompassing both pore-filling and patchy types. For grain-boundary occurrences, which involve the interaction between hydrate and grain structures. The load-bearing and cementing morphologies are characterized by hydrate providing structural support or interconnecting with sediment grains, whereas the grain-coating morphology manifests as hydrates enveloping sediment grains, creating the physical barrier.

1.2.3 Hydrate morphologies in fine-grained sediments

According to the research by Terzariol et al. (2020), the pore habit of hydrates can be determined by the ratio of vertical effective stress to capillary pressure difference; the ratio greater than one indicates the pore-invading type, while the ratio less than one suggests the grain-displacing type. In fine-grained sediments, due to high capillary pressures, hydrates predominantly exist either by pore-filling or grain-displacement, with the grain-displacing pore habit typically manifesting as isolated lenses and nodules (Holland et al., 2008). In certain specific deposits, hydrates may accumulate locally, forming discontinuous parallel lenses, with their distributions

and morphologies influenced by subsurface fluid dynamics, local geological structures, and the properties of the host medium (Jang and Santamarina, 2016). In heterogeneous permeable sediments, nodular hydrates can disrupt the homogeneity of the sedimentary layers; for instance, the accumulation of methane with locally high concentrations can facilitate the precipitation of hydrates in discrete nodular forms. Additionally, vein-like distributions of hydrates have been frequently observed in clay sediments when fluids containing abundant methane migrate and accumulate along sedimentary fractures (Lv et al., 2020). Due to the crustal movement, sediment may occur in layers, in which case hydrates commonly distribute evenly in a layered manner, with alternating high and low permeability layers aligned parallel to the bedding of the sedimentary layers (laminate) (Lei and Santamarina, 2019). The different pore habits of hydrates in fine-grained sediments are shown in Fig. 1.12.

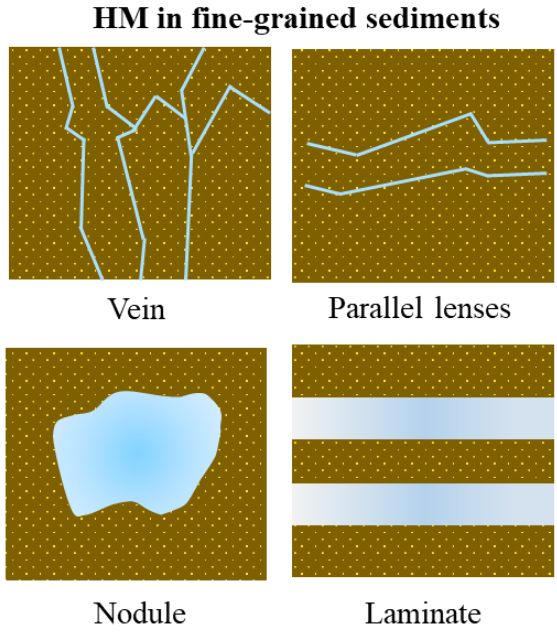

Figure 1.12: Schematic of different HM in fine-grained sediments

1.3 Gas hydrate application and extraction

1.3.1 Hydrate reservoir classification

In the 1980s, the scientific community initially believed that submarine hydrates were prevalent across the globe in stable *T-P* conditions. However, subsequent research has gradually revealed that the hydrate morphology in the stability zone is influenced by various geological and environmental factors, such as the salinity of pore water and regional geothermal flux (Minshull et al., 2020). These factors trigger complex geometrical configurations of the hydrate stability zones in both horizontal and vertical directions, leading to a highly uneven distribution of hydrate resources across different regions. Additionally, hydrate extraction is determined by multiple factors including temperature, pressure, gas sources, migration pathways, and storage spaces, which result in significant variability in the production characteristics and extraction difficulties of hydrates across various geological settings (Wei et al., 2024). Similar to other fossil fuels, the most accessible hydrate deposits typically contain fewer resources, while those with substantial reserves often pose severe extraction challenges. It has been reported that the potential value and extraction difficulty of different NGH deposits are distributed as a pyramid, as depicted in Fig. 1.13. From the top to the bottom of the pyramid, there is a progressive increase in both the difficulty of hydrate extraction and the volume of resources. The top layer of the pyramid is the sandy hydrate in the permafrost regions characterized by larger grain sizes, high porosity, and permeability, which are currently extractable with existing technologies and where research is comparatively abundant. In contrast, the bottom layer comprises dispersed hydrates in clay deposits that possess the largest resource volume and there is no precedent for successful extraction so far due to their low permeability. The middle layer consists of the hydrates stored in marine sandy sediment, which hold substantial resources with favorable porosity and permeability characteristics and are considered to have promising extraction potential (Pang et al., 2021).

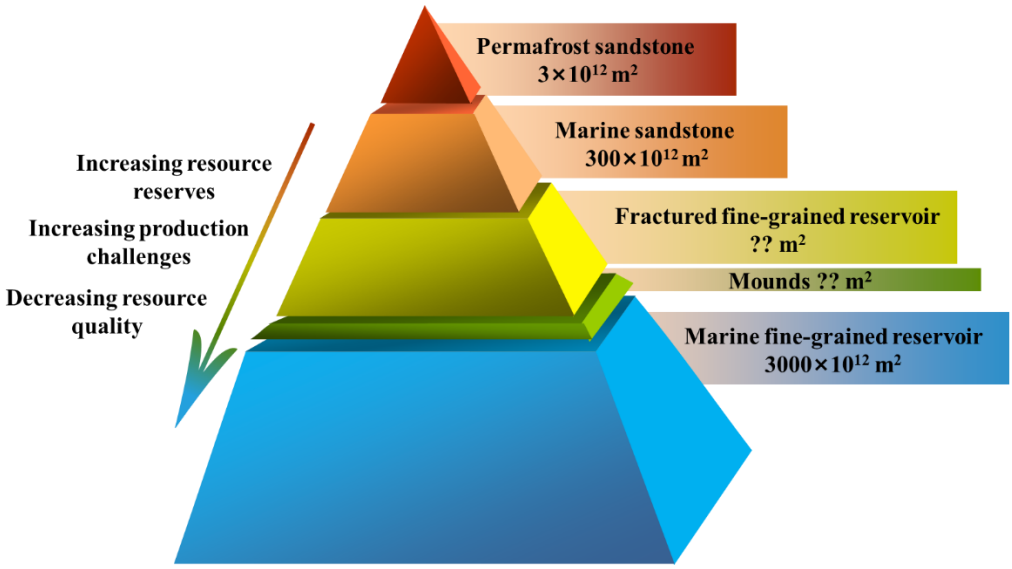

Figure 1.13: Resource pyramid for NGH (modified by Collett et al. (2009))

Based on the variations in geological structures and trapping conditions, NGH reservoirs can be further classified into four distinct types, as illustrated in Fig. 1.14 (Ersland, 2010; White et al., 2011). Type I reservoirs consist of a GHBS layer, a gas layer, and both above and below impermeable layers in which hydrates often exist at critical phase equilibrium, and the sedimentary layers aid in trapping the gas released during hydrate decomposition, which presents substantial extraction potential. Type II reservoirs include a GHBS layer and a water layer, along with the impermeable layers, with the primary distinction from Type I being the fluid phase beneath the hydrate layer. Type III reservoirs are comprised of only a GHBS layer and impermeable layers without the free gas layer, which are characterized by low S_h and low permeability; these reservoirs are prevalent in natural settings but are difficult to develop. Type IV reservoirs differ from the previous three types as hydrates are dispersed in low-permeability sediments as extensive nodular structures, their low S_h and non-stratigraphic distribution generally exclude these reservoirs from being targeted for extraction due to economic and technical constraints (Malagar et al., 2019).

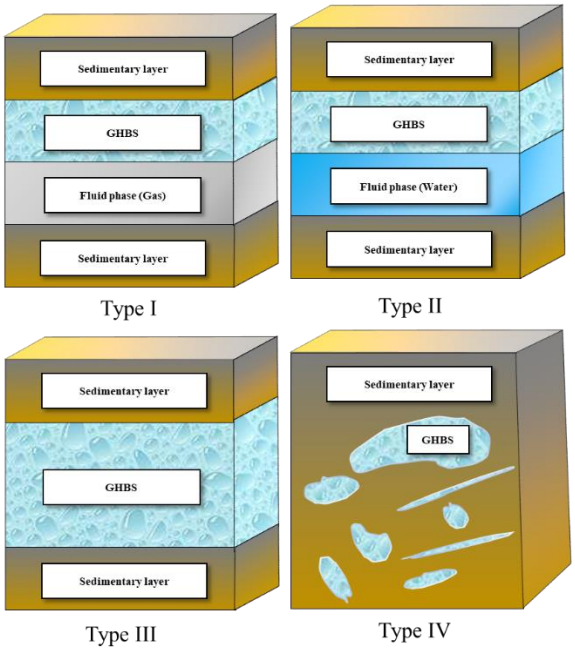

Figure 1.14: Classification of hydrate deposits

In summary, hydrate reservoirs that are suitable for large-scale commercial extraction should exhibit the following characteristics: a. Survey and sampling confirm high hydrate concentration in the reservoir; b. Stable geological structure of the reservoir conducive to safe extraction; c. Hydrate reservoir is effectively enclosed by geological traps to ensure the containment of produced gases; d. Produced alkane gases can be transported to natural gas markets via subsea pipelines, with the economic feasibility of extraction and transportation costs.

1.3.2 Methods for gas hydrate recovery

Since the 1930s, incidents of hydrate blockages in natural gas pipelines to the present studies showcasing the potential of hydrates as an energy resource have revolved around the issue of hydrate recovery. The key to the solution lies in inducing the dissociation of hydrates. In the gas production from GHBS, the phase equilibrium state of hydrates is of paramount importance, the specific principle involves altering *T-P* conditions of hydrates from their stable state to a non-stable zone below the phase equilibrium curve, thereby triggering decomposition. To date, three predominant techniques have been extensively employed for hydrate extraction: thermal stimulation, depressurization, and CO_2 replacement (Fig 1.15) (Zhao et al., 2015).

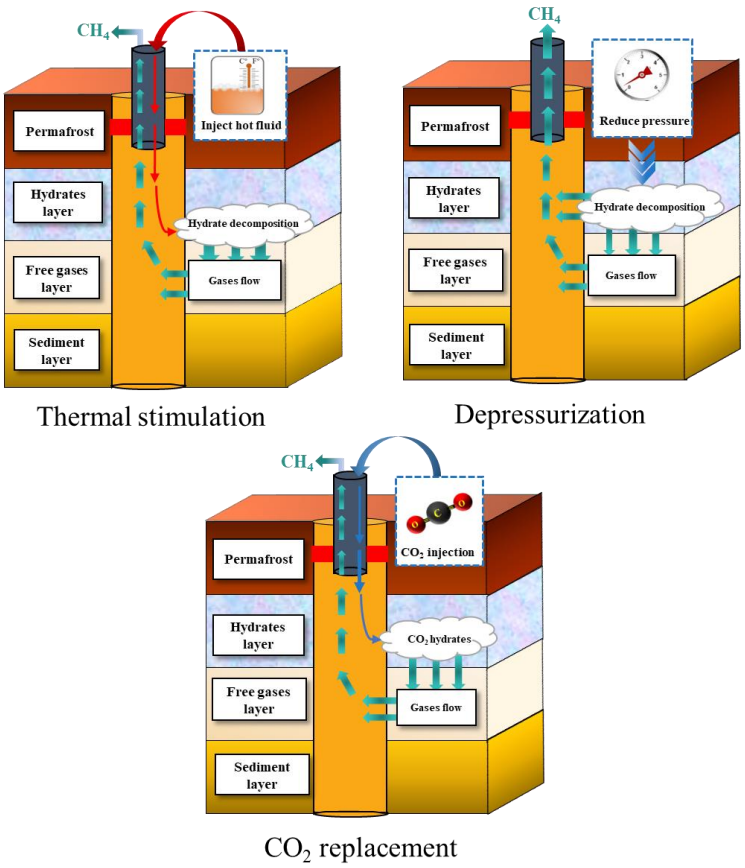

Figure 1.15: Methods for recovery hydrates in sediment deposits

Depressurization is the predominant technique for inducing hydrate dissociation. Compared to other methods, it is the most energy-efficient and boasts a higher gas production rate (Cui et al., 2021). This process entails reducing the reservoir pressure until below the hydrate equilibrium curve, prompting hydrate dissociation accompanied by the reduction in S_h (Zhang et al., 2015). It is crucial to note that hydrate dissociation is an endothermic reaction, which can provoke localized cooling and may consequently result in the reformation of hydrates. This is particularly problematic in reservoirs with low permeability, where it can cause blockages in gas production pipelines. Consequently, load-bearing capacity of deposits significantly diminishes, exposing a major drawback of this approach: GHBS are prone to volumetric deformation with a risk of settlement (Li et al., 2021).

Hydrate dissociation induced by thermal stimulation involves injecting heat fluids (including electromagnetic heating, steam injection) into GHBS, raising T to a point where it falls beneath the hydrate equilibrium curve (Wang et al., 2018). The migration of water and gas during the

process triggers localized thermal convection, which is believed to be interconnected with heat conduction. Therefore, thermal conductivity plays an indispensable role in this technique (Roostaie and Leonenko, 2020). Unlike depressurization, this technique demands substantial thermal energy with heat transfer processes susceptible to losses, leading to diminished energy efficiency. Additionally, heating causes heterogeneities in stress distribution within GHBS, potentially precipitating fractures and other structural damages. Analogous to depressurization, thermal stimulation weakens the bonds between particles and hydrates, reducing structural stability (Madhusudhan et al., 2019; Song et al., 2016).

CO_2 replacement is increasingly recognized as a promising environmentally-friendly approach for hydrate recovery, offering the dual benefits of natural gas recovery and CO_2 sequestration (Jung et al., 2010). The underlying principle leverages the equilibrium discrepancies between CH_4 hydrates and CO_2 hydrates under specific *T-P* conditions. CO_2 molecules are incorporated into the hydrate lattice by injecting CO_2 into CH_4-HBS, displacing methane molecules within GHBS (Prashant et al., 2005). Compared to other techniques, CO_2 replacement involves intricate procedures and necessitates precision equipment. However, the long-term stability of sequestered CO_2 in HBS poses unresolved challenges, with the potential for gas leakage remaining a critical issue (Chaturvedi et al., 2021).

The choice of dissociation methods during hydrate recovery hinges on reservoir characteristics and desired outcomes. Thermal stimulation provides a direct method for hydrate dissociation but necessitates high energy. Depressurization enhances energy efficiency but also raises possible geological issues. CO_2 replacement garners attention due to its distinct advantages, but the mechanical properties of CO_2-HBS require further examination (Cranganu, 2009; Komatsu et al., 2013). The applicability and limitations of the relevant methods are summarized in Table 1.3.

Table 1.3: Description of three strategies for NGH recovery

Strategies	Operated materials	Limitation	Applicability
Depressurization	Heating media	Affect the reservoir stability and block flow pipeline	Sedimentary layers with high permeability and high porosity

Thermal stimulation	Drilling and pump systems	High energy consumption and low decomposition efficiency	Low-temperature deposits or shallow reservoirs
CO_2 replacement	CO_2	The amount of injected CO_2 should be controlled	Regions required to strictly control greenhouse gas emission

1.3.3 Field trials for hydrate production

The trials for NGH recovery generally entail a systematic and multi-phased approach aimed at assessing the feasibility and potential of gas production from hydrate reservoirs. The process begins with geological exploration and assessment, which involves the use of seismic exploration techniques, geological drilling, and sample analysis to identify potential locations of hydrate reservoirs, and to evaluate their scale, depth, and stability (Hunter et al., 2011; Moridis et al., 2004). Following this, drilling operations are conducted to obtain core samples, which serve to validate the geological models and predictions previously established. Subsequently, test wells are installed to monitor the responses of the reservoir and to conduct preliminary gas production tests. This phase is crucial for observing the dynamic behavior of the hydrate reservoir under production conditions. The final step involves the use of experimental recovery technologies. This phase combines various recovery methods in small-scale trials to measure both methane production and reservoir response, whose primary objective is to assess the operational feasibility and efficiency of different recovery technologies (Collett et al., 2012).

In 2004, the Messoyakha NGH deposit located in the northwestern part of Western Siberia underwent commercial trial extraction by utilizing the depressurization method, with over half of the gas production resulting from hydrate decomposition (Makogon et al., 2005). In the early 21st century, the Mallik area of the Mackenzie Delta in Canada underwent several trial extractions, among which the Mallik 5L-38 well in layer A with relatively high S_h was extracted using thermal stimulation. The Mallik 2002 project employed a hot-water circulation system for thermal stimulation extraction; however, the gas production efficiency was low, making it challenging to meet the demands of large-scale commercial extraction. The Mallik 2007 project adopted a combined approach of depressurization and thermal stimulation for trial extraction, and results demonstrated that depressurization was more effective in well-conditioned hydrate reservoirs

compared to thermal stimulation (Fujii et al., 2008; Moridis et al., 2004). Despite the smooth progression of short-term trial extractions in this region, these efforts exposed an issue "how to supply the heat required for the phase transition decomposition of hydrates in long-term sustainable extraction". The Ignik Sikumi project on Alaska's North Slope achieved success in 2012 by displacing methane hydrates with CO_2 for the first time, illustrating that hydrates stored in the continent could be extracted using CO_2 replacement combined with depressurization, but it exhibited low efficiency when extracting hydrates in the deep sea (Collett et al., 2012; Hauge et al., 2014). In 2013, the world's first offshore trial extraction of generated hydrates in the Nankai trough was conducted via the depressurization method, though it was prematurely terminated due to the blockage of the equipment induced by sand production. A subsequent trial extraction for the Nankai trough in 2017 involved two wells over 36 d, yet challenges persisted in maintaining long-term production as gas production rates gradually declined (Noguchi et al., 2011; Yamamoto, 2015). From 2017 to 2020, three trial extractions conducted in the Shenhu area of the South China Sea encountered issues related to low porosity and permeability in the muddy fine-sand reservoirs. Chinese researchers managed to achieve stable gas production through independently developed equipment and an improved depressurization method, although the duration of trial extraction and the volume of gas production have yet to reach the thresholds for commercial development (Chen et al., 2018; Wei et al., 2018).

1.3.4 Climate changes induced by gas hydrate recovery

NGH are recognized as an energy resource with considerable potential but present significant climate hazard risks during the recovery. Compared to traditional fuels, hydrates are in a metastable state and maintain phase equilibrium only under specific *T*-*P* conditions. During exploratory drilling, factors such as frictional heating from the drill bit, variations in drilling pressure, the salinity of the drilling fluid, and recovery methods such as depressurization and thermal stimulation can disrupt the stability of hydrates, which can prompt the hydrate dissociation and the subsequent release of substantial amounts of alkanes (Gundersen, 2013). Alkanes are potent greenhouse gases, possessing a global warming potential of 25 times that of CO_2 (He et al., 2018). If these gases are not effectively captured and transported, or if the leakage occurs in the transport pipelines, they may be partially absorbed by the oceanic ecosystem, with the remainder escaping into the atmosphere, thereby exacerbating global warming. Furthermore, the increase in sea temperature and sea level induced by global warming will further affect the stability of marine

hydrate reservoirs, especially evident in shallow burial areas. In deeper burial areas, gases produced by hydrate dissociation must pass through thicker sediment layers, and the migration process to the overlying ocean or atmosphere involves passing through sediments that are still under hydrate-stable conditions. This may limit both the rate and the total amount of gas migration, potentially delaying the leakage of alkanes. Therefore, hydrate decomposition caused by artificial recovery and the consequent gas leakage has a significant impact on climate change, with natural factors reciprocally acting on hydrate dissociation to create a delayed cycle of dissociation and impact (Archer, 2007; Ruppel and Kessler, 2017).

1.3.5 Geological disasters caused by gas hydrate recovery

Submarine geohazards are frequently associated with GHBS, primarily due to changes in sediment stability triggered by hydrate dissociation. NGH function as a solid "cement" within these sediments, presenting in various morphologies and serving as a binding agent that fills pore spaces, which can enhance the structural stability and mechanical strength of the deposits. However, human activities including exploration and recovery of hydrates will alter the *T-P* conditions to which these hydrates are subjected, initiating hydrate dissociation. This process represents a complex multiphysics coupling phenomenon involving seepage, heat conduction, and strength reduction, as detailed in Fig. 1.16 (Liu et al., 2019; Wang et al., 2022; Wei et al., 2019). Hydrate dissociation is an endothermic process that absorbs heat from the surrounding environment. The effect of heat absorption and conduction can affect the temperature distribution of the surrounding sediments, thereby inducing thermal expansion or contraction. Moreover, hydrate dissociation generates water and alkanes, which suddenly alter the internal pressure within spaces previously occupied by the hydrates. Since alkanes have a much larger volume than solid hydrate, the rapid accumulation of gases increases the pore water pressure and meantime decreases the effective stress, and weakens the cementation between sediment particles. Consequently, the areas where hydrates have dissociated gradually lose shear strength due to insufficient consolidation. Once the sediment strength falls below a level that can resist gravitational or external disturbances (such as earthquakes), it heightens the risk of geohazards including liquefaction, settlement, foundation instability, and submarine landslides (Fig. 1.17) (Kvalstad et al., 2005; Sultan et al., 2004; Zhang et al., 2019). Although geological disasters directly related to hydrate extraction are rare, those associated with the stability of methane hydrates have been widely recorded and studied. As reported in the literature, historical events such as the Storegga Slide off the coast of Norway,

which involved approximately 3,500 km^3 of sediments, are believed to have been triggered by hydrate dissociation arising from the increase in seabed temperature or changes in seawater chemistry (Brown et al., 2006). Furthermore, geohazards such as the Beaufort Sea Slides off Alaska in the early 1990s and recent hydrate extraction trials in the Nankai Trough off the coast of Japan underscore the potential geological instability induced by hydrate dissociation (Colwell et al., 2004; Stow et al., 2012).

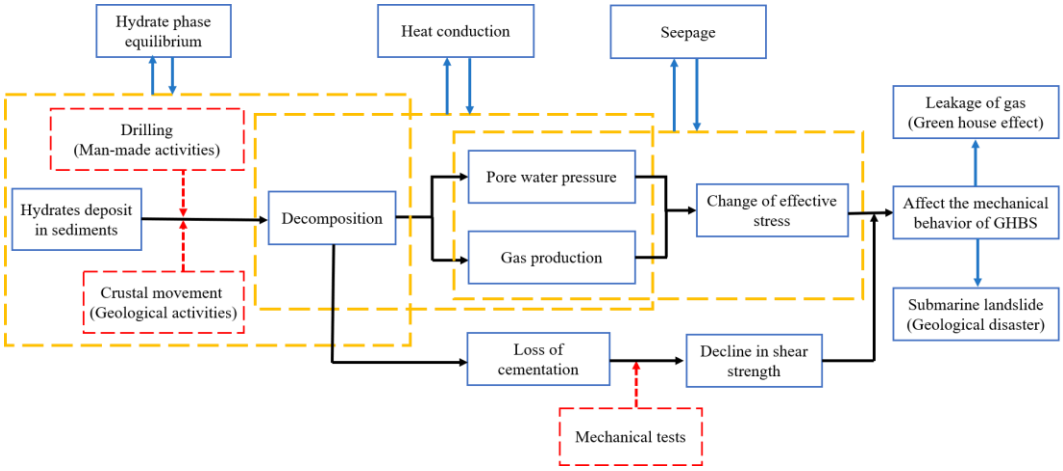

Figure 1.16: Several issues induced by hydrate decomposition (modified by Sultan et al. (2004))

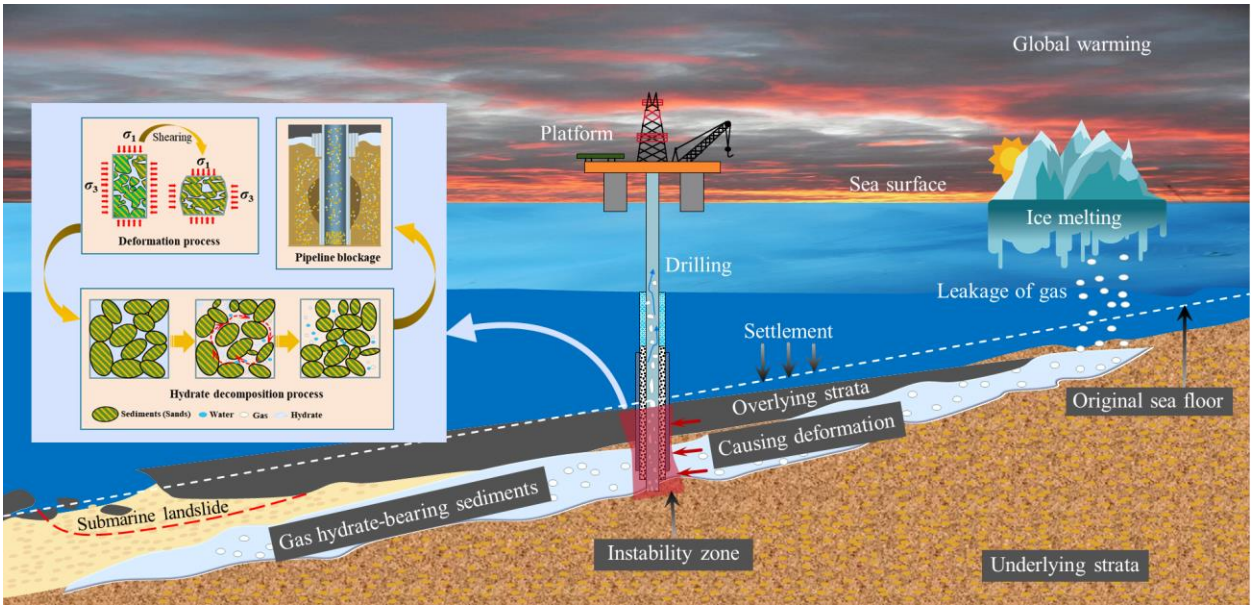

Figure 1.17: Schematic diagram of strength and deformation issues due to hydrate decomposition

1.4 Significance

1.4.1 The importance of exploring the geo-mechanical behavior of GHBS

The energy potential of gas hydrates is vast, prompting numerous international projects aimed at exploiting this untapped resource. However, hydrate recovery inevitably affects the stability of the surrounding sediments, and the risk of hydrate dissociation possibly triggers climate change and geological disasters. Understanding the mechanical properties of GHBS, such as strength, stiffness, and deformation characteristics, is essential for assessing the stability of hydrate deposits during gas production and mitigating potential geohazards. So far, extensive experiments conducted on GHBS have shown that the mechanical responses of sediments in the presence of hydrates are controlled by a wide range of factors, which can broadly be categorized into two groups: i. external stress loading paths; ii. internal matrix characteristics, including hydrate saturation, hydrate morphology, and sediment grain type. Therefore, it is necessary to compile and normalize existing mechanical test data to accurately characterize the geo-mechanical behavior of GHBS. This standardization analysis will not only support the validation of numerical models but also ensure the dependability of parameter relationships critical for effective modeling.

1.4.2 The importance of the constitutive modeling for GHBS

The geo-mechanical modeling of GHBS stands as a critical endeavor in understanding and predicting the complex behaviors of such sediments under various environmental and operational conditions. Advanced constitutive models are indispensable for simulating the enhancements in cohesion, dilation, compressibility, strength, and stiffness attributed to the formation of NGH. Traditional models, such as the Mohr-Coulomb and Drucker-Prager models, have provided foundational insights but are often restricted by the assumption of a unique yield surface shape. This assumption limits their flexibility in accurately capturing the diverse mechanical responses observed in GHBS, particularly under varying hydrate contents and sediment compositions.

The Hierarchical Single Surface (HISS) theory offers a significant advancement in this context. Unlike traditional models, HISS does not confine itself to a single yield surface shape. Instead, it employs a single yield surface with adjustable shape factors, allowing for the representation of a spectrum of yield surface characteristics by modifying just a few parameters.

This adaptability provides a more tailored approach to modeling the specific failure locus for different sediment types. Incorporating anisotropic effect into these models is also important because GHBS often exhibit pronounced anisotropic behaviors due to the directional properties of hydrate formations within the sediments. Traditional isotropic models fall short in capturing these directional dependencies, which are essential for accurate predictions of sediment behavior under stress.

The importance of developing geo-mechanical models for GHBS extends beyond academic interest, as it serves as a bridge between laboratory-scale experiments and real-world applications, allowing for the calibration and validation against observed field data. This iterative process of model refinement enhances the applicability of the models in supporting engineering decisions and geological predictions. Continuous improvements in computational methods and the integration of multi-physics approaches continue to push the boundaries of what these models can achieve, facilitating a deeper understanding of the geotechnical challenges posed by gas hydrates. In essence, the geo-mechanical modeling of GHBS is not merely a scientific pursuit but a practical necessity that informs the sustainable extraction of hydrate resources and the mitigation of related environmental risks.

1.5 Conclusions

This chapter is dedicated to describing the general characteristics of NGH bearing sediments, which involve key aspects: a. the energy value of hydrates; b. hydrate occurrence within sediments; c. the challenges of hydrate recovery from sedimentary layers. NGH, with their considerable carbon storage and high energy density, are recognized as one of the most promising energy resources globally, whose advantages depend on their unique structures. Also, structural features dictate the formation and stability of hydrates that can be describable via phase equilibrium curves. Additionally, gas compositions, inhibitors, and promoters can effectively alter the thermodynamic and kinetic conditions that influence hydrate formation. NGH are extensively distributed in marine sediments and permafrost, exhibiting varying forms of occurrence in coarse versus fine sediments. This variability significantly impacts the mechanical properties of host sediments and ultimately determines reservoir stability. Currently, three methods (thermal stimulation, depressurization, and CO_2 replacement) have been applied for hydrate extraction, each demonstrating own applicability

and limitations. During drilling, the instability of GHBS layers may pose uncontrollable potential risks, such as the leakage of greenhouse gas due to hydrate dissociation, submarine landslides induced by overburden collapse, and pipeline blockages caused by the leakage of particle sand during the deformation of host sediments. Therefore, understanding the geophysical-mechanical characteristics of sediments containing NGH is essential for the effective and safe recovery of hydrates. Constitutive modeling is an effective method that can replicate the stress-strain behavior of GHBS under various environmental conditions, which can save time and cost and avoid the challenges associated with synthesizing hydrates in the laboratory compared to experimental investigations. Given the limitations of the existing GHBS constitutive model, we have a strong interest in further modeling and characterizing its geo-mechanical behavior. The next chapter will elaborate on the basic physical properties of the host sediments and discuss the mechanical behavior of GHBS in response to various environmental and loading conditions.

Chapter 2. Fundamental physical-mechanical characteristics of GHBS

This chapter provides a thorough discussion on the fundamental properties of GHBS, with a particular focus on their thermal properties, fluid flow characteristics, and mechanical responses. Based on the discussion in Chapter 1 regarding the thermal conductivity involved in the decomposition of hydrates during extraction, thermal-related parameters including thermal conductivity, specific heat, thermal diffusivity, and reaction enthalpy are evaluated in Section 2.1. These parameters are assessed to quantify how GHBS respond to environmental temperature changes, covering both the heat transfer within the sediments and the energy required for hydrate decomposition, as well as the rate of heat propagation. Given that fluid permeability is crucial for gas production efficiency, the fluid flow properties of GHBS are described in section 2.2, emphasizing the importance of porosity and permeability. This section explains how hydrate content and distribution affect permeability, integrating experimental data and theoretical analysis to clarify how hydrates regulate fluid flow within host sediments. Additionally, the volumetric deformations of GHBS under isotropic loading are measured in terms of compressibility and compared with hydrate-free sediments, highlighting their distinct compressive behaviors. In Section 2.3, the importance of laboratory mechanical tests for predicting reservoir stability during the recovery of NGH is discussed, including methods of specimen preparation and the precision of testing equipment. The feasibility and limitations of current technologies are also assessed. In Sections 2.4 and 2.5, the mechanical responses of host sediments in the presence of hydrates and their variations in mechanical properties under the influence of external factors (effective stress, temperature, sediment matrix, loading rate, and porosity) are analyzed through normalizing data from the literature. Also, part of these sections reveals the control mechanisms of hydrates on the volumetric deformation and strengthening in host sediments from a micro perspective. Finally, the potential long-term deformation behavior of sediments due to prolonged hydrate extraction is discussed in Section 2.6.

2.1 Thermal property

The formation and decomposition of hydrates involve energy transformations, with the phase transition being particularly critical for heat conduction. The thermal properties of GHBS (Thermal conductivity, specific heat, thermal diffusivity, and reaction enthalpy) are crucial for the formation and stability of hydrates, as these parameters reflect the response of host sediment to thermal energy (Dangayach et al., 2015). The efficiency of hydrate extraction in submarine reservoirs depends significantly on these thermal properties. The thermal properties of different specimen components are summarized in Table 2.1, with the values measured under specific *T-P* conditions from existing literature except thermal diffusivity calculated using Equation 2.2.

Table 2.1: Comparison of the thermal-related parameters of different specimen components (Aromada et al., 2019; Hu and Xiao, 2023; Li et al., 2022; Waite et al., 2009)

Material	Thermal conductivity ($W / m \cdot K$)	Thermal diffusivity (m^2 / s)	Specific heat ($J / kg \cdot K$)	Density (kg / m^3)	Reaction enthalpy (kJ / mol)
Air	0.024 (273K)	183×10^{-7}	1010 (273K)	1.298 (272K)	11.57 (273K)
Water	0.58 (283K)	1.38×10^{-7}	4192 (283K)	999.7 (283K)	-285.83 (298K)
Ice	2.21 (270K)	11.7×10^{-7}	2052 (270K)	917 (273K)	-6.01 (273K)
Methane gas	0.0297 (260K, 1MPa)	18×10^{-7}	2170 (260K)	7.61 (260K, 1MPa)	-74.85 (298K)
Methane hydrate	0.57 (263K)	3.35×10^{-7}	2031 (263K)	929 (263K)	54 (281K)
CO_2 hydrate	0.53 (273K)	1.8×10^{-7}	2560 (271K)	1181 (270K)	63.18 (281K)

THF + water	0.47 (283K)	3.12×10^{-7}	4080 (282K)	982 (283K)	311.8 (298K)
$THF.17H_2O$					
THF hydrate	0.5 (261K)	2.55×10^{-7}	2020 (261K)	971 (273K)	130~163 (280K)
$THF.17H_2O$					
Quartz	7.7 to 8.4	41×10^{-7}	730 (273K)	2650	-

2.1.1 Thermal conductivity

Thermal conductivity (λ_T) is used to measure the ability of a material to transfer heat through a unit area per unit time under a unit temperature gradient in steady-state conditions. This parameter is the key to predicting the changes in heat flow within the sediment layer and the thickness of the hydrate stability zone, especially in the application of thermal stimulation for promoting hydrate decomposition, it is necessary to precise control over the thermal flow in the heating area, as which is related to the efficiency of gas production and the maximization of resource recovery (Cortes et al., 2009). Thermal conductivity is governed by Fourier's law, which provides the mathematical framework to quantify the rate of heat flow in response to a temperature gradient, given by the following (Narasimhan, 1999):

$$\lambda_T = -\frac{dQ}{dt}\frac{dx}{dT}\frac{1}{S} \tag{2.1}$$

Where Q is the amount of heat, t is the time, T is the temperature, x is the gradient, S is surface areas.

As demonstrated in Table 2.1, the thermal conductivities between particles, fluids, and air differ by nearly ten orders of magnitude. Given that GHBS are multiphase geomaterials, the geological heterogeneity of reservoirs directly determines their difference in thermal transmission efficiency. Heat transfer in GHBS involves three mechanisms: interparticle conduction, where heat is transferred through the contact points between sediment particles; particle-fluid-particle conduction, where heat is transferred through the fluid that envelops the particle contact points; and pore fluid transmission, where heat is conveyed via the fluids (water and gas) that fill in the pores (Yun and Santamarina, 2008). Thermal conductivity is typically obtained through laboratory experiment or in-site tests, with the majority of research relying on simulated and experimental data due to the challenges and costs associated with in-site measurement. Commonly laboratory

techniques employed for measuring thermal properties include the heat pulse probe method and the transient plane source method (Muraoka et al., 2019). Literature reports that the thermal conductivity of GHBS are determined by various factors including mineral composition, temperature, grain size, effective stress, and the characteristics and dimensions of pore spaces. The thermal conductivity of quartz is evidently higher than other soil-forming minerals such as clay or mica; meantime, the higher the quartz content in host sediment, the higher the overall structural thermal conductivity. Grain size influences thermal conductivity by the various contact areas between particles; larger particles such as coarse sand and gravel with greater contact areas possess higher efficiency in heat transfer (Pribnow and Umsonst, 1993; Tang et al., 2021). Water, as an excellent conductor of heat, can enhance thermal conductivity, particularly when it saturates particle contact points or fine pores (Lu et al., 2007). Thermal conductivity is inversely proportional to T due to the thermal expansion that increases lattice constants, thereby weakening interatomic interactions (Huang and Fan, 2005). Moreover, there is a positive relationship between thermal conductivity and vertical effective stress, this stems from the increased effective stress improves closer contact between sediment particles, thus boosting direct heat transfer between them (Cortes et al., 2009; Vargas and McCarthy, 2001) (Fig. 2.1). Although solid sand displays higher thermal conductivity than hydrates, sand containing hydrates demonstrates greater thermal conductivity, suggesting that hydrates enhance thermal transmission efficiency by increasing interparticle contact. In numerical modeling, thermal conductivity is often estimated using a two-phase model that combines the thermal conductivities of sediment particles and pore fluids. While the intricate multiphase systems may necessitate the consideration of interactions between hydrate, water, and gas, in many cases, the similar thermal conductivities of methane hydrate and water indicate that simplified models can still yield accurate approximations. However, in the case where pore spaces are predominantly occupied by gas, the thermal conductivity of gas is substantially lower than that of water and solid particles, and the simple averaging methods are no longer adequate. In these scenarios, the distribution and role of water at particle contact points must be considered, as even at low S_h, water can significantly enhance thermal conduction between crystal particles.

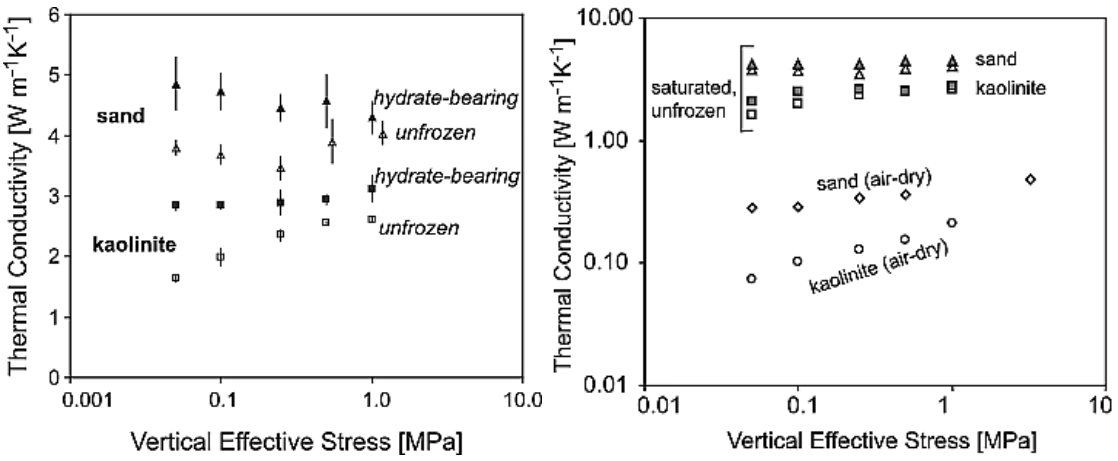

Figure 2.1: The change law of thermal conductivity under various effect factors (Cortes et al., 2009)

2.1.2 Specific heat

Specific heat (c^s) refers to the amount of heat required to raise the temperature of the material by 1°C, a physical quantity that is important during the dissociation of hydrates (Yang et al., 2019). Hydrate decomposition is an endothermic process; if insufficient thermal energy is available at the decomposed interface, the decomposition rate will be constrained. The specific heat of GHBS primarily depends on the mass fractions of minerals, water, and hydrates within the sediment. Unlike thermal conductivity, specific heat is not influenced by the distribution of pore sizes or interfacial effects, but directly correlates with the mass ratios of the material's components, with the expression represented by the following formula (Nakagawa et al., 2008):

$$\begin{cases} c^s_{GHBS} f_{GHBS} = c^s_m f_m (1-\phi) + c^s_w f_w (1-S_h)\phi + c^s_h f_h S_h \phi \\ f_{GHBS} = f_m (1-\phi) + f_w (1-S_h)\phi + f_h S_h \phi \end{cases} \tag{2.1}$$

Where c^s is the specific heat of each component, f is the mass fraction, the subscripts m, w, h, and GHBS represent the sediment mineral, water, hydrate, overall structure, respectively, S_h is the hydrate saturation, ϕ is the porosity.

As noted in Table 2.1, the specific heat of methane hydrate is 2031 J/(kg·K), which is approximately half that of water at its melting point (4218 J/(kg·K)), indicating that the presence of hydrates considerably reduces the specific heat, with greater reductions as the hydrate content increases. In reservoirs with high S_h, the reduced thermal storage capacity of the hydrates impairs their thermal stability and exacerbates the structural sensitivity to fluctuations in environmental T

(Zhao et al., 2015). An increase in porosity signifies a higher proportion of non-solid minerals in the pore space. Since the specific heat of gases is lower than that of solids and liquids, a higher porosity results in a reduction in overall specific heat (Waite et al., 2009).

2.1.3 Thermal diffusivity

Thermal diffusivity (κ_T) is a pivotal parameter that quantifies the rate of heat diffusion within a material, which is defined as the ratio of thermal conductivity to the product of density and specific heat (Vosteen and Schellschmidt, 2003). A higher value of thermal diffusivity implies that a material can respond more rapidly to changes in environmental T (Kumar et al., 2004). The formula for thermal diffusivity is expressed as:

$$\kappa_T = \frac{\lambda_T}{\rho \cdot c^s} \tag{2.2}$$

Where λ_T is the thermal conductivity, ρ is the density, c^s is the specific heat.

The integration of hydrates within sediments significantly enhances the thermal conductivity, and consequently increases the thermal diffusivity. As detailed in Table 2.1, the thermal diffusivity of THF hydrates (2.55×10^{-7} m^2 / s) is approximately twice that of water (1.38×10^{-7} m^2 / s). Waite et al. (2007) observed that in GHBS with 35% porosity and 35% S_h, the thermal diffusivity is 10% higher than in hydrate-free sediments (HFS). This augmentation is particularly pronounced in high-porosity sediments, such as those found near the surface on the Congo continental slope, where porosity reaches up to 74%. In such sediments, even S_h within the range of 19%-22%, the heating time is reduced by more than 10% compared to HFS, illustrating that GHBS exhibit higher thermal diffusivity and can respond more swiftly to T variations, with the degree of this response depending on porosity (Lucazeau et al., 2015). Kumar et al. (2004) investigated the thermal diffusivity of both methane hydrates and methane hydrate-bearing sediments, suggesting that the thermal diffusivity of methane hydrates exhibits a negative correlation with T, whereas that of HBS shows a positive correlation. This discrepancy indicates that the impact of T on thermal diffusivity is variable and dependent on the material composition (Zhao et al., 2018). In the context of hydrate recovery, when high-temperature hydrocarbon fluids pass through GHBS, the temperature of the sediment layer will be changed rapidly, which potentially affects the stability of the reservoir. Thus, it is imperative to examine the thermal diffusivity of hydrates.

2.1.4 Enthalpy of reaction

Reaction enthalpy (ΔH) quantifies the heat released or absorbed during a chemical reaction. The formation process of hydrates is exothermic, releasing heat into the surroundings, whereas the decomposition process is endothermic, absorbing heat from the environment (Avlonitis, 2005). The reaction equation is given by:

$$CH_4(g) + nH_2O\ (l) \rightleftarrows CH_4 \cdot nH_2O\ (s) \tag{2.3}$$

Where n is the hydration number.

The sign of the reaction enthalpy depends on the direction of heat flow; Hydrate formation reaction typically occurs under conditions of low T and high P, ΔH is negative for exothermic reaction. Conversely, hydrates decompose under conditions of rising T or falling P, a process that is inherently endothermic, with ΔH being positive. Current research indicates that the reaction enthalpy of GHBS is controlled by several factors, including the strength of hydrogen bonds, the size of guest molecules within cavities, and the occupancy of these cavities (Sloan, 1998). The strength of hydrogen bonds in the hydrate lattice significantly influences the reaction enthalpy, with approximately 80% of the decomposition enthalpy contributed by the strength of these bonds, which release and absorb the same amount of heat during the formation and decomposition of hydrates (Sloan and Fleyfel, 1992). Also, the cavities in the hydrate lattice occupied by guest molecules such as methane affect the reaction enthalpy; higher occupancy rates lead to greater changes in heat amount during hydrate formation or decomposition (Rydzy et al., 2007). The magnitude of the reaction enthalpy is dependent on guest molecule size; for instance, the decomposition enthalpy of methane hydrates is approximately +54 kJ/mol. If methane is replaced by ethane or larger molecules, the reaction enthalpy significantly increases. It has been reported that if 1% of methane is replaced by ethane, the reaction enthalpy will rise by about 30% (68.7 kJ/mol), and for propane hydrates, the reaction enthalpy is approximately 129.2 kJ/mol (Handa, 1986). Measurement of reaction enthalpy involves both experimental and numerical approaches. In the laboratory, Differential Scanning Calorimetry and Isothermal Titration Calorimetry are employed to capture the heat of formation and decomposition of hydrates (Fischer et al., 2014; Gupta et al., 2008). However, due to experimental complexities and challenges associated with sample preparation, the available data are limited. Therefore, most researches focus on numerical analysis. An alternative method for predicting reaction enthalpy involves using the Clausius-

Clapeyron equation, which combines the changes in *T-P* conditions with reaction enthalpy and compressibility, with the specific formula presented by (Brown, 1951):

$$\Delta H = -ZR_g \frac{dInP}{d(1/T)} \tag{2.4}$$

Where P is the pressure, T is the temperature, Z is the compressibility, R_g is gas constant, ΔH is the enthalpy.

It is noted to acknowledge that the Clausius-Clapeyron equation assumes the variation in compressibility of the gases or fluids is negligible, which has limited its applicability in area where the compressibility is subject to significant changes, such as deep-sea settings (Anderson, 2004). Despite the extensive measurements and estimations of thermal-related parameters of hydrates currently available, substantial gaps remain in our understanding of these systems. Future research should further take into account the differences in heat transfer between different types of hydrates (sI and sII). Additionally, there is a need for the development of mathematical models that can accurately describe the heat transfer dynamics within multiphase systems, especially for the unique properties and interactions of each phase.

2.2 Fluid flow property and compressibility

The flow characteristics of GHBS are crucial for assessing the potential of hydrate mining. The porosity (ϕ), permeability (K_1), and flow paths of fluids directly influence the efficiency and safety of natural gas extraction from sediment layers. The presence of hydrates reduces pore sizes and alters the shape of the pores, thereby impacting the behavior of fluids as they move through the hydrate-bearing system. Moreover, the pore habit of hydrates determines the fluid flow within pore spaces; specifically, hydrates in grain-coating morphology tend to obstruct flow channels and restrict fluid movement, whereas hydrates in a pore-filling morphology facilitate more optimal flow spaces for fluids. The dissociation of hydrates further complicates the flow properties of fluids. This process involves the transition from a single water-phase system to a multiphase system containing gas and water, accompanied by changes in water saturation and capillary pressure. Furthermore, the dissociation weakens the cementing effect of hydrates on sediment particles, potentially leading to the collapse of the particle skeleton supported by hydrates. Although the initial permeability may be relatively high, it tends to diminish as the particle structure degrades.

Therefore, in-depth research on quantification of the fluid flow properties of GHBS and their evolution during hydrate dissociation is key to better predicting the gas production efficiency from hydrate extraction.

2.2.1 Porosity

ϕ is a dynamic parameter, representing the volumetric fraction of unoccupied space within sediments. Hydrate formation or dissociation within pore spaces fills or releases voids, which alters the pore size and distribution, exerting a pronounced impact on ϕ of GHBS (Chatterjee et al., 2016; Cheng et al., 2023). Diverse techniques have been applied to calculate ϕ, with the standard approach involving the measurement of bulk and matrix densities (Bassiouni 1994), which is given by:

$$\phi = \frac{V_v}{V} = \frac{\rho_m - \rho_b}{\rho_m - \rho_f} \tag{2.5}$$

Where ϕ is the porosity, ρ_m is grain density, ρ_f is water density, ρ_b is bulk density, V_v is the pore volume, V is the total volume.

Compared to hydrate-free sediments, ϕ of GHBS is impacted by hydrate occurrences and inter-particle interactions. Seabed depth (h) associated with the phase equilibrium state of T-P dictates the stability of NGH. Kominz et al. (2011) presented there is a non-linear alteration in ϕ with the increase of h. Deeper layers with elevated pressures facilitate hydrate accumulation, markedly decreasing ϕ relative to shallower deposits, as represented in Equation 2.6.

$$\phi = a \cdot \exp(-h/b) \tag{2.6}$$

Where h is the seabed depth, a and b are the constants.

With depth-induced increases in vertical effective stress, sediments become more compacted, leading to a reduction in ϕ, which aligns with Equation 2.7 (Daigle et al., 2015).

$$\phi = \delta_1 - \delta_2 (\sigma_v^{'})^{\delta_3} \tag{2.7}$$

Where $\sigma_v^{'}$ is the vertical effective stress, δ_1, δ_2 and δ_3 are the constants.

Based on the above findings, He et al. (2013) categorized ϕ into low-frequency, mid-frequency, and high-frequency components. They found that ϕ in low-frequency variations are governed by compaction, grain size, and geothermal gradient. In contrast, mid-frequency variations correlate with grain size, and high-frequency is solely related to grain diameter. Additionally, the grain size distribution of marine sediment contributes to the disparities in ϕ; Fine-

grained sediments generally present lower ϕ, whereas coarse-grained sediments exhibit higher ϕ (Winters et al., 2007).

2.2.2 Permeability

GHBS exhibit intricate flow properties governed by sediment permeability, which characterizes the fluid transmission capacity of sediment matrix (Gong et al., 2023). K_1 of GHBS is intricately related to the stress state, with seabed sediments experiencing a spectrum of stresses from hydrostatic pressure. Shen et al. (2020) through triaxial tests demonstrated that an increase in effective confining stress leads to diminished K_1 in hydrate-bearing sands due to pore space occlusion by fine particles. For the high-permeability sediments, escalating effective stress decreases ϕ, subsequently reducing K_1 (Yoneda et al., 2021). Additionally, it may constrict flow pathways with increasing S_h, thus hindering fluid movement and decreasing K_1 (Li et al., 2014).

Experimental results have proven that K_1 is dependent on S_h, grain size, and pore distribution. Recognizing the relationship among ϕ, S_h, and K_1, researchers have sought to develop precise predictive models. Darcy's law is adapted to the flow of fluids in porous media, yet it does not reflect the relationship between K_1 and other factors (Darcy, 1856):

$$K_1 = \frac{\mu Q L}{\pi r^2 \Delta P} \tag{2.8}$$

Where μ is the viscosity of water, Q is the water flow rate, L and r are the length and radius of high-pressure reactor tube, respectively, ΔP is the differential pressure.

Pore geometry significantly influences K_1, with sediments featuring well-connected and larger pores displaying enhanced K_1. Hence, a power relationship between K_1 and ϕ has been proposed as follows (Phillips, 1991):

$$K_1 = \left(\frac{\phi_1}{\phi_0}\right)^N \tag{2.9}$$

Where ϕ_0, ϕ_1 is the initial and absolute porosity of GHBS respectively, N is about 2-3.

Research on the permeability models of granular materials traces its origins to Kozeny, who considered fluid flow through capillaries. He conceptualized the porous medium as an ensemble of capillary channels, establishing a power relationship between K_1 and ϕ: $K_1 \propto \phi^3$ (Kozeny, 1927). Carman recognized that flow paths were not strictly linear and the degree of curvature in flow paths had a substantial impact on K_1. Consequently, tortuosity (τ) (the ratio of average flow length

to the geometrical length) is introduced into Kozeny model, posing Kozeny-Carman equation (Carman, 1937; Matyka et al., 2008):

$$\begin{cases} K_1 = \dfrac{\phi^3 \cdot C}{\tau^2 \cdot S^2} \\ \tau = \dfrac{\langle \lambda_l \rangle}{L} \end{cases} \tag{2.10}$$

Where C is a shape factor, S is the specific surface related to the grain size, τ is the tortuosity, L is the geometrical length of the specimen, $<\lambda_l>$ is the average length of the fluid path.

HM also markedly dictates K_1 of GHBS, this is because hydrate distribution within pore space controls fluid flow pathways and permeation extent. The representative permeability models related to GHBS are summarized in Table 2.2, and corresponding impact of S_h and HM on K_1 of GHBS are illustrated in Fig. 2.2. Also, permeability data measured in the laboratory-synthetic and core GHBS are collected from the existing reports (Fig. 2.2), whose measurement methods include water flow, gas flow, nuclear magnetic resonance, and well-logging (Chen et al., 2018; Konno et al., 2015; Kleinberg et al., 2005; Kumar et al., 2010; Lee 2008; Li et al., 2014; Mahabadi et al., 2019; Wu et al., 2017; Yoneda et al., 2017; Zhai et al., 2015).

Parallel Capillary Model (PCM), favored for its simplicity and intuitive framework, conceptualizes the porous medium as a bundle of homogeneous capillaries aligned in parallel, in which fluids can flow freely. Kleinberg et al. (2003) classified PCM into two categories according to hydrate occurrences: one where hydrates cement the grain wall, displaying grain-coating morphology with a quadratic relationship; Another is pore-filling morphology where hydrates occupy the capillary, demonstrating a decline in K_1 with increasing S_h. Considering the capillary effect in hydrate nucleation, Kang et al. (2016) proposed a linear equation for grain-coating morphology. Nonetheless, due to the simplification of pore space, it is incapable in capturing K_1 of irregular porous media.

To account for the irregular flow path, Kozeny Grain Model (KGM) was developed based on Kozeny-Carman equation. Kleinberg et al. (2003) introduced saturation exponent (n) to reflect the various flow paths in exploring K_1 of GHBS in grain-coating. And Spangenberg (2001) found that once S_h exceeds 0.8, S_h has minimal effect on K_1. For the pore-filling morphology, it exhibited that pore area expanded with elevating S_h, alongside a linear relationship between saturation exponent (N) and S_h. Dai and Seol (2014) proposed a permeability model exclusively containing S_h within a

range from 0.05-0.75, incorporating a function of S_h for tortuosity and specific surface area without reliance on other empirical variables. Shen et al. (2020) developed an empirical reduction model that merges the simple and oblique cubic models, accounting for pore surface area both with and without hydrates. Guo et al. (2021) expanded the hydraulic radius concept into three dimensions and derived an advanced permeability model that includes the void ratio (e), which can reflect various pore habits.

Reservoir Simulator Models (RSM) are numerical models for simulating the flow of fluids in porous media, which can emulate physical and chemical interactions within GHBS. Masuda (2002) introduced the reduction exponent (a) to describe the impact of S_h on K_1, revealing an exponential decline in K_1 with increasing S_h. Moridis et al. (1998) proposed the Lawrence Berkley National Laboratory (LBNL) model, which illustrated K_1 for water (K_{rw}) and gas (K_{rg}) phases fluids during two-phase flow within porous media. Chen et al. (2018) combined the linear Corey model with an exponential function related to S_h and introduced a parameter (C) to indicate the degree of crystal coarsening, thus capturing the influence of S_h on K_1.

Recognizing that hydrates exhibit grain-coating morphology at lower S_h and pore-filling morphology at higher S_h, researchers proposed Hybrid Model to estimate K_1 of GHBS by integrating these two HM (Delli and Grozic, 2014, 2013). However, this model involves multiple empirical parameters, the determination of which requires further investigation.

Fig. 2.2 displays that most models suggest a curvilinear decline in K_1 with increasing S_h. For the given S_h, GHBS in grain-coating morphology demonstrate higher K_1 than those in pore-filling. Additionally, RSM predicts the fastest decline in K_1 with the increase of S_h, though it is limited to reflect changes in K_1 under S_h below 0.8. Some experimental data deviate from the predictions of the theoretical model, two possible reasons need to be considered: (1) Methods for hydrate formation, which may cause uneven distribution of hydrates within the pores; (2) Sediment properties, which exhibit distinct pore structures and particle arrangements. Notably, contemporary research on the permeability of GHBS focus on coarse-grained deposits where NGH manifest as pore-filling and grain-coating morphologies. In contrast, NGH frequently occur in fine-grained sediments with lens-like, nodular, massive, and vein morphologies, an area that remains under-researched.

Table 2.2: Summary of the existing permeability model for GHBS

Reference	Model type	HM	Model description
Masuda (2002)	RSM	Pore-filling / Cementing	$K_1 = (1-S_h)^a$ Where K_1 is the normalized permeability of GHBS, K_0 is the initial permeability of GHBS, S_h is hydrate saturation, a equals to 10,15.
Moridis et al. (1998)	RSM (LBNL)	NA	$K_{rw} = \sqrt{\frac{S_w - S_{rw}}{1-S_{rw}}}\left[1-(1-(\frac{S_w - S_{rw}}{1-S_{rw}})^{\frac{1}{m}})^m\right]^2$ / $K_{rg} = (1-\frac{S_w - S_r}{1-S_r})^{\frac{1}{2}}(1-(\frac{S_w - S_r}{1-S_r})^{\frac{1}{m}})^{2m}$ Where S_{rw} is the irreducible water saturation, S_w is water saturation and equals to 0.1, m = 0.46.
Chen et al. (2018)	RSM	Grain coating / Pore-filling	$K_{rg} = (1-S_h)\exp(-C \cdot S_h)$ Where C is the fitting parameter, C = 4.95 (best fit).
Kang et al. (2016)	PCM	Grain coating	$K_1 = -1.8S_h + 1$
Kleinberg et al. (2003)	PCM	Grain coating[a] / Pore-filling[b]	$^{(a)}K_1 = (1-S_h)^2$ / $^{(b)}K_1 = 1 - S_h^2 + \frac{2(1-S_h^2)}{\ln S_h}$
Kleinberg et al. (2003)	KGM	Grain coating[a] / Pore-filling[b]	$^{(a)}K_1 = (1-S_h)^{n+1}$ / $^{(b)}K_1 = \frac{(1-S_h)^{N+2}}{(1+\sqrt{S_h})^2}$ Where n is defined as 1.5 within the range of S_h (0, 0.8), $N = 0.7S_h + 0.3$.
Guo et al. (2021)	KGM	Grain coating[a] / Pore-filling[b]	$^{(a)}K_1 = \frac{(1-S_h)^3}{\left[1+(e_t S_h)^{\frac{2}{3}}\right]^2}$ / $^{(b)}K_1 = \frac{(1-S_h)^3}{(1+e_t S_h)^{\frac{4}{3}}}$ Where e_t is the total void ratio.
Dai and Seol (2014)	KGM	NA	$K_1 = \frac{(1-S_h)^3}{(1+2S_h)^2}$
Shen et al. (2020)	KGM	NA	$K_1 = (1-S_h)^{n+2}\left[\frac{A_0}{A(S_h)}\right]^2 = \frac{(1-S_h)^{n+2}}{(1+S_h^{\frac{2}{3}})^2}$ Where A_0 is the internal surface area of the pore space without hydrates, $A(S_h)$ is the internal surface area of the pore space with hydrates, n is the permeability reduction exponent.
Delli and Grozic (2014, 2013)	Hybrid model	Grain coating / Pore-filling	$K_1 = (S_h)^a K_1^{pf} + (1-S_h)^b K_1^{gc}$ Where K_1^{pf} and K_1^{gc} are the Kozeny grain coating and pore-filling model, respectively, a and b are the parameter related to S_h.

Reference	Model type	Model assumptions and applications
Masuda (2002)	RSM	Assumptions: (1) The flow paths of gas and liquid in pore spaces resemble a bundle of parallel cylindrical capillaries; (2) Hydrates grow on the wall of capillaries. Applications: It is applicable for specific sediment or pore habit.
Moridis et al. (1998)	RSM (LBNL)	Assumptions: (1) GHBS are porous media subject to capillary pressure effects; (2) The interior of porous media is isothermal; (3) Sediments are partially saturated with hydrates. Applications: It is applicable for predicting gas production from hydrate reservoirs.
Chen et al. (2018)	RSM	Assumptions: Gas was considered as the sole flow phase within the pore spaces. Applications: It is applicable to hydrates formed under excess gas method, as well as hydrates with diverse degrees of crystal coarsening and patch size.
Kang et al. (2016)	PCM	Assumptions: The flow paths of gas and liquid in pore spaces resemble a bundle of parallel cylindrical capillaries. Applications: It is particularly suited for homogeneously distributed hydrates synthesized in the laboratory and for conventional growth habits of hydrates.
Kleinberg et al. (2003)	PCM	
Kleinberg et al. (2003)	KGM	
Guo et al. (2021)	KGM	Assumptions: (1) Pore spaces can be regarded as capillaries with irregular geometries; (2) The shape factor remains unchanged with varying hydrate saturation; (3) Electrical tortuosity can substitute hydraulic tortuosity. Applications: It is applicable for capturing the impact of the pore habits of sediments and two hydrate morphologies on permeability.
Dai and Seol (2014)	KGM	
Shen et al. (2020)	KGM	
Delli and Grozic (2014, 2013)	Hybrid model	Assumptions: Permeability is jointly influenced by both grain coating and pore-filling growth habits. Applications: It is suitable for predicting the transition from hydrates in grain coating at lower hydrate saturation to pore-filling at higher hydrate saturation.

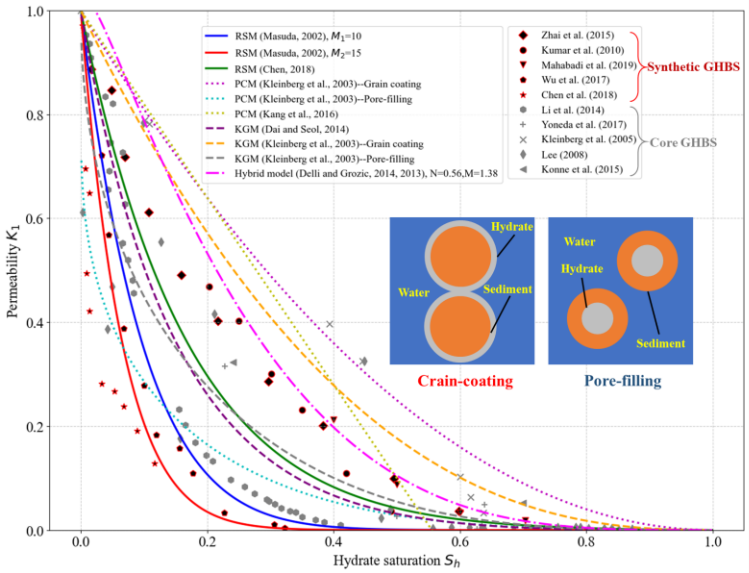

Figure 2.2: The impacts of S_h and HM on permeability of GHBS

2.2.3 Compressibility

Compressibility stands as a crucial characteristic in evaluating the ability of material undergoing volume deformation subjected to pressure, specifically referring to the reduction in volume and porosity of sediment matrix (Xu et al., 2022b). The compressibility of porous media encompasses two components: pore and bulk compressibility. Pore compressibility refers to the deformation of the pore space under applied pressure, while bulk compressibility describes the overall volumetric deformation of the sediment, incorporating both the solid matrix and pore space. This section aims to describe the bulk compressibility behavior of GHBS, with particular attention to pore collapse phenomena due to hydrate dissociation and the subsequent compaction of the sediment matrix. The results regarding the compressibility of GHBS are compiled through conducting oedometer tests and isotropic compression tests reported in the literature.

Fig. 2.3 illustrates the evolution of void ratio for GHBS and HFS under isotropic compression. Where L_A denotes HFS, while L_C and L_O represent GHBS with identical S_h in pore-filling and cementing type, respectively. The order of S_h is $L_A = 0 < L_B < L_C = L_O < L_D$. It is evident from the graph that the pore space was compacted with the increase of effective stress, leading to the decline in compressibility of GHBS upon reaching the volumetric yielding point (Nakashima et al., 2021). Compared to HFS (L_A), GHBS (L_B) exhibit enhanced cohesion owing to hydrates serving as the cementing agent among sediment particles, which subsequently diminish the compressibility of

the overall structure (Fang et al., 2022; Yang et al., 2008). Progressing from left to right, as S_h increases, the densification of sediment structure is pronounced and the cementation effect between hydrates and sediment matrix is strengthened, thus resulting in reduced compressibility (Zhou et al., 2021). Moreover, GHBS in cementing morphology compared to those in pore-filling endow greater cohesive strength, which necessitates a heightened level of effective stress to consolidate, indicating a reduction in compressibility (Lei et al., 2020; Priest and Hayley, 2019).

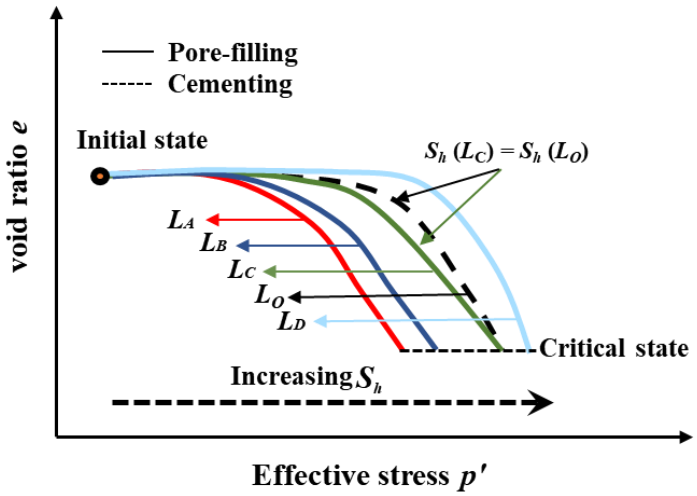

Figure 2.3: Schematic of the volumetric response of GHBS under isotropic compression

The compression index (C_c) (the slope of loading compression curve) serves as a critical indicator of material compressibility, which can be determined from the stress-volume response curve (Fang et al., 2022). Tan (2004) performed oedometer tests on various sediments containing hydrate, and each specimen adhered to the typical compression behavior where void ratio (e) nonlinearly decreases with increasing vertical effective stress (σ_v'), signifying the transition towards a more compact state for GHBS under loading (Fig. 2.4a). The compression curves of GHBS are summarized by the following features (Kim and Cho, 2014; Lei et al., 2020): (1) In contrast to granular soil, GHBS contribute greater initial stiffness due to the cementation of hydrates, manifesting as a comparatively gentle curve at low stress; (2) C_c intensifies as effective stress increases, indicating that particle rearrangement or hydrate dissociation weakens the cementing effect beyond yield stress, which is a process of gradual loss of stiffness and collapse of the structure; (3) Subsequent to a certain escalation in stress, C_c keeps constant, aligning with the

secondary compression stage seen in granular soil; (4) The compression trajectories for varying type of sediments tend towards parallelism or congruence subject to stress amplification.

Fig. 2.4b depicts the compression curves during 1D oedometer loading and unloading for sediment in three states: dry, water-saturated (hydrate-free), and hydrate-bearing (S_h = 0.8) (Kim et al., 2019). It is discernible that the curve for GHBS does not conform to a stable C_c after yielding but decreases exponentially, with a reduction in compressibility decreasing by half when S_h surpasses 0.8 compared to HFS. This suggests that the bonding degradation between hydrates and particles induced by hydrate dissociation during unloading precipitates a contraction in sediment volume (Santamarina et al., 2015). Fig. 2.4c demonstrates the correlation between void ratio e and effective stress $\sigma_v^{'}$, where C_c is determined by the gradient of the normal consolidation line (NCL) while the swelling index is decided by the gradient of the over consolidation line (OCL) (Nakashima et al., 2021; Yoneda et al., 2019). C_c tends to decline with increasing S_h, this is because structural support is fortified via the cementation effect of hydrates, markedly curtailing sediment compressibility. Moreover, the observation is similar to the tendency displayed in Fig. 2.4b, with a smaller C_c for GHBS than for HFS. Notably, GHBS with various S_h exhibit a minimal variation in the swelling index, which implies the swelling index is only controlled by host sediment. Additionally, as $\sigma_v^{'}$ increases, hydrate dissociation occurs, shifting the compression trajectory from NCL towards OCL, indicating a loss of structural support. This transition is marked by an evident reduction in e, reflecting the collapse of pore spaces previously occupied by hydrates, which is further confirmed in Fig. 2.4c (right figure). This pore collapse phenomenon leads to enhanced compaction of the sediment matrix, accompanied by accelerated volume contraction. Extended in practical scenarios when gas production from hydrate reservoirs, such behavior manifests as reservoir subsidence, which may affect geo-mechanical stability and pose risks to seafloor infrastructure.

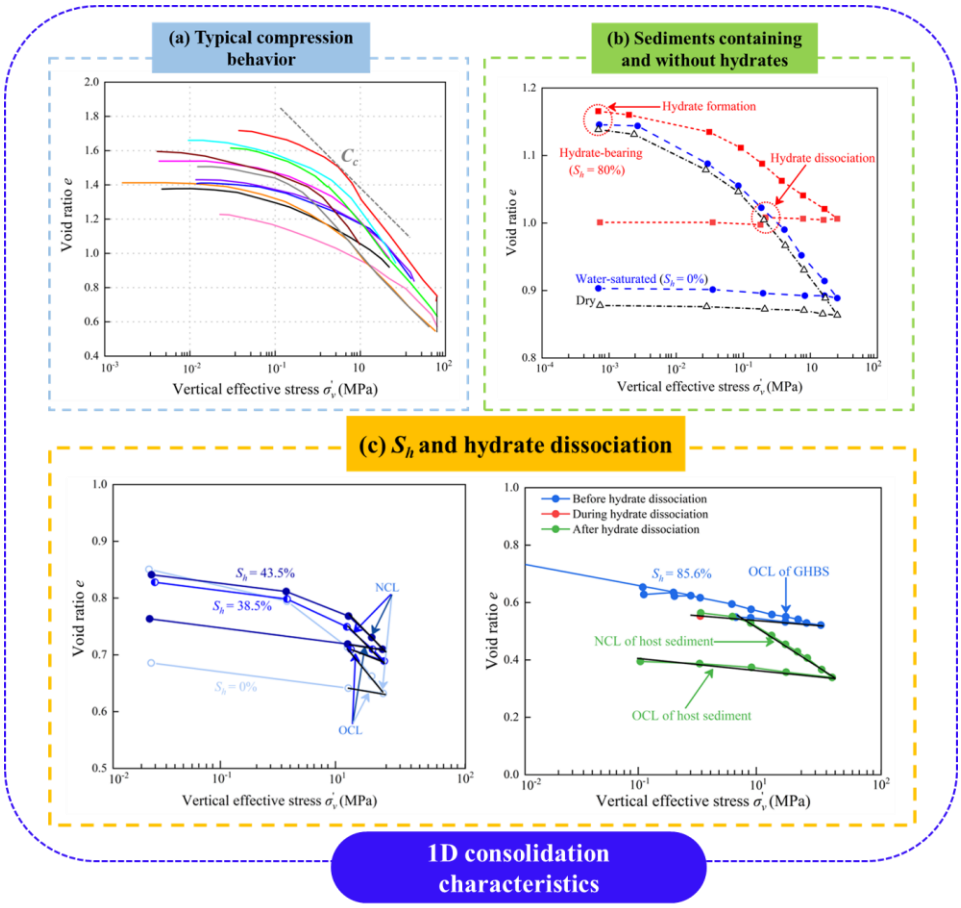

Figure 2.4: One-dimensional consolidation characteristics of sediments in the presence of hydrates (Kim et al., 2019; Nakashima et al., 2021; Tan 2004; Yoneda et al., 2019)

2.3 GHBS remolding methods and experimental techniques

In light of the technical challenges associated with the extraction of fine-grained sediments, contemporary research endeavors concentrate on the mechanical properties of coarse-grained sediments containing hydrates. Considering the high cost of obtaining core specimens and hydrate dissociation from the stable state during transportation, the majority of researchers conduct indoor tests using artificially synthesized hydrate-bearing sediments (HBS). Specifically, the mechanical investigations involved the employment of triaxial testing apparatus, with modified components to simulate geological conditions and to synthesize specimens. Through controlling initial test conditions, the effects of various factors on shear strength and elastoplastic deformation behavior of HBS can be captured (Liang et al., 2020). The following subsections review the methods for

specimen preparation, testing apparatuses, and initial conditions utilized in existing experiments, with brief discussions of the limitations and feasibility in current techniques.

2.3.1 Methods for specimen preparation in the laboratory

Two methods are utilized to obtain specimens for reliable experimental outcomes: a. in-site sampling; b. synthesis specimens in the laboratory. In-site sampling enables direct acquisition of NGH but requires abundant financial resources. Also, disturbances during the preparation process can compromise the purity of specimens (Liang et al., 2022). In contrast, preparing specimens in the laboratory circumvents these drawbacks, offering precise control over test conditions to ensure HBS accurately represent authentic mechanical behavior (Zhang et al., 2012).

The procedure for preparing HBS in the laboratory encompasses the selection of sediments, determination of grain size, drying treatments, adjusting initial water content, compaction, and injecting gas into the reactor. This is followed by *T-P* adjustments to stabilize GHBS, as shown in Fig. 2.5 (Pei et al., 2022). Four methods are predominantly used for the artificial synthesis of GHBS in laboratory settings: (a) Dissolved gas method (DGM); (b) Excess-driven method (EDM); (c) Ice seeding method (ISM) (d) Hydrate premixing method (HPM) (Fig. 2.6).

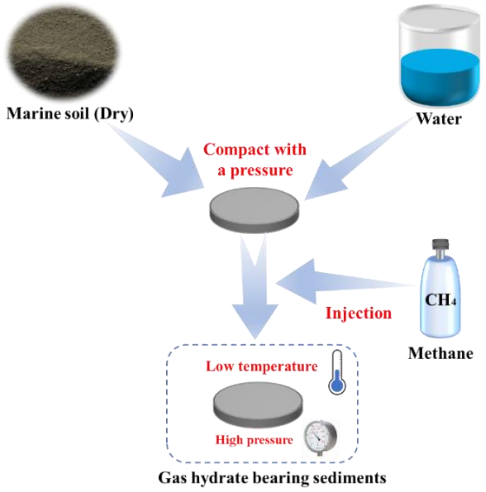

Figure 2.5: The general method for preparing HBS

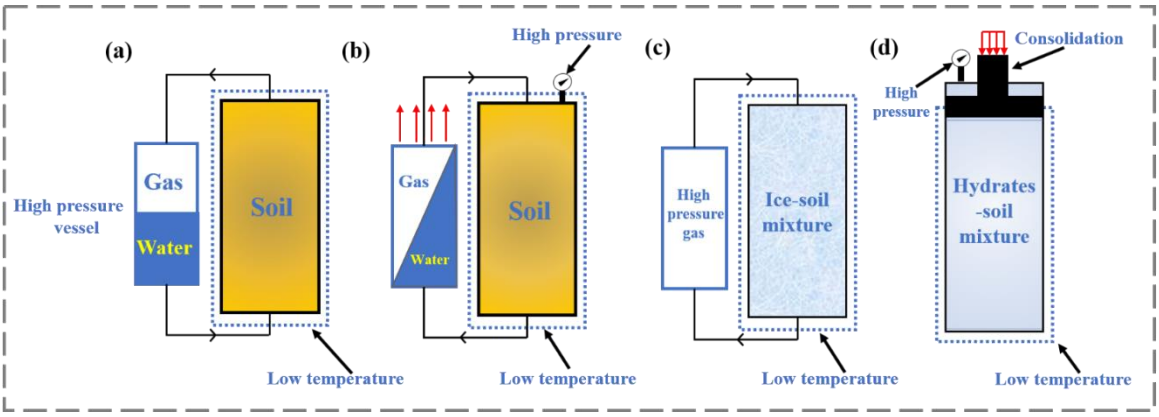

Figure 2.6: Diagram of various methods for indoor specimens' preparation: (a) DGM; (b) EDM; (c) ISM; (d) HPM

DGM stands out as the predominant technique in contemporary research for synthesizing HBS, particularly noted for its capacity to replicate the process of hydrate formation akin to marine settings (Choi et al., 2018; Hyodo et al., 2013a). The principle of DGM lies in enhancing gas solubility in water under high *P* and low *T* to initiate hydrate formation, essentially a phase transition process (Waite et al., 2008). This involves infusing purified gas into distilled or deionized water, with meticulous monitoring of gas concentration and *T*. A dropping in *T* occurs once optimal gas concentration is achieved, facilitating hydrate formation. The key benefit of DGM is the homogeneous hydrate distribution within sediments. Yet, the method struggles to achieve S_h beyond 60-70%, posing a challenge for the research simulating highly concentrated hydrate.

EDM relies on providing "excess" components (water or gases) required for hydrate formation, which can be categorized into Excess Gas Method (EGM) and Excess Water Method (EWM). EGM involves continuously injecting natural gas into moist soil under controlling *T-P* until hydrate formation, which allows for controlling S_h through gas volume and pressure adjustments (Rake and Pinkert, 2021; Shan et al., 2022). As for EWM, excessive water is added to dry soil, followed by gas injection under low *T* and high *P* to promote hydrate formation. Similar to EGM, both methods promote the likelihood of nucleation due to the extensive contact between gas and water. However, EGM exhibits a shorter reaction time but may yield uneven hydrate distribution at higher S_h (Choi et al., 2014; You et al., 2023).

ISM is recognized as the simplest and most effective technique to produce GHBS. The underlying principle is to utilize ice particles as nucleation points for hydrate formation (Chen et

al., 2018; Wu et al., 2022). The procedure involves mixing fine ice particles with sediment, then injecting high-*P* gas into ice-sediment mixture while adjusting *T* to achieve phase equilibrium. The ice-sediment interaction prompts a transition from solid ice to gaseous hydrate. Additionally, HM can be dictated by controlling the quantity of ice. However, the localized presence of ice particles presents difficulties in achieving uniform hydrate distribution, potentially inducing experimental errors.

The above three methods involve the pre-preparation of sediments, while HPM prepares hydrates in advance (Malagar et al., 2019; Zeng et al., 2023). The process includes mixing gas and water in high-*P* reactor to form hydrates, and then hydrates are frozen and crushed into fine particles. After mixing with sediments, stress is applied to consolidate the mixture. To prevent hydrate decomposition, the entire system maintains *T*-*P* conditions within the stability zone of hydrates. HPM accommodates diverse sediment particle sizes and accelerates experimental timelines through hydrate pre-synthesis. Nonetheless, potential hydrate decomposition during mixing and storage phases presents challenges in controlling S_h.

Table 2.3 represents a detailed description of methods for hydrate formation in the laboratory. Current techniques for preparing GHBS are sophisticated, and capable of generating hydrates within sediments of various grain sizes, yet there still exist limitations:

(1) GHBS prepared under different conditions across laboratories exhibit inconsistencies. It is recommended to develop a standardized preparation method and to periodically conduct cross-validation experiments.

(2) Certain methods lead to uneven distribution of hydrates. It is advisable to employ microfluidic technology and precise stirring equipment to address this issue.

(3) Maintaining precise *T*-*P* becomes a potential challenge while simulating high-pressure environment. This can be mitigated by integrating automated equipment and sensors to enable real-time monitoring and adjustment of preparation conditions.

Table 2.3: A summary of methods for hydrate formation in the laboratory

Method type	Applicable soil type	Advantages	Disadvantages
DGM	Fine-grained sediments (silts, clays)	-Allow for the control of gas concentration.	It requires precise pressure and temperature control.

		-Reproduce natural hydrate formation conditions.	
EDM	All types of soils	-Faster hydrate formation. -Simplicity in terms of setup.	Potential issues with ensuring hydrate distribution evenly.
ISM	Coarse sands	It can control the size and distribution of nuclei.	It requires to ensure only seeding ice participates in nucleation.
HPM	Various particle size of sediments	Allow for direct control of initial hydrate phase.	Potential for non-uniform distribution if not mixed thoroughly.

Method type	Suggested application in experiments
DGM	It is used for studying hydrates with high gas solubility (CO_2 hydrates), and it is well-suited for the analysis of hydrate formation rates due to the longer duration required to achieve specific hydrate saturations.
EDM	It is adaptable for exploring the influence mechanisms of different hydrate morphologies and saturations on shear strength. Notably, EGM is noteworthy for its capability to investigate the response of hydrate dissociation under diverse gas pressure.
ISM	It is applicable for assessing the impact of external factors (temperature, effective confining stress) on the mechanical behavior of GHBS.
HPM	It is suitable for tests necessitating precise control over hydrate distribution and saturation, especially in studying the heterogeneity of hydrate distribution.

2.3.2 Test apparatuses

Experimental research on the mechanics of GHBS predominantly utilizes triaxial apparatus, which can be modified in consideration of specific factors (Chen et al., 2022). Typically, the triaxial testers for GHBS is adapted from geotechnical triaxial instruments, augmented with a hydraulic air supply and temperature control system (Seol et al., 2019). Besides applying axial stress and controlling confining and back pressures, advanced triaxial instruments can modulate *T* to achieve the stability zone for hydrate formation. The devices offer precision up to 0.1°C and possess the capability for automatically collecting the load data every second (Liu and Li, 2021; Lu et al., 2021). Furthermore, the measurement of axial and radial strains as well as volumetric change is an indispensable component of GHBS triaxial apparatus. Basic control parameters for triaxial apparatuses are listed in Table 2.4.

Table 2.4: Basic parameters for typical triaxial apparatuses

Control method / Affiliation	Temperature control	Confining pressure control	Temperature control method	Temperature control accuracy	Confining pressure control accuracy	Maximum loading capacity
Institute of Geo-Resources and Environment, National Institute of Advanced Industrial Science and Technology, Japan (Masui et al., 2008)	243K to 293K	20 MPa	A cooling tank	0.5K	NA	200kN
National Institute of Advanced Industrial Science and Technology, Tsukuba, Japan (Miyazaki et al., 2011)	243K to 293K	20 MPa	A refrigerant liquid	0.5K	NA	200kN
Yamaguchi University, Japan (Hyodo et al., 2013a)	-35°C to 50°C	30 MPa	Incubator	0.1°C	0.1MPa	200kN
Dalian University of Technology, China (Luo et al., 2018)	-20°C to 25°C	30 MPa	Thermocouple	0.5°C	0.01MPa	60kN

Since 1996 in Japan, Yamaguchi University developed a low-temperature, high-pressure hydrate triaxial equipment. However, it did not control pore pressure and in-situ generation of specimens (Hyodo et al., 2016). By 2000, U.S. Geological Survey designed a testing laboratory instrument for GHBS that could replicate *T-P* conditions of hydrate layer, but it failed to monitor specimen volume change and stress-strain behavior. In 2008, the Institute of Geo-Resources and Environment enhanced the traditional triaxial instrument by introducing a precise temperature control system, which is achieved through water circulation from a cooling tank to the pressure vessel (Masui et al., 2008) (Fig. 2.7a). Subsequently, the instrument was improved by using refrigerant liquid (50vol% ethylene glycol aqueous solution) (Miyazaki et al., 2011) (Fig. 2.7b). Since 2013, Hyodo et al. (2013a) designed an instrument that minimized hydrate decomposition, applying the unsaturated method for hydrate synthesis. Notably, it can reproduce stress and temperature conditions of deep seabed with precise S_h calculations (Fig. 2.7c). Concurrently, advanced triaxial equipment DDW-600 was modified by Dalian University, which offered precise control over S_h and hydrate decomposition rate (Luo et al., 2018) (Fig. 2.7d).

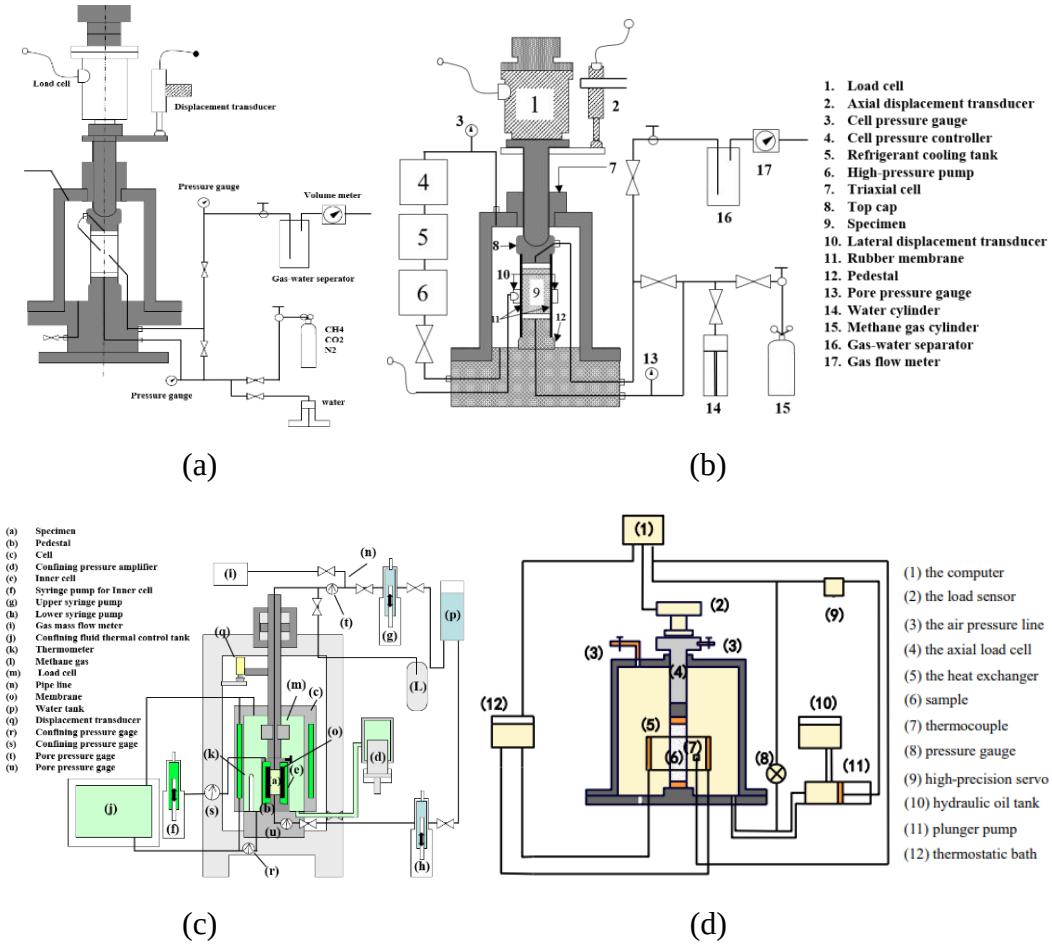

Figure 2.7: GHBS triaxial apparatuses: (a) Masui et al., (2008); (b) Miyazaki et al., (2011); (c) Hyodo et al., (2013a); (d) Luo et al., (2018)

Although triaxial instrument provides an effective approach to investigating the mechanical properties of GHBS, it encounters specific challenges:

(1) It is challenging to prepare in-site specimens. Coarse sand is often used in experiments to simulate sediments in deep seabed, which simplifies the true complexity of particle composition.

(2) Gas release from hydrate decomposition may skew results, it is recommended to equip the devices with high-precision gas collection systems and integrate real-time monitoring capabilities.

(3) Standardization of specimen sizes for triaxial testing is essential. Otherwise, it is difficult to compare the test results due to the size effect of specimens prepared through different instruments.

2.3.3 Initial conditions

Investigating the complex geo-mechanics of GHBS requires careful consideration of various test conditions including soil type, gas composition, S_h, σ', and T, as well as the employment of consolidated undrained (CU) and consolidated drained (CD) tests. The differing levels of σ' and S_h simulate varying environmental scenarios, affecting the mechanical response of sediments. T and gas composition are pivotal in determining the phase equilibria and chemical interactions within the hydrates.

The selection of soil type is the cornerstone of experimental research on GHBS, which exhibits distinctive characteristics when mixed with NGH. Toyoura sand is always chosen to be the host material due to its uniformly graded particles, minimal fine content, and high silica concentration (Hyodo et al., 2014a; Pinkert and Grozic, 2014). Besides Toyoura sand, coarse-grained soil such as quartz and silica sand are frequently selected owing to their chemical inertness and high compressive strength (Hyodo et al., 2017; Zhu et al., 2020). Fine-grained soil such as clay and silt with high plasticity is crucial for investigating hydrate dynamics (Li et al., 2019; Han et al., 2021). Montmorillonite clay, characterized by its high expansion and elevated cation exchange capacity, is adopt for analyzing the volumetric deformation of GHBS (Lee et al., 2013; Wang et al., 2019). Conversely, Kaolin clay is relatively stable with lower environmental sensitivity, making it suitable for exploring the impact of other variables on mechanical behavior of GHBS (Li et al., 2011a; Song et al., 2014).

The choice of gas composition has a certain influence on hydrate formation and dissociation in actual sedimentary environments. The primary constituents incorporated include CH_4, Synthetic THF, CO_2, and mixed gases such as CH_4-CO_2. Methane, prevalent in GHBS, can form hydrates readily due to its small molecular structure, which exhibits notable stability (Li et al., 2016; Zhang et al., 2012). THF is characterized by a pronounced sensitivity to water, and it is capable of nucleation rapidly and copious hydrate production. THF is utilized in experimental settings due to its minimal synthesis requirements, serving as the substitute for CH_4 hydrates (Lee et al., 2007; Mahabadi et al., 2019). CO_2, useful in gas replacement studies, initiates displacement reactions when injected into alkane hydrates (Jung et al., 2010; Jung and Santamarina, 2010). Mixed gases are applicable to simulate sedimentary environment where multiple gases coexist and dissociation may occur simultaneously (Sun et al., 2022). Under equivalent concentration, the strength of CO_2

HBS surpasses that of CH_4 HBS, while the strength of THF-HBS is comparable to that of methane HBS (Zhang et al., 2011).

The roles of S_h, σ', and T on the mechanical behavior of GHBS merit detailed examination. S_h determines the hydrate distribution, with an improved linkage between particles at higher S_h. Adjusting σ' replicates reservoir stress condition, further boosting closer particle arrangement and structural compactness. Elevated T precipitates hydrate dissociation, weakening inter-particle cohesion (Santamarina and Ruppel, 2010; Jiang et al., 2017; Xu et al., 2022c, 2023).

In CU test, volume remains constant during shearing, enabling the analysis of variation in strength and pore water pressure (u) of GHBS under short-term stress. Conversely, CD test elucidates effective stress paths, serving as a pivotal method to examine the mechanical behavior of GHBS under long-term consolidation. Unlike CU test, it exhibits a transition from strain hardening to softening after yielding while applying CD test (Yan et al., 2023; Yoneda et al., 2015b; Yoneda et al., 2019).

2.4 Influence of hydrate saturation on the mechanical responses of GHBS

2.4.1 Measurement methods for hydrate saturation

The widely intuitive method adopted in experimental research is pressure drop method, which hinges on the observed decrease in pressure consequent to hydrate dissociation. S_h is quantified by the difference in pressure before and after the dissociation reaction (Wang et al., 2021):

$$S_h = \frac{\Delta P_g V_g M_h}{R_g T V_p \rho_h} \times 100\% \tag{2.11}$$

Where ΔP_g is the difference in gas pressure before and after reaction, V_g is the gas volume, V_p is the pore volume, M_h is the hydrate molar mass, R_g is the gas content, T is the temperature, ρ_h is the hydrate density.

Based on pressure drop method, Li et al. (2021) introduced a corresponding compressibility factor to measure S_h:

$$S_h = \frac{P_g V_m (M_{CH_4} + 5.75 M_{H_2O})}{\rho_h R_g Z T} \tag{2.12}$$

Where Z is the corresponding compressibility factor of methane, P_g is the gas pressure, V_m is the volume of methane, ρ_h is the hydrate density, M_{CH_4} is the molar mass of methane, M_{H_2O} is the molar mass of water.

Dong et al. (2020) assumed that under stable *T*-*P* conditions, capillary effects are negligible while applying excess gas. There is no variation in gas pressure during the reaction, gas and liquid are fully mixed in the presence of SDS solution. They proposed the following formula for computing S_h:

$$S_h = \frac{V_w \rho_{SDS} (n \cdot M_w + M_c)}{n \cdot \rho_w V_p M_w} \tag{2.13}$$

Where V_w is the volume of water, M_c, M_w is the molar mass of methane and water, respectively, n represents hydration number, n=5.75, ρ_w and ρ_{SDS} are the water and SDS solution density.

Luo et al. (2018) employed ice powder method for prepare methane HBS and suggested that S_h can be deduced through measuring the mass difference in hydrate-containing ice before and after hydrate dissociation, which is given by:

$$\begin{cases} m_h = \dfrac{M_h}{M_g} \times (m_{bef} - m_{aft}) \\ S_h = \dfrac{V_h}{V_i + V_h} = \dfrac{\dfrac{m_h}{\rho_h}}{\dfrac{m_{bef} - m_h}{\rho_i} + \dfrac{m_h}{\rho_h}} \end{cases} \tag{2.14}$$

Where V_i is the volume of ice, m_{bef} and m_{aft} are the mass of ice-hydrate mixtures before and after dissociation, M_h and M_g are the molar mass of hydrates and gas, ρ_i and ρ_h are the ice and hydrate density.

The above direct measurement techniques for assessing S_h are grounded in hydrate dissociation, where the gas volume or mass is detected before and after the reaction. These methods are characterized by their convenience in operation, making them adaptable for determining S_h in laboratory settings. In contrast, indirect methods such as resistivity measurements are susceptible to the influences of pore fluid, sediment matrix, and other variables, which can skew the precision of the outcomes (Dong et al., 2019; Wang et al., 2011).

2.4.2 Stress-strain behavior of sediments in the presence of hydrates

Research on stress-strain characteristics of GHBS and HFS predominantly conducts controlled mechanical experiments to mimic the response of deep-sea sediments to overlying stress

under constant confining pressure (Zhang et al., 2012). The majority of reports on these characteristics are based on drained triaxial test, providing further insights into the interrelations among deviatoric stress, axial strain, and volumetric strain. Where deviatoric stress represents the difference between the principal stress and the secondary principal stress. It serves as a key indicator of the stress component that is responsible for inducing shear deformation in sediments. Axial strain is defined as the ratio of the change in vertical length to the original vertical length, which is employed to evaluate the extent of deformation that sediments undergo under axial loading. Volumetric strain is the ratio of total volume deformation to the original volume of sediments during compression or expansion processes. Additionally, the specimens are subjected to the combined internal effects of normal stress and shear stress.

To effectively illustrate the impact of hydrate on stress-strain relation for soils, it is imperative to consider stiffness and strength – two indicators for evaluating material's resistance to deformation (Wang et al., 2022). Stiffness can be quantified as the magnitude of tangent modulus, which is obtained from the initial slope of stress-strain curve (ratio of deviatoric stress to axial strain). The strength for the specimen undergoing strain softening is the maximum deviatoric stress, while strength is identified at the deviatoric stress corresponding to 15% axial strain in cases of strain hardening. Uchida et al. (2012) posited that hydrate filling pore spaces render the sediment structure denser, which is akin to bonded soil. Fig. 2.8 presents the conceptual diagram of stress-strain curve and volume change for dense soil under CD test. It can be found that soils with higher density and bonding display enhanced strength, stiffness, and dilatancy, which is attributed to increased grain contact and interlocking (Vafaei et al., 2021). Notably, strain softening is ascribed to the shear-induced interlocking breakage (Zhu et al., 2010).

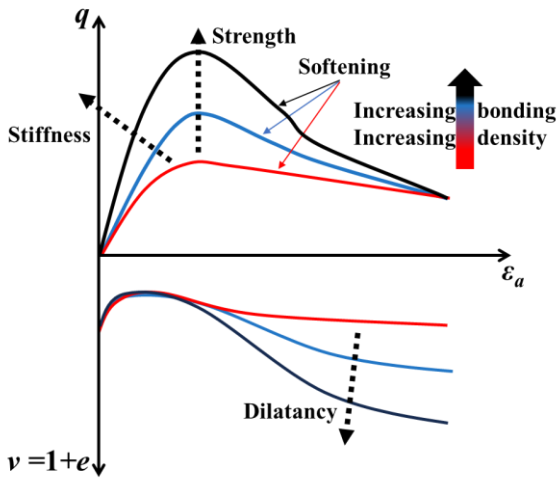

Figure 2.8: The relationship among stress, strain, and volume for bonded soil (modified by Uchida et al. (2012))

Extending from existing literature, researchers have identified profound discrepancies in the mechanical response of GHBS under triaxial loading compared to HFS, as depicted in Fig. 2.9a. The stress-strain behavior of HFS can be classified into two phases: a. initial elastic linear phase; b. elastoplastic phase. Conversely, besides the above two phases, GHBS manifest an additional phase of strain softening or hardening after yielding (Wu et al., 2022, 2019). This is attributed to a reduction in cohesive bonds among hydrates and particles, triggering hydrate dissociation and rearrangement of internal porous structure (Jiang et al., 2017). HFS exhibit strain hardening due to the increased frictional force between particles, enhancing the compaction, but without additional cementing effect. Correspondingly, the volumetric response of HFS is characterized by compressive consolidation, whereas GHBS exhibits initial compression followed by dilatancy (Zhou et al., 2020). This phenomenon stems from particle fragmentation induced by shearing at elevated stress coupled with hydrate decomposition. The released fluids in conjunction with fragmented particles migrate to pore spaces, which induce the redistribution of porous structure, facilitating volumetric expansion of GHBS (Hyodo et al., 2014b; Lee et al., 2010). In the absence of hydrate cementation, HFS undergo compaction through friction and interparticle contact. As the stress increases, the contact area between particles enlarges, further compressing the voids.

Extensive research has demonstrated that the contribution of hydrate to stress-strain behavior of sediment hinges on S_h and HM (Wu et al., 2019). The corresponding stress-strain and volume

relationships of GHBS are depicted in Fig. 2.9b. The stress-strain curve indicates enhanced structural compactness and a consequent increase in strength and stiffness of GHBS under higher S_h, which can be attributed to the intensified interlocking and cementation effects provided by hydrates (Miyazaki et al., 2010). Post-yield, there is a tendency to shift from strain hardening to softening (Deusner et al., 2019), which corresponds to the shift in shear strength dominance from interparticle friction to cohesion provided by hydrates. For the GHBS in cementing morphology, hydrates bonding with sediment particles generate greater cohesive force compared to those in pore-filling, with an evident enhancement in strength and stiffness (Luo et al., 2022). This is because the enhanced cohesion generated in cementing states converts into additional resistance and necessitats greater stress to achieve a specific deformation compared to the pore-filling counterpart. Furthermore, hydrate decomposition when subjected to higher stress leads to the detachment of bonded particles, prompting structural reorganization and inducing strain softening (Zhu et al., 2022). Correspondingly, the volumetric responses of GHBS transform from compression to noticeable expansion as S_h increases. GHBS in cementing type compared to those in pore-filling shows pronounced dilation after a more transient compression phase, which is due to the rearrangement between particles provoked by hydrate dissociation (Wu et al., 2020b).

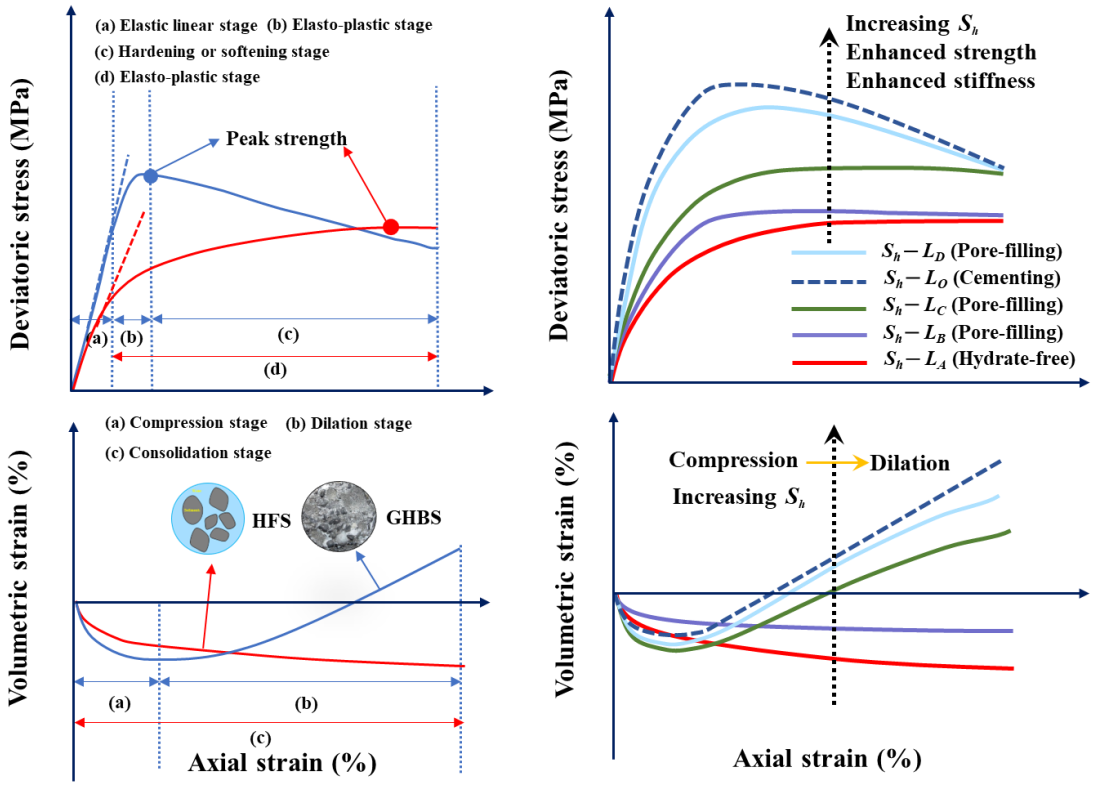

Figure 2.9: Schematic of stress-strain behavior of GHBS: (a) Comparison of mechanical behavior between GHBS and HFS; (b) Impacts of HM and S_h on mechanical responses of GHBS

2.4.3 Mechanisms of volumetric deformation and strength failure in GHBS

Once subjected to shear stress, GHBS experience volume deformation and strength alteration that can be ascribed to various factors: a. Fluctuations in pore water pressure; b. The dependency of shear stress on hydrate morphology and the destruction or reorganization of hydrate; c. The reorganization and displacement of particles, culminating in void formation; d. Cementation effect (Kajiyama et al., 2017b; Li et al., 2020). Fig. 2.10 delineates the strength and dilation failure mechanism of sediments in diverse hydrate morphologies, facilitating a pore-scale elucidation in the mechanical behavior of GHBS with varying S_h.

In HFS (S_h =0), particle rearrangement occurs upon shearing, leading to changes in particle configuration, which undergo compression in looser particles and expansion in denser particles. The shear strength is governed by interparticle friction and contact dynamics, resulting in the disintegration of sediment structure until shear stress exceeding the strength (Santamarina and Shin, 2009). For sediments with minimal hydrate content (S_h =0~25%), hydrates exhibit pore-filling type

and sparsely distribute without bonding to sediments, with minimal enhancement in strength, which is primarily controlled by interparticle friction. Additionally, sediment particles undergo rotational realignment at lower confining pressure, whereas hydrate disintegration occurs at higher confining pressure. The fragmented hydrates irregularly occupy the void space, with some directly interfacing with sediment particles, escalating localized density and potential for expansion (Waite et al., 2009).

As S_h increases, hydrate morphology transitions to the load-bearing state (S_h =25~40%), wherein hydrate serves as an interparticle bridge, collectively enduring stress loads. In this phase, hydrates contribute to greater shear strength compared to the previous phase, yet the cementation strength provided by hydrates remains inferior to the applied shear stress, precipitating hydrate fragmentation and amplified volumetric expansion. At higher S_h (S_h =40~60%), hydrates form a cemented structure through adhering sediment particles. The cementation strength surpasses the shear stress, with the breakage of localized hydrate particles. Shear strength is largely dictated by the adhesion and tensile strength imparted by hydrates. Localized hydrate-sediment cementation clusters inhibit particle rearrangement during shearing, with minimal sediment particle fracturing and redistribution (Yoneda et al., 2016). The enhanced dilation is due to the aggregation of fragmented particles. When hydrates occupy most pore space (S_h >60%), hydrates and sediments form clusters in grain-coating morphology, where the sediment particles are fully enveloped by hydrates, generating a compacted structure. Hydrates play a pivotal role in stress support, with the mechanical behavior of entire structure dominated by hydrates. The robust cementation exerted by hydrates markedly bolsters the overall stability and shear resistance of sediments. Additionally, the shear-induced dilation is contingent upon the shear plane; shearing along hydrates provokes less dilation, while shearing along the commentating interface of hydrate-sediment triggers the liberation of numerous hydrate particles, thereby inducing more dilation (Hou et al., 2022).

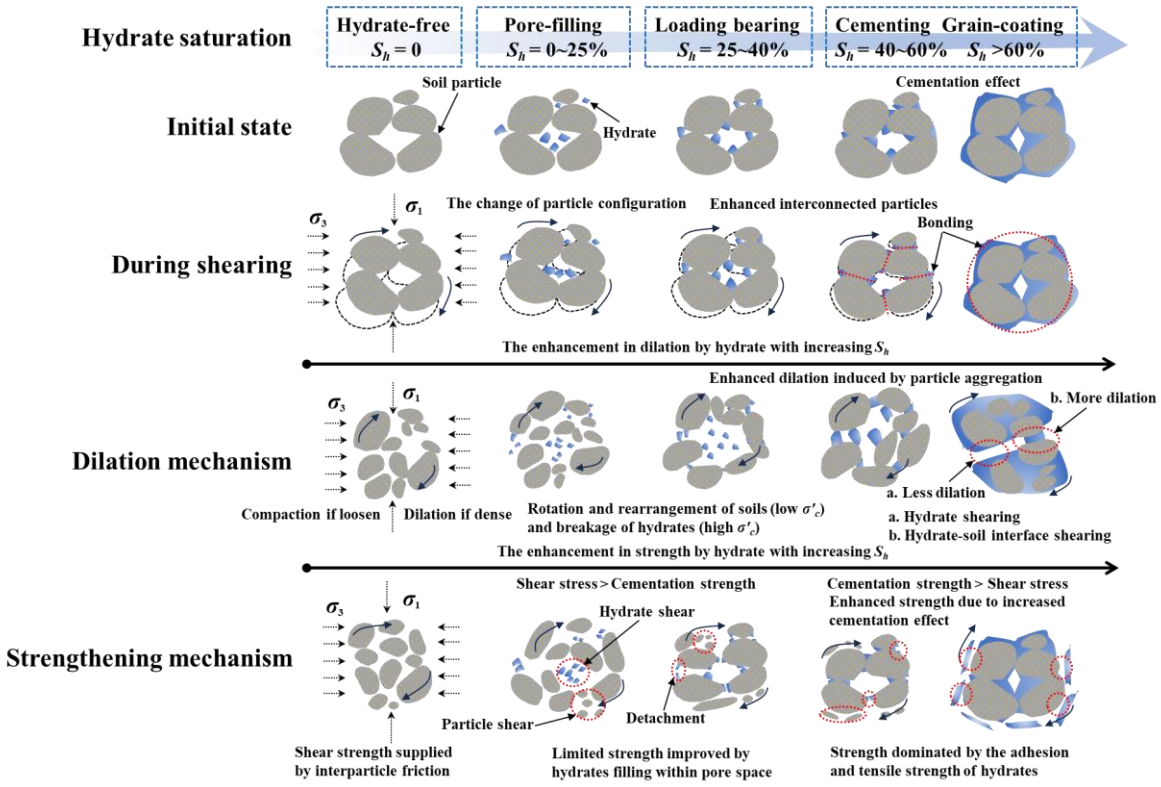

Figure 2.10: Mechanisms controlling the strength and dilation failure for sediments in the presence of hydrates

2.4.4 Analysis of the variation in mechanical parameters related to hydrate saturation

The strength enhancement of host sediments provided by hydrates has been extensively validated through experimental investigations. Fig. 2.11 presents recent research findings on the mechanical responses of sediments at varying S_h, including stress-strain relationships and volumetric deformation curves (Hyodo et al., 2013a; Masui et al., 2008; Miyazaki et al., 2011; Yan et al., 2017). It is evident that the deviatoric stress in GHBS is much higher than HFS. As S_h increases, the difference in maximum deviatoric stress becomes more pronounced, shifting from strain softening to strain hardening (blue curve). Additionally, higher S_h induces a greater negative value of volumetric strain, signifying a shift from compaction to dilatancy. However, the axial strain at which dilatancy occurs varies depending on the composition of sediment particles.

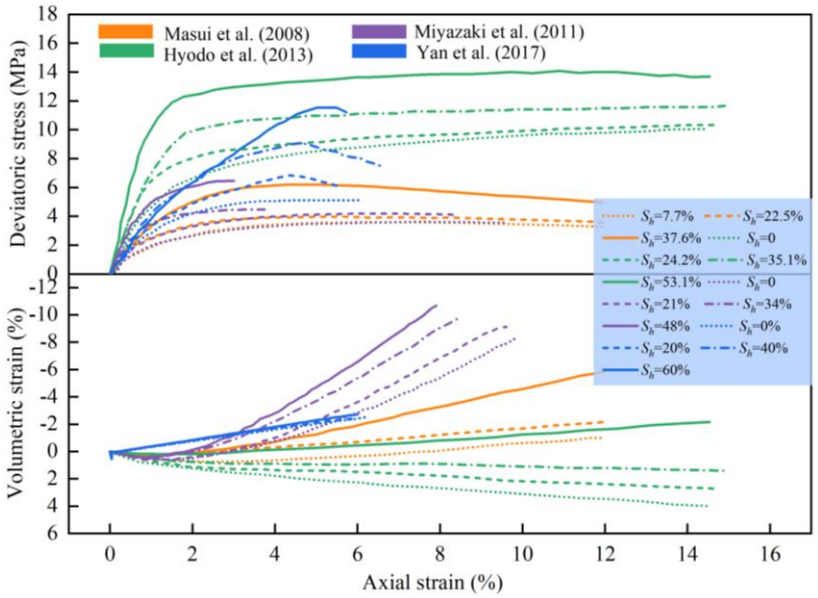

Figure 2.11: Mechanical responses of host sediments in the presence of hydrates

Deep-sea sediments containing hydrates demonstrate significant disparities in mechanical properties corresponding to variation in S_h. In view of this, through a comprehensive review of existing literature pertaining to HBS, we explore the influence of S_h on mechanical parameters, including cohesion (c), internal friction angle (φ), peak strength (σ_s), elastic modulus (E_{50}), Poisson's ratio (v) and dilatancy angle (ψ), the change of which with respect to S_h are depicted in Figs. 2.12-17.

Table 2.5 consolidates the mechanical test results that examine the effects of S_h on c and φ. c and φ, as pivotal parameters in Mohr-Coulomb failure criterion, which determine shear strength and load-bearing capacity of HBS. c functions as the "adhesive force" between sediment particles, reflecting the cementation effect. As shown in Fig. 2.12, Li et al. (2021) investigated the effect of S_h on strength response of methane hydrate-bearing sand under direct shear test, revealing an exponential increase in c as S_h elevates, which is consistent with the result reported by Miyazaki et al. (2011). In addition to this phenomenon occurring in coarse-grained sediments, the same upward trend in c with increasing S_h is observable in fine-grained sediments including clay and clayey silt. However, a relationship approximating linearity for fine-grained sediments can be discerned through fitting, which is different from coarse-grained sediments (Dong et al., 2022; Wang et al., 2020). Notably, it is evident that when $S_h < 50\%$, the improvement in c by hydrates is

relatively small, whereas above 50%, a substantial cementation effect transpires (Liu et al., 2013); This is attributed to the increase in S_h implying that hydrates occupy an augmented pore space, which inhibit pore water flow, resulting in mitigating u and augmenting effective stress, consequently enhancing c (Liu et al., 2018; Masui et al., 2005; Miyazaki et al., 2009; Zhang et al., 2018). φ epitomizes the frictional resistance, with the majority of HBS exhibiting φ within 0°-40°. Contrary to the correlation observed between c and S_h, numerous studies have substantiated that S_h is not the determinative factor affecting φ (Dong et al., 2020; Li et al., 2021; Yan et al., 2012; Sun et al., 2013; Zhang et al., 2015). From the results represented in Fig. 2.13, it can be seen that a rather insubstantial impact of S_h on φ, demonstrating irregular changes with the increase of S_h. When $S_h < 55\%$, Zhang et al. (2011) exhibited a unique trajectory correlating φ and S_h, where a substantive quadratic increase in φ with rising S_h. This is posited to stem from hydrates filling the pore medium, potentially enhancing the resistance to interparticle sliding.

Table 2.5: Summary of the mechanical tests related to c and φ (Effected by S_h)

Reference	Soil type	Hydrate type	Test conditions	Porosity ϕ (%)
Masui et al. (2005)	Toyoura sand	Methane hydrates	Excess-driven method, CD triaxial test	37.7
Miyazaki et al. (2009)	Toyoura sand	Methane hydrates	Excess-driven method, CD triaxial test	37.7
Sun et al. (2013)	Sand	Methane hydrates	Dissolved gas method, CD triaxial test	-
Wang et al. (2020)	Clay	Methane hydrates	Unsaturated soil method, CD triaxial test	45
Zhang et al. (2018)	Silt sand	Methane hydrates	Soil-water mixing method, CD/CU triaxial test	40
Dong et al. (2020)	Sand	Methane hydrates	Excess-driven method, triaxial shear test	40
Li et al. (2021)	Quartz sand	Methane hydrates	General formation method, triaxial shear test	40
Zhang et al. (2011)	Quartz sand	Methane hydrates	General formation method, triaxial shear test	-
Liu et al. (2013)	Clayey silt	Synthetic THF hydrates	Pre-freezing method, triaxial shear test	39.7

Dong et al. (2022)	Reconstituted clayey silt	Synthetic THF hydrates	Hydrate premixing method, triaxial shear test	43
Zhang et al. (2015)	Silty clay	Synthetic THF hydrates	General formation method, CU triaxial test	52.1
Yan et al. (2012)	Sand	CO_2 hydrates	Unsaturated soil method, triaxial shear test	44.4
Liu et al. (2018)	Sand	CO_2 hydrates	Soil-water mixing method, direct shear test	40

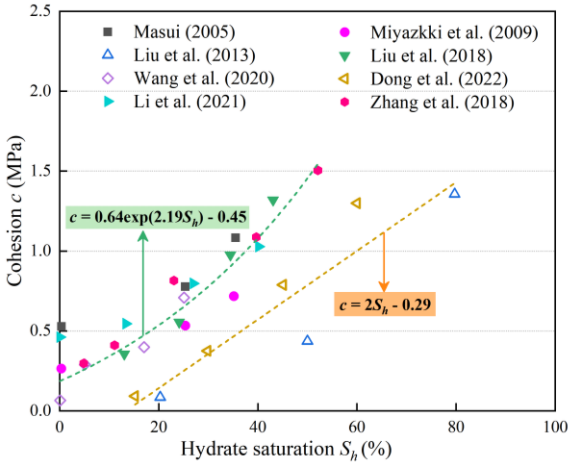

Figure 2.12: Change of c with varying S_h

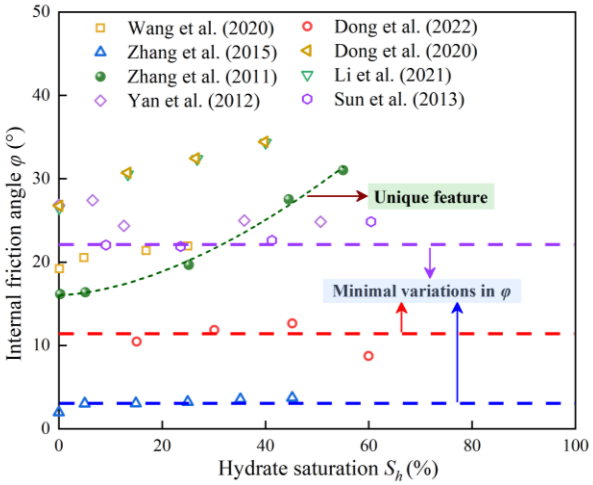

Figure 2.13: Change of φ with varying S_h

Table 2.6 summarizes various mechanical experiments on the strength and stiffness of HBS affected by S_h. σ_s is denoted as peak deviatoric stress, serving as an indicator of maximum stress that sediments can endure before failure. The deviatoric stress corresponding to 15% axial strain (ε_a) is taken when strain hardening occurs, while maximum deviatoric stress is considered subjected to strain softening. Stiffness, quantifiable as the secant elastic modulus, is defined as the ability of HBS to resist deformation, which can be obtained from the initial slope of stress-strain curve. Figs. 2.14-2.15 show the relationship among S_h, σ_s and E_{50} of HBS under the effective confining stress of 1MPa. It can be found that both σ_s and E_{50} gradually increase with an increase in S_h, exhibiting an exponential relationship: $\sigma_s / E_{50} = a + b \cdot (S_h)^c$ (Miyazaki et al., 2011; Yang et al., 2023), Masui et al. (2005) suggests that this phenomenon depends on the cementation effect between hydrates and sediment particles. At lower S_h, the contribution of hydrates to σ_s and E_{50} is marginal since hydrates in pore-filling morphology are dispersed within pore space without forming inter-particle connections and generating evident cohesive forces (Xu et al., 2022a; Li et al., 2018); Meanwhile, sediments are prone to weakening under elevated shear stress. Conversely, when S_h exceeds 50%, the cementing structure forms between hydrates and sediment particles; HM transitions from pore-filling to cementing type, which intensifies the adhesion within sediment particles and subsequently improves the cementing strength provided by hydrates, thereby bolstering both σ_s and E_{50} (Yun et al., 2007; Ghiassian and Grozic, 2013). Furthermore, compared to loosen HBS with higher proportion of fine particles, denser HBS and those containing more coarse particles demonstrate enhanced σ_s and E_{50} (Dong et al., 2019; Hyodo et al., 2013a; Li et al., 2021; Wang et al., 2022), a consequence of greater resistance to fracture for coarse particles upon shearing; According to Mohr-Coulomb criterion, coarse-grain sediments exist greater shear strength due to higher frictional force (Bagherzadeh and Mirghasemi, 2009). The superior grading of materials possesses a larger coordination number per particle surface area, accentuating the cementation effect of hydrates (Luo et al., 2018). Denser HBS implies that hydrates and particles are relatively tight, impeding relative sliding among particles under shear stress. Nonetheless, not all experimental data adhere to the general trend of stiffness varying with S_h. When S_h is approximately 40%, the elastic modulus fluctuates around 0.4 GPa. On the one hand, the grain size of Toyoura sand utilized by Masui et al. (2005) is greater than No.8 silica sand used by Miyazaki et al. (2011), correspondingly exhibiting higher E_{50}, which aligns with the previous discussion. On the other hand, an initial rise followed by a decline in E_{50} with increasing S_h suggests a shift in HM

from pore-filling to cementing, which may induce particle reorganization and structural instability (You et al., 2022).

Table 2.6: Summary of mechanical tests on HBS related to peak strength and stiffness (Effected by S_h)

Reference	Soil type	Hydrate type	Hydrate morphology	Test conditions	T (°C)
Dong et al. (2019)	Sand	Methane hydrates	Pore filling	Excess-driven method, triaxial shear test	1
Hossein and Jocelyn (2013)	Ottawa sand	Methane hydrates	Cementing	Dissolved gas method, CU triaxial test	5
Yang et al. (2023)	Fine-grained sediment (silt)	Methane hydrates	Cementing	Excess-driven method, CD triaxial test	2
Li et al. (2018)	Fine sands	Methane hydrates	Pore filling	General formation method, triaxial shear test	1
Xu et al. (2022a)	Toyoura sand	Methane hydrates	Pore filling	Excess-driven method, CD triaxial test	1
Masui et al. (2005, 2007)	Toyoura sand	Methane hydrates	Pore filling / Cementing	Excess-driven method, CD triaxial test	5
Miyazaki et al. (2011)	Toyoura sand / No.8 sillica sand	Methane hydrates	Pore filling	Excess-driven method, CD triaxial test	5
Li et al. (2021)	Quartz sand	Methane hydrates	Pore filling	General formation method, triaxial shear test	1
Wang et al. (2020)	Clay	Methane hydrates	Pore filling	Unsaturated soil method, CD triaxial test	1
Hyodo et al. (2013a)	Toyoura sand	Methane hydrates	Pore filling	General formation method, CD triaxial test	5

Yun et al. (2007)	Sand	Synthetic THF hydrates	Pore filling / Cementing	Ice seeding method, CU / CD triaxial test	-10

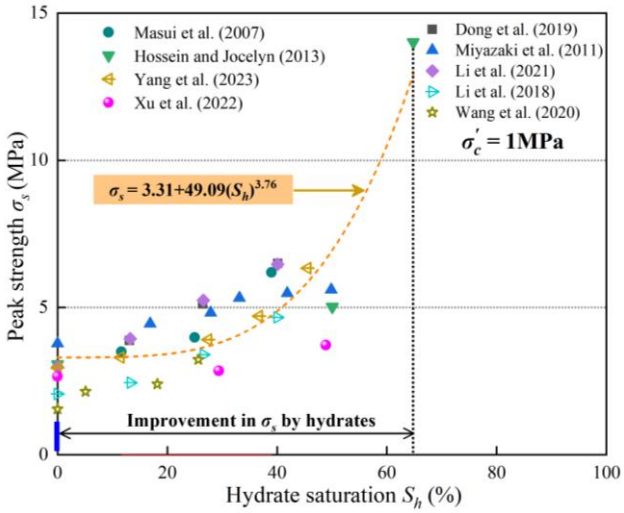

Figure 2.14: Hydrates contribution to the peak strength

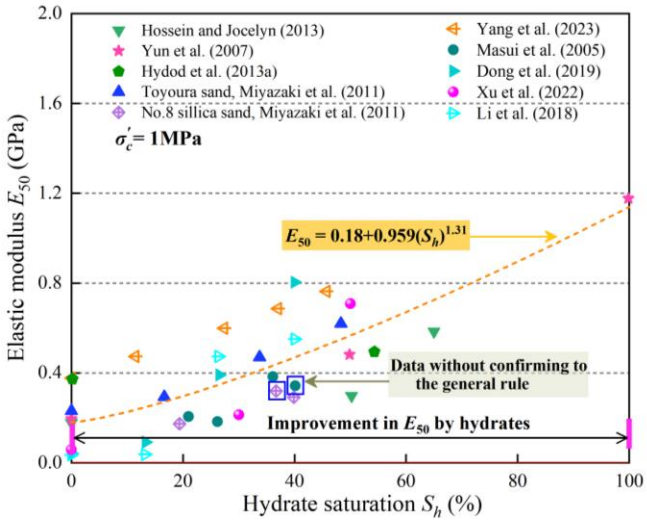

Figure 2.15: Hydrates contribution to the stiffness

v (the ratio of lateral strain to axial strain ε_a) can characterize the compressibility and expansibility of material media. Fig. 2.16 illustrates the correlation between v and S_h of HBS. It suggests that with an increase in S_h, limited experimental results indicate a consequent rise in v while the majority exhibits a parabolic declining trend (Yan et al., 2017; Yang et al., 2023). Notably, when S_h < 50%, numerous irregular points do not conform to a clear trend, propounding

that S_h is not a decisive factor impacting v (Masui et al., 2008; Miyazaki et al., 2011). Possible explanations for the observed trends include: (1) An amplification in S_h enhances the structural stiffness, thereby diminishing the lateral deformation capacity, which in turn improves v (Yang et al., 2020); (2) Hydrate occurrence within the sediments alter the stress distribution, resulting in a reduction or insignificant variation in v (Priest et al., 2009; Zhao et al., 2019).

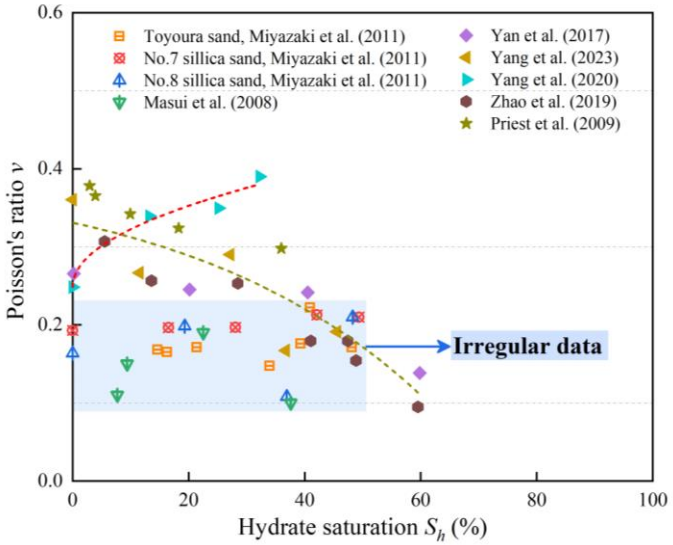

Figure 2.16: Change of v with varying S_h

ψ (the ratio of volumetric strain ε_v to shear strain ε_s) represent the volume deformation of material medium during shearing. ψ of HBS can be derived from the ratio of ε_v to ε_a, as presented in Equation 2.15 (Soga et al., 2006).

$$\psi = \arcsin\frac{\varepsilon_v}{\varepsilon_v - 2\varepsilon_a} \tag{2.15}$$

The relationship between ψ and S_h has been fitted and plotted according to the existing literature as shown in Fig. 2.17. It is evident that ψ progressively increases with increasing S_h, producing a greater volumetric expansion of HBS upon shearing (Le et al., 2018; Li et al., 2023; Zhou et al., 2021). Overall, it adheres to a power function: $\psi = a + b \cdot (S_h)^c$ (Choi et al., 2018; Masui et al., 2006); where the coefficients are related to HM, for the pore-filling type, b<1 while c>1; For the cementing type, b>1 while c<1. Compared to HBS in pore-filling morphology, HBS in cementing morphology generates larger ψ at lower S_h (Masui et al., 2005). The narrow in this gap occurs as S_h increases, especially when S_h exceeds 50%, and the impact degree of HM on ψ becomes minimal (Liu et al., 2018).

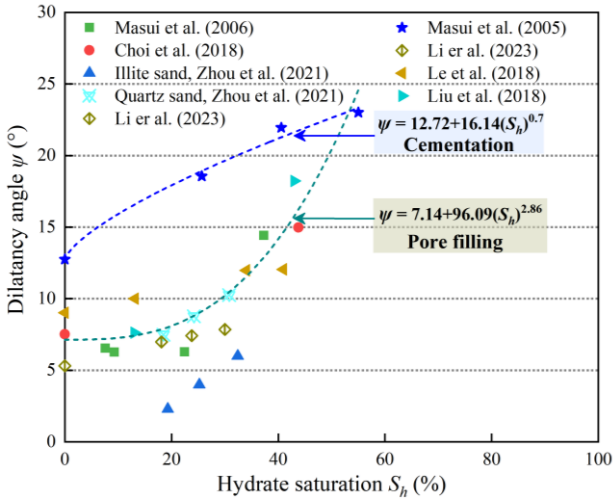

Figure 2.17: Change of ψ with varying S_h

2.4.5 Influence of hydrate dissociation on mechanical behavior of GHBS

To ensure the rationality of hydrate recovery, it is necessary to address a multitude of challenges concerning hydrate dissociation, such as volumetric deformation of sediment matrix, stress relaxation, reservoir instability, and changes in pore water pressure. In view of these, numerous researchers have embarked on a series of mechanical tests to delve into the impact of hydrate dissociation on mechanical properties of HBS. Considering the environment and feasibility, the predominant methods employed in the laboratory to induce hydrate dissociation encompass: thermal stimulation, depressurization, and CO_2 replacement (Wang et al., 2020; Yoshimoto et al., 2023). Table 2.7 tabulates some of the mechanical tests on hydrate dissociation induced by previously mentioned methods.

From the perspective of thermal stimulation, Wu et al. (2020a) combined X-ray Computed Tomography with triaxial tests to analyze the mechanical characteristics of hydrate-bearing sand during dissociation. The results exhibited that the continual decline in shear strength and elastic modulus was attributed to the loss of cementation, and the secondary formation of hydrates after dissociation led to a reduction in K_1. Song et al. (2014) identified the reduction in σ_s for hydrate-bearing clays stems from the decreased c. Moreover, the lower the $\sigma_c^{'}$ is, the smaller the residual strength (σ_r) displays after failure, and it tends to decelerate the rate of decreasing σ_r under a low dissociation rate. Further, they also found that strain-softening behavior appears at higher T; σ_r diminishes with dissociation time (t_d), with a more pronounced reduction rate under high T (Song et al., 2016). Differing from sands, Song et al. (2019) observed that when HBS dissociated after

undergoing thermal stimulation, whose σ_s is dependent on the hydrate concentration, and the attenuation ratio is proportional to S_h, as shown in Fig. 2.18.

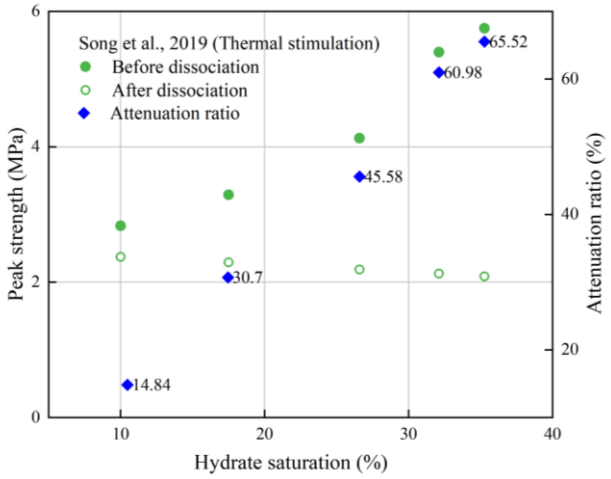

Figure 2.18: The dependency of effective parameters on S_h under thermal stimulation

In cases of depressurization, Zhang et al. (2018) investigated the mechanical properties of HBS with varying initial S_h during hydrate dissociation. The results indicated that σ_s decreased by 30%-90% compared to the initial state. Furthermore, the magnitude of reduction intensified with an increase in initial S_h due to the disruption of the bond between particles and hydrates. Correspondingly, E_{50}, φ, and c also decreased. Choi et al. (2020) reported that the stability of HBS is related to the initial deviatoric stress (q_i). Volumetric contraction occurs after depressurization, and HBS at lower q_i remains stable upon re-pressurization, whereas those at higher q_i undergo instability and rupture. Similarly, Li et al. (2018) noted that volume of HBS undergoes contraction after dissociation and it transforms HM into load-bearing at higher S_h, causing evident stress relaxation. Further, Li et al. (2023) found that the volumetric deformation of HBS is independent of depressurization times but is controlled by overburden stress, with settlement doubling as the stress level increased from 0.7 to 0.9.

CO_2 replacement is progressively emerging as a trend in hydrate recovery. Liu et al. (2016, 2013) through CD triaxial test demonstrated that a greater volumetric proportion of CO_2 substantially enhances σ_r and E_{50} of HBS. Consistent with this perspective, Luo et al. (2020b, 2017) observed that σ_r exceeds that of the prior state after CO_2 replacement, with a reduction in compressibility, substantiating improved structural stability. Hyodo et al. (2014a) supported these

findings by employing consolidated shear test, examining that CO_2 distributes uniformly within the pore spaces after replacement.

Each of the discussed methods for hydrate dissociation presents specific constraints. In response, several researchers have initiated comprehensive mechanical investigations through the comparison of these approaches. Lee et al. (2020) observed that when only considering depressurization, a dropping in σ_s occurs at the dissociation rate of 20% while σ_s rebounds after CO_2 replacement, which is depicted in Fig. 2.19. This suggests that initial strength is independent of dissociation rate, and the replacement reaction can enhance the stability of HBS. Hyodo et al. (2013b) indicated that hydrate dissociation induced by thermal stimulation produces greater ε_a in specimens with increasing initial shear stress, resulting in the failure of specimens in the metastable consolidated region, whereas depressurization leads to collapse in the stable equilibrium zone under effective stress. Luo et al. (2020a) discerned that during depressurization, hydrate-bearing silty experiences substantial deformation without failure, emphasizing the decisive role of effective stress in volumetric changes during dissociation. On the other hand, HBS with varying S_h exhibited varying degrees of damage after dissociation induced by thermal stimulation. Contrasting multiple dissociation methods, Li et al. (2016) and Liu et al. (2014) concluded that the stability of HBS dissociated via depressurization surpasses those via thermal stimulation, with HBS under CO_2 replacement exhibiting the highest σ_s and E_{50} (Fig. 2.20).

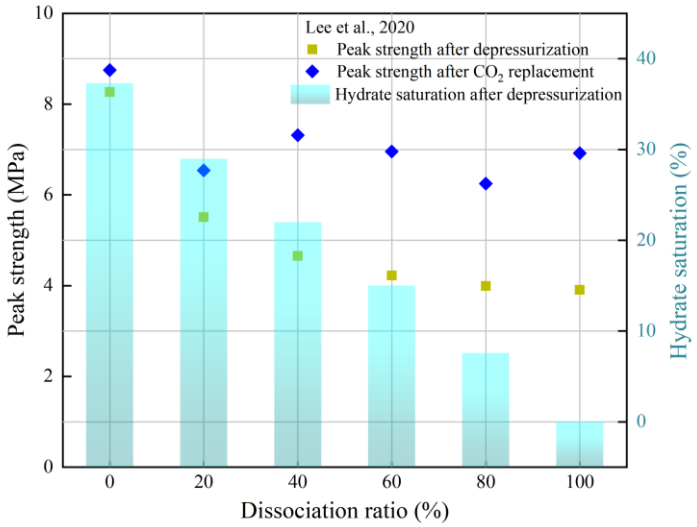

Figure 2.19: The dependency of peak strength on dissociation ratio under depressurization and CO2 replacement

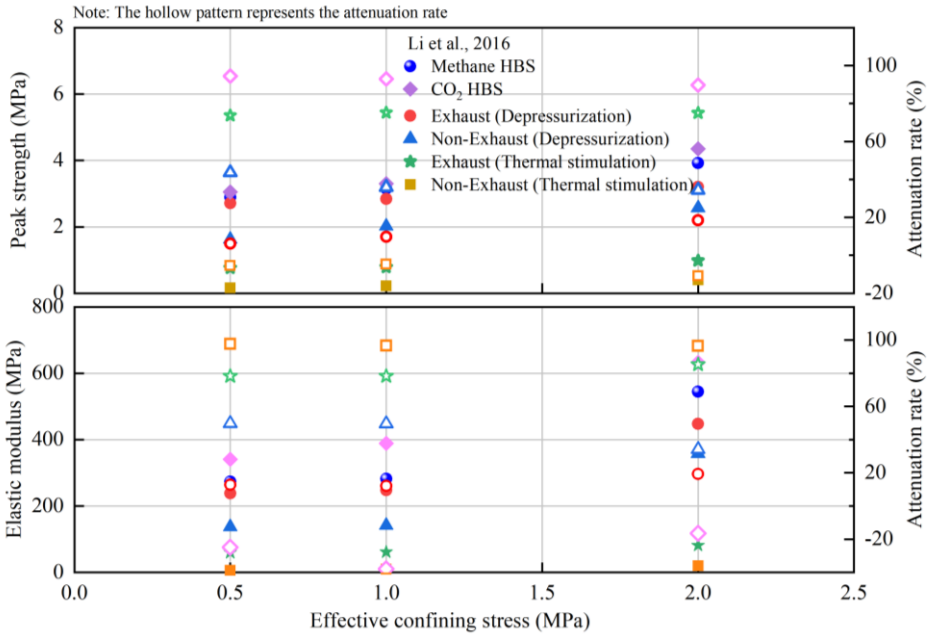

Figure 2.20: The variation in effective parameters under various dissociation methods

Despite CO_2 replacement method being considered the most promising technology for hydrate exploitation, the displacement reaction mechanism of this approach remains unclear in current research. Ensuring the maintenance of gas transmission pipelines is vital for efficient extraction. Meantime, it is imperative to integrate CO_2 replacement with other techniques such as depressurization and thermal stimulation hold considerable research value.

Table 2.7: Summary of mechanical tests on HBS related to hydrate dissociation

Reference	Dissociation method	Soil type	Gas composition	Test conditions	Initial S_h (%)	σ' (MPa)
Wu et al. (2020a)	Thermal stimulation	Fujian sand	Xenon gas	General formation method, CD triaxial test / X-ray CT	0, 35.75, 36.29	3
Song et al. (2014,2016)	Thermal stimulation	Kaolin clay	Methane	Ice-seeding method, CU triaxial test	25-30	0.5, 1, 2
Song et al. (2019)	Thermal stimulation	Silty	Methane	Ice-seeding method, CU triaxial test	0-35	1, 2, 3

Zhang et al. (2018)	Depressurization	Silt sandy	Methane	Gas saturated method, CD / CU triaxial test	19, 38, 50	1, 2, 3, 5
Choi et al. (2020)	Depressurization	Silica sand-kaolinite mixture	Methane	Brine-injection and heating-cooling method, CD triaxial test	40	6.21
Li et al. (2018)	Depressurization	Quartz sand	Methane	General formation method, CU triaxial test	33-38, 56.14	NA
Li et al. (2023)	Depressurization	Silica sand and clay	Methane	Excess-driven method, CD triaxial test / triaxial creep test	0, 27, 28	3
Luo et al. (2017)	CO_2 replacement	Mixture of kaolin clay and quartz sand	CO_2-CH_4	Ice-seeding method, CD triaxial test	30	2.5, 3.75, 5, 7.5, 10
Luo et al. (2020b)	CO_2 replacement	Silty	CO_2-CH_4	Excess-driven method, isotropic consolidation and shear test	0-30	0.2, 1, 2, 3
Hyodo et al. (2014a)	CO_2 replacement	Toyoura sand	CO_2-CH_4	Ice-seeding method, isotopically consolidated shear test	0, 31-47	1, 2, 5
Liu et al. (2013, 2016)	CO_2 replacement	Kaolin clay	CO_2-CH_4	Ice-seeding method, CD triaxial test	30	2.5, 3.75, 5, 7.5, 10
Li et al. (2016)	Thermal stimulation / Depressurization / CO_2 replacement	Kaolin clay	CO_2-CH_4	Ice-seeding method, CD triaxial test	NA	0.5, 1, 2
Lee et al. (2020)	Depressurization / CO_2 replacement	Quartz sand	CO_2-CH_4	Excess-driven method, CD / CU triaxial test	35-37, 28.9	NA

Liu et al. (2014)	Thermal stimulation / Depressurization / CO_2 replacement	Kaolin clay	CO_2-CH_4	Ice-seeding method, CD triaxial test	30	2
Luo et al. (2020a)	Thermal stimulation / Depressurization	Clayey silt	Methane	Excess-driven method, CD triaxial test	0-33	1
Hyodo et al. (2013b)	Thermal stimulation / Depressurization	Toyoura sand	Methane	Unsaturated soil method, isotopically consolidated shear test	31.5, 38.2, 43.2, 46, 47.3, 48	1, 3, 5

2.5 Influence of other factors on the mechanical responses of GHBS

2.5.1 Analysis of the variation in mechanical parameters related to effective confining stress

σ_c' affects the mechanical properties of HBS due to applied lateral restraint stress, which is defined as the difference between confining stress and u. σ_c' is expected to simulate the pressures exerted on HBS in marine environments from overlying strata, largely attributable to the burial depth (Handin et al., 1963). Fig. 2.21 presents the mechanical responses of sediments with S_h ranging from 26 to 30% under various σ_c' (Dong et al., 2020; Li et al., 2018; Miyazaki et al., 2011; Yang et al., 2023). Observations indicate that with an increase in σ_c', the deviatoric stress correspondingly rises. Coarse-grained sediments, which exhibit dilatancy under low σ_c', display similar behaviors even under high σ_c'. Conversely, fine-grained sediments, which demonstrate volumetric contraction, maintain this trend regardless of the applied σ_c'. Although higher σ_c' typically triggers a certain degree of volumetric compaction, with the extent of volumetric deformation largely depending on the sediment composition. Table 2.8 presents a compilation of mechanical tests that demonstrate the impact of σ_c' on methane HBS.

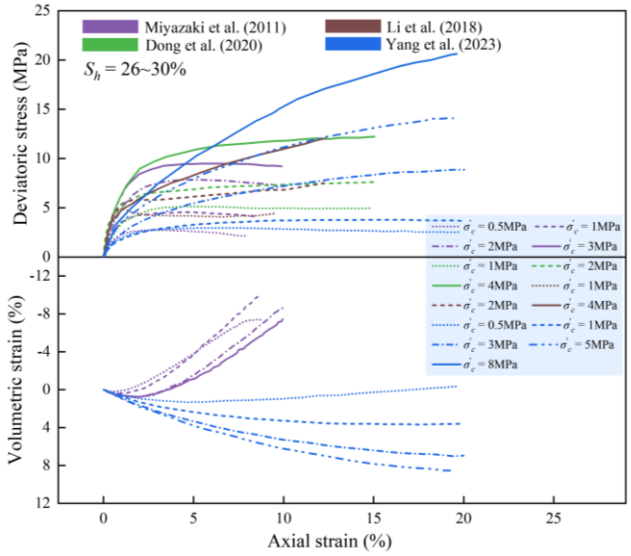

Figure 2.21: Mechanical responses of GHBS with respect to $\sigma_c^{'}$

Table 2.8: Summary of mechanical tests on methane HBS related to strength and stiffness (Effected by $\sigma_c^{'}$)

Reference	Soil type	Test conditions	S_h (%)	T (°C)
Li et al. (2011)	Kaolin	General formation method, triaxial shear test	30	-10
Wang et al. (2018)	Montmorillonite clay	Ice seeding method, triaxial shear test	30	-3
Xu et al. (2022a)	Toyoura sand	Excess-driven method, CD triaxial test	30	1
Li et al. (2021)	Quartz sand	General formation method, triaxial shear test	26.6	1
Dong et al. (2020)	Sand	Excess-driven method, triaxial shear test	26.6	1
Li et al. (2018)	Intermediate fine sands	General formation method, triaxial shear test	26.6	1
Yang et al. (2023)	Fine-grained sediment (silt)	Excess-driven method, CD triaxial test	26.6	2
Miyazaki et al. (2011)	Toyoura sand	Excess-driven method, CD triaxial test	27-34	5
Wang et al. (2020)	Clay	Unsaturated soil method, CD triaxial test	25	1

Figs. 2.22-2.23 depict the variations in σ_s and E_{50} of HBS with S_h within the range of 25-34% under various $\sigma_c^{'}$. It exhibits an enhancement in σ_s and E_{50} of HBS with the increase of $\sigma_c^{'}$. This

amplification is mainly due to $\sigma_c^{'}$ restricting crack propagation while bolstering inter-particle connections and friction, and partially owing to the intensified bonding between hydrates and sediment particles (Li et al., 2021; Miyazaki et al., 2011). Additionally, the increment of σ_s is more pronounced than that in E_{50} with increasing $\sigma_c^{'}$. Through fitting the experimental results (red dashed line), it seems that σ_s linearly increases with $\sigma_c^{'}$, especially undergoing a qualitative improvement under high $\sigma_c^{'}$ ($\sigma_c^{'}$ > 5MPa) (Dong et al., 2020; Yang et al., 2023), while E_{50} exhibits a parabolic trend (Xu et al., 2022a). Further analysis shows that compared to coarse-grained sediments, methane hydrate-bearing clay (fine-grained sediments) exhibits less improvement in σ_s and E_{50}, this aligns with the understanding that well-graded sediment mediums where fine particles occupy voids among coarse particles result in denser overall structure (Wang et al., 2022; Wang et al., 2019). For the fine-grained sediments, methane hydrates would be more dispersed, the cementation effect could be limited as $\sigma_c^{'}$ increases. Conversely, for the coarse-grained sediments, hydrates tend to easily form cementing structures that provide substantial support. Notably, some experimental results deviate from the anticipated trend (red solid line); Li et al. (2018) investigated the shear performance of medium-fine sediments, revealing that sediments with S_h = 26.6% demonstrated a marked reduction in E_{50} at lower $\sigma_c^{'}$ and followed by a slow increase. This is possibly due to hydrate dissociation induced by the increased initial $\sigma_c^{'}$, and subsequent hydrate formation as $\sigma_c^{'}$ further elevated into a stable region. Li et al. (2011) utilized kaolinite to simulate marine sediments, identifying a subtle decreasing trend in both σ_s and E_{50} at higher $\sigma_c^{'}$ ($\sigma_c^{'}$ >5MPa). This phenomenon may arise from the particles undergoing localized crushing under high $\sigma_c^{'}$, triggering the rearrangement of particles and generation of new voids, which result in a loosened structure (Xu et al., 2022a).

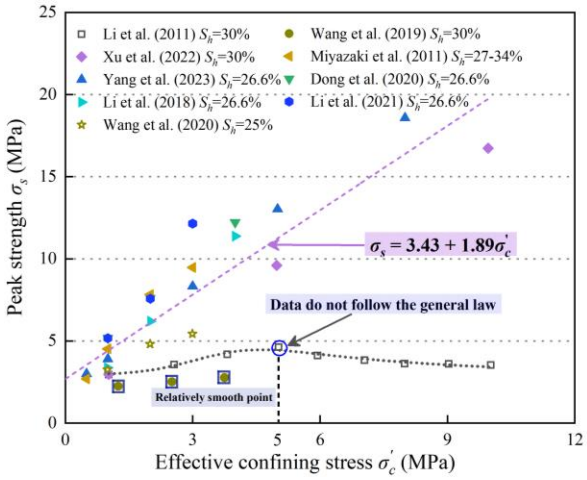

Figure 2.22: Change of σ_s with varying σ_c'

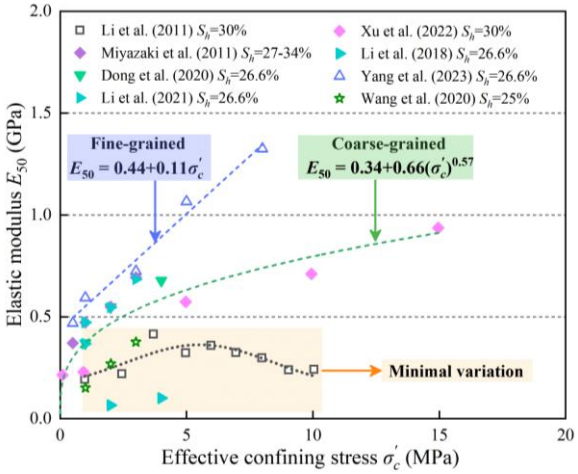

Figure 2.23: Change of E_{50} with varying σ_c'

Fig. 2.24 illustrates how v of HBS varies in relation to σ_c'. Overall, v presents a noticeable descending trend with increasing σ_c', adhering to the power law: $v = 0.48 + 0.15(\sigma_c')^{0.3}$, which is driven by two reasons: i. As previously mentioned, it displays greater E_{50} as σ_c' escalates, constraining the lateral deformation; ii. Sediment matrix becomes more compacted with increasing σ_c', and the applied axial stress reduces the porosity and subsequently decreases the ability to deformation (Choi et al., 2018; Miyazaki et al., 2012; Yang et al., 2020). Yet, experimental results under low σ_c' (σ_c' =0.5, 1MPa) reveal insignificant variations in v, which might be attributed to the facilitation of micro-crack generation at lower σ_c', with axial compression and lateral expansion occurring simultaneously (Yan et al., 2017; Yang et al., 2023).

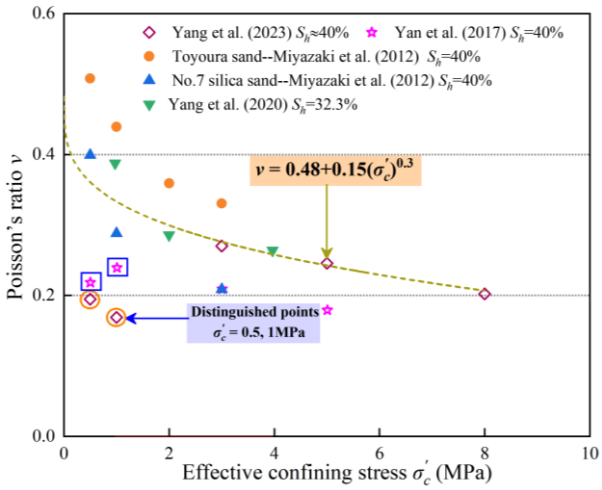

Figure 2.24: Change of ν with varying σ_c'

2.5.2 Analysis of the variation in mechanical parameters related to temperature

The nucleation of NGH relies on specific *T*-*P* conditions. Fluctuations in *T* alter the stable phase equilibrium condition of hydrates, subsequently impacting the distribution and stability of hydrates. Fig. 2.25 synthesizes results from multiple reports to compare the mechanical responses of GHBS under various *T*. It is clear that deviatoric stress curves demonstrate a strong sensitivity to *T*; at lower *T*, the sediments exhibit higher peak deviatoric stresses and tend to strain hardening. Additionally, the volumetric response of host sediments transitions from initial compaction to expansion under low *T*, with this variation being particularly evident at lower *T*. In contrast, at higher *T*, sediments display compact behavior and continue to experience volumetric contraction. Table 2.9 lists the mechanical tests conducted on HBS concerning *T*.

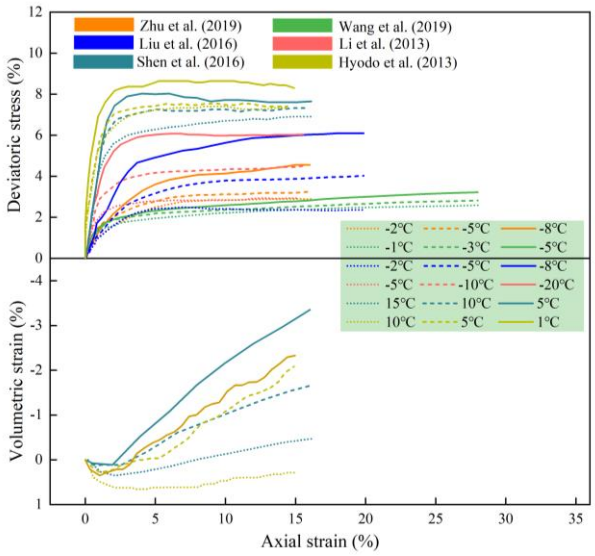

Figure 2.25: Mechanical responses of GHBS with respect to *T*

Table 2.9: Summary of mechanical tests on HBS related to mechanical parameters (Effected by *T*)

Reference	Soil type	Hydrate type	Test conditions	S_h (%)	σ_c' (MPa)
Hyodo et al. (2013a)	Toyoura sand	Methane hydrates	General formation method, CD triaxial test	26.6	3
Wang et al. (2019)	Montmorillonite clay	Methane hydrates	Ice seeding method, triaxial shear test	30	2.5
Li et al. (2011)	Kaolin clay	Methane hydrates	Hydrate premixing method, triaxial shear test	30	5
Zhu et al. (2015)	Kaolin clay	Methane hydrates	Ice seeding method, dynamic triaxial shear test	30	2
Zhu et al. (2020)	Kaolin clay, quartz sand	Methane hydrates	Ice seeding method, triaxial shear test	30	2.5
Shen et al. (2021)	Silica sand	Methane hydrates	Excess-driven method, CD triaxial test	59.2	3
Liu et al. (2013, 2016)	Kaolin clay	CH_4-CO_2 hydrates	Ice seeding method, triaxial shear test	30	5

Figs. 2.26-2.27 illustrate the variations in σ_s, c, and φ of HBS associated with T. It can be observed that both σ_s and c tend to decline linearly as T increases (Li et al., 2011b; Liu et al., 2013; Liu et al., 2016). This phenomenon is attributed to the thermal expansion of hydrate crystals or

sediment particles at elevated *T*, degrading the resistance to deformation. In addition, the weakening in *c* due to hydrate dissociation at higher *T* provokes sediment particles to lose adhesion with hydrates, thereby diminishing the bond strength (Hyodo et al., 2013a). It is noteworthy that σ_s and *c* decrease significantly when *T* is below 0°C, whereas such changes are comparatively muted above 0°C (Shen et al., 2021). This can be explained by the fact that water molecules freeze into ice crystals when *T* below 0°C (Zhu et al., 2020); the phase transition of water accompanied by volumetric expansion precipitates the disruption of sediment structure, consequently effectuating a substantial reduction in both *c* and σ_s (Wang et al., 2019; Zhu et al., 2015). It is also noted that upon holding constancy in other factors such as *P* and S_h, σ_s of HBS with varying *T* hinges on *c*, which exhibit uncorrelated with φ. This is manifested in the graph where φ appears to be exclusively associated with the sediment type, demonstrating an indiscernible correlation with *T*.

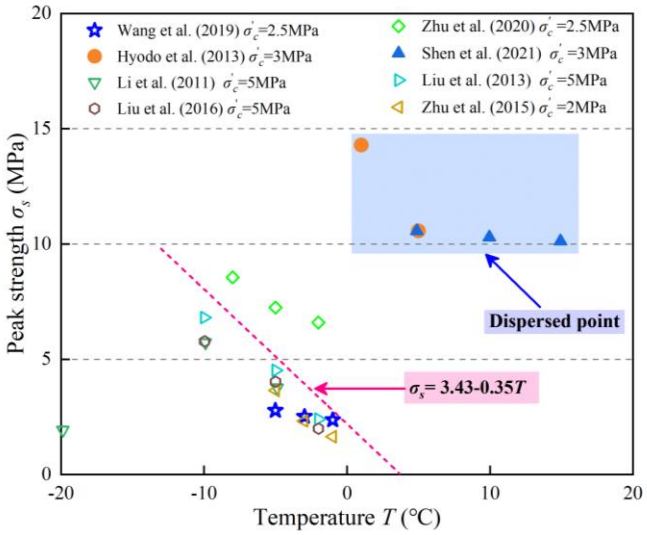

Figure 2.26: Change of σ_s with varying *T*

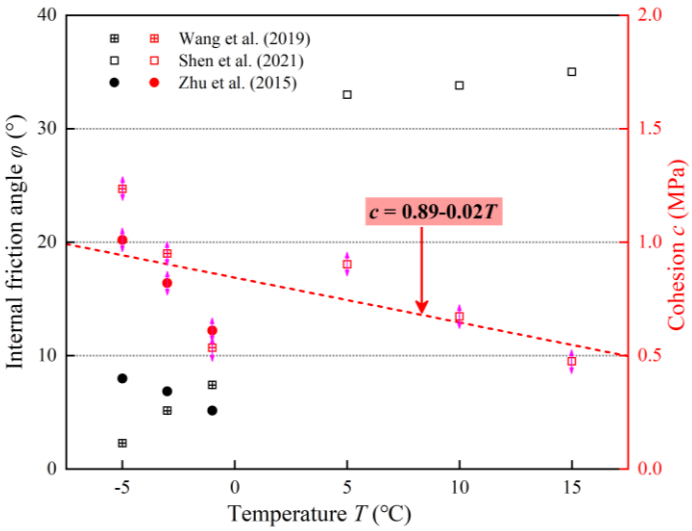

Figure 2.27: Change of c and φ with varying T

2.5.3 Influence of sediment composition, strain rate, and porosity on mechanical behavior of GHBS

Geological processes and the diversity of sedimentary environments contribute to the variance in sediment composition and particle characteristics, which in turn determine the configuration of pore space, thus affecting the interaction between hydrate and sediment matrix. Masui et al. (2005) observed that the strength and stiffness of synthesized GHBS with similar particle sizes closely approximate those of natural GHBS. Li et al. (2011b) discovered that GHBS with higher kaolin volume ratio shows enhanced strength with minimal alteration in stiffness, emphasizing the dependency of cohesion on kaolin content. Under constant average particle size, Hyodo et al. (2017, 2015) demonstrated that CH_4-HBS with higher fine content display augmented shear strength and dilatancy, particularly in a looser state, aligning with the findings of Teerawattanasuk and Voottipruex (2014). Kajiyama et al. (2017a) indicated that the cementation effect of CH_4-HBS increases with an increase in fine content, consequently improving the strength, while Young's modulus inversely relates to fine content. Luo et al. (2018) suggested that a higher proportion of larger particles contributes to the increased φ, amplifying the strength. Further, due to superior material gradation, wider particle size distribution in GHBS results in a larger coordination number per particle surface area, intensifying hydrate cementation and failure strength (Miyazaki et al. (2012)). Hu et al. (2022) reported that shear modulus rises with particle size while the damping ratio tends to decrease. Additionally, the presence of hydrates mitigates

the impact of particle size on the mechanical properties of GHBS. Fig. 2.28, integrating results from the aforementioned studies, illustrates the variability in mechanical responses of GHBS with respect to different sediment compositions. Sediments with higher fine content (FC = 22.9% or 25%), a larger volume ratio of soil particles (KVR = 60%), and larger grain sizes (HS5) generally exhibit higher peak stresses (solid lines), indicating stronger shear strength and a tendency toward strain hardening. Additionally, sediments with higher fine content transition from volumetric compression to dilation at lower axial strain, displaying more pronounced expansion.

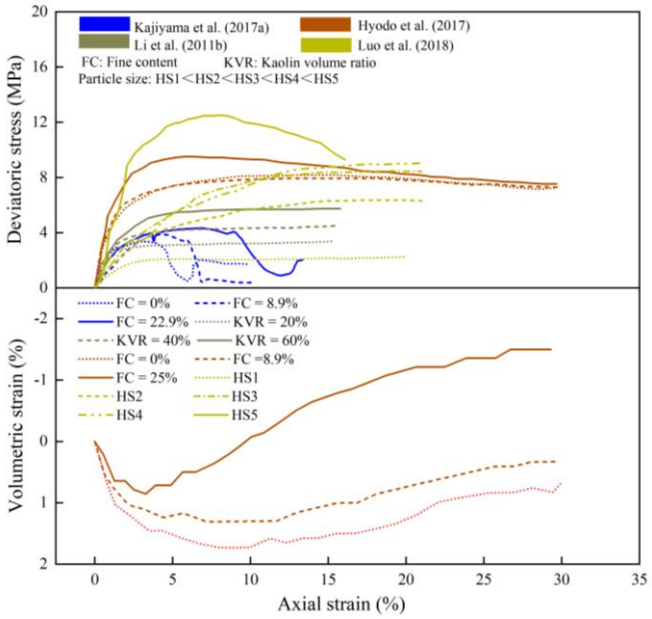

Figure 2.28: Mechanical responses of GHBS with respect to sediment composition

GHBS display distinct time-dependent behavior associated with the variation in strain rate. Miyazaki et al. (2010) found that the effect of strain rate on HFS is negligible but significant in GHBS. Li et al. (2011a) noted that the peak strength of GHBS is directly proportional to strain rate and observed a hardening tendency at a higher rate and a softening tendency at a lower rate. Deusner et al. (2019) showed that marked hardening behavior and earlier onset of peak strength occurs at higher strain rate, with less dilatancy mobilization after softening. Liu et al. (2013) revealed that increased interparticle friction at a higher strain rate results in greater failure strength. Wu et al. (2023) observed that under high S_h, both peak strength and stiffness escalate with increasing strain rate, exhibiting notable volume compression at a lower rate. Notably, the sensitivity of strain rate to GHBS is dependent on hydrate content than hydrate morphology.

Overall, a higher strain rate abbreviates the interaction time between sediment particles and hydrates, triggering an earlier peak in the cementation effect and thereby strengthening GHBS, as depicted in Fig. 2.29.

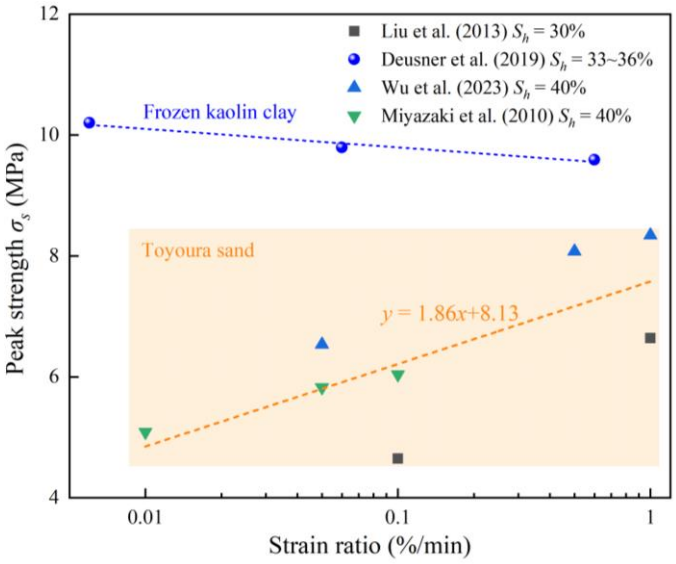

Figure 2.29: Peak strength versus strain ratio

Porosity ϕ (the ratio of pore volume to the total volume) directly reflects the sediment density as well as the distribution and stability of hydrate. Liu et al. (2013) recognized that the strength of CO_2-HBS increases linearly with a decline in ϕ, which is consistent with the observation of Li et al. (2011a) on CH_4-HBS. Hyodo et al. (2017) noted that increased compaction reduces e, boosting both dilatancy and shear strength. Wang et al. (2019) indicated that lower ϕ accompanied by heightened initial density leads to a reduction in pore space and the thickness of hydrate films, consequently augmenting the failure strength without altering stiffness. Wu et al. (2021) reported that GHBS under low ϕ exhibit earlier attainment of peak stress ratio and minimum dilatancy rate. Zhu et al. (2015) delved into the strengthening mechanism of ϕ on GHBS, suggesting a diminish in φ with increasing ϕ, accompanied by a gradual strength degradation. Overall, reduced ϕ increases density as pore space being occupied by hydrates, amplifying the cementation effect. Concurrently, more contact points between particles further enhance frictional force, contributing to the additional shear strength (Fig. 2.30).

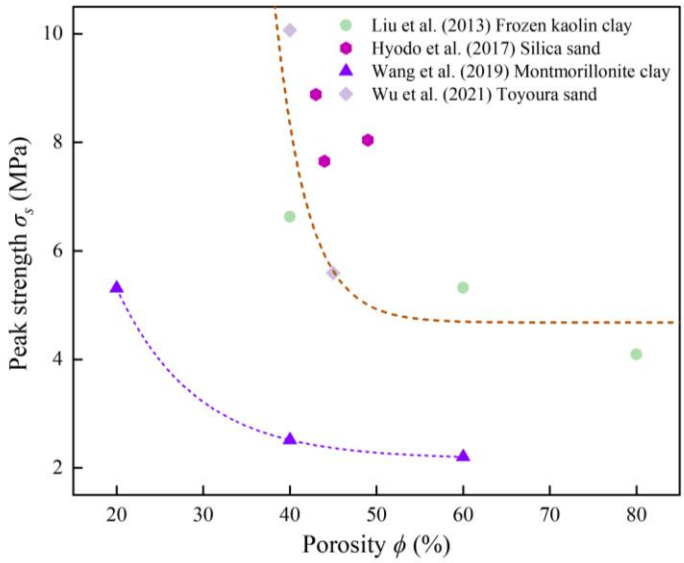

Figure 2.30: Peak strength versus porosity

2.6 Time-dependent deformation characteristics in GHBS

Creep behavior (the enduring deformation that solid materials exhibit under prolonged constant loading) is characterized as time-dependent strain variation. The creep of GHBS unfolds in three phases: I. diminishing creep (initial creep stage); II. steady creep (secondary creep stage); III. accelerating creep (tertiary creep stage) (Zhu et al., 2022) (Fig. 2.31). The inflection points from diminishing creep stage to steady creep stage termed rheological starting point, while the intersection between steady and accelerating creep stage is referred to the creep damage point. Initial stage: GHBS undergoes initial deformation where strain escalates over time, yet the strain rate ($\dot{\varepsilon}$) decreases. This phenomenon is primarily due to the densification and reorientation of sediment particles. The frictional resistance of particles escalates as the sediment structure is subjected to the applied load, precipitating the deformation. Secondary stage: strain continues to increase over time under stable $\dot{\varepsilon}$, indicating a dynamic balance among deviatoric stress, internal resistance of sediments, and cementation strength provided by hydrates. Tertiary stage: $\dot{\varepsilon}$ increases exponentially, with strain rapidly increasing until specimen failure. This is attributed to the gradual breakage of bonding between sediment and hydrate under sustained stress. with microcrack propagation inducing notable strength and stiffness reduction (Nakashima et al., 2021). However, Wang et al. (2012) subdivided the creep behavior into four stages, bifurcating the initial stage into

transient creep process and damping creep process. The former reflects the immediate elastic or plastic deformation of specimen upon loading, whereas the latter is indicative of a decreasing strain rate towards a constant rate.

Under stable creep stress, HFS manifest only initial and secondary creep stages, while hydrate-bearing sands demonstrate a distinct tertiary creep stage, which stems from the role of hydrates as an interparticle cementing agent. The cementation effect is weakened with hydrate dissociation over time, which leads to the redistribution of particles and considerable axial deformation, further escalating $\dot{\varepsilon}$. This observation is substantiated by Miyazaki et al. (2017) by introducing the concept of equivalent creep stress (the ratio of applied creep stress to the strength of materials) (Wang and Xu, 2021).

Creep in GHBS correlates strongly with deviatoric stress q, where elevated q engenders greater axial strain ε_a and $\dot{\varepsilon}$; this is because once q surpasses the cementation strength of hydrates and the frictional resistance between particles, consequently triggering the deterioration in cementation structure and substantial axial deformation. Also, effective confining stress σ_c' emerges as a crucial factor influencing creep behavior. It is noted that both ε_a and $\dot{\varepsilon}$ exhibit an inverse relationship with σ_c', reaching the rheological onset point in advance at higher σ_c'. This is attributed to the fact that higher σ_c' inhibit inter-particle movement and promote particle bonding, enabling the structure to withstand augmented external stress. Furthermore, T is a non-negligible factor. Lower T strengthens the structure by facilitating the transition of hydrate into ice, with a reduction in ε_a and $\dot{\varepsilon}$ (Li et al., 2019; Li et al., 2016). Conversely, higher T facilitates hydrate dissociation, which compromises the cementation structure and consequently diminishes the strength. Typically, the tertiary stage occurs associated with elevated stress levels and higher T. Besides, GHBS with larger porosity experience greater creep strain, which is dependent on the change in internal cementation (van der Waals forces among soil particles, hydrates, and cementation between soil particles and hydrates) (Wang et al., 2012).

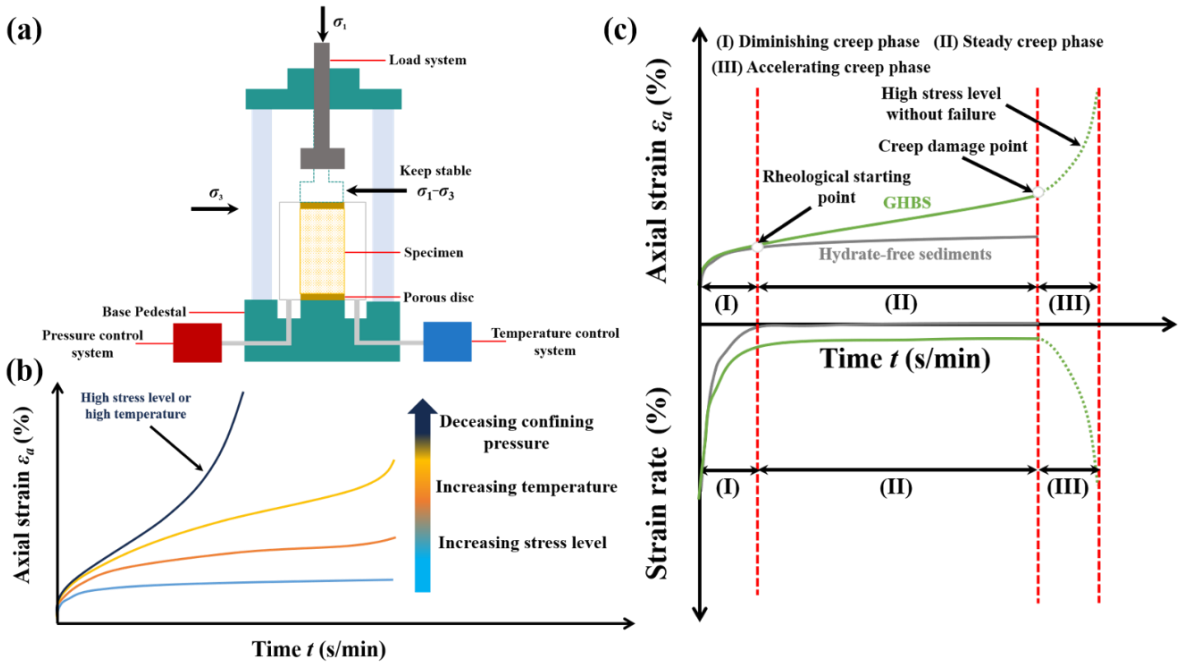

Figure 2.31: Schematic of the creep behavior of sediments without and with hydrate presence: (a) Creep test; (b) Creep curves of GHBS under various factors; (c) Comparison between HFS and GHBS

2.7 Conclusions

In this chapter, we have systematically reviewed the geo-physical-mechanical performance of GHBS, aiming to offer valuable insights for future research endeavors. The main aspects of our discussion include: a. intrinsic properties of GHBS including thermal property, fluid flow property, and compressibility; b. methods for specimen remolding in the laboratory associated with test apparatuses, and initial test conditions; c. mechanical response of host sediments in the presence of hydrates; d. influences of external conditions (effective confining stress, temperature, porosity, strain rate, sediment composition, sustained loading) on mechanical properties of GHBS. The following conclusions can be drawn:

(1) The porosity of GHBS hinges on burial depth, effective stress, and grain size. As the depth and effective stress escalate, sediment particles become increasingly compacted, leading to a decline in porosity. Conversely, coarse-grained sediments exhibit higher porosity relative to those shown in fine-grained counterparts.

(2) The permeability of GHBS is significantly influenced by HM and S_h. Permeability decreases in a parabolic trend that opens upward with an increase in S_h. For the coarse-grained sediments, HM are predominantly categorized into pore-filling and grain-coating types. GHBS in grain-coating type exhibit higher permeability compared to those in pore-filling due to the latter occupying more pore space, thus increasing the flow resistance.

(3) Hydrates act as a cementing agent between sediment particles, resulting in the structure of GHBS that demonstrates greater compactness and lower compressibility compared to HFS. The sediment matrix is compacted with increasing effective stress, followed by considerably diminishing the compressibility upon reaching the volumetric yield point. Moreover, the cementation between hydrates and sediment matrix strengthens while the sediment structure becomes denser at higher S_h, progressively reducing compressibility. Notably, GHBS in cementing type requires greater effective stress to achieve consolidation due to the enhanced bond strength provided by hydrates, as opposed to GHBS in pore-filling morphology.

(4) The post-yield stress-strain behavior of GHBS deviates from that of HFS, manifesting either strain hardening or softening. Softening is ascribed to the reorganization of the porous framework, a consequence of hydrate dissociation under high stress. HFS undergo volume compaction and progressive consolidation when subjected to loading. GHBS initially display volume compression but subsequently transitions into the volumetric expansion phase. This is induced by hydrate dissociation coupled with the migration of fractured particles into pore spaces, provoking the reconfiguration of sediment matrix.

(5) The relationship between c and S_h exhibits a dependency on particle size. For the coarse-grained sediments, c increases exponentially with S_h while a linear relationship for the fine-grained sediments. c increases gradually when S_h is below 50% but escalates significantly beyond this threshold. φ is independent of S_h and solely determined by soil type. The strength and stiffness of HBS are positively correlated with c, especially in sediments containing abundant coarse grains with greater interparticle friction, which reflect enhanced shear strength. The cementation effect of hydrates is more pronounced in well-graded sediments with larger specific surface areas per unit particle. v does not show a clear correlation with S_h, but ψ follows a power function, revealing evident volumetric expansion upon shearing. HBS in cementing morphology exhibit a larger dilatancy at lower S_h compared to those in pore-filling morphology.

(6) The augmentation of strength in GHBS is predominantly attributed to a constellation of

factors: greater $\sigma_c^{'}$ facilitating the interlocking between hydrates and sediment particles; thermal expansion at higher T reducing shear strength; larger particle size and well-graded distribution contributing to strengthening; higher strain rate shortening the interaction time between particles; and lower ϕ enhancing the structural density.

(7) The stability of HBS after hydrate dissociation triggered by thermal stimulation is influenced by the initial stress state and S_h. The residual strength displays a decline trend with dissociation time. Following depressurization, HBS demonstrate noteworthy stability, with the degradation degree of strength and stiffness being intimately linked to initial stress conditions. Compared to other methods, HBS manifest the highest residual strength and stiffness after CO_2 replacement.

(8) GHBS experience three distinct creep phases: diminishing, steady, and accelerating. Notably, the accelerating phase manifests exclusively under specific conditions such as high T, high stress level, and low $\sigma_c^{'}$. Furthermore, GHBS characterized by higher porosity undergo larger creep strain.

Chapter 3. Recent developments in the constitutive models for GHBS

In geotechnical engineering, constitutive model is the essential tool for delineating the stress-strain relationship of materials subjected to applied load, which can be expressed in the form of equations based on continuum mechanics to predict the strength and deformation characteristics of materials (Desai and Faruque, 1984). Specifically, the development of constitutive model for GHBS is designed to encapsulate the interaction between sediment matrix and NGH, as well as the geo-mechanical properties of sediments (Xie, 2019).

Constitutive models of GHBS can be systematically organized into five categories, each underpinned by a unique theoretical framework: a. Constitutive model based on Mohr-Coulomb criterion succinctly delineates the initial yield condition of materials; b. Constitutive model based on Drucker-Prager failure criterion provides a smooth yield surface suitable for dealing with more complex three-dimensional stress state; c. Extended Duncan-Chang model applying elastic theory can express the material properties in a non-linear form; d. Critical State model offers precise insights into the continuous deformation characteristic of sediments at the critical state; f. Creep constitutive model can be adaptable to simulating the deformation response of GHBS subjected to prolonged loading scenarios.

3.1 Constitutive model with Mohr-Coulomb criterion

Mohr-Coulomb (M-C) criterion is the cornerstone in exploring the constitutive relationship of geotechnical materials, establishing the failure criteria through two principal parameters: internal friction angle and cohesion. This criterion assumes that the stress relationship adheres to a linear trajectory upon yielding (Mayne et al., 2009). For GHBS, the constitutive model derived from M-C criterion takes into account the impact of hydrate saturation and confining pressure on mechanical parameters such as c, φ, dilatancy angle (ψ), Young's modulus (E_{50}), and shear strength (τ_f). Nevertheless, it is imperative to acknowledge that this model is confined to depicting the initial

failure characteristic of materials at yield onset and does not extend to post-yield plastic flow or softening behavior.

3.1.1 Extended on Mohr-Coulomb strength theory

Mohr-Coulomb strength theory represents the linear response of the material's shear strength to normal stress, as delineated in Equation 3.1. Subsequent to the adaptation of M-C strength equation in the presence of hydrate, Jung and Santamarina (2011) described the influence of c on the shear strength of GHBS through a functional relationship with S_h, revealing a positive correlation between S_h and shear strength τ_f (Equation 3.2).

$$\tau_f = \sigma_n \tan\varphi + c \tag{3.1}$$

$$\tau_f = \sigma_n \tan\varphi + aS_h\sigma_t \tag{3.2}$$

Where σ_n is the normal stress on the failure surface, σ_t is the tensile stress of hydrates, a is the constant.

In addition to S_h, the impact of effective confining stress σ_c' on shear strength cannot be overlooked. Building upon Jung's model, Xu et al. (2023) proposed a linear relationship between c and σ_c', alongside the nonlinearity between the strength envelope and φ (Sukkarak et al., 2017). Integrating these considerations, they put forward an equation that can describe the combined effect of σ_c' and S_h on shear strength, which is given as:

$$\tau_f = aS_h\sigma_t + \alpha S_h\sigma_c' + \sigma_n \tan(\varphi_0 - b\cdot\log\frac{\sigma_c'}{p_a}) \tag{3.3}$$

Where φ_0 is the initial friction angle, a, b, and α are the constants, p_a is the atmosphere pressure.

3.1.2 Extended on Mohr-Coulomb failure criterion

The failure strength of GHBS refers to the critical strength threshold at which the sediment fails under ultimate stress conditions, which is primarily determined by S_h and current stress state. Hence, extended M-C failure criterion for GHBS can be expressed as follows (Dong et al., 2020; Labuz and Zang, 2015):

$$\tau_f = \frac{2\cos\varphi(S_h)}{1-\sin\varphi(S_h)}c(S_h) + \frac{2\sin\varphi(S_h)}{1-\sin\varphi(S_h)}\sigma_c' \tag{3.4}$$

Where c and φ represent the equations related to S_h.

Li et al. (2013) posited that M-C failure criterion is more applicable for GHBS under low confining pressure and subsequently derived the following formula:

$$\tau_f = \sqrt{(\frac{\sigma_1 - \sigma_c^{'}}{2})^2 - (\frac{\sigma_1 + (1-(k/m)\exp(-\sigma_c^{'}/m))\sigma_c^{'}}{2-(k/m)\exp(-\sigma_c^{'}/m)} - \frac{\sigma_1 + \sigma_c^{'}}{2})^2} \tag{3.5}$$

Where σ_1 represents the axial principal stress, k and m are the fitting parameters.

To elucidate the impact of S_h on mechanical properties of GHBS, Klar et al. (2010) assumed that hydrates and soil are two separate continua and proposed a single-phase elastoplastic constitutive model for GHBS based on the principle of effective stress. This model emphasized that the improvement in strength observed in soil-hydrate composites is attributed to the cohesive effect contributed by hydrates rather than frictional friction. Furthermore, the linear correlations among the effective index such as cohesion, dilatancy angle, and elastic modulus with respect to S_h were established, with corresponding equations exhibiting as:

$$\begin{cases} f(\sigma_1, \sigma_c^{'}, S_h) = \sigma_1 - \sigma_c^{'}\frac{1+\sin\varphi}{1-\sin\varphi} - 2c(S_h)\sqrt{\frac{1+\sin\varphi}{1-\sin\varphi}} \\ \sin\psi = \delta_1 S_h \quad E_{50} = \delta_2 + \delta_3 \cdot S_h \end{cases} \tag{3.6}$$

Where $c(S_h) = aS_h$, a, δ_1, δ_2, and δ_3 are the constants.

Numerous studies have shown that the presence of hydrates could strengthen GHBS through magnifying c but with irrelevant to φ. Moreover, GHBS at higher S_h exhibited greater dilatancy (Cha et al., 2016). In response to this phenomenon, Pinkert et al. (2014) proposed a nonlinear relationship between S_h and c and formulated an expression to characterize ψ for GHBS, with the function representing as follows:

$$\begin{cases} \sin\psi = \sin(\delta_1 - \delta_2\,\mathrm{In}(\frac{\sigma_c^{'}}{1MPa})) + \delta_3 S_h(1-\exp(-\frac{-\gamma_1}{\delta_4})) \\ c = c_1(1-\exp(-\frac{\sigma_c^{'}}{\gamma_2})) + c_2(S_h)^{c_3} \quad E_{50} = a(\frac{\sigma_c^{'}}{1MPa}) + bS_h \end{cases} \tag{3.7}$$

Where $\sigma_c^{'}$ is the effective confining stress, δ_1, δ_2, δ_3, δ_4, c_1, c_2, c_3, a, b γ_1 and γ_2 are the constants.

Leveraging the above discussed correlation, Pinkert et al. (2015) developed a strain softening model for GHBS related to deviatoric behavior, which can explain how c varies with S_h, plastic shear strain ε_s^p, and porosity ϕ. The specific expression is given by:

$$c(\varepsilon_s^p) = c_1\left[1-\exp(-\frac{\sigma_c^{'}}{\gamma_2})\right] + c_2(S_h)^{c_3}\left\{1-\frac{1}{\delta_3 S_h}\sin\left[\delta_1 - \delta_2\mathrm{In}(\frac{\sigma_c^{'}}{1MPa})\right]\left[1-\exp(-\frac{\delta_3 S_h \varepsilon_s^p}{\phi})\right]\right\}^{c_3} \tag{3.8}$$

Where δ_1, δ_2, δ_3, c_1, c_2, c_3, and γ_2 are the constants.

Rowe (1962) expanded the stress-dilatancy model to simulate the deformation in frictional-viscous Mohr-Coulomb soil during shearing. Employing this model, Pinkert (2017) performed a comparative analysis of experimental data, discovering that critical friction angle (φ_{cs}) is predictive of stress-strain response for GHBS and this model can effectively characterize the strength variation in relation to S_h. The stress-dilatancy model for GHBS can be expressed as:

$$\frac{\sigma_1}{\sigma_c'}=\left[\tan^2\left(\frac{\pi}{4}+\frac{\varphi_{cs}}{2}\right)+\frac{2c}{\sigma_c'}\tan\left(\frac{\pi}{4}+\frac{\varphi_{cs}}{2}\right)\right]\left(1-\frac{\dot{\varepsilon}_v}{\dot{\varepsilon}_1}\right) \tag{3.9}$$

Where $\dot{\varepsilon}_v$ and $\dot{\varepsilon}_1$ are the volumetric and axial strain rates, respectively.

Statistical damage theory is frequently employed to describe the randomness in the failure of geotechnical materials. Liu et al. (2017) merged this theory with M-C failure criterion to develop an innovative damage-softening statistical constitutive model for GHBS, which successfully illustrates the enhanced mechanical properties of sediment under high S_h. Additionally, it characterizes the strain-softening phase and nonlinear stress-strain relationship. Weibull distribution parameters (m, F_0) were utilized to represent the correlation between peak strength and strain, with the specific expression as follows:

$$\begin{cases} m=\dfrac{-F_f\left[\tau_f+(1-2\nu)\sigma_c'\right]}{E_{50}\varepsilon_f \ln\left[\dfrac{\tau_f+(1+2\nu)\sigma_c'}{E_{50}\varepsilon_f}\right]\left[\tau_f-(\tau_f+2\sigma_c')\right]\sin\varphi} \\ F_0=\left[\dfrac{-F_f^m}{\ln\left(\dfrac{\tau_f+(1-2\nu)\sigma_c'}{E_{50}\varepsilon_f}\right)}\right]^{\frac{1}{m}} \end{cases} \tag{3.10}$$

Where E_{50} is the elastic modulus, ν is the Poisson's ratio, τ_f and ε_f are the peak stress and peak strain, respectively, F_f is the distribution variable.

3.1.3 Features and limitations

Table 3.1 has delineated the features of constitutive models formulated in accordance with Mohr-Coulomb criterion. It is noted that strength, stiffness, and confining pressure have been considered in all models. Essentially, the constitutive models for GHBS based on M-C criterion define yield conditions via dilatancy angle and cohesion. S_h and σ_c' are incorporated in these models to intuitively reflect the improvement in mechanical properties of sediments provided by hydrates. However, there are several limitations that require to overcome:

(1) M-C criterion is dependent on the linear assumption, but the mechanical response of GHBS is nonlinear as exhibited in the experimental investigation, especially for the progressive strengthening before yielding due to hydrate contribution cannot be well-presented.

(2) M-C criterion focuses on the initial failure traits, neglecting post-yield plastic flow and strain softening in GHBS. However, GHBS would lose strength progressively beyond peak stress, with significant strain softening under drained conditions, as proven in Section 2.4.

(3) Hydrate-related dilatancy equation struggles to accurately predict the volumetric deformation of GHBS; as discussed in Section 2.4, the dilatancy angle is not simply linearly related to S_h, and hydrate occurrence has a certain influence on its evolution law.

(4) It simplifies the mechanical improvement as the effect of S_h on cohesion; however, as observed in the experimental results, hydrate contribution for host sediment varies significantly with hydrate morphology, even at the same saturation level. In addition, during hydrate dissociation, strength loss was not proportional to cohesion reduction, which is contradicted by M-C assumptions.

Table 3.1: Characteristics of constitutive model with M-C criterion for GHBS reported in the existing literature

Reference / Features	Klar et al. (2010)	Li et al. (2013)	Jung and Santamarina (2011)	Pinkert et al. (2014)	Pinkert et al. (2015)	Pinkert (2017)	Liu et al. (2017)
Strength	Y	Y	Y	Y	Y	Y	Y
Stiffness	Y	N	N	Y	Y	Y	Y
Dilation	Y	N	N	Y	Y	Y	N
Cohesion	Y	N	N	Y	Y	Y	N
Effective confining pressure	Y	Y	Y	Y	Y	Y	Y
Strain softening	N	N	N	Y	Y	Y	Y
Bonding and damage effects	N	N	N	Y	Y	N	N

Volumetric deformation	N	N	N	N	N	N	N
Hydrate morphology	N	N	N	N	N	N	N
Hydrate dissociation	N	N	N	N	N	N	N
Thermodynamics	N	N	N	N	N	N	N

3.2 Constitutive model based on Drucker-Prager criterion

3.2.1 Drucker-Prager criterion

Drucker-Prager (D-P) model presents a yield surface that is notably smoother and more continuous than that of M-C model, which is capable of encapsulating the correlation between the yield strength of materials and stress (Alejano and Bobet, 2012). Initially conceptualized in the 1950s by Drucker and Prager, this model was designed to describe the plastic behavior of metallic materials (Drucker and Prager 1952), it was later extended to geotechnical materials. Within the field of GHBS research, D-P model has been recognized for its efficacy in streamlining the yield characterization of material, which makes it exceptionally advantageous for analyzing complex three-dimensional stress states, which can be expressed as:

$$\sqrt{J_2} = \alpha I_1 + \beta \tag{3.11}$$

$$\begin{cases} I_1 = \sigma_1 + \sigma_2 + \sigma_3 \\ J_2 = \dfrac{1}{6}\left[(\sigma_1 - \sigma_2)^2 + (\sigma_1 - \sigma_3)^2 + (\sigma_3 - \sigma_2)^2\right] \end{cases} \tag{3.12}$$

Where α and β are material constants, J_2 is the second invariant of the stress deviator tensor, I_1 is the first invariant of the stress tensor, σ_1, σ_2, and σ_3 are the principal stresses.

3.2.2 Extended Drucker-Prager model

In the context of conventional triaxial test, where σ_2 equals σ_3, it is imperative to consider the influence of S_h and stress state on the strength of GHBS. This prediction can be achieved by the application of subsequent formula while employing D-P criterion: (Zhang et al., 2015):

$$\sigma_1 - \sigma_3 = \sqrt{3}K_f(S_h) + \sqrt{3}\beta(S_h)\cdot(\sigma_1 + 2\sigma_c^{'}) \tag{3.13}$$

Where σ_1-σ_3 is the deviatoric stress, $K_f(S_h)$ and $\beta(S_h)$ are the functions of S_h.

To accurately reflect the strain hardening observed in GHBS at lower S_h (S_h < 40%) and the strain softening tendency at higher S_h (S_h > 40%), Zhang et al. (2018) innovatively integrated D-P criterion into hypoplastic model, which can facilitate an effective prediction of the changes in strength (Equation 3.14). Nonetheless, it should be acknowledged that the model exhibits optimal applicability only under the condition characterized by minimal temperature fluctuation and does not consider the potential dissociation of hydrates.

$$\sigma_1-\sigma_3=\frac{\sqrt{3}K_f(S_h)}{1-\sqrt{3}\beta(S_h)}+\frac{3\sqrt{3}\beta(S_h)}{1-\sqrt{3}\beta(S_h)}\sigma_c^{'} \tag{3.14}$$

According to the D-P theory, β in the aforementioned equation is closely determined by φ in Mohr-Coulomb criterion, while K_f hinges on both φ and c. Xu et al. (2023) indicate that φ is correlated with $\sigma_c^{'}$, and c is dependent on both S_h and $\sigma_c^{'}$. Equation 3.14 was modified based on these findings, suggesting that the strength of GHBS is not solely linearly associated with S_h but also follows a power relationship with $\sigma_c^{'}$, which is formulated as

$$\sigma_1-\sigma_3=\gamma(\sigma_c^{'})^{\alpha}+\zeta S_h\sigma_c^{'}+\beta\cdot S_h\sigma_t \tag{3.15}$$

Where σ_t is the tensile stress of hydrates, $\sigma_c^{'}$ is the effective confining stress, ζ, γ, α and β are the material parameters.

Through the fitting of experimental parameters, Dong et al. (2020) posited that the failure strength exhibits a linear relationship with $\sigma_c^{'}$ and S_h, besides this correlation, a power relationship with respect to S_h has been found, as presented by the subsequent function:

$$\sigma_1-\sigma_3=(a\cdot S_h+b)\sigma_c^{'}+c\exp(d\cdot S_h) \tag{3.16}$$

Where a, b, c, and d are the constants.

To model the degradation of hydrate, Sun et al. (2016) developed an elastoplastic constitutive model for GHBS on the basis of D-P framework in p-q space. This advanced model is capable of predicting the augmentation in strength and stiffness using a function that contains S_h and can reflect the material softening phenomenon via the correlation between c and bonding factor. Additionally, the model adopts the assumption of isotropic expansion to estimate the volumetric strain. The yield and dilatancy equation can be given as:

$$\begin{cases} f = q - Fp' - c(S_h) = 0 \\ D = -\left[\dfrac{a \cdot \sigma_c'}{p_a} + b\right]\varepsilon_s^p - c \cdot \dfrac{\sigma_c'}{p_a} - d \cdot (S_h) \end{cases} \tag{3.17}$$

Where q is the deviatoric stress, p' is the mean effective stress, $c(S_h)$ is the cohesion equation that related to hydrate saturation, F is the slope of yield surface, D is the dilatancy ratio, a, b, c and d are the coefficients of fitting curves, p_a is the atmosphere pressure, ε_s^p is the plastic shear strain.

The mechanical properties of GHBS are determined not only by S_h and hydrate morphology but also related to structural alterations within sediments occasioned by strain. To elucidate the impact of strain rate on strain hardening and softening, Deusner et al. (2019) introduced a residual friction parameter (α_{res}) into D-P yield function to describe the effect of strain rate owing to the change in sediment structure. The yield function, alongside the internal variables pertaining to the friction parameter, is delineated as follows:

$$\begin{cases} \alpha = \beta + \alpha_{res} \\ f = q + \alpha(\chi_h)p' - c(S_h) = 0 \end{cases} \tag{3.18}$$

Where α is the total mobilized frictional resistance, β is a dilatancy component, α_{res} is a residual friction component, χ_h denotes the vector of internal plastic variables related to hardening-softening behavior.

Similarly, building on the above elastoplastic D-P model, Teixeira Parente et al. (2019) derived a mechanical model that can express the secondary hardening phase of GHBS according to the strain evolution law caused by friction and expansion. They simplified the model through dimensionality reduction employing the active subspace method and performed Bayesian inference on the model. The principal internal parameters governing macro stress expansion in this model adhere to the following empirical evolution law:

$$\begin{cases} c = c(S_h) \\ \beta = \beta^*(S_h) \cdot \lambda_1 \cdot \exp(1 - \bar{\lambda}^{m_\beta}) \\ \alpha_{res} = \alpha_{res}^I(S_h) + \Delta\alpha_{res}(S_h) \cdot (1 + \dfrac{1}{\lambda_2})^{-1} \cdot \lambda_1^{m_\alpha} \end{cases} \tag{3.19}$$

Where c is the cohesion, β is the material dilatancy, α_{res} is the residual frictional resistance, β^*, α_{res}^I, $\Delta\alpha_{res}$, λ_1, and λ_2 are experimental equations that associated with S_h, m_α and m_β are the empirical coefficients that control the evolution ratio of dilation and frictional resistance.

Weibull distribution and D-P criterion are both applicable for describing the deformation characteristic of GHBS. Li et al. (2016) and Zhang et al. (2023) developed a damage statistical constitutive model, which can capture strain softening and hardening phenomena of GHBS. The transition process hinges on the combined effects of S_h and $\sigma_c^{'}$, which is represented through the conjugate feature of parameters m and F_0 in the modified model, expressed as:

$$\sigma_1 = \exp\left[-(\frac{F}{F_0})^m\right] E_{50}\varepsilon_1 + 2v\cdot\sigma_c^{'} + \left\{1-\exp\left[-(\frac{F}{F_0})^m\right]\right\}\left[(\tan^2\alpha - 2v)k + 2c\cdot\tan\alpha\right] \quad (3.20)$$

Where m and F_0 are the parameters related to the effective stress, hydrate saturation, and dissociation, v is the Poisson's ratio, E_{50} is the elastic modulus, k is the model parameter, $\alpha = \pi/4 + 2/\varphi$, φ and c are the internal friction angle and cohesion, respectively, F is the microunit strength.

3.2.3 Features and limitations

Table 3.2 has delineated the attributes of constitutive models founded on D-P criterion, exhibiting substantial parallel to the formulations derived within M-C framework. The D-P-based constitutive model for GHBS features a smooth and continuous yield surface, which can grasp the geo-mechanical behavior under complex stress conditions. This model is developed on a three-dimensional stress plane, associating failure strength with the parameters related to S_h and $\sigma_c^{'}$. Under specific conditions, it can reflect strain softening and volumetric yield. However, there are several issues that warrant further consideration:

(1) D-P model assumes isotropic material, whereas in reality, sediments exhibit evident anisotropy attributed to the heterogeneous distribution of hydrates.

(2) D-P model generally assumes a constant temperature; however, as the analysis of temperature impact presented in Section 2.5, GHBS experiences thermal expansion and strength degradation when heated, thermal effect should not be non-negligible.

(3) D-P model is relatively complex, along with parameters derived from experiments, but their significance is not clear and requires further calibration, so the model might fail to generalize to different scenarios.

Table 3.2: Characteristics of constitutive model based on D-P criterion for GHBS reported in the existing literature

Features \ Reference	Zhang et al. (2015)	Dong et al. (2020)	Zhang et al. (2018)	Xu et al. (2023)	Sun et al. (2016)	Deusner et al. (2019)	Teixeira Parente et al. (2019)	Li et al. (2016)
Strength	Y	Y	Y	Y	Y	Y	Y	Y
Stiffness	Y	Y	N	N	Y	Y	Y	Y
Dilation	N	N	N	N	Y	Y	Y	Y
Cohesion	Y	Y	Y	Y	Y	N	Y	Y
Effective confining pressure	Y	Y	Y	Y	Y	Y	Y	Y
Strain softening	N	N	N	N	Y	Y	Y	Y
Bonding and damage effects	N	N	N	N	Y	Y	Y	Y
Volumetric deformation	N	N	Y	N	Y	Y	Y	Y
Hydrate morphology	N	N	N	N	Y	Y	Y	N
Hydrate dissociation	N	N	N	N	N	N	N	N
Thermodynamics	N	N	N	N	N	N	N	N

3.3 Non-linear elastic model based on Duncan-Chang model

3.3.1 Duncan-Chang model

Duncan-Chang (D-C) model, a non-linear elastic framework extensively acknowledged for its capability to delineate the stress-strain behavior of soils, was initially introduced by Kondner (1963). The key parameters including tangent modulus (E_t), Young's modulus (E_{50}), bulk modulus (K'), axial strain (ε_a), Poisson's ratio (v), and failure ratio (R_f), allow for predicting the mechanical response of soils from the initial to moderate stage of strain. D-C model characterizes the strain

hardening in soils through an approximately hyperbolic relationship, which is written as (Duncan and Chang, 1970; Kondner and Horner, 1965):

$$\sigma_1-\sigma_3=\frac{\varepsilon_a}{b\varepsilon_a+a}=\frac{1}{(\frac{a}{\varepsilon_a})+b} \tag{3.21}$$

Where σ_1-σ_3 represents the deviatoric stress, ε_a is the axial strain, a =1/E_i and b = 1/q_{ult}, E_i is the initial tangent elastic modulus and q_{ult} is the maximum deviatoric stress.

Janbu (1963) proposed a function which can represent the relationship between tangent elastic modulus E_i and $\sigma_c^{'}$:

$$E_t=K_n\cdot p_a(\frac{\sigma_c^{'}}{p_a})^n \tag{3.22}$$

Where p_a represents the atmosphere pressure, K_n and n are the material parameters, $\sigma_c^{'}$ is the effective confining stress.

3.3.2 Extended Duncan-Chang model

Temperature variation can alter the cementation effect provided by hydrates, thereby affecting the stiffness of GHBS. Consequently, Sun et al. (2023) expanded the above equation by incorporating the thermal effect on E_t (Equation 3.23). Nonetheless, this model fails to illustrate how the dependence of R_f on $\sigma_c^{'}$ and T.

$$E_t=a^{bT^2-cT+d}p_a(\frac{\sigma_c^{'}}{p_a})^{-\alpha T^2+\beta T-\gamma} \tag{3.23}$$

Where a, b, c, d, α, β, and γ are the constants.

Yan et al. (2017) refined the D-C model to better encapsulate the distinct stress-strain characteristic of GHBS. Through fitting experimental data, a proportional relationship between R_f and $\sigma_c^{'}$ was identified. Additionally, it has been proven that initial Poisson's ratio v diminishes as $\sigma_c^{'}$ increases. Drawing upon this observation, a linear correlation between v and S_h was established while considering the presence of hydrates, which satisfies the following equation:

$$\begin{cases} R_f=\delta_1+\delta_2\cdot\sigma_c^{'} \\ v=-\dfrac{d\varepsilon_l}{d\varepsilon_a}=\dfrac{-aS_h-b\log(\sigma_c^{'})+c}{\left[1-(\alpha+\beta S_h+\gamma\log(\sigma_c^{'}))\varepsilon_a\right]^2} \end{cases} \tag{3.24}$$

Where a, b, c, δ_1, α, β, γ, δ_1 and δ_2 are the constants, ε_l is the lateral strain.

The strength dependency on S_h hinges on cohesion, as opposed to internal friction angle (Masui et al. (2005)). Hence, Miyazaki et al. (2012) incorporated M-C failure theory into D-C model, taking into account the influence of S_h and $\sigma_c^{'}$ on mechanical properties (Equation 3.25). However, it did not still address volumetric strain and was unable to represent the volumetric deformation of GHBS.

$$\begin{cases} \tau_f = \dfrac{2\cos\varphi}{1-\sin\varphi}c + \alpha(S_h)^{\beta} + \dfrac{2\sin\varphi}{1-\sin\varphi}\sigma_c^{'} \\ E_{50} = 1 + \delta_1 S_h^{\delta_2} \\ E_t = (1 - R_f \dfrac{q}{\tau_f})^2 \cdot E_{50} \end{cases} \tag{3.25}$$

Where α, β, δ_1, and δ_2 are material parameters.

Ma and Xu (2021) suggested that the cementation effect induced by hydrates plays a pivotal role in mitigating deformation under effective stress. Based on this opinion, the bulk modulus K' was adapted into D-C model to assess the abilities of GHBS to resistance deformation. Empirical findings from their study revealed a positive correlation between K' and S_h, and an inverse relationship between K' and $\sigma_c^{'}$. Furthermore, R_f decreases linearly with S_h. The empirical relationship is quantitatively expressed in the subsequent formula:

$$\begin{cases} K^{'} = (a\sigma_c^{'} + b)\exp\left[(c\exp(-d\cdot\sigma_c^{'}))S_h\right] \\ E_t = K' p_a (\sigma_c^{'} / p_a)^{\delta_1 - \delta_2 S_h} \\ R_f = \delta_3 - \delta_4 S_h \end{cases} \tag{3.26}$$

Where a, b, c, d, δ_1, δ_2, δ_3, and δ_4 are the constants, R_f is the failure ratio.

Considering the magnitude of strain, Yu et al. (2011) categorized the stress-strain response of GHBS into two phases: rapid structural failure and complete failure. Then D-C model was modified to describe the material properties in different phases by setting the stiffness modulus. Furthermore, this model not only incorporates variables such as T and $\sigma_c^{'}$ but also introduces a damage factor ω to reflect the bonding degradation, yielding the following expression:

$$\sigma_1 - \sigma_3 = \frac{\varepsilon_a}{\dfrac{1}{(1-\omega)E_{i1} + \omega E_{i2}} + \dfrac{\varepsilon_a}{(1-\omega)(A_1 + A_2\sigma_c^{'}) + \omega(aT+b)^{-1}}} \tag{3.27}$$

Where ω is the damage factor, T is the temperature, E_{in} is the initial elastic modulus related to σ_c' and T, in which n represents the phase number, A_1, A_2, a and b are the constants.

Temperature can prompt the transition from strain hardening to softening in GHBS in certain situations. Also, hydrate dissociation markedly weakens the shear strength of host sediments, with the impact becoming more pronounced over time. In response to these phenomena, Song et al. (2016) modified D-C model by integrating the impacts of both dissociation time t_d and T on structural characteristics of GHBS. However, this equation can only characterize the hardening behavior while ignoring the softening. The failure strength can be expressed as:

$$\tau_f = a - bT - (c + dT + \alpha T^2)t_d + \left[\delta_1 + \beta \exp(T / \delta_2)\right] t_d^{\,2} \tag{3.28}$$

Where t_d is the dissociation time, a, b, c, d, α, β, δ_1, and δ_2 are the constants.

Typically, the nonlinear constitutive model of GHBS struggles to depict the strain softening phenomena. To address this limitation, Yan et al. (2021) introduced the concept of "strain softening index", which is defined as the slope of linear fit of stress-strain curve after 3% of peak strength. Further, the following formula was used to describe the progressive damage experienced by the sediments under shearing after reaching the peak strength:

$$\omega = 1 - \exp(-n\varepsilon_a) \tag{3.29}$$

Where ω is the damage factor, n is the model parameter related to σ_c' and S_h, ε_a is the axial strain.

3.3.3 Features and limitations

Table 3.3 has illustrated the features of non-linear elastic models, showcasing their enhanced ability to cover a broader spectrum of properties relative to the model developed in accordance with M-C and D-P criteria. Overall, the nonlinear elastic model can generally reflect the stress-strain trend and elucidate the strain hardening observed in sedimentary media. The establishment of such models mostly relies on the fitting relationship derived from experimental data. Mechanical responses of GHBS are evaluated through a functional correlation between effective parameters (hydrate saturation, effective confining pressure, temperature, dissociation time, axial strain) and indexes such as strength, stiffness, and lateral deformation. Yet, there are several aspects to be noted:

(1) Nonlinear elastic model can only describe the strain hardening phenomena, but GHBS typically exhibits initial strain hardening due to hydrate-induced strengthening, followed by strain softening as the hydrate bonds progressively fail, which has been shown in the discussion of stress-

strain behavior in Section 2.4. In addition, this model ignores the dilatancy and volumetric changes of GHBS, while GHBS exhibits strong dilatancy at high S_h, which is contradicted by the volume assumption in D-C model.

(2) Nonlinear elastic model overlooks the impact of hydrate decomposition, but GHBS undergoes evident stiffness and strength degradation during hydrate dissociation as presented in Section 2.4, which the nonlinear model cannot capture.

(3) Similar to M-C criterion, the nonlinear elastic model simplifies the assumption by primarily attributing variation in mechanical properties of GHBS to S_h, but as concluded in Section 2.4, GHBS with cementing hydrates demonstrates greater strength than pore-filling hydrates, even at identical S_h.

Table 3.3: Characteristics of nonlinear elastic model for GHBS reported in the existing literature

Reference / Features	Sun et al. (2023)	Yan et al. (2017)	Miyazaki et al. (2012)	Ma and Xu (2021)	Yu et al. (2011)	Song et al. (2016)	Yan et al. (2021)
Strength	Y	Y	Y	Y	Y	Y	Y
Stiffness	Y	Y	Y	Y	Y	Y	Y
Dilation	N	N	N	N	N	N	N
Cohesion	N	N	Y	N	N	N	Y
Effective confining pressure	Y	Y	Y	Y	Y	N	Y
Strain softening	N	N	N	N	N	N	Y
Damage ratio	Y	Y	Y	Y	N	Y	Y
Volumetric deformation	N	N	N	N	N	N	N
Hydrate morphology	N	N	N	N	N	N	N
Hydrate dissociation	N	N	N	N	N	Y	N

Thermodynamics	Y	N	N	N	Y	Y	N

3.4 Critical state model

The majority of constitutive models for GHBS focus on shear strength and stiffness, frequently neglecting volumetric deformation (Dong et al., 2024). Nonetheless, the process of hydrate exploitation can precipitate substantial volumetric changes within host sediments, potentially triggering instability in adjacent geological strata, which has been evidenced by marine settlement or landslide found in some cases. Understanding the evolution law in volume is imperative for the prediction and mitigation of such geohazards, thereby ensuring hydrate extraction safely. In response to this gap, a contingent of researchers has initiated the integration of critical state concepts into the constitutive modelling of GHBS.

The critical state theory represents a core principle in contemporary soil mechanics, highlighting a stable state that soil can reach under prolonged shearing, termed the critical state (Britto and Gunn, 1987). This theory differs from M-C criterion mainly in that the latter focuses on defining the loss of strength of soil at maximum stress angle, whereas the critical state model (CSM) concentrates on volume change in soils and provides a detailed description of soil transition from its initial consolidated state to the critical state. Although nonlinear elastic model can characterize strain hardening occurring in soil, CSM offers a more holistic prediction of both hardening and softening responses, demonstrating excellent versatility across intricate stress pathways. While constitutive models rooted in D-P criterion can capture the plastic deformation of soils to some extent but tend to ignore soil dilatancy. In contrast, CSM is better equipped to handle these issues.

3.4.1 Extended on modified Cam-clay model

The critical state model adapted from the modified Cam-clay model (CCM) stands as a classic application of critical state theory, which establishes a circular yield surface using three basic parameters (effective stress, void ratio, and deviatoric stress) to articulate the response of GHBS across various stress states (Roscoe et al., 1958). The size of the yield surface dynamically evolves with the accumulation of plastic strain (ε^p) during shearing. Also, the adaptability of modified

CCM extends into grasping the hardening and softening characteristics of soils and simulating complex stress paths. Associated flow rule ($f=g$) is applied in modified CCM to govern the plastic deformation behavior of soil. Hardening parameter (p_{cs}) is introduced to represent plastic volumetric strain (ε_v^p), which determines the capacity to undergo volumetric changes. The mathematical expression for this yield function is given by:

$$f = q^2 + M^2 p^2 - M^2 p_{cs} p' \tag{3.30}$$

Where p' is the mean effective stress, q is the deviatoric stress, and M is the critical stress ratio.

In CCM, p_{cs} is derived from the volumetric response of soils subjected to isotropic loading, which is contingent upon two parameters: the slope of swelling line (λ) and the slope of normal compression line (κ), with the function as follows:

$$p_{cs} = \frac{\lambda - \kappa}{1+e} \frac{dp_{cs}}{d\varepsilon_v^p} \tag{3.31}$$

Where e is void ratio.

On the basis of CCM, Uchida et al. (2012) introduced two hardening parameters (p_{cc} and p_{cd}) to describe the dilation and cohesion enhancement in the presence of hydrates, both of which are related to effective hydrate saturation (S_h^e). In addition, the degradation factor (χ) is defined to consider hydrate dissociation upon shearing. To facilitate a smoother transition from elastic to plastic behavior, subloading surface ratio (R) is employed in yield function (Hashiguchi, 1989). Nonetheless, it is important to acknowledge that this model is limited to the shape of yield surface as an ellipse. The methane hydrate critical state (MHCS) model can be represented as:

$$f = q^2 + M^2 (p' + p_{cc})\left[p' - R(p_{cs} + p_{cd} + p_{cc})\right] \tag{3.32}$$

Where p_{cc} and p_{cd} represent the enhancement in cohesion and dilation induced by hydrates, respectively.

Considering the impact of intermediate principal stress, Lin et al. (2015) further modified MHCS model by employing the concept of Spatially Mobilized Plane (SMP), which comprises three main components (Nakai and Matsuoka, 1983): i. Differ from the traditional MHCS model, SMP model introduces a parameter (χ_2) to represent the effect of hydrate accumulation habits on hydrate dissociation during shearing; ii. Account for the incremental volumetric yielding (p_{cd}) induced by hydrates; iii. SMP sub-loading yield surface is introduced, allowing plastic deformation

to occur across diverse loading trajectories (Hashiguchi et al., 2005). Building upon these considerations, SMP yield function is proposed as follows:

$$\mathrm{In}\left(\frac{p^{'}}{R(p_{cs}+p_{cd})}\right)+\frac{1}{\beta}(\frac{p_s}{Mp^{'}})^{\beta}=0 \tag{3.33}$$

Where β governs the shape of yield surface related to the particle size, p_{cd} and p_{cs} are the hardening parameters, p_s represents the shear stresses on SMP.

From the perspective of thermodynamics, Sun et al. (2015) improved the MHCS model by utilizing the dissipation function to automatically calculate the flow rule (Collins and Hilder, 2002). Considering the limitations of the traditional MHCS model, which is constrained to a singular yield surface. Hence, the spacing ratios α and γ are introduced to simulate different shapes of yield surface, enabling the accurate representation of stress softening and dilatancy behavior in this model. Additionally, it considers the anisotropies in critical state line under tensile and compressive directions through two stress ratios M_e and M_c. The advanced model can be expressed in the following form:

$$\frac{\left(p'-\frac{1}{2}\gamma\left(p_{cd}+p_{cs}\right)R+(1-\gamma)p_{cc}R\right)^2}{((1-\gamma)p'+R(\frac{1}{2}\gamma(p_{cd}+p_{cs})+p_{cc}))^2}+\frac{q^2}{(\frac{2M_cM_e}{M_c+M_e}((1-\alpha)p'+\alpha\rho^{'})+\frac{M_c-M_e}{M_c+M_e}q+RMp_{cc})^2}=1 \tag{3.34}$$

Where ρ' is the mean shift stress, γ is the spacing ratio related to the stored plastic and dissipated work, α represents the relationship between the maximum deviatoric stress and the deviatoric stress at critical state point on yield surface, M_c and M_e are the slopes of the critical state lines in the compressive and tensile directions, respectively, p_{cs}, p_{cc} and p_{cd} equal to the hardening parameters displayed in MHCS.

Recognizing the intricate interaction between the strength and dilatancy of GHBS, Uchida et al. (2016) introduced a unified hardening parameter (p_{cd}) that encapsulates both the augmented cohesion and dilatancy effects attributed to hydrate presence, further simplifying MHCS model. This model posits that hydrates act as bonding agents between adjacent soil particles, impeding their relative movement, which is identified as the mechanism for increased strength of sediments. The enhanced yield function is given by:

$$f=q^2+M^2p'\left[p'-R(p_{cs}+p_{cd})\right] \tag{3.35}$$

Given the heterogeneity of hydrates, the anisotropy in GHBS is an important factor that cannot be ignored. To address this challenge, Zhou et al. (2018) based on MHCS model introduced a rotating yield surface (β_{an}) to model the strength anisotropy of sediments and then developed three types of anisotropic methane hydrate critical state (AMHCS) models: i. AMHCS-H model, which considers the heterogeneous distribution of hydrates in each soil layer with different hydrate saturations; ii. AMHCS-T model, which accounts for the anisotropy of turbidites formed in the absence of hydrates; iii. AMHCS-TH model, which combines the consideration of anisotropic turbidite layers and various hydrate saturations. The definition for the proposed AMHCS model is as follows:

$$f = (q - \beta_{an} p')^2 + (M^2 - \beta_{an}{}^2)(p' + p_{cc})\left[p' - R(p_{cs} + p_{cd} + p_{cc}) \right] \tag{3.36}$$

Where β_{an} is the parameter defining the amount of tilt of the yield surface, p_{cs}, p_{cc} and p_{cd} equal to the hardening parameters displayed in MHCS.

To model the anisotropy induced by stress and the mechanical properties of under-consolidated soils, Sun et al. (2019) developed an innovative constitutive model for GHBS that primarily relied on two loading surfaces: i. Sub-loading surface, to describe the nonlinear stress-strain relationship prior to structural yielding; ii. Super-loading surface, to reflect the structural characteristics of GHBS. The hardening rule of this model is aligned with those previously proposed by Uchida et al. (2012), besides, the extended model introduces an additional structural parameter to represent the under-consolidated state of sediments. The associated yield function is delineated as follows:

$$f = \mathrm{In}(p' + p_{cc}) + \mathrm{In}\left(1 + \frac{\eta^{*2} p'^2}{(M^2 - \beta_{an}{}^2)(p' + p_{cc})^2}\right) + \mathrm{In}R^* - \mathrm{In}R - \mathrm{In}(p_{cs} + p_{cc}) \tag{3.37}$$

Where η^* represents the difference between the stress ratio and anisotropic stress tensor, β_{an} is an anisotropic state variable, R^* and R represent the similarity of super-loading to normal yield surface and super-loading to sub-loading yield surface, respectively, p_{cc} and p_{cs} equal to the hardening parameter proposed in MHCS model.

Abundant studies have proved that the mechanical behavior of GHBS depends on S_h and hydrate occurrence where hydrate morphology affects the strength and deformation properties of sediment to a notable extent. In light of these findings, Yan and Wei (2017) investigated the

mechanical response of GHBS in various hydrate morphologies under loading. Effective hydrate saturation S_h^e was introduced into MHCS model to characterize various hydrate morphologies:

$$S_h^e = \left\langle S_h - LS_h^c \right\rangle \tag{3.38}$$

Where $< >$ is Macaulay brackets, $<x>= x$ when $x \geq 0$, $<x>= 0$ when $x \leq 0$, L=0 represents the cementing type, L=1 represents the pore-filling or load bearing type, S_h is total hydrate saturation, S_h^c is the critical hydrate saturation.

Building upon S_h^e conceptualized by Yan and Wei (2017), Liu et al. (2020) proposed a unified formula, particularly applicable to commenting and pore-filling type (Equation 3.39). In addition, combining the drop-shaped yield function proposed by Yao et al. (2019) and considering both the solid phase and hydrate contribution, an advanced elastoplastic constitutive model for GHBS was developed as follows (Equation 3.40):

$$S_h^e = S_h\left\{1-\exp\left[-(\frac{S_h}{S_h^c})^3\right]\right\} \tag{3.39}$$

$$f = \mathrm{In}\left[(1+\frac{(1+\chi_c)q^2}{M^2 p'^2 - \chi_c q^2})p' + p_{cs}\right] - \mathrm{In}(p_0 + p_{cs}) - \frac{H(1+e)}{\lambda-\kappa} \tag{3.40}$$

Where H is the hardening parameter, χ_c is the critical state parameter, p_{cs} is the volumetric yield stress, p_0 is the initial mean effective stress, e is the void ratio, S_h^c= 0 when hydrate morphology in cementing type, S_h^c= 25%~40% in pore-filling type.

Similarly, Iwai et al. (2022) observed that GHBS with various hydrate morphologies exhibit unique stress-strain and dilatancy characteristics. The total hydrate saturation could be categorized into cementation type (CM-type S_{cem}^H), load-bearing type (LB-type S_{lb}^H), and pore-filling type (PF-type S_{pf}^H) and defined the proportion of induvial type of hydrate saturation in total hydrate saturation (S_r^H) as hydrate morphology ratio (α, β, γ). Through the analysis of the relationship between morphology ratio and S_h, the hardening rules manifested across various hydrate morphologies were elucidated. The evolution in hardening parameters ($p_{cem}^{'}$ and $p_{lb}^{'}$) can be expressed as:

$$\begin{cases} dp_{cem}^{'} = a_{cem}b_{cem}(\alpha S_r^H)^{b_{cem}-1}(\alpha dS_r^H - m_\alpha \alpha \left| d\varepsilon_s^p \right| S_r^H) \\ dp_{lb}^{'} = a_{lb}b_{lb}(\beta S_r^H)^{b_{lb}-1}\left\{\beta dS_r^H + \left(m_\alpha \alpha \left| d\varepsilon_s^p \right| + m_\gamma \gamma d\varepsilon_v^p\right) S_r^H\right\} \end{cases} \tag{3.41}$$

Where α, β, and γ are the morphology ratios for the CM-type, LB-type, and PF-type, respectively, S_r^H is the total hydrate saturation, ε_s^p and ε_v^p are the plastic shear strain and plastic volumetric strain,

respectively, α_{cem}, b_{cem}, α_{lb}, and β_{lb} are the material constants related the mechanical enhancement by hydrates, m_α and m_γ are the degradation factors related to CM-type and PF-type, respectively.

Considering the cementation effect of hydrate and damage in structured soil, Wang et al. (2022) based on elastoplastic and damage mechanics theories incorporated two hardening parameters into modified CCM model: i. One is to describe the hardening phenomenon exhibited in structured soil; ii. Another is to characterize the enhancement in cohesion by hydrates. Meantime, the unified hardening framework proposed by Yao et al. (2009) was adopted to more accurately describe the strain hardening and softening behavior of GHBS across different occurrence habits. The corresponding yield function is obtained as follows:

$$f = \mathrm{In}(\frac{p'+p_{cc}}{p_0})+\mathrm{In}(\frac{p'}{p'+p_{cc}}+\frac{\eta^2}{M^2})-\frac{H(1+e_0)}{\lambda-\kappa}+\mathrm{In}\left[1-\exp(-c_a\varepsilon_s^p-c_b)\right] \tag{3.42}$$

Where H is the unified hardening parameter, p_{cc} is the enhanced cohesion provided by hydrates, p_0 is the initial mean effective stress, e_0 is the initial void ratio, ε_s^p is the plastic shear strain, η is the current stress ratio, c_a is the parameter controlling the damage ratio of structure, c_b is the parameter reflecting the strength of initial structure which is related to S_h.

Sultan and Garziglia (2011) integrated the concept of hydrate fraction as a state variable into a critical state framework, laying the groundwork for a new constitutive model specifically designed to encapsulate the strain softening and degradation phenomena to GHBS, which was constituted according to two assumptions: i. Hydrate formation impedes the normal consolidation of sediments while dissociation induces sediment collapse; ii. The compressibility of GHBS decreases with increasing hydrate content and tends to approach the compressibility of pure hydrate. The yield equation can be written as:

$$q=\frac{2}{3}p'\frac{q_p}{p_p}\pm\sqrt{M^2\left(p'p_p-p'^2\right)+\frac{1}{9}\frac{p'}{p_p}q_p^{\,2}} \tag{3.43}$$

Where q_p and p_p are the projection of the additional stress tensor in the q-p diagram.

The Hierarchical Single Surface framework can comprehensively capture the strength and deformation of soils through a single and continuous stress surface, which is celebrated for its exceptional adaptability and flexibility (Desai et al., 1986). Leveraging the advantages of HISS framework, Gai and Sánchez (2017) proposed the Hierarchical Single Surface-Methane Hydrate (HISS-MH) model to accommodate the diverse yield surface shapes of GHBS by adjusting several parameters. Moreover, some elements proposed by MHBS model are integrated into HISS-MH

model including sub-loading surface ratio, cementation, and bonding degradation. The expression for HISS-MH yield surface is as follows:

$$f = \frac{a}{M^2} q^2 - 3^2 \gamma p'^2 + 3^2 \gamma p'^n (R(p_{cs} + p_{cd}))^{2-n} \tag{3.44}$$

Where a and γ are constants, n is the parameter related to the transition from compressive to dilative volume change, p_{cs} is the pre-consolidation stress, p_{cd} is the strength enhancement by hydrates.

Given the phase variation in hydrate and the structural change in sediment during loading and dissociation, Sánchez et al. (2017) incorporated the concept of stress distribution into the HISS-MH model to capture the individual mechanical contribution of hydrate and soil skeleton. Additionally, damage theory was utilized to track the hydrate degradation under loading (Kachanov, 1986). The stress component of hydrate and sediment together constitute the global effective stress, expressed as follows:

$$d\sigma' = d\sigma_s' + \frac{C_h \chi}{1 + C_h \chi} d\sigma_h = \left[D_s + (\frac{\chi}{1 + C_h \chi})^2 D_h \right] d\varepsilon + \left[d_{C_h} + \sigma_h (\frac{\chi}{1 + C_h \chi} - C_h (\frac{\chi}{1 + C_h \chi})^2) \right] dC_h \tag{3.45}$$

Where C_h is the volumetric concentration of methane hydrate ($C_h = S_h \cdot \phi$), χ is the strain partition variable during loading, D is the stiffness matrix, σ represents the portion of stress, d_{Ch} shows the effect of hydrates on effective stress, the subscript s and h represent the host sediment and hydrate, respectively.

HISS-MH model can work well for predicting the mechanical responses of GHBS. However, it is unable to evaluate the effects of temperature and strain rate. Further, Zhou et al. (2022) expanded the HISS-MH model by adding three components: i. An enhanced hardening law was proposed to characterize the high expansion observed in MHBS; ii. The pre-consolidation stress expression was added to the term associated with thermal effect; iii. Perzyna's overstress theory was used to analyze the dependency of mechanical behavior on strain rate. The hardening law results from the combined effects of shear plastic strain and volumetric plastic strain (Nova, 2004):

$$\begin{cases} dp_{cs} = \dfrac{1 + e_0}{\lambda + \kappa} p_{cs} (d\varepsilon_v^p + \alpha_s d\varepsilon_s^p) \\ p_{cs} = p_{cs0} (1 - r_T \log \dfrac{T}{T_0}) \end{cases} \tag{3.46}$$

Where α_s is a parameter controlling the effect of the deviatoric strain on hardening, T_0 is the reference temperature, p_{cs} is the pre-consolidation mean stress, p_{cs0} is the pre-consolidation mean

stress at T_0, r_T is a model parameter related to the effect of temperature, ε_s^p and ε_v^p are shear plastic strain and volumetric plastic strain, respectively.

The critical state models proposed based on modified CCM often consider the contribution of hydrates while incorporating other effective parameters to capture the different geo-mechanical characteristics of the host sediments. The evolution of the yield surfaces within this framework can be summarized in the following figure:

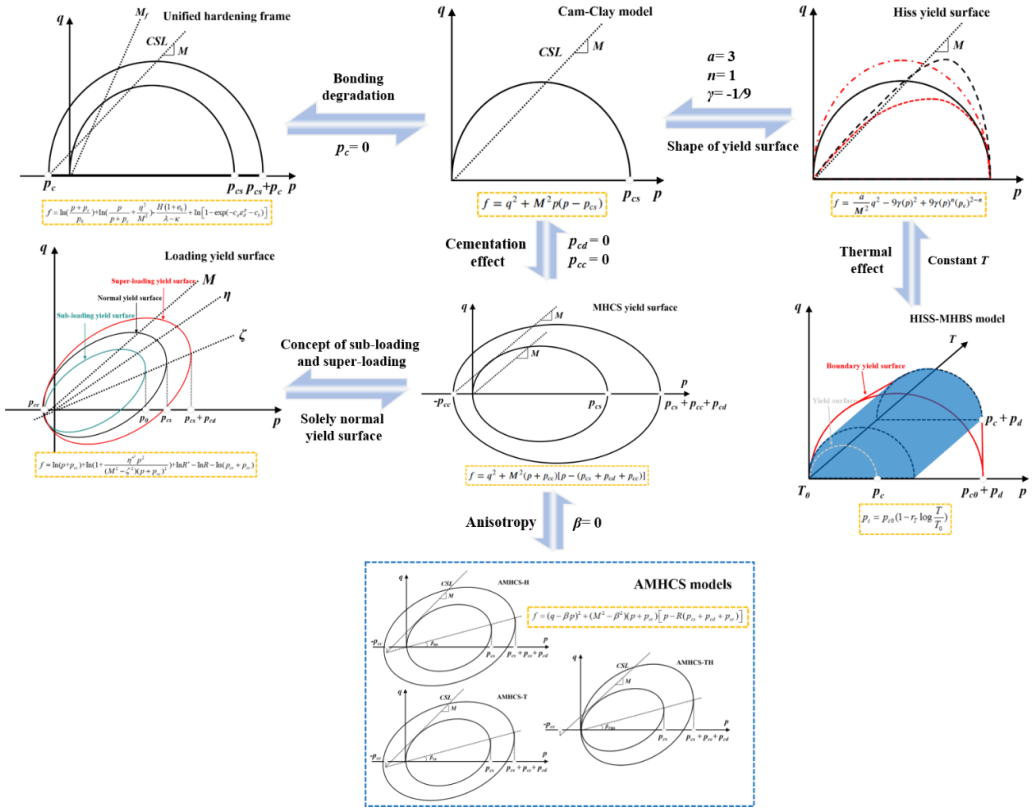

Figure 3.1: Schematic of yield surfaces for critical state model extended on modified CCM

3.4.2 Extended on state-dependent model

Numerous studies have indicated that sand as kind of frictional material, the plastic strain induced by constant stress ratio at lower confining pressure is negligible. Additionally, it has been observed that sands undergo limited plastic volumetric change prior to reaching yield stress (Manzari and Dafalias, 1997). Consequently, the deformation characteristics of sands is largely dependent on the stress ratio. Based on this insight, Li et al. (1999) posited that sands demonstrate minimal plastic deformation before reaching a critical stress ratio. The yield trajectory of sands

can be approximated as a straight line that maintains a constant stress ratio (Poorooshasb et al., 1966). On the *q*-*p* plane, the yield function adhering to this behavior can be represented as follows:

$$f = q - Mp' \tag{3.47}$$

Where q is the deviatoric stress, p' is the mean effective stress, M is the critical stress ratio.

Considering the cementation provided by hydrates, a hardening parameter p_{cd} was introduced into the above equation, which is given by (Shen et al., 2016):

$$f = q - M(p' + p_{cd}) \tag{3.48}$$

Where p_{cd} represents the bonding effect of hydrates.

GHBS experience volume changes and exhibit dilatancy during shearing, which depends on the prevailing stress state. Therefore, state-dependent dilatancy theory has been adopted for the modelling of CSM where dilatancy is defined as the difference between critical stress ratio M and current stress ratio η (Rowe and Taylor, 1997). Also, it can be found in previous studies that dilatancy is not only linked to the stress ratio but also hinges on the internal state of material. Subsequently, within the critical state framework, Li and Dafalias (2000) incorporated a state-dependent parameter (φ_0) that is defined as the difference between critical and current void ratio into the dilatancy model to better reflect material expansion, as depicted in the following equation:

$$\begin{cases} D(\varphi_0) = d_0\left[\exp(m\cdot\varphi_0) - \dfrac{\eta}{M}\right] \\ \varphi_0 = e - e_c = e - (e_{c0} - \delta_1(p'/\,p_a)^{\delta_2}) \end{cases} \tag{3.49}$$

Where d_0 and m are positive modeling parameters, φ_0 is the state parameter, e_c is the critical void ratio whose initial value is e_{c0}, p_a is the atmosphere pressure, δ_1 and δ_2 are the material constants.

Shen et al. (2016) discovered that for S_h below 60%, M increases nonlinearly with respect to S_h. Consequently, the dilatancy model for MHBS was refined that characterize the evolution law of cementation by employing a proportional factor, the corresponding expression is given by:

$$D(\varphi_0) = \frac{d_0}{M + A(S_h)^B}\left[(M + A(S_h)^B)\exp(m\cdot\varphi_0 - m_b\sqrt{p_{cd}\,/\,p_a}) - \eta\right] \tag{3.50}$$

Where A and B are model parameters, p_a is the atmosphere pressure, p_{cd} represents the cementation effect of hydrates, m and m_b are the positive parameters.

The above model involves too many model parameters and is relatively complex. Therefore, Yuan et al. (2020) simplified the dilatancy equation proposed by Wan and Guo (1998) by refining

a new state parameter that was expressed by the ratio between critical and current void ratio, whose equation only includes three model parameters:

$$\begin{cases} D(\varphi_0) = M\varphi_0^m - \eta \\ \varphi_0 = \dfrac{e}{e_c} = \dfrac{e}{e_{c0} - \delta_1 (p'/\ p_a)^{\delta_2}} \end{cases} \tag{3.51}$$

Where m, δ_1, and δ_2 are the model constants.

The mechanical characterization of MHBS within the stable regions has been relatively underexplored in reported literature. In response to this phenomenon, Ng et al. (2020) established a state-dependent model based on the theoretical framework of bounding surface plasticity, which introduces a phase parameter (L) to capture the coupling effects of current temperature (T_1) and pore pressure (P_1) for hydrate formation (Dafalias, 1986). Finally, by combining the correlations among S_h, phase parameter, and current stress state, a novel dilatancy model was established as follows:

$$\begin{cases} D(\varphi_0) = \dfrac{d_0}{\eta}\left[M(\rho / \rho_i)^{\alpha} \exp(m \cdot \varphi_0) - \eta \right] \\ \varphi_0 = e - e_c = e - e_{c0} + \delta_1 (p'/\ p_a) - a(1+L)^c [\exp(b \cdot S_h) - 1] \\ L = \min\left(\sqrt{(\dfrac{T_1 - T_b}{245})^2 + (\dfrac{P_1 - P_b}{1})^2} \right) \end{cases} \tag{3.52}$$

Where d_0, m, α, δ_1, a, b, and c are material constants, η is the current stress ratio, ρ and ρ_i are the Euclidean distances of the actual and image stress states, respectively, L is the minimum distance of T-P state, T_b and P_b are the temperature and pore pressure on the phase boundary with a minimum distance to current T-P state, respectively.

3.4.3 Features and limitations

Table 3.4 presents the characteristics of the critical state model for GHBS as reported in the literature. When compared with the extended models based on M-C criterion, D-P criterion, and D-C model, critical state model can reproduce most mechanical performance in GHBS, even including volumetric yield and strain softening, which involves several aspects: a. The evolution of pre-consolidation stress in sediments can be evaluated through an isotropic loading curve; b. Incorporating hardening parameters to describe the contribution of hydrates to the overall structure; c. Introducing the degradation factor to explain the bonding damage between sediment particles due to hydrate dissociation; d. Rotating yield surface to simulate the anisotropic distribution of

hydrate; e. Utilizing sub-loading surface concept to achieve a smooth transition from elasticity to plasticity; f. Introducing effective hydrate saturation or relative morphology ratio to quantify the impact of hydrate morphology; g. Considering thermodynamic coupling in modelling. Despite these advancements, there are still some limitations that pose challenges to modelling:

(1) Certain models are confined to predefined yield surface shapes (e.g., elliptical) and cannot capture the stress-strain characteristic of GHBS across diverse yield surface geometries.

(2) Most models are only applicable to hydrate-bearing sands and coarser granular soils, while for finer particles containing hydrate, the interparticle bonding effects due to electrochemical and van der Waals forces would affect their mechanical response, which require different constitutive formulations.

(3) While critical state models adeptly address stress change caused by temperature variation, GHBS behavior under temperature changes is not just a thermal expansion issue, which also involves hydrate dissociation, gas migration, and pore pressure evolution.

(4) All the mentioned models omit considerations of pore fluid dynamics, which on one hand determine the pore pressure of material; And on the other hand, the interactions between pore fluids and sediment particles such as capillary and electrochemical effects are related to mechanical response of GHBS.

Table 3.4: Characteristics of critical state models for GHBS reported in the existing literature

Reference / Features	Sultan et al. (2011)	Uchida et al. (2012)	Lin et al. (2015)	Sun et al. (2015)	Shen et al. (2016)	Uchida et al. (2016)
Strength	Y	Y	Y	Y	Y	Y
Stiffness	Y	Y	Y	Y	Y	Y
Dilation	Y	Y	Y	Y	Y	Y
Cohesion	N	Y	N	Y	Y	Y
Effective confining pressure	Y	Y	Y	Y	Y	Y
Strain softening	Y	Y	Y	Y	Y	Y
Bonding and damage effects	Y	Y	Y	Y	Y	Y

Volumetric deformation	Y	Y	Y	Y	Y	Y
Hydrate morphology	N	Y	Y	Y	Y	Y
Hydrate dissociation	N	N	N	N	N	N
Thermodynamics	N	Y	N	Y	N	Y
Yield surface shape	N	N	N	Y	N	N
Anisotropy	Y	N	Y	N	N	N

Reference / Features	Gai et al. (2017)	Sánchez et al. (2017)	Yan and Wei (2017)	Zhou et al. (2018)	Sun et al. (2019)	Yuan et al. (2020)
Strength	Y	Y	Y	Y	Y	Y
Stiffness	Y	Y	Y	Y	Y	Y
Dilation	Y	Y	Y	Y	Y	Y
Cohesion	N	N	Y	Y	Y	Y
Effective confining pressure	Y	Y	Y	Y	Y	Y
Strain softening	Y	Y	Y	Y	Y	Y
Bonding and damage effects	Y	Y	Y	Y	Y	Y
Volumetric deformation	Y	Y	Y	Y	Y	Y
Hydrate morphology	Y	Y	Y	Y	Y	Y
Hydrate dissociation	Y	Y	N	N	N	N
Thermodynamics	Y	N	N	Y	N	N
Yield surface shape	Y	Y	N	N	N	N
Anisotropy	N	N	N	Y	Y	N

Reference / Features	Liu et al. (2020)	Ng et al. (2020)	Zhou et al. (2022)	Wang et al. (2022)
Strength	Y	Y	Y	Y
Stiffness	Y	Y	Y	Y
Dilation	Y	Y	Y	Y
Cohesion	N	N	Y	Y
Effective confining pressure	Y	Y	Y	Y
Strain softening	Y	Y	Y	Y
Bonding and damage effects	Y	Y	Y	Y
Volumetric deformation	Y	Y	Y	Y
Hydrate morphology	Y	N	Y	Y
Hydrate dissociation	N	N	N	N
Thermodynamics	N	Y	Y	N
Yield surface shape	Y	Y	N	N
Anisotropy	N	N	N	N

3.5 Creep constitutive model

The evaluation of the long-term stability of GHBS is paramount for forecasting potential risks during hydrate extraction. The primary features and determinants of creep have been synthesized in Section 2.6, drawn from existing experiments. The establishment of constitutive models is vital for precise simulation and numerical prediction of the deformation behavior of GHBS under sustained loading conditions. Currently, the report on creep constitutive model for GHBS in the literature is scarce, primarily focusing on mathematical fitting of experimental data and extension of classical elasto-viscoplastic model. Key models employed include Nishihara model, Perzyna model, Bingham model, among others (Perzyna, 1966). Creep model integrates a series of elements—viscous, viscoelastic, viscoplastic, and viscoelastoplastic—via mechanical components such as springs, dampers, and sliders to simulate three phases of creep behavior, aiming to

characterize the dynamic interrelations among stress, strain, strain rate, and time (Wang et al., 2014).

3.5.1 Fitted model through experiment

The high-temperature creep law offers an effective method for characterizing creep strain rate during steady-state creep phase of crystalline materials, which is also applicable to GHBS (Poirier, 1985) (Equation 3.53). Durham et al. (2003) successfully implemented this law in their analysis of a triaxial creep experiment conducted on sediments containing pure methane hydrates. Under substantial effective confining pressure changes ($\sigma_c^{'}$ from 0 to 100MPa), it noted that the model parameter A_2 is considerably greater than $\sigma_c^{'} \cdot A_3$. Consequently, the equation can be approximated as Equation 3.54:

$$\dot{\varepsilon} = A_1(\sigma_{cs})^n \exp(-\frac{A_2 + \sigma_c^{'} A_3}{R_g T}) \tag{3.53}$$

$$\dot{\varepsilon} = A_1(\sigma_{cs})^n \exp(-\frac{A_2}{R_g T}) \tag{3.54}$$

Where $\dot{\varepsilon}$ is the axial creep strain rate within steady creep stage, σ_{cs} is the creep stress, T is the temperature, $\sigma_c^{'}$ is the effective confining stress, R_g is the gas content, A_1, A_2, A_3, and n are the material constants.

Upon the analysis of the viscoplastic behavior presented in GHBS, certain researchers have embarked on the development of creep models grounded in the empirical fitting of experimental data. Specifically, Yan et al. (2019) ascertained through uniaxial creep test that total strain in the elastic stage is comprised of elastic strain and creep strain. Upon the transition into the plastic region, the composition of total strain evolves to plastic strain, elastic strain, and creep strain. Also, it has been found that the creep curve bears resemblance to those of permafrost near 0°C. Based on this observation, a creep model was derived by:

$$\varepsilon = (\frac{\sigma}{A(1+T_n)^B})^C t_c^{\ D} \tag{3.55}$$

Where ε is the strain, σ is the stress, T_n is the negative temperature, t_c is the creep time, A, B, C, D is the experimental fitting parameters.

Wang et al. (2012) demonstrated that the cementation effect contributed by hydrates within host sediment is correlated with porosity. Similarly, the viscoplastic behavior of GHBS is also

dependent on porosity. Then, an equation was developed that can delineate the evolution of strain over time, which allows for the calibration of model parameters to match various experimental curves. Nonetheless, this model does not account for the impact of the ratio between shear stress and normal stress on the creep curve.

$$\varepsilon = (\frac{\sigma}{\delta_2})^{\frac{1}{m}} t_c^{\frac{\delta_1}{m}} \tag{3.56}$$

Where δ_1, δ_2, and m are the fitting parameters.

Given the significance of drilling fluid density in ensuring wellbore stability and mitigating stress concentration, coupled with the observation that NGH undergo an accelerating creep process exclusively under elevated stress, Li et al. (2022) assumed accelerating process has no impact on wellbore stability. Their scrutiny was directed toward data emanating from the creep decay phase, suggesting it could be represented by a logarithmic function. Furthermore, they proposed a linear correlation between creep parameters and S_h, culminating in the establishment of a creep model.

$$\varepsilon = (l_1 S_h + l_2) \cdot \exp(l_3 \sigma_{cs}) \cdot \lg(t_c) \tag{3.57}$$

Where l_1, l_2 and l_3 are the constants, σ_{cs} is the creep stress.

The development of GHBS creep model predicated on the fitting of experimental data is relatively straightforward and can be used for initially predicting creep deformation. Nonetheless, these are inevitably marred by several deficiencies:

(1) Parameter specificity constrains the models' applicability across varied conditions, diminishing their universality.

(2) Limited time scale, data from short-term experimental observations are insufficient to support the prediction of long-term creep behavior.

(3) Most models struggle to forecast the accelerating creep phase, oversimplifying the creep process.

3.5.2 Extended visco-elastic-plastic model

The Nishihara model is extensively applied to describe the creep characteristic of geotechnical materials, which is consist of Kelvin body in series with viscoplastic body. Fig. 3.2 illustrates the representation of the components in Nishihara creep model, where I, II, and III represent Hooke element, Kelvin element, and ideal viscoplastic element, respectively. It is

optimally suited for steady-state creep analysis yet does not encompass the accelerating creep phase (Nishihara, 1952).

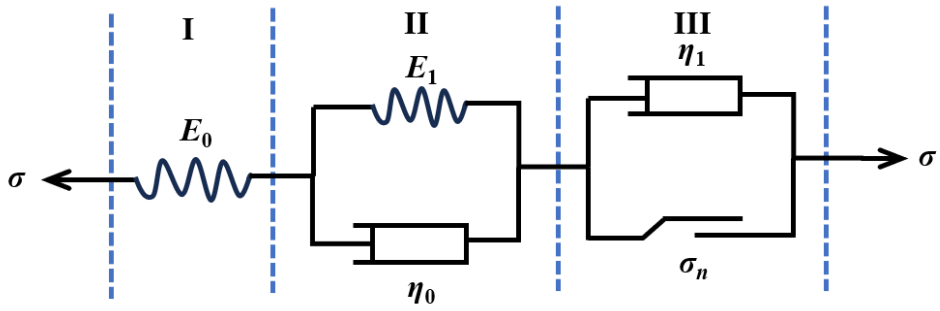

Figure 3.2: Schematic diagram of the components of Nishihara creep model

To elucidate the accelerating creep phase of GHBS, Hu et al. (2024) posited three assumptions: i. A nonlinear relationship between viscosity coefficient and creep time; ii. Permanent failure of GHBS occurs solely upon the axial load surpassing the long-term load; iii. Damage in GHBS is isotropic. A novel creep model was formulated based on Nishihara model, in which a linear viscous element was replaced by linear viscous element in Kelvin element to better reflect steady creep stage. Furthermore, a time-dependent damage elasticity element was undertaken to simulate the accelerating creep process, characterized by implementing a time threshold to articulate the delay of damage onset for GHBS.

$$\varepsilon(t)=\begin{cases}\dfrac{\sigma}{E_0}+\dfrac{\sigma}{E_1}\left[1-\exp\left(-\dfrac{E_1(\exp(\alpha_c t_c)-1)}{\eta_0\alpha_c}\right)\right] & \sigma<\sigma_{cs}\\ \dfrac{\sigma}{E_0}+\dfrac{\sigma}{E_1}\left[1-\exp\left(-\dfrac{E_1(\exp(\alpha_c t_c)-1)}{\eta_0\alpha_c}\right)\right]+\dfrac{\sigma-\sigma_{cs}}{\eta_1}t_c+\dfrac{\sigma-\sigma_{cs}}{E_2}\exp\left(-\dfrac{t_c}{t_\omega}\omega\right) & \sigma\geq\sigma_{cs}\end{cases} \tag{3.58}$$

Where ε is the total strain, E_0, E_1, and E_2 are the elastic modulus in Hooke element, Kelvin element, and ideal visoplastic element, respectively, η_0 and η_1 are the viscosity coefficients in Kelvin element and in viscoplastic element, respectively, t_ω is the time threshold, ω is the damage-related parameter, α_c is the creep parameter.

The creep behavior of GHBS can be differentiated into the diminishing creep phase and the accelerating phase. Li et al. (2023) refined the attenuation creep process into a rapidly decreasing phase and a nonlinear slowly decreasing phase. To address the shortcomings of Kelvin model in capturing the slowly decreasing phase, a creep model was established that amalgamates nonlinear viscous elements with Kelvin model, thereby effectively simulating the attenuation creep behavior

of GHBS. Additionally, this model accommodates the viscoplastic deformation observed in GHBS by integrating a nonlinear Newtonian element, particularly in the accelerating phase. Utilizing long-term strength σ_{cs} as the phase threshold, the visco-elastic-plastic model can be expressed as:

$$\varepsilon(t)=\begin{cases}\dfrac{\sigma}{E_0}+\dfrac{\sigma}{E_1}\left[1-\exp(-\dfrac{E_1}{\eta_1}t_c)\right]+\dfrac{\sigma}{k\eta_2}t_c^{\,k} & \sigma<\sigma_{cs}\\ \dfrac{\sigma}{E_0}+\dfrac{\sigma}{E_1}\left[1-\exp(-\dfrac{E_1}{\eta_1}t_c)\right]+\dfrac{\sigma}{k\eta_2}t_c^{\,k}+\dfrac{\sigma}{2\eta_3}t_c^{\,2} & \sigma\geq\sigma_{cs}\end{cases} \tag{3.59}$$

Where ε is the total strain, E_0 and E_1 are the elastic modulus in Hooke element and in Kelvin element, η_1, η_2, and η_3 are the viscosity coefficients of visco-elastic element, viscous element, and viscous element in accelerating creep phase, respectively, k refers to the fitting parameters.

Regarding the time-dependent behavior of CO_2 hydrate foundations, Yoshimoto and Kimoto (2022) and Iwai et al. (2019) extended an elasto-viscoplastic model, which is an expansion of the constitutive framework initially proposed by Adachi and Oka (1982). The improvement in this model is demonstrated in two aspects: i. Kinematic hardening, where the hardening parameter was introduced within the yield surface concept to reflect strain hardening and softening. Generalized Hooke's law was applied to calculate elastic strain rate, while the overstress flow law for viscoplastic strain rate (Perzyna, 1963); ii. Hydrate contribution, which involves the sensitivity of shear modulus, hardening parameters, and viscoplastic parameters to S_h. The creep model can be presented as follows:

$$\dot{\varepsilon}_{ij}^{\,e}=\frac{1}{2G}s_{ij}+\frac{\kappa}{3(1+e)}\frac{\dot{p}'}{p'}\delta_{ij} \tag{3.60}$$

$$\begin{cases}\dot{e}_{ij}^{\,vp}=C_1 p'\exp(mf_y)\dfrac{\eta_{ij}^{*}-\eta_{ij(0)}^{*}}{\bar{\eta}^{*}}\\ \dot{\varepsilon}_{mn}^{\,vp}=C_2 p'\exp(mf_y)\left\{\eta-\dfrac{\eta_{mn}^{*}(\eta_{mn}^{*}-\eta_{mn(0)}^{*})}{\bar{\eta}^{*}}\right\}\end{cases} \tag{3.61}$$

Where s_{ij} is the deviatoric stress tensor, δ_{ij} is Kronecker delt, p' is the mean effective stress, $\dot{p}'$ is the time differentiation for p', C_1, C_2 and m are the viscoplastic parameters, $\dot{\varepsilon}_{ij}^{\,e}$ is the elastic strain rate tensor, $\dot{e}_{ij}^{\,vp}$ and $\dot{\varepsilon}_{ij}^{\,vp}$ are the viscoplastic deviatoric strain rate tensor and volumetric strain rate, respectively, η is the stress ratio, η_{mn}^{*} and $\bar{\eta}^{*}$ are the stress ratio tensor and the relative stress ratio,

respectively, f_y is the static yield function, e is the void ratio, κ is the swelling index, G is the shear modulus.

Weibull distribution is instrumental in assessing the variation in the fracture threshold of brittle materials during creep. To simulate the creep characteristic of cement between hydrate particles, Xu and Wang (2023) proposed an innovative parallel-bar creep model. This model conceptualizes hydrate as numerous equidistant bars, each representing an intergranular bond, which is founded on three assumptions: i. Each bar contributes equally to the structural strength; ii. The axial creep of each bar is equivalent to the overall structural axial creep; iii. The fracture threshold of each bar is independent and adheres to Weibull distribution. This model is extended based on the parallel-bar model proposed by Krajcinovic and Silva (1982), which is given by:

$$D_{weibull} = 1 - \exp\left[-\left(\frac{A_1 t_c (\sigma_{cs})^n \exp(-\frac{A_2}{R_g T})}{\varepsilon_0} \right)^k \right] \tag{3.62}$$

Where ε_0 and k are Weibull parameters, A_1, A_2, and n are the material constants.

3.5.3 Limitations and prospects

In summary, current constitutive models for the creep behavior of GHBS exhibit notable deficiencies and struggle to theoretically simulate the mechanical response due to hydrate cementation. The scope and determinants of these models fall short of fulfilling the requirements for predicting the long-term deformation of hydrate reservoirs within practical engineering scenarios. Hence, further discussions on the promising breakthroughs in the creep model for GHBS are needed, focusing on several key areas:

(1) The difficulty of capturing the accelerating creep phase, where existing literature relies on segmented function with an explicit threshold for creep strain, which may produce potential discontinuities. Future efforts should concentrate on the formulation of a unified model that can delineate all creep phases, with parameters that can depict phase transition.

(2) The micro-mechanism in creep of GHBS requires further exploration. Multi-scale modelling techniques such as Molecular Dynamics (MD) and Discrete Element Method (DEM) offer potential solutions. MD can model the intermolecular interactions and microstructural alterations within GHBS at the atomic level, and DEM for the calibration of macroscopic parameters, which holds promise for optimizing the creep model.

(3) The potential for hydrate dissociation induced by the changes in reservoir temperature and pressure has not yet been covered in existing models. The integration of thermodynamic dissociation model for hydrate with creep models, along with the introduction of relevant dependency parameters, represents a vital direction for future research.

(4) The cementation effect of hydrates largely hinges on its concentration and occurrence. The development of creep models that include parameters related to hydrate pore habits is also necessary.

3.6 Insights and evaluation on constitutive equations of GHBS

In our previous section, we systematically reviewed the constitutive models for GHBS across various theoretical frameworks while discussing their applicability and limitations. To further optimize these models for precise prediction of response mechanisms on GHBS during the recovery of hydrates, we delve deeply into the reported constitutive models. Our emphasis lies in synthesizing and critically evaluating the mechanical equations pertinent to the presence of hydrates, especially concerning strength, stiffness, and bonding degradation equations.

3.6.1 Evaluation of strength equations

The quantification of failure strength is of paramount importance, providing critical information on the elastoplastic deformation of materials subjected to shear stress until failure, which has been thoroughly investigated through the triaxial test. Subsequently, strength prediction equations have been established with the aid of classic theoretical frameworks. Table 3.5 has compiled the strength equations for GHBS reported in current literatures, revealing that the strength attributes are primarily influenced by three aspects: a. Interparticle friction and cohesion of the sediment matrix, similar to the description in Section 2.4.3; b. Cementation strength provided by hydrates; c. External applied stress (Pinkert and Grozic, 2015). The contribution of hydrates to strength is reflected in the term associated with S_h, manifesting in three forms: a. Linear correlation, $\tau_f \propto aS_h$ (Yang et al. 2020); b. Power-law correlation, $\tau_f \propto (S_h)^a$ (Miyazaki et al., 2012; Santamarina and Ruppel, 2010); c. Exponential correlation, $\tau_f \propto \exp(S_h)$ (Zhou et al., 2023). Additionally, the enhancement of strength by effective confining stress exhibits two distinct patterns: a. Linear correlation (Dong et al., 2020); b. Inverse exponential correlation (Li et al., 2013; Pinkert and Grozic, 2014).

Upon preliminary examination, a nonlinear augmentation in failure strength corresponding to S_h is discerned. Effective stress plays a key role in governing interparticle frictional strength, with the degree of influence exerted by hydrates on strength being intimately linked to porosity (Song et al., 2014). Utilizing M-C strength criterion, the strength equation incorporates the term containing S_h to reflect c contributed by hydrates, along with confining pressure to describe c of host sediments. In addition, this equation encompasses additional variables, it is noted that t_d correlates negatively with strength. Also, the suction within GHBS demonstrates marked sensitivity to strength enhancement facilitated by hydrates, exhibiting a positive correlation. Predicated on M-C failure criterion, the strength equation is simplified into one interaction where failure strength is directly proportional to both $\sigma_c^{'}$ and S_h, substituting the material's φ and c with the function contingent upon S_h. Conversely, extended D-C model focuses solely on $\sigma_c^{'}$, neglecting the impact of hydrate. After integrating with M-C failure criterion, it bifurcates failure strength into components attributable to the host sediment and hydrates. For a straightforward and practical approach to predicting the strength of GHBS, it is desirable to add the term associated with S_h into the modified M-C strength equation. Nevertheless, given the complexity introduced by pore habits of hydrates and other determinants affecting the sensitivity to strengthening under cementing action, deeper exploration is imperative to ascertain the precise model parameters.

Table 3.5: Summary of strength equations for GHBS in the existing literature

Article	Theoretical framework	Strength equations	Parameters
Santamarina and Ruppel (2010)	NA	$\tau_f = a\sigma_n + b \cdot \tau_h (S_h / \phi)^c$	a, b, and c are the coefficients, σ_n is the normal stress, ϕ is the porosity, τ_h is the hydrate strength, S_h is the hydrate saturation.
Yang et al. (2020)	Mohr-Coulomb strength criterion	$\tau_f = c_0 + a \cdot S_h + \sigma_n \tan\varphi$	c_0 is the cohesion of host sediment, φ is the internal friction angle, a is the constant.
Pinkert and Grozic (2014)	Mohr-Coulomb strength criterion	$\tau_f = \sigma_n \tan\varphi + c_1\left[1-\exp(-\sigma_c^{'}/\omega)\right] + c_2 S_h^{c_3}$	$\sigma_c^{'}$ is the effective confining stress, ω, c_1, c_2, c_3 are the constants.

Song et al. (2014)	Mohr-Coulomb strength criterion	$\tau_f = a \cdot \exp(-t_d / b) + c + \sigma_n(\delta_1 - \delta_2 \cdot t_d)$	a, b, c, δ_1, and δ_2 are the fitting parameters, t_d is the dissociation time.
Zhou et al. (2023)	Mohr-Coulomb strength criterion	$\tau_f = \tau_{f0} + \frac{\alpha}{1/s_T + \beta}\exp(mS_h)$	α, β and m are the empirical parameters, s_T is the total suction of GHBS, τ_{f0} is the shear strength of host sediment.
Dong et al. (2020)	Mohr-Coulomb failure criterion	$\tau_f = \frac{2\cos(aS_h+b)}{1-\cos(aS_h+b)}[c\cdot\exp(d\cdot S_h)] + \frac{2\sin(aS_h+b)}{1-\sin(aS_h+b)}\sigma_c'$	a, b, c and d are the fitting parameters.
Li et al. (2013)	Duncan-Chang model	$\tau_f = \sigma_n + a\exp(-\sigma_c' / b)$	a and b are the fitting parameters.
Miyazaki et al. (2012)	Duncan-Chang model / Mohr-Coulomb failure criterion	$\tau_f = \tau_{f0} + \alpha(S_h)^\beta$	α and β are the model parameters.

3.6.2 Evaluation of stiffness equations

The stiffness matrix is fundamental in developing constitutive models, quantifying stress-strain behavior during the transition from elastic to elastoplastic phases (Sheng and Fredlund, 2008). The core of deriving the elastoplastic matrix lies in capturing the evolution of stiffness modulus (elastic modulus, shear modulus, and bulk modulus). In essence, the stiffness modulus serves as a pivotal metric for characterizing the stiffness of GHBS. Table 3.6 summarizes the stiffness equations for GHBS reported in existing literature, with a particular emphasis on the contribution of hydrates to stiffness. This is most apparent in the term combining S_h with various coefficients. The interrelation between S_h and stiffness follows three patterns: a. Linear correlation with both being directly proportional (Dong et al., 2022; Klar et al., 2010; Pinkert and Grozic, 2014; Sun et al., 2015; Uchida et al., 2012, 2016; Wang et al., 2022); b. Exponential relationship (Miyazaki et al., 2012); c. Power relationship (Ma and Xu, 2021).

The stiffness equation as informed by M-C criterion considers only a simplistic linear relationship, which is dictated by its theoretical assumption. It is also observed that σ_c' exerts a discernible effect on stiffness in a positive correlation. Despite D-P criterion being the improvement of M-C framework, it similarly adheres to a linear relationship in stiffness equation

with respect to S_h due to the unchanged assumption. Moreover, given that $\sigma_c^{'}$ modulates material stiffness by augmenting frictional contact forces, two terms related to $\sigma_c^{'}$ have been introduced to the equation: one serving as a weighting coefficient and the other formulated as a power expression, denoting the nonlinear impact of $\sigma_c^{'}$ on stiffness. The stiffness equation derived from D-C model encompasses the mentioned three relationships involving numerous fitting parameters, yet its applicability is circumscribed, especially concerning the power term which posits an increase in stiffness attributable to S_h reduces the sensitivity to $\sigma_c^{'}$ (Yan et al., 2021). Most CSM default to a linear correlation with S_h for the ease of numerical computations, incorporating the hydrate contribution with stiffness modulus of remolded soil, which can be quantified as the multiplication of material coefficients and S_h. Nevertheless, the majority of CSM prefer effective over actual S_h in considerations of hydrate degradation upon shearing. The subsequent subsection will further explore the degradation equation and the relationship between effective and actual S_h.

Table 3.6: Summary of stiffness equations for GHBS in the existing literature

Article	Theoretical framework	Stiffness equations	Parameters
Klar et al. (2010)	Mohr-Coulomb criterion	(a) $E_{50} = a + bS_h$	E_{50} is the elastic modulus, S_h is the hydrate saturation, a, b are the constants.
Pinkert and Grozic (2014)	Mohr-Coulomb criterion	(a) $E_{50} = a(\sigma_c^{'} / p_a)^b + c \cdot S_h$	$\sigma_c^{'}$ is the effective confining stress, a, b, and c are the fitting parameters, p_a is the atmosphere pressure.
Miyazaki et al. (2012)	Mohr-Coulomb criterion	(b) $E_{50} = E_i + E_i a(S_h)^b$	E_i is the elastic modulus of host sediment, a and b are the fitting parameters.
Dong et al. (2022)	Drucker-Prager criterion	(a) $E_{50} = (a\sigma_c^{'} + b)S_h + c(\sigma_c^{'})^d$	a, b, c, and d are the fitting parameters.
Ma and Xu (2021)	Duncan-Chang model	(c) $E_{50} = (a + b \cdot S_h)(\sigma_c^{'} / p_a)^{(c - d \cdot S_h)}$	a, b, c, and d are the fitting parameters.
Yan et al. (2021)	Duncan-Chang model	(a) $E_{50} = (E_i + a \cdot S_h)(\sigma_c^{'} / p_a)^b$	a and b are the model constants.
Uchida et al. (2012); Sun et al.	Critical state model	(a) $E_{50} = 3(1-2v)K^{'} + a \cdot S_h^e$	K' is the bulk modulus of host sediment, S_h^e is the effective hydrate saturation, v is the

(2015); Uchida et al. (2016)			Poisson's ratio, a is the material constant.
Wang et al. (2022)	Critical state model	[a] $E_{50} = E_i + a\chi \cdot S_h^e$	a is the model parameter, χ is the degradation parameter.

3.6.3 Evaluation of bonding degradation equations

Within the comparative analysis presented in previous sections regarding the assumptions and applicability of diverse theoretical models, it has been substantiated that critical state model can describe the mechanical characteristics of GHBS to the greatest extent. Diverging from conventional CSM, the significant difference in CSM for GHBS lies in the hardening rule. The hardening parameters are utilized to delineate the enhancement in material's strength during elastoplastic deformation and to determine the yield threshold, which also serves as the critical point distinguishing between strain hardening and softening (Soga and O'sullivan, 2010). The hardening parameters specific to GHBS consist of two components: a. The frictional resistance within host sediments, termed pre-consolidation stress; b. The cohesive bonding and volumetric expansion engendered by hydrate presence (Shen et al., 2022). The hardening parameters contributed by hydrates can be reflected through equations pertaining to effective hydrate saturation S_h^e. This is because the bonding structure formed by hydrate cementation progressively degrades upon shearing, implying that S_h is not a static variable but rather subject to dynamic fluctuation. Accordingly, a degradation parameter χ is necessitated to represent the variation in S_h. This mechanism further explains why GHBS experience strain softening under specific condition.

Table 3.7 presents a summary of degradation equations pertinent to GHBS reported in the literature. Within the framework of CSM, the analysis of hydrate bond degradation substantially leverages the foundational work by Uchida et al. (2012). These investigations aim to introduce a degradation factor to establish a link between effective and actual S_h, where χ diminishes as plastic shear strain increment escalates (Gai et al., 2017; Sun et al., 2015; Wang et al., 2022). Given the variability in the degradation extent of hydrates across various pore habits, it has been proposed to decompose χ into the product of two parameters (χ_1, χ_2), reflecting hydrate accumulation habit alongside its corresponding degradation magnitude (Lin et al., 2015). To separately refine the degradation effect for GHBS in pore-filling, load-bearing, and cementing types, the degradation equation incorporates the morphology ratio (the proportion of different hydrate morphologies in total hydrate) multiplied by S_h (Iwai et al., 2022). It is assumed that hydrate degradation occurred

in GHBS with cementing type adhering to the accumulation of ε_s^p, while those in pore-filling type follow plastic volumetric strain increment, with the degradation in load-bearing type determined by an additional set of morphology ratio. Additionally, in consideration of the anisotropy in GHBS, hydrate degradation provokes a transition from anisotropy to isotropy. This process can be represented by a linear correlation between the rotated angle of yield surface (β_H) and S_h, with β_H approaching zero as ε_s^p increases (Zhou et al., 2018). In examining the degradation effects under various consolidation states of host sediment, the degradation factor can be divided into two aspects: one for depicting the decline in shear strength across different hydrate occurrences (χ_a), and the other for simulating degradation effects under under-consolidated conditions (χ_b), both of which are subjected to ε_s^p (Sun et al., 2019). Moreover, the damage law effectively explains material degradation caused by hydrate dissociation, with the introduction of a damage variable (L) revealing the evolution of partition variables (χ_p), thus presenting the response of pre-consolidation stress to hydrate degradation (Sánchez et al., 2017). The shift in normal compression line and critical state line is contingent upon interparticle bonds (ζ), with hydrate degradation precipitated by plastic deformation as well as bond disruption triggered by the variation in S_h, which suggests that ε_s^p and ε_v^p contribute equally to the deterioration in bonding structure (Ng et al., 2020).

To accommodate the prerequisites of numerical simulations, the majority of researchers have conceptualized S_h^e as the product of a degradation factor and actual S_h. The evolution of degradation factor primarily depends on the changes in ε_s^p, with model parameters intimately related to hydrate occurrence. Despite these advancements, certain limitations persist:

(1) The current equation's reliance on a single parameter falls short of effectively encapsulating the diversity of hydrate pore habits. It is recommended to develop a formula that correlates S_h^e with the saturation across different hydrate morphologies. This should take into account the degradation of hydrate bonds contingent upon S_h^e.

(2) While the inclusion of morphology ratios aids in distinguishing the degradation impacts of various hydrate morphologies, the abundance of model parameters necessitates sensitivity analysis to refine the model for improved predictability.

(3) Existing degradation equations overlook the sensitivity of hydrate degradation to temperature fluctuations and the movement of gas and water within the host sediment. It is advised

to integrate thermodynamics and multiphase flow dynamics into the degradation equation to fully capture the degradation behavior.

Table 3.7: Summary of degradation equations for GHBS in the existing literature

Article	Degradation equations	Parameters
Uchida et al. (2012, 2016); Gai et al. (2017); Sun et al. (2015); Wang et al. (2022)	$S_h^e = \chi S_h \quad d\chi = -m\chi d\varepsilon_s^p$	S_h^e is the effective hydrate saturation, χ is the degradation factor, S_h is the hydrate saturation, m is the material constant, ε_s^p is the plastic shear strain.
Lin et al. (2015)	$S_h^e = \chi_1\chi_2 S_h \quad d\chi_1 = -m_0(\chi_2)^h \chi_1 d\varepsilon_s^p$	χ_1 is a degradation parameter, χ_2 is related to the hydrate accumulation habit, m_0 and h are the model constants.
Sun et al. (2019)	$d\chi_a = -m_1\chi_a d\varepsilon_s^p \quad d\chi_b = -m_2\chi_b d\varepsilon_s^p$	χ_a and χ_b are the structure factors, m_1 and m_2 are the material constants.
Iwai et al. (2022)	$\begin{cases} S_{cem}^H = \alpha S_r^H \\ S_{lb}^H = \beta S_r^H \\ S_{pf}^H = \gamma S_r^H \end{cases} \quad \begin{cases} d\alpha = -m_\alpha \alpha \lvert d\varepsilon_s^p \rvert \\ d\gamma = -m_\gamma \gamma \lvert d\varepsilon_v^p \rvert \\ d\beta = -d\alpha - d\gamma \\ \alpha+\gamma+\beta = 1 \end{cases}$	S_{cem}^H, S_{lb}^H, and S_{pf}^H are the hydrate saturation of CM-type, LB-type, PF-type, S_r^H is the total hydrate saturation, α, β, and γ are the morphology ratios, m_α and m_γ are the material parameter related to the CM-type and PF-type, ε_s^p and ε_v^p are the plastic shear strain and volumetric strain, respectively.
Sánchez et al. (2017)	$\alpha_{hd} = \chi_p \phi S_h \quad \chi_p = \chi_0 \exp(-\frac{L}{2})$	χ_p is the partition parameter, χ_0 is the initial partition parameter, L is damage variable, ϕ is the porosity, α_{hd} represents the effect of hydrate degradation on pre-consolidation pressure.
Zhou et al. (2018)	$\beta_H = \omega\chi_\beta S_h \quad d\chi_\beta = -m_1\chi_\beta d\varepsilon_s^p$	β_H is the rotated parameter, χ_β is the degradation factor, m_1 is the mechanical parameter, ω is the model parameter.
Ng et al. (2020)	$\xi_0 = a\chi_0 \quad d\xi = \xi(-x\lvert d\varepsilon^p \rvert + d\chi/\chi)$ $d\chi = \alpha\beta \exp(\beta S_h) dS_h$	ξ represents the shift of normal compression line due to bonding whose initial value is ξ_0, $d\varepsilon^p$ is the plastic strain increment, x is the degradation factor, χ is the shift of critical state line in which χ_0 is the initial value, α and β are the constants.

3.7 Conclusions

Drawing upon the extant literature about GHBS, this chapter concentrates on the contemporary advancements in understanding the development of constitutive models for GHBS. The following conclusions have been deduced:

(1) Constitutive model based on M-C criterion integrates equations that involve S_h and $\sigma_c^{'}$, effectively replacing the internal friction angle and cohesion. This simplifies the impact of hydrates on strength, stiffness, and dilation into a linear relationship. However, these models neglect the nonlinear behavior of GHBS, failing to capture volumetric yield and strain softening.

(2) Constitutive model utilizing D-P criterion proposes the nonlinear relation that correlates failure strength with $\sigma_c^{'}$ and S_h, which can represent strain softening and volumetric yield under certain condition. Nonetheless, these models ignore the anisotropic distribution of hydrates and phase changes induced by temperature fluctuations.

(3) Nonlinear elastic model extended from D-C model can reflect the stress-strain and strain hardening characteristics of GHBS, which allow for directly quantifying the sensitivity of strength, stiffness, and lateral deformation to various factors. Yet, it falls short in simulating strain softening, volumetric deformation, and hydrate dissociation.

(4) CSM can predict most mechanical properties pertinent to GHBS, especially in volumetric yield and strain softening, yet few models represent diverse shapes of yield surface and anisotropy effect. Additionally, existing models are primarily applicable to coarse-grained sediments, and further need to be validated for fine-grained sediments, also with a gap in accounting for the effects of thermal phase transitions and pore fluid.

(5) Creep model delineates the relationship between strain, strain ratio, and time, employing a strain threshold to demarcate the accelerating creep phase. However, these models are prone to potential discontinuities, an issue that could be rectified through the development of the unified model. The combination of creep model with multiscale modelling techniques such as Molecular Dynamics and Discrete Element Method presents a promising avenue for exploration. Further considerations could incorporate hydrate dissociation and hydrate accumulation habits into creep models.

(6) The contribution of hydrates to the strength and stiffness of GHBS can be explained through linear, power-law, and exponential expressions. Similarly, confining pressure exhibits linear or inverse exponential dependency on strength. However, the model parameters that involve hydrate morphology necessitate further validation. Linear relationship is commonly adopted in stiffness equation, typically formulated as the product of material parameter and S_h. The equation that combines effective hydrate saturation with degradation factor can be simplified to their multiplication, suggesting a pathway for modelling bonding degradation triggered by hydrate dissociation. The degradation factor depends on the evolution of plastic shear strain. Nonetheless, the current reliance on singular parameters is insufficient to encapsulate various hydrate pore habits. Sensitivity analysis, alongside the incorporation of temperature fluctuations and multiphase flow dynamics, could provide valuable insights into hydrate degradation.

Chapter 4. The proposed constitutive model for GHBS

In the research of GHBS, understanding their mechanical behavior is crucial for predicting the stability and rheological properties of submarines. In Chapter 2, we indicate that the presence of NGH significantly impacts the physical and mechanical properties of sediments, including shear strength, compressibility, and permeability. However, due to the multiphase feature and complex microstructure of GHBS, as well as the distribution of hydrates within the pores, even experimental investigations can generally capture their mechanical characteristics, but in some fine-scale scenarios and specific contexts, mathematical physical models and numerical modeling can more accurately reproduce their detailed mechanical responses. Therefore, numerical analysis methods are widely used to simulate and predict the mechanical behavior of these sediments. The core of the numerical approach focuses on developing robust constitutive models that serve as a theoretical basis for modeling the mechanical response of GHBS. In Chapter 3, we have comprehensively compiled the existing geotechnical models, including those based on the M-C criterion, D-P criterion, nonlinear elastic models, CSM, and creep models. Given the inherent limitations of models under different theoretical frameworks—for instance, models based on the M-C criterion cannot reflect strain softening behavior, those based on the D-P criterion fail to consider volumetric deformation, and nonlinear elastic models assume an elastic domain within the yield surface—we found that constitutive models based on critical state theory exhibit excellent in characterizing the mechanical properties of GHBS. Currently, advanced critical state models can effectively assess the volumetric deformation and elastoplastic stress-strain behavior of GHBS. Yet, most models assume the material is isotropic, overlooking the cross anisotropy presented in the sedimentary layer, which would limit their application in practical engineering. Hence, to better evaluate deformation and settlement in reservoirs containing hydrates during extraction, my work is to propose a new elastoplastic constitutive model for GHBS based on HISS framework, which can reflect the anisotropic effects of sediments and structural dilatancy. This model has been validated against experimental data from existing literature via the numerical approach, confirming its reliability and applicability.

4.1 Introduction of modified Cam-clay model

4.1.1 Basic stress-strain equation

In 1963, Roscoe from the University of Cambridge introduced the Cam-clay model, which was formulated based on the results of drained and undrained triaxial tests on normally consolidated and over-consolidated soils (Roscoe and Schofield, 1964; Roscoe et al., 1958). This model, grounded in the associated flow rule and the principle of energy conservation, was the first to introduce crucial concepts such as the critical state line, yield surface, and the *p*-*q* stress space. However, constrained by classical plasticity theory, the model had shortcomings such as sharp corners on the failure surface, difficulty in determining the direction of plastic strain, and hard in effectively reflecting the dilatancy of soil. To address these issues, Roscoe and Burland modified the Cam-clay model in 1968 (Roscoe and Burland, 1968). The primary improvements included reshaping the yield surface from sharp corners to an elliptical form and enhancing the model's ability to predict plastic deformation before entering the critical state. The stress-strain relationship derived from the modified CCM is presented as follows (Britto and Gunn, 1987).

Hydrostatic stress *p*', termed as mean effective stress, is defined as the average of the three principal stresses acting at a point under a specific stress state, which is closely related to volume changes:

$$p' = \frac{\sigma_{11}^{'} + \sigma_{22}^{'} + \sigma_{33}^{'}}{3} = \frac{I_1}{3} \tag{4.1}$$

Where I_1 is the first stress tensor invariant.

Deviatoric stress *q* represents the residual stress component after the removal of hydrostatic stress, which is primarily associated with the material's shear deformation:

$$s_{ij} = \sigma_{ij}^{'} - p^{'}\delta_{ij} \tag{4.2}$$

$$J_2 = \frac{1}{2} s_{ij} s_{ji} \tag{4.3}$$

$$q = \sqrt{3J_2} \tag{4.4}$$

Where J_2 is the second deviatoric stress tensor invariant, δ_{ij} is the Kronecker delta (with δ_{ij} =1 if $i = j$ and δ_{ij} =0 if $i \neq j$), $\sigma_{ij}^{'}$ is the stress tensor, s_{ij} the deviatoric stress tensor.

According to elastoplastic theory, a material's strain (increment) can be divided into elastic strain (increment) ε^e and plastic strain (increment) ε^p. Elastic strain is reversible, which reflects the recoverable deformations within the material's elastic limits. In contrast, plastic strain is irreversible, indicating permanent deformation of materials that occurs after yielding:

$$\varepsilon(d\varepsilon) = \varepsilon^e + \varepsilon^p (d\varepsilon^e + d\varepsilon^p) \tag{4.5}$$

Strain, induced by deformation within the material, can be categorized into volumetric strain ε_v and shear strain ε_s, each further divisible into elastic and plastic components:

$$\varepsilon = \varepsilon_v + \varepsilon_s \tag{4.6}$$

$$\begin{cases} \varepsilon_v = \varepsilon_v^e + \varepsilon_v^p \\ \varepsilon_s = \varepsilon_s^e + \varepsilon_s^p \end{cases} \tag{4.7}$$

Upon triaxial stress loading, volumetric strain can be expressed by the sum of the principal strains:

$$\varepsilon_v = \varepsilon_{11} + \varepsilon_{22} + \varepsilon_{33} = tr\left(\varepsilon_{ij}\right) \tag{4.8}$$

Shear strain is given as:

$$\varepsilon_s = \varepsilon_{ij} - \frac{1}{3} tr\left(\varepsilon_{ij}\right)\delta_{ij} \tag{4.9}$$

Where ε_{ij} is the strain tensor.

4.1.2 Elastic behavior

Modified Cam-clay model provides a detailed description of the nonlinear elastic behavior of soil within small strain ranges, assuming the soil serves as an isotropic material. Within this model, the relationship between strain and stress during elastic phase is determined using the bulk modulus K and shear modulus G. During unloading or reloading processes, the soil exhibits dilatancy characteristics, thus the bulk modulus is employed to describe these changes:

$$\begin{cases} V = 1 + e \\ K = \dfrac{V}{\kappa} p' \end{cases} \tag{4.10}$$

Where e is the void ratio, V is the specific volume, κ is the slope of the swelling line, p' is the mean effective stress.

The void ratio e is defined as the ratio of pore volume V_v to particle volume V_s:

$$e = \frac{V_v}{V_s} = \frac{V - V_s}{V_s} = \frac{V}{V_s} - 1 \tag{4.11}$$

Assume Poisson's ratio is constant, the shear modulus can be expressed as follows:

$$G = \frac{3K^{'}(1-2v)}{2(1+v)} \tag{4.12}$$

According to Hooke's Law (Hooke, 1678), the relationship between volumetric elastic strain and bulk modulus, as well as shear elastic strain and shear modulus, can be articulated:

$$d\varepsilon_v^e = \frac{dp^{'}}{K} \tag{4.13}$$

$$d\varepsilon_s^e = \frac{dq}{3G} \tag{4.14}$$

In matrix form, the above relationship can be represented as:

$$\begin{Bmatrix} dp^{'} \\ dq \end{Bmatrix} = \begin{bmatrix} K & 0 \\ 0 & 3G \end{bmatrix} \begin{Bmatrix} d\varepsilon_v^e \\ d\varepsilon_s^e \end{Bmatrix} \tag{4.15}$$

4.1.3 Hardening parameter and yield function

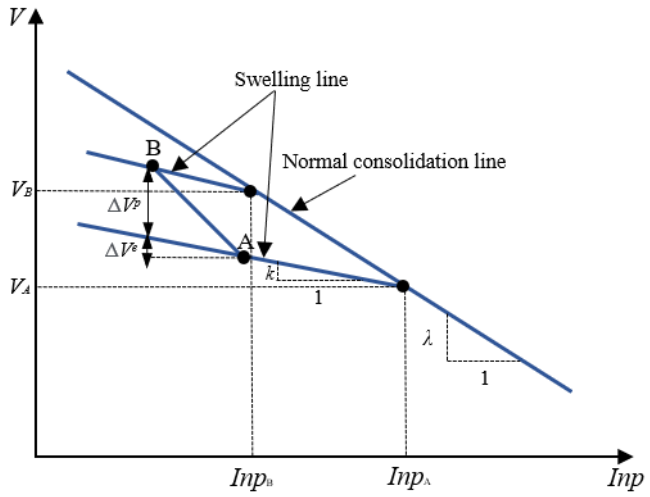

Figure 4.1: Schematic diagram of consolidation line (*V* - *Inp*)

As seen in Fig. 4.1, the specific volume and mean pressure at the intersection of the swelling line and normal consolidation line are referred to as normal consolidation specific volume and normal consolidation pressure, considering an incremental change in stress bringing the point from

state *B* to state *A*. At *B*, there is a corresponding consolidation volume V_B, and consolidation pressure p_B; At *A*, there is a corresponding consolidation volume V_A, and consolidation pressure p_A; The increment of plastic volume change ΔV^p, is measured by the vertical distance between swelling lines (associated with points *A* and *B*):

$$\Delta V^p = (\lambda - \kappa)\frac{dp_{cs}^{'}}{p_{cs}^{'}} \tag{4.16}$$

After the division of the left and right member by specific volume, modified Cam-Clay model set volumetric yield stress $p_{cs}^{'}$ as the hardening parameter, increasing with plastic volumetric strain increment $d\varepsilon_v^p$:

$$dp_{cs}^{'} = \frac{Vp_{cs}^{'}}{\lambda - \kappa} d\varepsilon_v^p \tag{4.17}$$

Modified CCM features an elliptical yield surface (Fig. 4.2), where the soil remains in an elastic state as long as the stress state is within the yield surface ($f < 0$). When $f = 0$ and $df = 0$, the current stress state is on the yield surface, which requires the stress correction. The yield function is expressed as follows:

$$f = \frac{q^2}{M^2} + p^{'}(p^{'} - p_{cs}^{'}) \tag{4.18}$$

Where *M* is critical stress ratio.

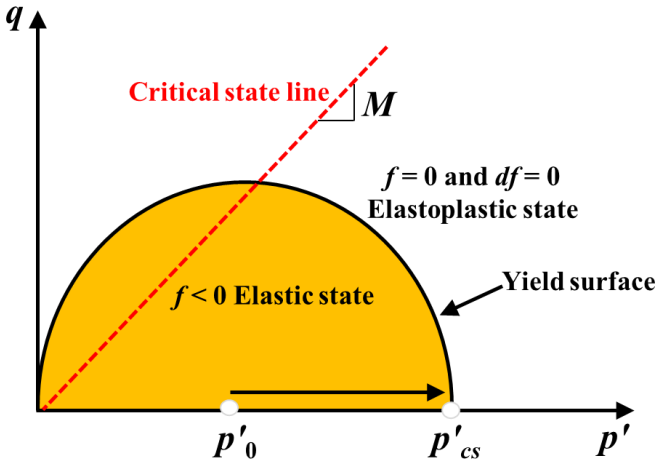

Figure 4.2: Diagram of the yield surface for modified CCM

4.1.4 Flow rule and consistency condition

Modified CCM utilizes the associated flow rule, whereby the plastic potential function is identical to the yield function ($f = g$) (Lubliner, 2008). Consequently, the increment of plastic strain depends on the plastic multiplier Λ:

$$\begin{cases} d\varepsilon_v^p = \Lambda \dfrac{\partial g}{\partial p'} \\ d\varepsilon_s^p = \Lambda \dfrac{\partial g}{\partial q} \end{cases} \tag{4.19}$$

Where Λ is the plastic multiplier.

The yield function is fully differentiated to get the consistency condition:

$$df = \frac{\partial f}{\partial q} dq + \frac{\partial f}{\partial p'} dp' + \frac{\partial f}{\partial p_{cs}'} dp_{cs}' = 0 \tag{4.20}$$

By incorporating the flow rule and hardening parameters into the consistency equation, the plastic multiplier can be calculated:

$$\begin{cases} d\Lambda = \dfrac{\dfrac{\partial f}{\partial p'} dp' + \dfrac{\partial f}{\partial q} dq}{A} \\ A = -\dfrac{\partial f}{\partial p_{cs}'} \dfrac{V p_{cs}'}{\lambda - \kappa} \dfrac{\partial f}{\partial p'} \end{cases} \tag{4.21}$$

Where A is the hardening parameter.

The plastic multiplier is further used to compute the increment of plastic strain tensor, which leads to the derivation of the increment of elastic strain tensor:

$$d\varepsilon_{kl}^p = d\Lambda \frac{\partial g}{\partial \sigma_{kl}'} \tag{4.22}$$

$$d\varepsilon_{kl}^e = d\varepsilon_{kl} - d\varepsilon_{kl}^p \tag{4.23}$$

Multiply both sides by elastic matrix C_{ijkl}^e, stress tensor increment can be obtained:

$$d\sigma_{ij}' = C_{ijkl}^e d\varepsilon_{kl} - C_{ijkl}^e d\Lambda \frac{\partial g}{\partial \sigma_{kl}'} \tag{4.24}$$

The elastic matrix is given as:

$$C_{ijkl}^{e}=\begin{pmatrix} \frac{E(1-v)}{(1-2v)(1+v)} & \frac{vE}{(1-2v)(1+v)} & \frac{vE}{(1-2v)(1+v)} & & & \\ \frac{vE}{(1-2v)(1+v)} & \frac{E(1-v)}{(1-2v)(1+v)} & \frac{vE}{(1-2v)(1+v)} & & & \\ \frac{vE}{(1-2v)(1+v)} & \frac{vE}{(1-2v)(1+v)} & \frac{E(1-v)}{(1-2v)(1+v)} & & & \\ & & & \frac{E}{(1+v)} & & \\ & & & & \frac{E}{(1+v)} & \\ & & & & & \frac{E}{(1+v)} \end{pmatrix} \tag{4.25}$$

Subsequently, after substituting the plastic multiplier into Equation 4.24, the stress-strain constitutive relationship of the modified CCM is yielded as follows:

$$d\sigma_{ij}^{'}=C_{ijkl}^{ep}d\varepsilon_{kl} \tag{4.26}$$

In this relationship, the elastoplastic matrix is expressed as:

$$C_{ijkl}^{ep}=C_{ijkl}^{e}-\frac{C_{ijkl}^{e}\frac{\partial f}{\partial\sigma_{ij}^{'}}\frac{\partial g}{\partial\sigma_{kl}^{'}}C_{ijkl}^{e}}{\frac{\partial f}{\partial\sigma_{ij}^{'}}C_{ijkl}^{e}\frac{\partial g}{\partial\sigma_{kl}^{'}}-\frac{\partial f}{\partial p_{cs}^{'}}\frac{Vp_{cs}^{'}}{\lambda-k}\frac{\partial g}{\partial p^{'}}} \tag{4.27}$$

4.1.5 Numerical applications

Obtaining mechanical parameters through experimental research is the basis for simulation. Table 4.1 presents the material parameters for the modified CCM, it exhibits two consolidated states (OCR=1, 2, 5), and OCR refines the ratio between pre-consolidation stress and initial mean effective stress. All the simulated results are highly consistent with experimental outcomes.

Table 4.1: Model parameters for modified Cam-clay model

Parameter	Value	Meaning
V	1.788	Specific volume
M	1.2	Critical stress ratio
λ	0.077	Slope of compression line
κ	0.0066	slope of swelling line
v	0.3	Poisson's ratio
$p_{cs}^{'}$	200 kPa, 500kPa	Pre-consolidation stress
p'	100kPa (Over consolidated state),	Mean effective stress

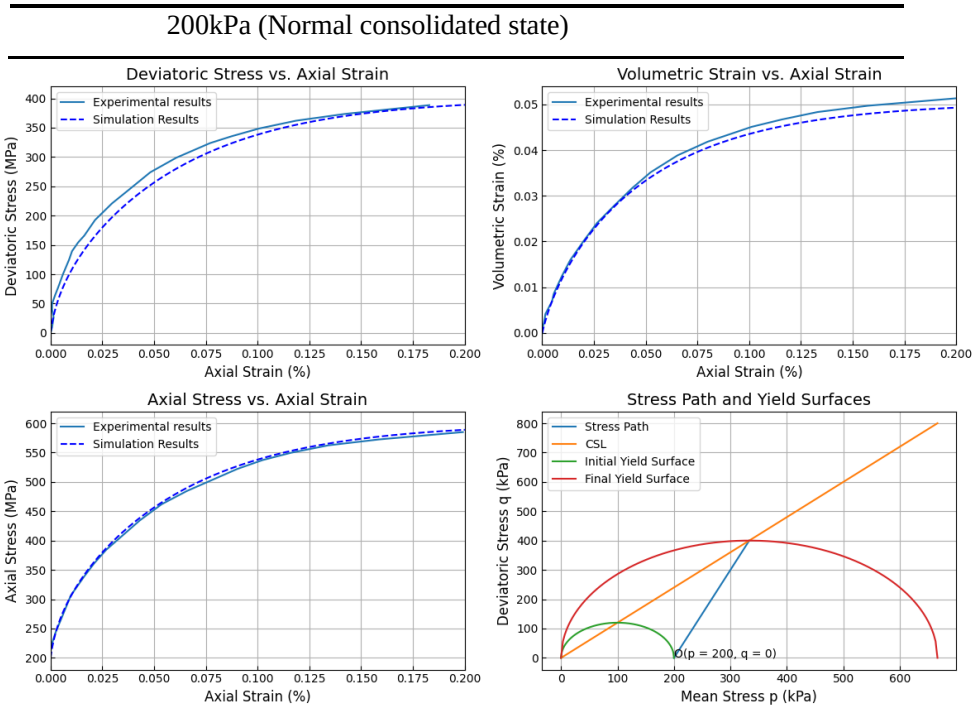

Figure 4.3: Numerical results for normal consolidated soil (OCR=1)

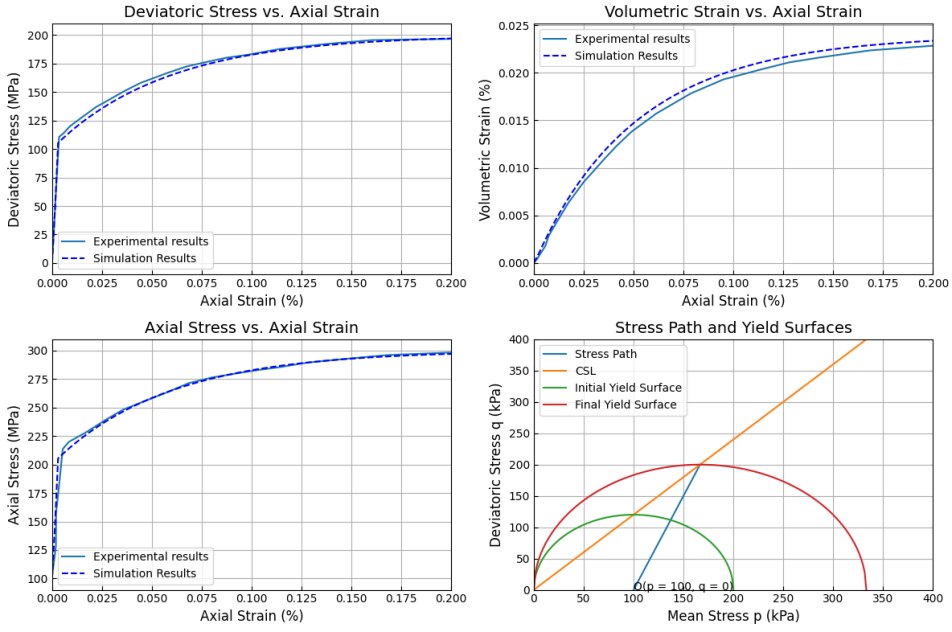

Figure 4.4: Numerical results for over consolidated soil (OCR=2)

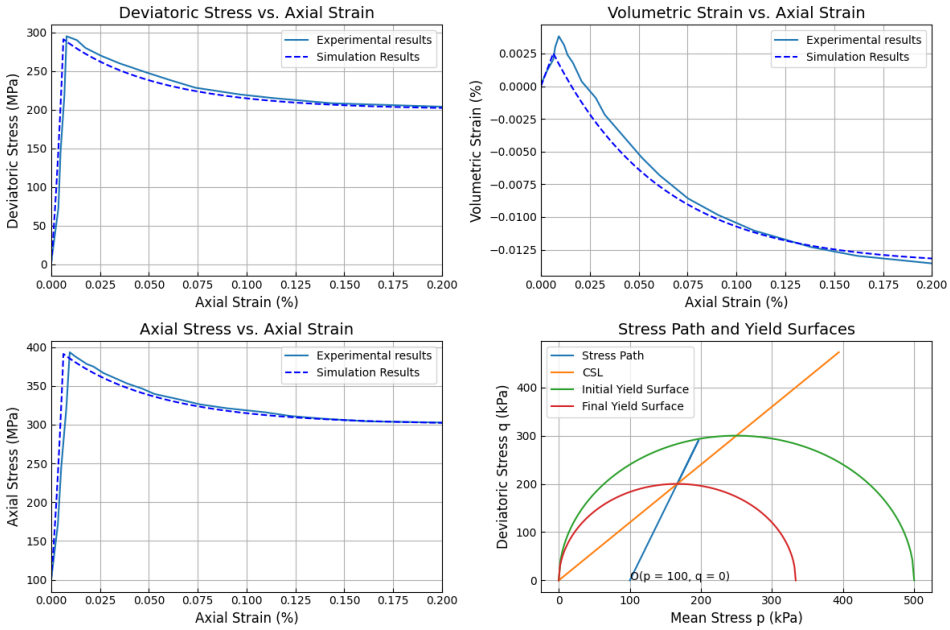

Figure 4.5: Numerical results for over consolidated soil (OCR=5)

4.2 Model theory

4.2.1 Hierarchical single surface theory

In traditional soil and rock mechanics research, researchers commonly employ multiple yield surface models to characterize the yielding behavior of materials under various stress paths. While comprehensive in theory, the complexity of these models increases the difficulty of analysis and numerical calculations. To streamline this process, the Hierarchical Single Surface (HISS) theory was proposed in the 1980s by Desai and others, aimed primarily at developing constitutive models for geological materials such as soil, rock, and concrete (Desai et al., 1986). The core of HISS theory lies in simplifying constitutive modeling by implementing a hierarchical single yield surface, which refines the description of complex mechanical behaviors of materials (Desai, 1989). This method offers the advantage of a singular, smooth yield surface with a distinct normal direction at each point, facilitating the consistent distribution of plastic strain increments across the yield surface and accurately capturing behaviors like shear contraction and dilation.

The hierarchical structure of HISS theory enables the model to evolve from a basic model (S0 model), which describes the isotropic hardening behavior of initially isotropic materials, to more

sophisticated models by incorporating correction terms. The S0 model posits that the plastic strain increment is aligned with the normal direction of yield surface. The S1 model introduces a non-associated flow rule to modify the plastic potential function, where plastic strain increment deviates from the normal direction of the yield surface. The S2 model considers stress-induced anisotropy, which is characterized by the movement of a single plastic potential surface within and possibly intersecting the yield surface. Additionally, there are strain-softening models that enrich the basic model by incorporating damage variable that reflects the material's softening behavior.

The yield function from HISS theory framework is typically represented by a polynomial expansion of the stress tensor and the plastic strain tensor (Desai et al., 1991):

$$\begin{cases} F = J_2 + (\alpha(I_1)^n - \gamma(I_1)^2)(1-\beta S_r)^{-0.5} \\ \Downarrow \\ F(p,q,S_r) = \dfrac{q^2}{3} + \dfrac{[\alpha(3p)^n - \gamma(3p)^2]}{\sqrt{(1-\beta S_r)}} \end{cases} \tag{4.28}$$

Where $J_2 = s_{ij}s_{ij} / 2$, $I_1 = \mathrm{tr}(\sigma_{ij})$, $J_2 = s_{ij}s_{jk}s_{kl} / 3$, S_r is the stress ratio, $S_r = 3\sqrt{3}J_3 J_2^{-1.5} / 2$, α, β, γ, and n are the model parameter that controls the shape of yield surface.

In HISS model, the impact of four main parameters (α, β, n, and γ) on the shape of the yield surface is thoroughly analyzed. Common parameters for sand materials are selected, and the results are displayed on the p-q plane (Desai et al., 1990; Wang et al., 2014). By controlling the variation of a single parameter while keeping others constant, it can be observed that all the yield surfaces consistently exhibit a bullet-shaped form (Fig. 4.6). Specifically, α primarily controls the overall size of the yield surface, while n and γ both influence the size of the yield surface and the initial tangential slope. Meanwhile, β predominantly determines the specific shape of the yield surface within the principal stress space.

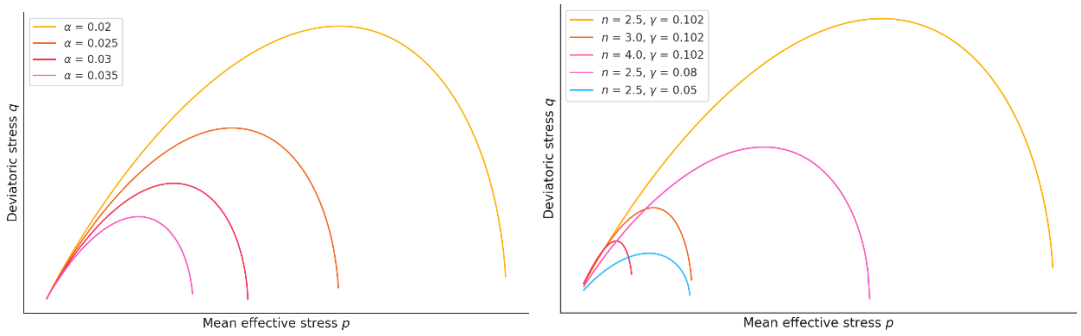

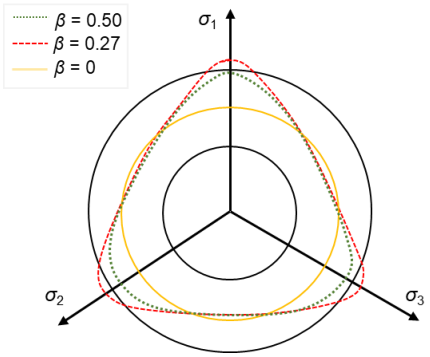

Figure 4.6: The change of yield surface induced by shape parameters

4.2.2 Subloading surface theory

In traditional plasticity theory, it is generally assumed that material behavior within the yield surface is entirely elastic, and plastic flow occurs when the stress state reaches or exceeds the yield surface. Traditional model often overlooks the nonlinear responses and progressively increasing plastic effects as the stress state approaches the yield surface. To address this issue, T. Hashiguchi proposed the subloading surface theory in the 1980s (Fig. 4.7) (Hashiguchi, 1989). This theory posits a subloading surface positioned within the main yield surface, specifically designed to describe the plastic behavior of materials before they fully engage the main yield surface. Distinct from traditional yield surfaces, the subloading surface facilitates plastic deformation even before conventional yielding. The subloading yield surface, similar in shape to the main yield surface, can expand within the stress space in response to changes in stress states until it eventually coincides with the main yield surface. When the stress state lies on the subloading surface, the material demonstrates elastoplastic behavior (Hashiguchi and Chen, 1998).

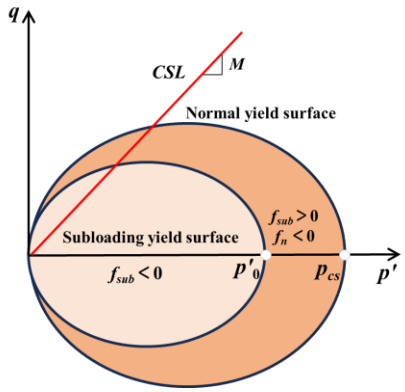

Figure 4.7: Schematic diagram of subloading surface relative to normal yield surface

The dynamics of the subloading yield surface, encompassing both expansion and contraction, are delineated through the introduction of a scaling factor (Equation 4.29) (Hashiguchi and Okayasu, 2000). This factor modifies the area ratio between the subloading and the normal yield surfaces, effectively capturing changes in the material's stress state.

$$\begin{cases} f_{sub}(\sigma_{ij},\zeta) = f_n(\sigma_{ij}, R\cdot\zeta) \\ R = \dfrac{p_0^{'}}{p_{cs}} \end{cases} \tag{4.29}$$

Where ζ is the internal variable, $p_0^{'}$ is the initial effective confining stress.

In subloading surface theory, the scaling factor evolves as plastic deformation accumulates, which illustrates the nonlinear enhancement effects as the material nears the main yield surface. This evolutionary relationship is articulated as follows:

$$dR = U\left|d\varepsilon_{ij}^{p}\right| \tag{4.29}$$

U relies on the shape of the yield surface and the stress path, and needs to meet certain conditions: when R = 0, the material exhibits an entirely elastic state, and corresponding subloading surface is similar to a point; when $0 < R < 1$, the material remains sub-yielding state without reaching the main yield surface; when R =1, the subloading yield surface aligns perfectly with the main yield surface, where the material has entered the yield state; when $R > 1$, the material displays unconventional plastic deformation, often accompanied by softening behavior, which is described by the following formula:

$$\left.\begin{array}{ll} R=0: U=+\infty & \text{Elastic state} \\ 0<R<1: U>0 & \text{Sub-yield state} \\ R=1: U=0 & \text{Normal-yield state} \\ R>1: U<0 & \text{Super-yield state} \end{array}\right\} \tag{4.31}$$

4.3 Proposed elastoplastic constitutive model

4.3.1 Yield function

Most constitutive models for GHBS are derived based on critical state theory, among which the modified Cam-clay model is fundamental and commonly used. On the one hand, GHBS exhibit consolidated behavior similar to soils under triaxial stress conditions; on the other hand, the

presence of hydrates in sediment pores imparts mechanical properties akin to denser soils, as discussed in detail in Chapter 2. Despite its effectiveness, the modified CCM has limitations, notably its restriction to a standard elliptical yield surface. While this model effectively predicts the mechanical responses of GHBS under triaxial stress states, its practical application in real-world engineering poses significant challenges, particularly under the complex stress conditions found in deep-sea sediments. A key advantage of the HISS theory is its flexibility in not confining the yield surface to any predetermined shape, thereby accommodating different material types and stress states. Within the HISS framework, by incorporating shape parameters into the modified CCM, a single yield surface can adapt to various yielding conditions. The yield function is specified as follows:

$$f = \frac{a}{M^2} q^2 - 9\gamma (p')^2 + 9\gamma (p')^n (p_c)^{2-n} \tag{4.32}$$

Where a, γ, and n are the shape parameters, q is the deviatoric stress, p' is the mean effective stress, p_c is the pre-consolidation pressure, M is the critical stress ratio.

In the above equation, the shape of yield surface is governed by three coefficients a, γ, and n. Drawing from Gai et al. (2017), we have listed several shape parameters appropriate for GHBS yield surface in Table 4.2. It is observed that modified CCM is one of the yield surfaces, which emerges upon substituting these parameters into the yield function (S1). Equation 4.33 presents all the yield equations, while the corresponding yield surfaces are depicted in Fig. 4.8.

Table 4.2: Parameters related to controlling the shape of yield surface

Parameters	S1(modified CCM)	S2	S3	S4
a	1	0.9	0.9	0.9
n	1	3	5	0.95
γ	-1/9	1/9	1/9	-0.13

$$\begin{cases} f = \dfrac{1}{M^2} q^2 + p'^2 - p' p_c & \text{(S1)} \\ f = \dfrac{9}{10M^2} q^2 - p'^2 + p'^3 (p_c)^{-1} & \text{(S2)} \\ f = \dfrac{9}{10M^2} q^2 - p'^2 + p'^5 (p_c)^{-3} & \text{(S3)} \\ f = \dfrac{9}{10M^2} q^2 + 1.17 p'^2 - 1.17 p'^{0.95} p_c^{1.05} & \text{(S4)} \end{cases} \tag{4.33}$$

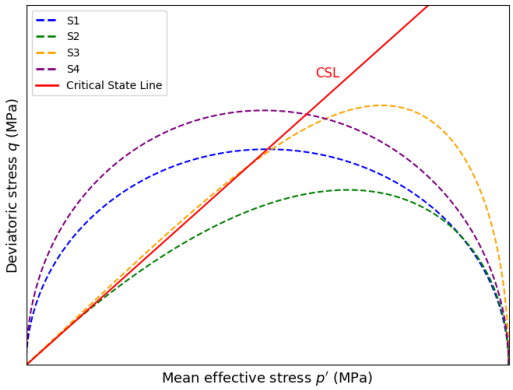

Figure 4.8: Schematic diagram of various shapes of yield surface in *p*-*q* space

As outlined in Section 2.4.3, hydrate particles serve as fillers within the sediment skeleton, bonding loose grains and augmenting the sediment's structural strength. Upon shearing, the rearrangement and slippage of particles may induce volumetric changes, with hydrates contributing to increased expansiveness of the structure. We have confirmed in section 2.5.1 that the enhanced cohesion primarily arises from the cementing effect of the hydrates, significantly bolstering structural strength. Uchida et al. (2012) proposed that the improvement in sediment cohesion and dilation due to hydrates warrant separate discussion. In his constitutive model, two additional hardening parameters were introduced to reflect these effects, respectively. However, subsequent research indicates that strength and expansiveness are interconnected, with these two enhanced mechanisms driven by hydrates occurring simultaneously. Consequently, it is available to simplify the hydrate contribution, and the additional strength improvement for host sediment provided by hydrates can be effectively represented by a dependent hardening parameter p_d, as depicted in the following yield function (Uchida et al., 2016):

$$f = \frac{a}{M^2} q^2 - 9\gamma (p')^2 + 9\gamma (p')^n (p_c + p_d)^{2-n} \tag{4.34}$$

Subloading surface theory suggests that materials can undergo nonlinear plastic deformation even when the stress state remains within the yield surface. Thus, to facilitate a smooth transition from elastic to plastic phases, a scaling factor R is introduced within the yield surface (Fig. 4.9):

$$f = \frac{a}{M^2} q^2 - 9\gamma (p')^2 + 9\gamma (p')^n (R(p_c + p_d))^{2-n} \tag{4.35}$$

Assuming that for GHBS, the stress state point consistently lies on the subloading surface, and the expression for the scaling factor is as follows:

$$R = \frac{p^{'}}{p_c + p_d} \tag{4.36}$$

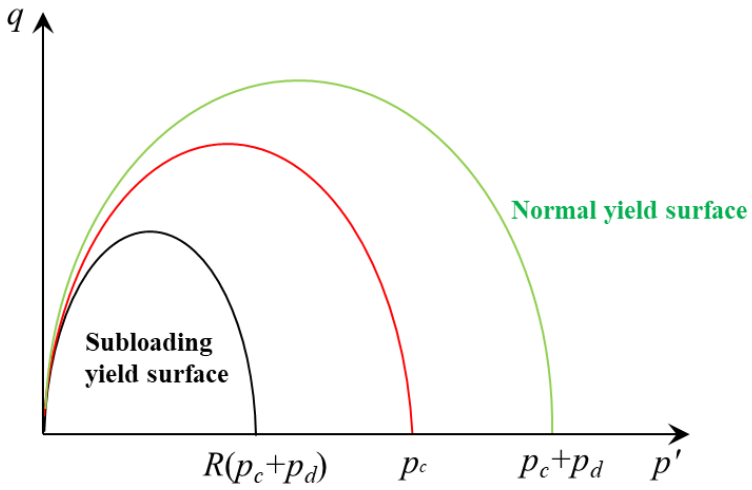

Figure 4.9: Schematic diagram of subloading yield surface

4.3.2 Hardening law

Within the context of this theory, two pivotal hardening parameters (p_c and p_d) are defined on the yield surface:

Pre-consolidation stress p_c, also known as the volumetric yield stress, is an important hardening parameter in geotechnical engineering (Solanki and Desai, 2008). It denotes the stress level at which material shifts from an elastic to a plastic state, accompanied by significant volumetric changes. As course-grained soils undergo various loading and unloading paths, pre-consolidation stress continues to evolve, mirroring soil's hardening or softening behavior. During the recovery of hydrates from coarse-grained sediments, pre-consolidation stress represents the historical maximum stress state of host sediment. If applied stress exceeds the pre-consolidation stress, sediments would undergo volumetric yield, leading to plastic deformation and settlement. Furthermore, hydrate extraction often triggers hydrate decomposition by reducing pore pressure, progressively causing the effective stress to surpass the pre-consolidation stress and heightening the risk of sediment instability. Hence, the volumetric yield stress can be delineated as follows:

$$\begin{cases} \dfrac{dp_c}{p_c} = \dfrac{d\varepsilon_v^p}{C_p} \\ C_p = \dfrac{\lambda - \kappa}{1+e} \end{cases} \tag{4.37}$$

Where λ is the slope of normal compression line, κ is the slope of swelling line, $d\varepsilon_v^p$ is the plastic volumetric strain increment.

By integrating both sides, we can obtain the evolution law of the volumetric yield stress as a function of plastic volumetric strain as follows:

$$p_c = p_{c0} \exp(\frac{\varepsilon_v^p}{C_p}) \tag{4.38}$$

Where p_{c0} is the initial value of volumetric yield stress.

Drawing on a simplification of hardening parameters from Uchida's (2016) model, hardening parameter p_d has been implemented to represent the cementing effects of hydrates within course-grained sediments. The magnitude of improvement in both strength and dilation of the whole structure provided by hydrates is dependent on S_h, as proposed by the empirical formula from Miyazaki et al. (2012). The expression is as follows:

$$p_d = \alpha(\chi S_h)^\beta \tag{4.39}$$

Where p_d controls the strength enhancement provided by hydrates, χ is the degradation factor, which reflects the hydrate decomposition upon shearing, α and β are the constants, which are related to the hydrate occurrence, S_h is the hydrate saturation.

The term χS_h denotes the effective hydrate saturation S_h^e, recognizing that hydrates may gradually decompose upon shearing, which reduces the effective hydrate saturation and weakens the cementing effect. This degradation effect is quantified by a degradation factor χ that decreases with plastic shear strain, with the rate of reduction being proportional to the current state of degradation. This evolutionary law is articulated as:

$$d\chi = -\mu\chi d\varepsilon_s^p \tag{4.40}$$

Furthermore, after integrating the above formula, we can delineate the relationship between the degradation factor and plastic shear strain (Yuan et al., 2020):

$$\chi = \chi_0 \exp(-\mu\varepsilon_s^p) \tag{4.41}$$

Where χ_0 is the initial degradation factor, the value of which equals to 1, μ is the degradation parameter, which represents the degradation rate, $d\varepsilon_s^p$ is the plastic shear strain increment.

The incremental form of the hardening parameter p_d, informed by these relationships, can be determined as follows:

$$dp_d = \alpha\beta\chi^\beta S_h^{\beta-1}(dS_h - uS_h d\varepsilon_s^p) \tag{4.42}$$

During the loading process, the area of subloading surface evolves in response to changes in the initial stress state. The accumulation of plastic strain directly influences the evolution of the scaling factor R, which can be represented by the following expression:

$$dR = U\left|d\varepsilon_{kl}^p\right| \tag{4.43}$$

$$U = -\eta InR \tag{4.44}$$

$$R_{\text{inter}} = R + dR \tag{4.45}$$

Where $\left|d\varepsilon_{ij}^p\right|$ is the total plastic strain increment vector, η is a sub-loading coefficient, the subscript inter represents the value after iteration, U is a monotonically decreasing function of R, as illustrated in Fig. 4.10.

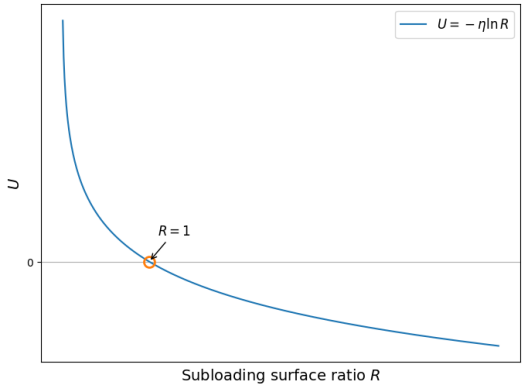

Figure 4.10: The relationship between U and R

The module of the plastic strain increment refers to the total plastic deformation of the sediment, both shear and volumetric plastic deformations are taken into account in a scalar form to eliminate directional complications:

$$\left|d\varepsilon_{kl}^{p}\right|=\sqrt{d\varepsilon_{kl}^{p}\cdot d\varepsilon_{kl}^{p}}=\sqrt{(d\varepsilon_{11}^{p}\cdot d\varepsilon_{11}^{p}+d\varepsilon_{22}^{p}\cdot d\varepsilon_{22}^{p}+d\varepsilon_{33}^{p}\cdot d\varepsilon_{33}^{p})} \tag{4.46}$$

4.3.3 Cross-anisotropy in elastic phase

In the constitutive model for GHBS, the sediment's stress-strain behavior within the elastic range is described by its elastic relationship. Within the limits of small deformations, this relationship generally adheres to Hooke's law and assumes isotropic loading conditions. The elastic response is governed by the bulk and shear modulus, which collectively determine the overall stiffness of sands. Regarding the bulk modulus of GHBS, it is often postulated to be comparable to that of the matrix sediment, indicating that the contribution of hydrates to the bulk modulus is negligible. This assumption is based on the idea that the bulk modulus largely relies on the stiffness and configuration of the particle skeleton, while hydrates merely fill the inter-particle pores and exert minimal impact on the stiffness of sediment skeleton. The expression for the bulk modulus of GHBS is as follows (Uchida et al., 2012):

$$\begin{cases} K_{hs}^{'}=K^{'}+K_{h} \\ K_{h}\approx 0 \end{cases} \tag{4.47}$$

Where $K_{hs}^{'}$ represents the bulk modulus of GHBS, $K^{'}$ is the bulk modulus of soil skeleton, K_h is the bulk modulus of hydrate.

The bulk modulus for soil skeleton is given by:

$$K^{'}=\frac{1+e}{\kappa}p^{'} \tag{4.48}$$

Contrary to prevalent opinions, we posit that the presence of hydrates indeed contributes to an increase in the bulk stiffness of sediments, especially at higher S_h, primarily for two reasons: i. Hydrates possess inherent stiffness and are less compressible than the fluids in sediment pores. Thus, when hydrates fill these pores, the overall compressibility of the structure will decrease, consistent with our description in Section 2.2.3; ii. The cementation effect of hydrates impedes the relative movement of sediment particles under loading, thereby diminishing volumetric deformation. Based on the data presented in the existing literature, we have established a relationship between S_h and stiffness modulus, which reveals a linear correlation, as shown in Fig. 4.11. The bulk modulus for GHBS can be expressed as (Feng et al., 2020):

$$K_{hs}^{'}=K^{'}(1+\xi S_{h}) \tag{4.49}$$

Where S_h is the hydrate saturation, ξ is the fitting parameter.

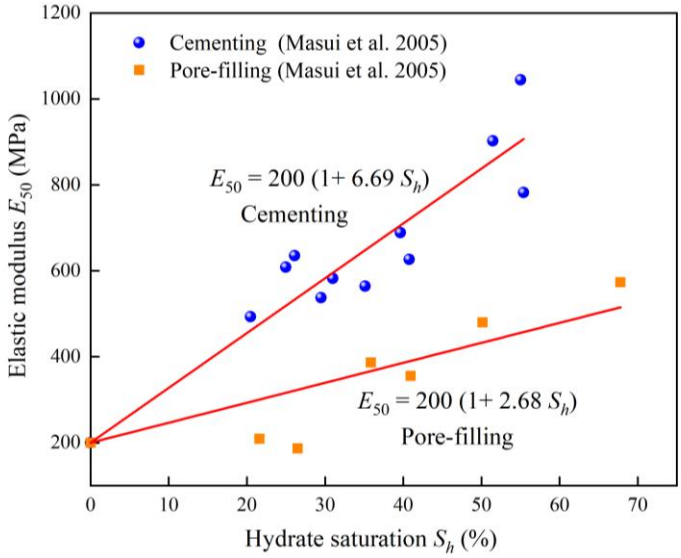

Figure 4.11: Elastic modulus versus hydrate saturation (Masui et al. 2005)

In terms of isotropic materials, the formula for the elastic constitutive relationship can be expressed as:

$$\begin{Bmatrix} d\varepsilon_v^e \\ d\varepsilon_s^e \end{Bmatrix} = \begin{bmatrix} \frac{1}{K_{hs}^{'}} & 0 \\ 0 & \frac{1}{3G} \end{bmatrix} \begin{Bmatrix} dp^{'} \\ dq \end{Bmatrix} \tag{4.50}$$

Where G is the shear modulus.

The stress-strain relationship can be given through the isotropic flexibility matrix:

$$\begin{pmatrix} \varepsilon_{11} \\ \varepsilon_{22} \\ \varepsilon_{33} \\ \varepsilon_{23} \\ \varepsilon_{31} \\ \varepsilon_{12} \end{pmatrix} = \frac{1}{E} \begin{pmatrix} 1 & -\nu & -\nu & 0 & 0 & 0 \\ -\nu & 1 & -\nu & 0 & 0 & 0 \\ -\nu & -\nu & 1 & 0 & 0 & 0 \\ 0 & 0 & 0 & 1+\nu & 0 & 0 \\ 0 & 0 & 0 & 0 & 1+\nu & 0 \\ 0 & 0 & 0 & 0 & 0 & 1+\nu \end{pmatrix} \begin{pmatrix} \sigma_{11}^{'} \\ \sigma_{22}^{'} \\ \sigma_{33}^{'} \\ \sigma_{23}^{'} \\ \sigma_{31}^{'} \\ \sigma_{12}^{'} \end{pmatrix} \tag{4.51}$$

However, GHBS show limited forms of anisotropy due to their layer distribution. A transversely isotropic material possesses an axis of symmetry because its properties are independent of the sample's rotation about the symmetry axis. In soil mechanics, transverse isotropy is also termed cross-anisotropy. It is assumed that the elastic properties of materials hinge on their sedimentary type and stress history. The behavior of cross-anisotropy material can be

explained by an anisotropic elastic matrix depending on five constants (C_{11}, C_{12}, C_{33}, C_{23}, and C_{44}), which is shown as (Liu and Zheng, 2019):

$$C_{ijkl}^{e}=\begin{pmatrix} C_{11} & C_{12} & C_{12} & 0 & 0 & 0 \\ C_{12} & C_{33} & C_{23} & 0 & 0 & 0 \\ C_{12} & C_{23} & C_{33} & 0 & 0 & 0 \\ 0 & 0 & 0 & C_{33}-C_{23} & 0 & 0 \\ 0 & 0 & 0 & 0 & C_{44} & 0 \\ 0 & 0 & 0 & 0 & 0 & C_{44} \end{pmatrix} \tag{4.52}$$

In general, when subjected to uniaxial tension loading, the stress in the axial direction $\neq 0$, while the stresses in other directions equal to 0, according to the Hooke's law, we can get:

$$\begin{cases} \varepsilon_1=\dfrac{1}{E_1}\sigma_1^{'} \\ \varepsilon_2=-\dfrac{v_{12}}{E_1}\sigma_1^{'} \\ \varepsilon_3=-\dfrac{v_{13}}{E_1}\sigma_1^{'} \\ \varepsilon_{12}=\varepsilon_{13}=\varepsilon_{23}=0 \end{cases} \tag{4.53}$$

Where E_1 is the Young's modulus in axial direction.

Similarly, assume this situation happening in different directions, the relationship between the flexibility coefficient and elastic constant can be extended as follows:

$$\begin{cases} \varepsilon_{11}=\dfrac{1}{E_1}\sigma_{11}^{'}-\dfrac{v_{21}}{E_2}\sigma_{22}^{'}-\dfrac{v_{31}}{E_3}\sigma_{33}^{'} \\ \varepsilon_{22}=-\dfrac{v_{12}}{E_1}\sigma_{11}^{'}+\dfrac{1}{E_2}\sigma_{22}^{'}-\dfrac{v_{32}}{E_3}\sigma_{33}^{'} \\ \varepsilon_{33}=-\dfrac{v_{13}}{E_1}\sigma_{11}^{'}-\dfrac{v_{23}}{E_2}\sigma_{22}^{'}-\dfrac{1}{E_3}\sigma_{33}^{'} \\ \varepsilon_{12}=\dfrac{\sigma_{12}^{'}}{2G_{12}} \\ \varepsilon_{23}=\dfrac{\sigma_{23}^{'}}{2G_{23}} \\ \varepsilon_{31}=\dfrac{\sigma_{31}^{'}}{2G_{31}} \end{cases} \tag{4.54}$$

Where G_{12}, G_{23}, and G_{31} are the shear moduli in different directions, E_1, E_2, and E_3 are the Young's moduli in various directions.

The flexibility matrix can be expressed as:

$$(C^{e}_{ijkl})^{-1}\sigma'_{ij} = \varepsilon_{kl} \tag{4.55}$$

GHBS can be assumed to be layered anisotropic media, as depicted in Fig. 4.12. In this regard, each sedimentary layer is considered a homogeneous medium associated with isotropic properties in the horizontal direction. Still, it differs from that in the vertical direction, with variations in elastic coefficients across different orientations (Pegah and Liu, 2020). Apply two Poisson's ratios v_V and v_H to control the deformation caused by loading applied to the horizontal plane and vertical axis, respectively. E_H and E_V are used to describe the elastic modulus displayed in the horizontal plane and vertical axis. G_H and G_V explain the shear modulus across the horizontal and vertical directions.

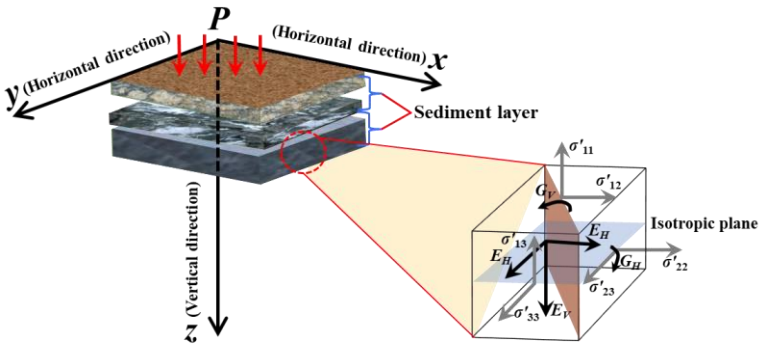

Figure 4.12: General representation of the anisotropic sediments

The flexibility matrix can be modified as follows (Liu and Zheng, 2019):

$$\begin{pmatrix}\varepsilon_{11}\\ \varepsilon_{22}\\ \varepsilon_{33}\\ \varepsilon_{23}\\ \varepsilon_{31}\\ \varepsilon_{12}\end{pmatrix}=\begin{pmatrix}\frac{1}{E_V} & -\frac{\nu_V}{E_V} & -\frac{\nu_V}{E_V} & 0 & 0 & 0\\ -\frac{\nu_V}{E_V} & \frac{1}{E_H} & -\frac{\nu_H}{E_H} & 0 & 0 & 0\\ -\frac{\nu_V}{E_V} & -\frac{\nu_H}{E_H} & \frac{1}{E_H} & 0 & 0 & 0\\ 0 & 0 & 0 & \frac{1}{2G_H} & 0 & 0\\ 0 & 0 & 0 & 0 & \frac{1}{2G_V} & 0\\ 0 & 0 & 0 & 0 & 0 & \frac{1}{2G_V}\end{pmatrix}\begin{pmatrix}\sigma'_{11}\\ \sigma'_{22}\\ \sigma'_{33}\\ \sigma'_{23}\\ \sigma'_{31}\\ \sigma'_{12}\end{pmatrix} \tag{4.56}$$

After transforming the above flexibility matrix, we can get the stiffness matrix, in which the items related to the matrix parameter are represented as follows:

$$\begin{cases} C_{11}=A(1-(\nu_H)^2)=M_V\\ C_{33}=A(\frac{E_H}{E_V}-(\nu_V)^2)=M_H\\ \mathrm{C}_{12}=\mathrm{A}\nu_H(1+\nu_H)\\ C_{23}=A(\frac{E_H}{E_V}\nu_H+(\nu_H)^2)\\ C_{33}-C_{23}=\frac{E_H}{1+\nu_H}=2G_H\\ \mathrm{C}_{44}=2\mathrm{G}_V \end{cases} \tag{4.57}$$

Where $A=E_H/(1+\nu_H)[(\frac{E_H}{E_V})(1-\nu_H)-2(\nu_V)^2]$, M_H and M_V are the deformation modulus across the horizontal and vertical direction, respectively.

Therefore, we can get the elastic stress-strain relationship for the anisotropic material:

$$\begin{pmatrix}\sigma_{11}^{'}\\ \sigma_{22}^{'}\\ \sigma_{33}^{'}\\ \sigma_{23}^{'}\\ \sigma_{31}^{'}\\ \sigma_{12}^{'}\end{pmatrix}=\begin{pmatrix} M_V & Av_H(1+v_H) & Av_H(1+v_H) & 0 & 0 & 0\\ Av_H(1+v_H) & M_H & A(\frac{E_H}{E_V}v_H+(v_H)^2) & 0 & 0 & 0\\ Av_H(1+v_H) & A(\frac{E_H}{E_V}v_H+(v_H)^2) & M_H & 0 & 0 & 0\\ 0 & 0 & 0 & 2G_H & 0 & 0\\ 0 & 0 & 0 & 0 & 2G_V & 0\\ 0 & 0 & 0 & 0 & 0 & 2G_V \end{pmatrix}\begin{pmatrix}\varepsilon_{11}\\ \varepsilon_{22}\\ \varepsilon_{33}\\ \varepsilon_{23}\\ \varepsilon_{31}\\ \varepsilon_{12}\end{pmatrix} \tag{4.58}$$

The anisotropic elastic matrix encompasses six parameters involving the horizontal and vertical direction: two Young's moduli (E_H and E_V); two shear moduli (G_H and G_V); two Poisson's ratios (v_H and v_V). Compared to the isotropic materials, it can be assumed that the anisotropy effect can be explained by multiplying the stiffness coefficients to increase the stiffness in a horizontal direction by an anisotropy factor α_*, the shift form is given by:

$$C_{original}=\begin{pmatrix} C_{11} & C_{12} & C_{12}\\ C_{12} & C_{11} & C_{12}\\ C_{12} & C_{12} & C_{11}\end{pmatrix}\xrightarrow{\alpha_*}C_{ansitropy}=\begin{pmatrix} C_{11}^* & \alpha_* C_{12}^* & \alpha_* C_{12}^*\\ \alpha_* C_{12}^* & (\alpha_*)^2 C_{11}^* & (\alpha_*)^2 C_{12}^*\\ \alpha_* C_{12}^* & (\alpha_*)^2 C_{12}^* & (\alpha_*)^2 C_{11}^*\end{pmatrix} \tag{4.59}$$

Though the multiple formulation is able to alternative, the above equation is considered the most effective hypothesis referred to Lodge et al. (1955). For $\alpha_* = 1$, the sediments are isotropic. For $\alpha_* > 1$, the sediments exhibit stronger stiffness horizontally than vertically. For $\alpha_* < 1$, the sediments are stiffer vertically than horizontally.

Under the above assumption, the isotropic parameters E and v can be replaced by E^* and v^* that can reflect the anisotropic behavior, the modified form is given by:

$$\begin{pmatrix}\sigma_{11}^{'}\\ \sigma_{22}^{'}\\ \sigma_{33}^{'}\\ \sigma_{23}^{'}\\ \sigma_{31}^{'}\\ \sigma_{12}^{'}\end{pmatrix}=\frac{E^*}{(1+v^*)(1-2v^*)}\begin{pmatrix} 1-v^* & \alpha_* v^* & \alpha_* v^* & 0 & 0 & 0\\ \alpha_* v^* & \alpha_*^2(1-v^*) & \alpha_*^2 v^* & 0 & 0 & 0\\ \alpha_* v^* & \alpha_*^2 v^* & \alpha_*^2(1-v^*) & 0 & 0 & 0\\ 0 & 0 & 0 & \frac{\alpha_*^2(1-2v^*)}{2} & 0 & 0\\ 0 & 0 & 0 & 0 & \frac{\alpha_*(1-2v^*)}{2} & 0\\ 0 & 0 & 0 & 0 & 0 & \frac{\alpha_*(1-2v^*)}{2}\end{pmatrix}\begin{pmatrix}\varepsilon_{11}\\ \varepsilon_{22}\\ \varepsilon_{33}\\ \varepsilon_{23}\\ \varepsilon_{31}\\ \varepsilon_{12}\end{pmatrix} \tag{4.60}$$

Where E^* and v^* represent the modified values of Young's modulus and Poisson's ratio, α_* is the anisotropy parameter.

Through the comparison between Equation 4.56 and Equation 4.60, we can get the correlation between original elastic constants and modified parameters, as displayed in the following:

$$\begin{pmatrix} E_V = E^* \\ E_H = \alpha_*^{\,2} E^* \\ \nu_V = \dfrac{\nu^*}{\alpha_*} \\ \nu_H = \nu^* \\ 2G_V = \dfrac{\alpha_* E^*}{1+\nu^*} \\ 2G_H = \dfrac{\alpha_*^{\,2} E^*}{1+\nu^*} \end{pmatrix} \tag{4.61}$$

In case of anisotropic materials, considering the cross-coupling between volumetric and distortional effects, Equation 4.50 can be modified to (Graham and Houlsby, 1983):

$$\begin{bmatrix} dp' \\ dq \end{bmatrix} = \begin{bmatrix} K^* & J \\ J & 3G^* \end{bmatrix} \begin{bmatrix} d\varepsilon_v^e \\ d\varepsilon_s^e \end{bmatrix} \tag{4.62}$$

Where K^* and G^* are used to distinguish the bulk modulus and shear modulus for anisotropic materials, $d\varepsilon_v^e$ is the elastic volumetric strain increment, $d\varepsilon_s^e$ is the elastic shear strain increment, J is a parameter that reflects the cross-dependency of shear strain on mean effective stress as well as volumetric strain on deviatoric stress.

When subjected to conventional triaxial test, we have $\sigma'_{22} = \sigma'_{33}$ and $\varepsilon_{22} = \varepsilon_{33}$, so we can get these basic equations:

$$\begin{cases} dp' = \dfrac{d\sigma'_{11} + 2d\sigma'_{33}}{3} \\ dq = d\sigma'_{11} - d\sigma'_{33} \\ d\varepsilon_s^e = \dfrac{2}{3}(d\varepsilon_{11} - d\varepsilon_{33}) \\ d\varepsilon_v^e = d\varepsilon_{11} + 2d\varepsilon_{33} \end{cases} \tag{4.63}$$

As for the standard form of the elastic stiffness matrix, we can simplify it by multiplying the second and third columns by α_* to give this basic form:

$$\begin{pmatrix} d\sigma'_{11} \\ d\sigma'_{22} \\ d\sigma'_{33} \end{pmatrix} = \begin{pmatrix} A^* & \alpha_* B^* & \alpha B^* \\ \alpha_* B^* & \alpha_*^2 A^* & \alpha_*^2 B^* \\ \alpha_* B^* & \alpha_*^2 B^* & \alpha_*^2 A^* \end{pmatrix} \begin{pmatrix} d\varepsilon_{11} \\ d\varepsilon_{22} \\ d\varepsilon_{33} \end{pmatrix} \tag{4.64}$$

With the derivation using the basic equations, the stiffness coefficients consisting of A^*, B^* and α_* are given by:

$$\begin{cases} K^* = [A^* + 4\alpha_* B^* + 2\alpha_*^2 (A^* + B^*)]/9 \\ G^* = [A^* - 2\alpha_* B^* + \alpha_*^2 (A^* + B^*)/2]/3 \\ J = [A^* + \alpha_* B^* - \alpha_*^2 (A^* + B^*)]/3 \end{cases} \tag{4.65}$$

Therefore, according to Equation 4.60 combined with the above equation, we can calculate the stiffness coefficients:

$$\begin{cases} K^* = \dfrac{E^*}{9(1+v^*)(1-2v^*)}(1-v^* + 4\alpha_* + 2\alpha_*^2) \\ G^* = \dfrac{E^*}{6(1+v^*)(1-2v^*)}(2-2v^* - 4\alpha_* v^* + \alpha_*^2) \\ J = \dfrac{E^*}{3(1+v^*)(1-2v^*)}(1-v^* + \alpha_* v^* - \alpha_*^2) \end{cases} \tag{4.66}$$

When stress applied in hydrostatic loading path, only volume change occurs without shearing, which implies $dq = 0$, so we can get:

$$J d\varepsilon_v^e + 3G^* d\varepsilon_s^e = 0 \tag{4.67}$$

After transforming the above equation, we can obtain the additional parameter that controls the anisotropy in sediments through isotropic compression testing:

$$\frac{d\varepsilon_s^e}{d\varepsilon_v^e} = -\frac{J}{3G^*} = -\frac{2(1-v^* + \alpha_* v^* - \alpha_*^2)}{3(2-2v^* - 4\alpha_* v^* + \alpha_*^2)} \tag{4.68}$$

In the case of the undrained test, $d\varepsilon_v^e = 0$, that means in p-q plane, the stress path is no longer vertical, with dependent on α_*:

$$\frac{dq}{dp'} = \frac{3G^*}{J} = \frac{3(2-2v^* - 4\alpha_* v^* + \alpha_*^2)}{2(1-v^* + \alpha_* v^* - \alpha_*^2)} \tag{4.69}$$

For the anisotropic Poisson's ratio v^*, it was quantified similarly to the isotropic parameter v, we can assume this value to be the constant:

$$v^* = \frac{B^*}{A^* + B^*} = v \tag{4.70}$$

Considering the stiffness coefficient varying with the stress variation, it is required to reflect the correlation between the stress increment and modified Young's modulus. By applying the

compression modulus, which measures the compressibility of the material in the one-dimensional compression test, it is limited that no lateral deformation occurs, that is, the lateral strain is 0 ($\varepsilon_{22} = \varepsilon_{33} = 0$, $\Upsilon_{ij} = 0$). Substituting it into Equation 4.59, the relationship between the axial strain and the mean effective stress can be obtained as follows:

$$\frac{dp^{'}}{d\varepsilon_{11}} = \frac{E^{*}(1-v+2v\alpha_{*})}{3(1+v)(1-2v)} \tag{4.71}$$

In case of GHBS, if we assume it to be the isotropic material while only subjected to the axial compression, we have:

$$\frac{dp^{'}}{d\varepsilon_{11}} = K_{hs}^{'} \tag{4.72}$$

Combined with the above equations, the formula for the stiffness coefficient depending on stress is derived:

$$\begin{cases} \dfrac{dp^{'}}{d\varepsilon_{11}} = \dfrac{E^{*}(1-v+2v\alpha_{*})}{3(1+v)(1-2v)} = (1+\xi S_{h})\,p^{'}\dfrac{1+e}{\kappa} \\ E^{*} = \dfrac{3(1+v)(1-2v)(1+\xi S_{h})(1+e)\,p^{'}}{\kappa(1-v+2v\alpha_{*})} \end{cases} \tag{4.73}$$

After substituting anisotropic Young's modulus into Equation 4.60, the elastic stress-strain relationship is modified to:

$$\begin{pmatrix} \sigma_{11}^{'} \\ \sigma_{22}^{'} \\ \sigma_{33}^{'} \\ \sigma_{23}^{'} \\ \sigma_{31}^{'} \\ \sigma_{12}^{'} \end{pmatrix} = \frac{3(1+\xi S_{h})(1+e)\,p^{'}}{\kappa(1+v-2v\alpha_{*})} \begin{pmatrix} 1-v & \alpha_{*}v & \alpha_{*}v & 0 & 0 & 0 \\ \alpha_{*}v & \alpha_{*}^{2}(1-v) & \alpha_{*}^{2}v & 0 & 0 & 0 \\ \alpha_{*}v & \alpha_{*}^{2}v & \alpha_{*}^{2}(1-v) & 0 & 0 & 0 \\ 0 & 0 & 0 & \dfrac{\alpha_{*}^{2}(1-2v)}{2} & 0 & 0 \\ 0 & 0 & 0 & 0 & \dfrac{\alpha_{*}(1-2v)}{2} & 0 \\ 0 & 0 & 0 & 0 & 0 & \dfrac{\alpha_{*}(1-2v)}{2} \end{pmatrix} \begin{pmatrix} \varepsilon_{11} \\ \varepsilon_{22} \\ \varepsilon_{33} \\ \varepsilon_{23} \\ \varepsilon_{31} \\ \varepsilon_{12} \end{pmatrix} \tag{4.74}$$

It is noted that if $\alpha_{*} = 1$, this elastic behavior is suitable for the isotropic material.

4.3.4 Flow rule and consistency function

The flow rule is pivotal for determining the direction and rate of plastic deformation. In this study, we adopted the associated flow rule, which posits that the plastic potential function is identical to the yield function. Consequently, the direction of the plastic strain increment is aligned with the normal to the yield surface, and the incremental form can be expressed as follows:

$$d\varepsilon_{kl}^{p} = \Lambda \frac{\partial g}{\partial \sigma_{ij}^{'}} = \Lambda \frac{\partial f}{\partial \sigma_{ij}^{'}} \tag{4.75}$$

The yield function includes effective parameters such as p', q, σ', p_c, p_d, R, so the consistency equation can be written as:

$$df = \frac{\partial f}{\partial \sigma_{ij}^{'}} d\sigma_{ij}^{'} + \frac{\partial f}{\partial p_c} dp_c + \frac{\partial f}{\partial p_d} dp_d + \frac{\partial f}{\partial R} dR \tag{4.76}$$

Where:

$$\frac{\partial f}{\partial \sigma_{ij}^{'}} d\sigma_{ij}^{'} = \frac{\partial f}{\partial p^{'}} \frac{\partial p^{'}}{\partial \sigma_{ij}^{'}} d\sigma_{ij}^{'} + \frac{\partial f}{\partial q} \frac{\partial q}{\partial \sigma_{ij}^{'}} d\sigma_{ij}^{'} \tag{4.77}$$

$$\begin{cases} \dfrac{\partial q}{\partial \sigma_{ij}^{'}} = \dfrac{3}{2} \dfrac{s_{ij}}{q} \\ \dfrac{\partial p^{'}}{\partial \sigma_{ij}^{'}} = \dfrac{1}{3} \delta_{ij} \end{cases} \tag{4.78}$$

By computing the differentials in the formula, we derive the results as follows:

$$\frac{\partial f}{\partial p^{'}} = 9\gamma \left[(n(p^{'})^{n-1} (R(p_c + p_d))^{2-n} - 2p^{'}) \right] \tag{4.79}$$

$$\frac{\partial f}{\partial q} = \frac{2a}{M^2} q \tag{4.80}$$

$$\frac{\partial f}{\partial \sigma_{ij}^{'}} = \left(\frac{3as_{ij}}{M^2} + 3\gamma \left[(n(p)^{n-1} (R(p_c + p_d))^{2-n} - 2p^{'}) \right] \delta_{ij} \right) d\sigma_{ij}^{'} \tag{4.81}$$

$$\frac{\partial f}{\partial p_c} = 9(2-n)\gamma (p^{'})^{n} R^{2-n} (p_c + p_d)^{1-n} \tag{4.82}$$

$$\frac{\partial f}{\partial p_d} = 9(2-n)\gamma (p^{'})^{n} R^{2-n} (p_c + p_d)^{1-n} \tag{4.83}$$

$$\frac{\partial f}{\partial R} = 9(2-n)\gamma (p^{'})^{n} R^{1-n} (p_c + p_d)^{2-n} \tag{4.84}$$

Substituting Equations 4.77-4.84, 4.38, 4.42 4.43, 4.74 and 4.75 into Equation 4.76 yields the expression for the plastic multiplier:

$$\Lambda = -\frac{(\frac{\partial f}{\partial p'}\frac{\partial p'}{\partial \sigma_{ij}'}+\frac{\partial f}{\partial q}\frac{\partial q}{\partial \sigma_{ij}'})d\sigma_{ij}+\alpha\beta\chi^{\beta}(S_h)^{\beta-1}\frac{\partial f}{\partial p_d}dS_h}{\alpha\beta\mu(\chi S_h)^{\beta}\frac{\partial f}{\partial p_d}\frac{\partial g}{\partial q}+\eta InR\frac{\partial f}{\partial R}\left|\frac{\partial g}{\partial \sigma_{ij}'}\right|-p_c\frac{V}{\lambda-\kappa}\frac{\partial f}{\partial p_c}\frac{\partial g}{\partial p'}} \tag{4.85}$$

According to the elastic assumption:

$$\begin{cases} d\varepsilon_{kl} = d\varepsilon_{kl}^{e} + d\varepsilon_{kl}^{p} \\ d\sigma_{ij}' = C_{ijkl}^{e} d\varepsilon_{kl}^{e} \end{cases} \tag{4.86}$$

The elastic matrix is given by:

$$C_{ijkl}^{e} = \frac{3(1+\xi S_h)(1+e)p'}{\kappa(1+\nu-2\nu\alpha_*)}\begin{pmatrix} 1-\nu & \alpha_*\nu & \alpha_*\nu & 0 & 0 & 0 \\ \alpha_*\nu & \alpha_*^2(1-\nu) & \alpha_*^2\nu & 0 & 0 & 0 \\ \alpha_*\nu & \alpha_*^2\nu & \alpha_*^2(1-\nu) & 0 & 0 & 0 \\ 0 & 0 & 0 & \frac{\alpha_*^2(1-2\nu)}{2} & 0 & 0 \\ 0 & 0 & 0 & 0 & \frac{\alpha_*(1-2\nu)}{2} & 0 \\ 0 & 0 & 0 & 0 & 0 & \frac{\alpha_*(1-2\nu)}{2} \end{pmatrix} \tag{4.87}$$

Integrating the plastic flow rule and the previously stated assumptions about elasticity into the consistency equation results in the determination of the plastic multiplier as follows:

$$\Lambda = -\frac{(\frac{\partial f}{\partial p'}\frac{\partial p'}{\partial \sigma_{ij}'}+\frac{\partial f}{\partial q}\frac{\partial q}{\partial \sigma_{ij}'})C_{ijkl}^{e}d\varepsilon_{kl}+\alpha\beta\chi^{\beta}(S_h)^{\beta-1}\frac{\partial f}{\partial p_d}dS_h}{H+\frac{\partial f}{\partial \sigma_{ij}'}C_{ijkl}^{e}(\frac{\partial g}{\partial \sigma_{ij}'})^{T}} \tag{4.88}$$

The expression for hardening parameter *H* is defined as:

$$H = p_c\frac{V}{\lambda-\kappa}\frac{\partial f}{\partial p_c}\frac{\partial g}{\partial p'}-\alpha\beta\mu(\chi S_h)^{\beta}\frac{\partial f}{\partial p_d}\frac{\partial f}{\partial q}-\eta InR\frac{\partial f}{\partial R}\left|\frac{\partial g}{\partial \sigma_{ij}'}\right| \tag{4.89}$$

Further, after shifting Equation 4.86, it can be obtained by:

$$d\sigma_{ij}' = C_{ijkl}^{e}d\varepsilon_{kl} - C_{ijkl}^{e}\Lambda\frac{\partial g}{\partial \sigma_{ij}'} \tag{4.90}$$

Substitute the plastic multiplier into the above formula (Klar et al., 2010):

$$d\sigma_{ij}' = C_{ijkl}^{ep}d\varepsilon_{kl} + C_{ijkl}^{S_h}dS_h \tag{4.91}$$

Where the elastoplastic matrix C_{ijkl}^{ep} is calculated by:

$$C_{ijkl}^{ep}=\frac{\frac{\partial g}{\partial q}\mu\alpha\beta(\chi S_h)^{\beta}\frac{\partial f}{\partial p_d}+\eta InR\frac{\partial f}{\partial R}\left|\frac{\partial g}{\partial \sigma_{ij}^{'}}\right|-p_c\frac{V}{\lambda-\kappa}\frac{\partial f}{\partial p_c}\frac{\partial g}{\partial p'}}{\frac{\partial g}{\partial q}\mu\alpha\beta(\chi S_h)^{\beta}\frac{\partial f}{\partial p_d}+\eta InR\frac{\partial f}{\partial R}\left|\frac{\partial g}{\partial \sigma_{ij}^{'}}\right|-p_c\frac{V}{\lambda-\kappa}\frac{\partial f}{\partial p_c}\frac{\partial g}{\partial p'}+\frac{\partial f}{\partial \sigma_{ij}^{'}}C_{ijkl}^{e}\left(\frac{\partial g}{\partial \sigma_{ij}^{'}}\right)^{T}}C_{ijkl}^{e} \tag{4.92}$$

The improvement of stiffness by hydrates is expressed in terms of a matrix containing hydrate saturation, which can be written as:

$$C_{ijkl}^{S_h}=-\frac{\frac{\partial g}{\partial \sigma_{ij}^{'}}C_{ijkl}^{e}\alpha\beta(\chi S_h)^{\beta}\frac{\partial f}{\partial p_d}/S_h}{\frac{\partial g}{\partial q}\mu\alpha\beta(\chi S_h)^{\beta}\frac{\partial f}{\partial p_d}+\eta InR\frac{\partial f}{\partial R}\left|\frac{\partial g}{\partial \sigma_{ij}^{'}}\right|-p_c\frac{V}{\lambda-\kappa}\frac{\partial f}{\partial p_c}\frac{\partial g}{\partial p'}+\frac{\partial f}{\partial \sigma_{ij}^{'}}C_{ijkl}^{e}\left(\frac{\partial g}{\partial \sigma_{ij}^{'}}\right)^{T}} \tag{4.93}$$

As mentioned in Section 2.1, the thermal properties of GHBS are crucial, particularly during the extraction of hydrates from sedimentary reservoirs. The decomposition and recrystallization of hydrates involve temperature changes that can induce thermal expansion or contraction of the material, leading to changes in stress. Thus, it is essential to consider thermal expansion effects in the constitutive model.

Due to the anisotropic expansion in various directions, according to the law of thermal expansion, the volumetric strain of material is directly proportional to the temperature variation. The proportionality constant is the coefficient of thermal expansion:

$$\begin{cases}\dfrac{\Delta V}{V_0}=\varepsilon_v=\beta_T\Delta T\\ \beta_T=\dfrac{2\alpha_*^2+1}{3}\beta_{ist}\end{cases} \tag{4.94}$$

Where V_0 is the initial volume, ΔV is the volume change, ε_v is the volumetric strain, ΔT is the temperature variation, β_T is the thermal expansion coefficient, the subscript *ist* represents the isotropic.

Observations indicate that sediments with higher porosity exhibit a weaker response to temperature fluctuations. Accordingly, we have integrated the temperature dependency of the material into the model, which is encapsulated by the following equation:

$$\begin{cases}\dfrac{\partial \sigma_{ij}^{'}}{\partial T}dT=\beta_T K_{hs}^{'}\delta_{ij}dT=C_{ijkl}^{ep}(1+\xi S_h)\beta_T\dfrac{\delta_{ij}}{3}dT\\ \beta_T=\dfrac{2\alpha_*^2+1}{3}((1-\phi)\beta_s+\beta_h\phi S_h+\phi(1-S_h)\beta_f)\end{cases} \tag{4.95}$$

Where ϕ is the porosity, C_{ijkl}^{ep} is the elastoplastic matrix, T is the temperature, the subscript *s*, *h*, and *f* represent the soil, hydrate and fluid, respectively.

In summary, the elastic-plastic constitutive model considering the shape of yield surface and thermodynamic effects can be expressed as:

$$d\sigma_{ij}^{'} = C_{ijkl}^{ep} d\varepsilon_{kl} + C_{ijkl}^{S_h} dS_h + \frac{\partial \sigma_{ij}^{'}}{\partial T} dT \tag{4.96}$$

4.3.5 Model parameters

The proposed constitutive model involves 19 model parameters, where 12 parameters are related to the mechanical properties of host sediments, and 7 parameters correspond to the hydrates. Parameters related to host sediments include: 6 conventional parameters from soil mechanics e, κ, λ, p_c, v, and M; 3 shape-dependent parameters from HISS yield surface: a, n, and γ; 2 parameters associated with the subloading surface: R and η; 1 parameter control the cross-anisotropy in elastic phase: α_*. Parameters describing the contribution by hydrates include: S_h, α, β, χ, μ, p_d, and ξ. Table 4.3 represents the meaning of corresponding model parameters.

Table 4.3: Detailed explanation for the model parameters

Parameter	Meaning
κ	The slope of swelling line in *e-Inp* space
λ	The slope of compression line in *e-Inp* space
e	The ratio between pore volume and sediment volume (Initial value e_0)
p_c	Preconsolidation stress (Initial value p_{c0})
M	Critical stress ratio
v	Poisson's ratio
a, γ	Shape parameters that control the size of yield surface
n	Shape parameter that affects the location of the critical point of shear expansion and shear contraction
R	Subloading surface ratio (Initial value R_0)
η	Parameter that controls the plastic deformations that may occur inside initial yield surface
α_*	Anisotropy factor

S_h	Hydrate saturation (Initial value S_{h0})
α, β	Parameters depending on the type of pore habit and hydrate concentration
χ	Degradation factor (Initial value χ_0)
μ	Parameter that reflects dissociation rate of hydrates
p_d	Hardening parameter that describes the strength enhancement contributed by hydrates
ξ	Parameter that reflects the stiffness enhancement provided by hydrates

The determination of e, κ, λ, p_c, v and M:

e is defined as the ratio between pore volume and sediment volume, which can be measured through a standard consolidation test. κ can be obtained through the unloading curve (rebound curve) produced by the host sediments under consolidated test. λ can be determined through the loading curve (compression curve) during consolidation. p_c is determined with the variation in plastic volumetric strain. The value of M equals the generalized stress ratio when $d\varepsilon_v = 0$. v can be calculated through the ratio between coefficient of lateral pressure and coefficient of earth pressure K_0 (Equation 4.97).

$$v = \frac{K_0}{1 + K_0} \tag{4.97}$$

The determination of a, n, γ, R, η and α_*:

a, n, and γ can be modified to adapt various host sediments. R is determined by the variation in plastic strain. The value of η can be determined by the degree of curvature of the normal compression curve in compression test. α_* can be determined through isotropic compression (dq = 0) or undrain triaxial testing ($d\varepsilon_v^e$ = 0).

The determination of S_h, α, β, χ, μ, p_d, and ξ:

S_h is defined as the ratio of hydrate volume to the total pore volume, which can be measured through pressure drop method. p_d is mainly determined by the hydrate concentration. α and β describe the influence of hydrate saturation and morphology on hardening parameter p_d, which can be measured according to the triaxial test results. χ and μ quantify the extent of hydrate dissociation during shearing, which are determined through the triaxial test. ξ is determined in terms of the variation in elastic-related parameters with respect to hydrate saturation, which can be calculated through the fitting correlation.

4.4 Numerical analysis

4.4.1 Program implementation

The developed elastoplastic model utilizes tensorial formulations and is further developed and scripted using Python within the Anaconda software, accommodating various loading paths including hydrostatic stress loading, triaxial stress loading, hydrostatic strain loading, and triaxial strain loading. Set the implementation of triaxial strain control as an example, which follows the procedural steps outlined in the flow chart (Fig. 4.13):

(1) Set n as the number of incremental steps, starting the iterative calculations at the first step. Initialize variables and constants, such as the initial elastic modulus and material parameters, and then compute the elastic matrix C^{e}_{ijkl}.

(2) Calculate the strain increment $d\varepsilon_{kl}$ based on predefined strain value and incremental step. The trial stress σ^{trial} is computed using the elastic relationship $d\sigma^{'}_{ij} = C^{e}_{ijkl} d\varepsilon_{kl}$, which yields the effective stress p' and deviatoric stress q. Determine initial hardening parameters p_c and p_d following established hardening rules.

(3) The new stress state and hardening parameters are input into the yield surface equation to assess if the trial stress is within or on the yield surface. Elastic loading occurs if $F(\sigma^{trial}) \leq 0$, otherwise, it exhibits elastoplastic loading that requires plastic adjustment when $F(\sigma^{trial}) > 0$.

(4) If loading is elastic, update the stress state directly where the elastoplastic matrix equals the elastic matrix. Proceed to the next incremental step.

(5) Determine whether the current plastic behavior transitions from elasticity or continues from previous plastic behavior by evaluating the yield function value of the preceding increment. If $F(\sigma^{n-1}) \leq 0$, the material was in an elastic state before the current increment; if $F(\sigma^{n-1}) > 0$, the increment continues the previous plastic behavior.

(6) If the current plastic behavior is a transition from elasticity, compute the elastic component of the strain increment for the current loading step, along with the remaining strain increment for elastoplastic loading. Set this remaining strain increment as the initial strain increment for the subsequent step; if the current increment continues the previous plastic behavior, proceed directly with this strain increment.

(7) To make the stress state always on the yield surface, we need to perform the elastoplastic correction, which involves the development of residual equations correcting the stress increment and equivalent plastic strain increment in accordance with the iterative Newton-Raphson method (Equation 4.98). Simultaneously, compute the plastic multiplier to update hardening parameters after multiple iterations.

(8) Resubstitute the updated stress state and hardening parameters into the yield function and compute the yield value. If $F\ (\sigma^{update}) \leq 10^{-6}$, the stress state is deemed sufficiently close to the yield surface, which satisfies the convergence criteria, and after that update the elastoplastic matrix. If $F\ (\sigma^{update}) > 10^{-6}$, further iterative adjustments are required until convergence is achieved.

(9) Finally, encapsulate stress state, strain, and hardening parameters for each loading step using history loading variables. Save the compiled data and generate visualization plots.

$$\begin{bmatrix} C^{-1} & 0 & r_n \\ 0 & -1 & h_n \\ F_{\sigma_{ij}}^{(k)} & F_{\bar{\varepsilon}^p}^{(k)} & 0 \end{bmatrix} \begin{bmatrix} \Delta\sigma_{ij}^{(k)} \\ \Delta\bar{\varepsilon}^{p(k)} \\ \delta\Lambda^{(k)} \end{bmatrix} = -\begin{bmatrix} a^{(k)} \\ b^{(k)} \\ F^{(k)} \end{bmatrix} \tag{4.98}$$

Where C is the stiffness matrix, $\delta\Lambda$ is the plastic multiplier increment in Newton-Raphson iteration, r and h are the flow direction and hardening parameter, respectively, $\bar{\varepsilon}^p$ is the equivalent plastic strain, a is the elastic predicted stress residual, b is the equivalent plastic strain increment residual, F is the yield function value, n represents the increment step, k represents the iteration number.

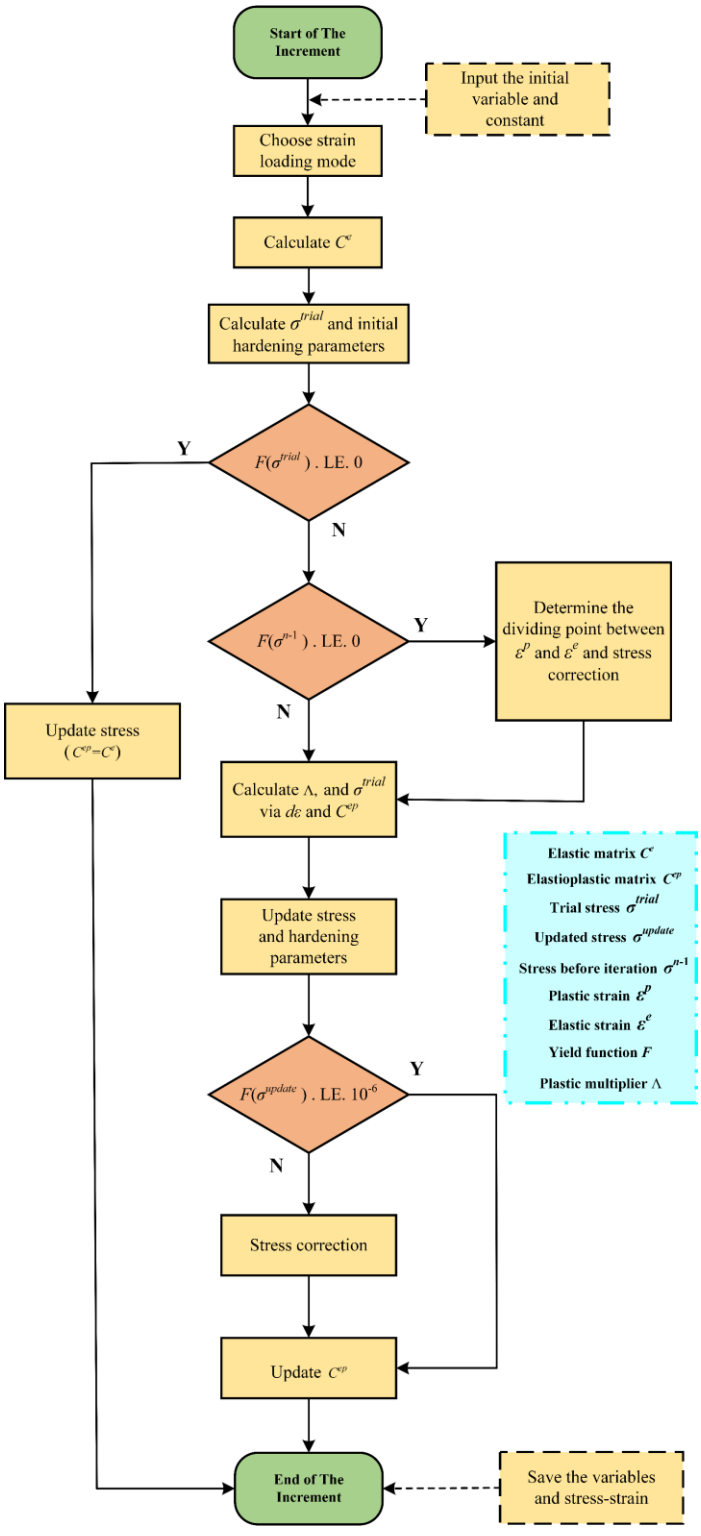

Figure 4.13: Procedures for the program implementation

4.4.2 Triaxial test using synthetic GHBS

To validate the accuracy of this model, this study employs the described numerical analysis procedure and compares the results with experimental data from various types of GHBS (In-situ natural GHBS and synthetic GHBS). The parameter settings for the simulations are detailed in Section 4.3.5.

Masui et al. (2005) synthesized Toyoura sand containing hydrates with different pore habits, where specimens prepared using the ice-seeding method primarily exhibited pore-filling features, while those prepared via the partial water saturation method were predominantly cementing. To replicate conditions of natural GHBS at depths below 800m in deep-sea environments, triaxial compression tests were conducted with a pore pressure of 8 MPa, a constant temperature of 278 K, and an initial effective confining pressure of 1 MPa. Experimental conditions are summarized in Table 4.4. The model parameters for simulation are listed in Table 4.5.

Table 4.4: Detailed experimental conditions (Masui et al. (2005))

Features	Type I	Type II	Type III
Host specimen type	Synthetic Toyoura sand (Pure)	Mixture of sand with ice	Mixture of sand with water
Pore habit	Hydrate free	Pore filling	Cementing
Temperature	278K		
Effective confining pressure	1MPa		
Hydrate saturation	0	40.9%	40.7%
Porosity	36.3% ~ 42.9%		
Test type	CD test		

Table 4.5: Numerical modelling parameters (Masui et al. (2005))

Parameters	Type I	Type II	Type III
κ	0.003	0.003	0.003
λ	0.18	0.18	0.18
e_0	0.587	0.587	0.587
p_c (MPa)	12	12	12

M	1.07	1.07	1.07
R_0	0.09	0.06	0.05
v	0.2	0.2	0.2
a	1	1	1
γ	-1/9	-1/9	-1/9
n	1	1	1
η	15	15	15
α_*	0.66	0.4	0.2
S_{h0}	0	0.409	0.407
α (MPa)	-	25	68
β	-	1.6	1.6
χ_0	1	1	1
μ	-	1.5	5.5
ξ	-	2.28	6.69

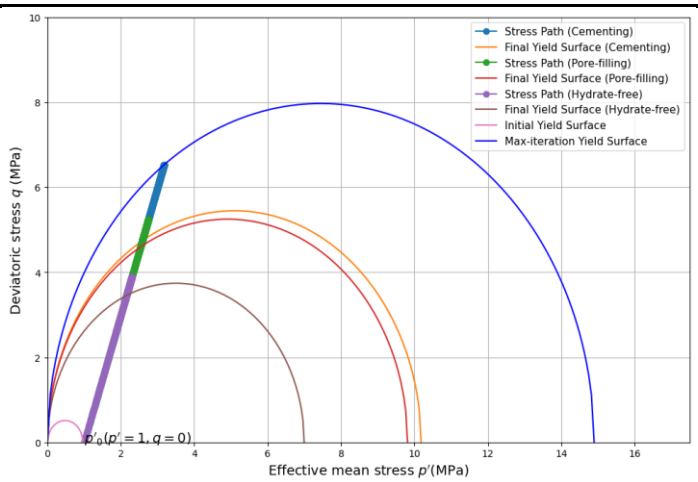

Figure 4.14: Simulations for the stress paths and yield surfaces with various hydrate morphologies

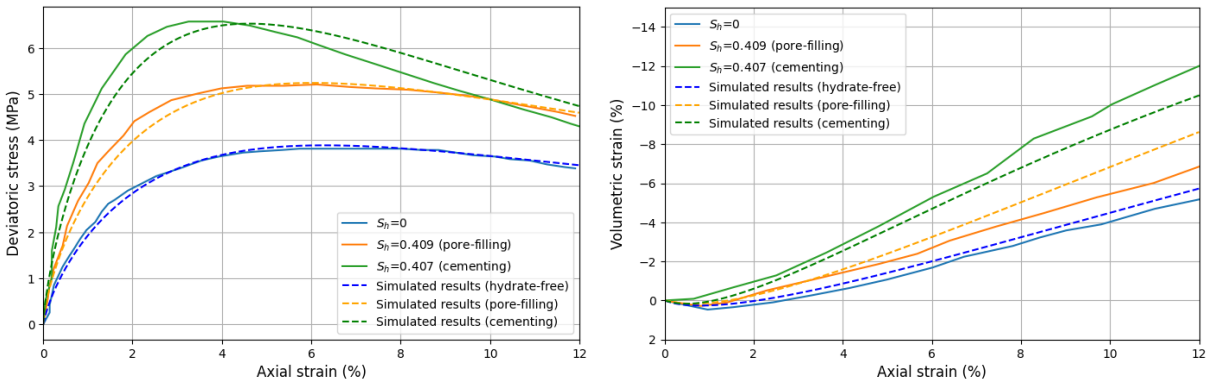

(a) Stress-strain curve (b) Volume change curve

Figure 4.15: Numerical modeling for the mechanical response of GHBS through the comparison between experimental results obtained from Masui et al. (2005)

Fig. 4.14 shows the changes in stress paths and yield surfaces concerning different hydrate morphologies. Fig. 4.15 illustrates a comparison between the experimental results and the simulation outcomes for specimens with varying hydrate occurrences. The model successfully predicts the stress-strain responses of the sediments, with consistent trends across the curves. For HFS and GHBS in pore-filling morphology, the stress-strain curves show hardening behavior, while GHBS in cementing morphology displays a strain-softening characteristic. The numerical simulations reveal a more pronounced hardening effect than the experimental results. Additionally, the volume strain follows a similar trend: at lower axial strain, the specimen undergoes volume compaction, whereas at higher axial strain, it tends to expand. Numerical predictions show greater volumetric expansion in hydrate-free and pore-filling forms, with those in cementing exhibiting less dilatancy. The shape coefficient of S1 yield surface was utilized in this simulation, which can be regarded as MCCM incorporating the cementing effect of hydrates. Under the specific situation, the model demonstrated good predictive performance.

Hyodo et al. (2013b) synthesized methane hydrate-bearing sand in the laboratory using Toyoura sand as the host material, employing cooling and pressurization methods to achieve porosities ranging from 40% to 45%. Subsequently, to mimic real-world conditions, the synthesized HBS were subjected to triaxial shear drainage tests. During the test, the confining pressure was maintained at 5 MPa, the temperature was controlled at 5°C, and the shear rate was set at 0.1%/min. The hydrate saturation of each specimen exhibited evident variation. Specific test

conditions are documented in Table 4.6, while the parameters used for simulation are detailed in Table 4.7.

Table 4.6: Detailed experimental conditions (Hyodo et al. (2013b))

Features	sI	sII	sIII	sIV
Specimen type	Synthetic Toyoura sand (Pure)	Synthetic methane hydrate-bearing sand		
Pore pressure	10MPa			
Temperature	5℃			
Effective confining pressure	5MPa			
Hydrate saturation	0	24.2%	35.1%	53.1%
Porosity	39% ~ 45.7%			
Test type	CD test			

Table 4.7: Numerical modelling parameters (Hyodo et al. (2013b))

Parameters	sI	sII	sIII	sIV
κ	0.004	0.004	0.004	0.004
λ	0.18	0.18	0.18	0.18
e_0	0.65	0.656	0.645	0.67
p_c (MPa)	10	10	10	10
M	1.15	1.15	1.15	1.15
R_0	0.5	0.38	0.32	0.23
ν	0.2	0.2	0.2	0.2
a	0.9	0.9	0.9	0.9
γ	-0.13	-0.13	-0.13	-0.13
n	0.95	0.95	0.95	0.95
η	65	65	65	65
α_*	2	1.5	1.5	2
S_{h0}	0	0.242	0.351	0.531
α (MPa)	-	31	31	31

β	-	1.6	1.6	1.6
χ_0	1	1	1	1
μ	-	1	1	1
ξ	-	2.66	2.66	2.66

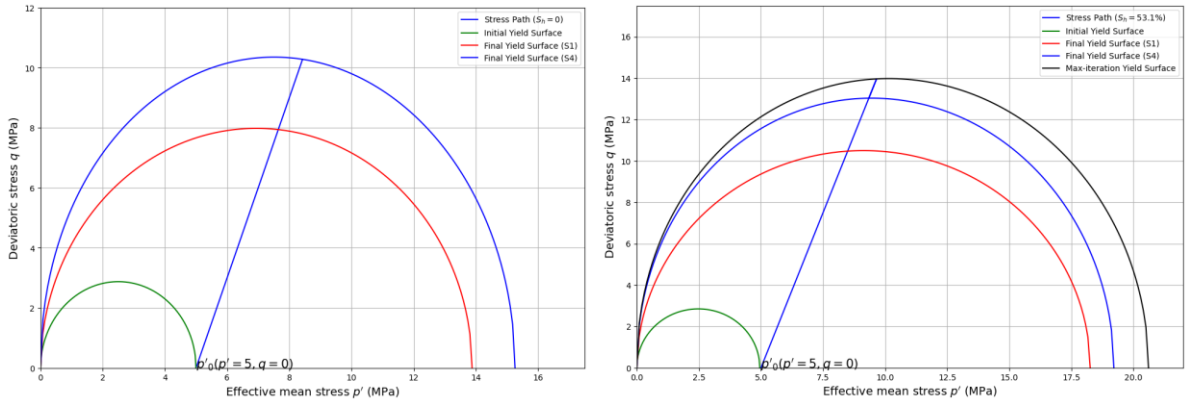

(a) $S_h = 0$ (b) $S_h = 0.531$

Figure 4.16: Visualization of predicted yield surface with stress path in *p-q* space (S1 and S4 model)

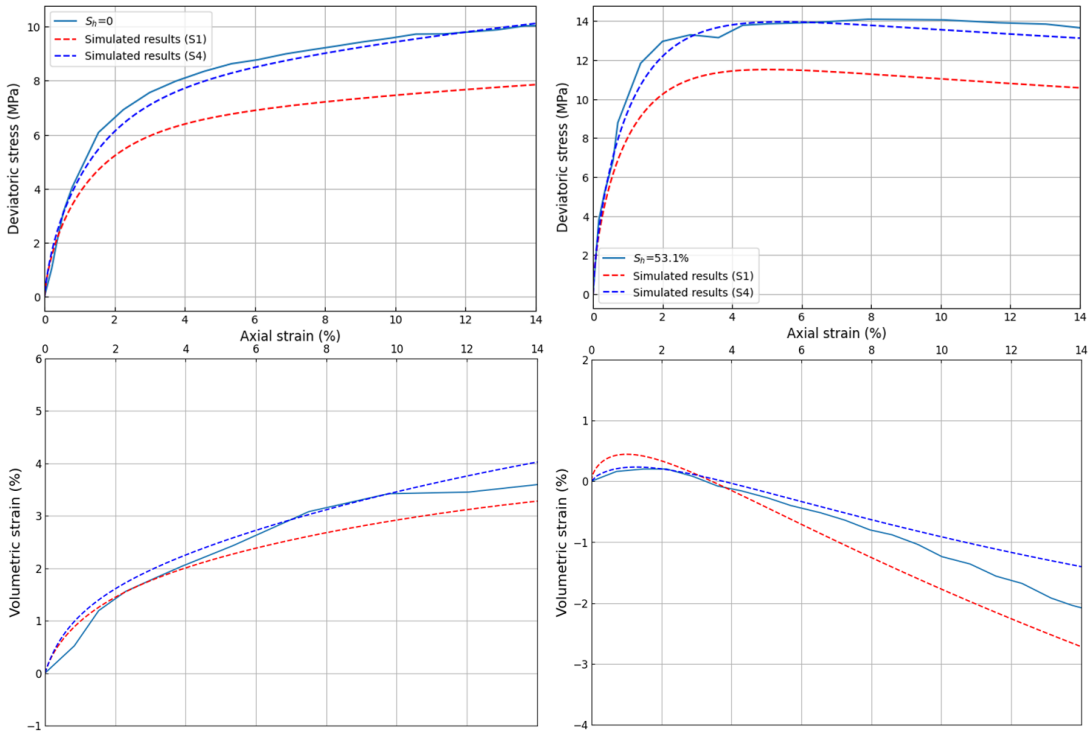

(a) $S_h = 0$ (b) $S_h = 0.531$

Figure 4.17: Comparative analysis of stress-strain and volumetric behavior of GHBS using S1 and S4 model

To make sure the applicability of different models, it is imperative to visualize the mechanical properties of GHBS under varying yield surfaces and S_h through simulation. The yield surface shape factors were tailored for the S1 and S4 yield surfaces, as depicted by the stress paths on the *p*-*q* plane in Fig. 4.16 and corresponding stress-strain characteristics shown in Fig. 4.17. When S_h = 0, due to the impact of subloading surface ratio, the material immediately enters the elastoplastic phase, and the stress path gradually approaches and intersects with the final yield surface. Both numerical results for S1 and S4 models exhibit hardening behavior, with the S4 model predicting a broader yield surface that can better reflect structural effects and dilatancy features, aligning more closely with experimental observations. Conversely, premature failure occurs in the result using S1 model at lower deviatoric stress, exhibiting significantly reduced stiffness and strength compared to those using S4 model. When S_h = 0.531, the presence of NGH markedly influences the sediment's mechanical behavior, leading to a regressive stage for stress paths characterized by strain softening. The final yield surfaces predicted by S1 and S4 models show a marked increase in size compared to the case with S_h = 0, with the S4 model again demonstrating a wider yield range and more accurately capturing the increase in stiffness and the contribution of bond breakage due to hydrates, aligning better with experimental data. Therefore, in subsequent numerical calculations, the S4 model exhibiting superior performance is selected for analysis.

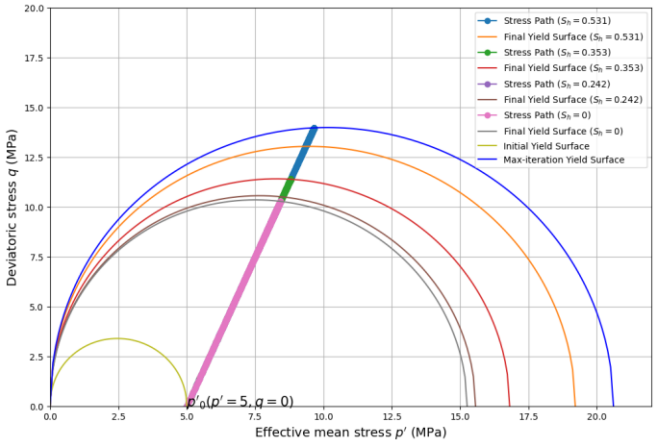

Figure 4.18: Simulations for the stress paths and yield surfaces under various S_h

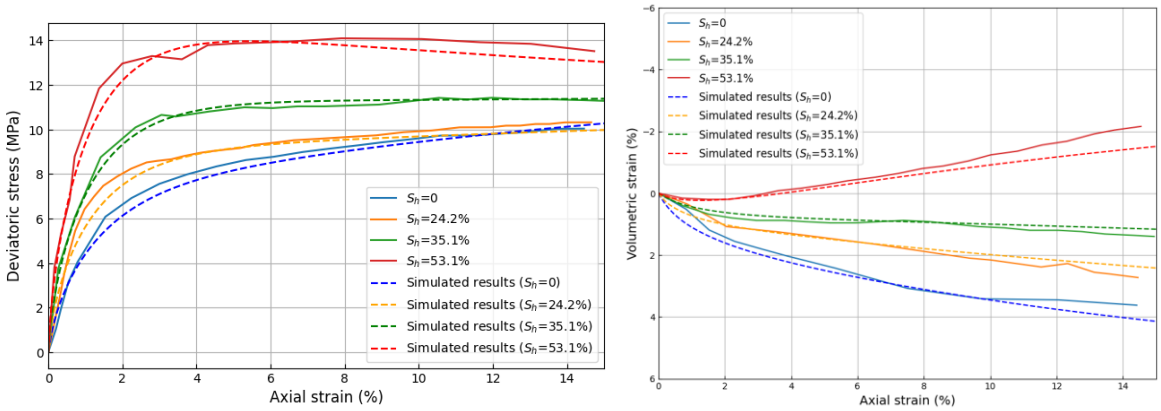

(a) Stress-strain curve (b) Volume change curve

Figure 4.19: Numerical modeling for the mechanical response of GHBS through the comparison between experimental results obtained from Hyodo et al. (2013b)

Fig. 4.18 presents the variation in stress paths and yield surfaces under various S_h. Fig. 4.19 compares numerical results with experimental data, demonstrating that adjusting the shape coefficient of the HISS yield surface can accurately simulate the stress-strain relationship and volumetric changes of synthetic GHBS under triaxial drained conditions. The stress-strain curves show pronounced hardening behavior, aligning closely with experimental outcomes across various saturation levels. However, it is important to note that when S_h is above 50%, the model predicts a noticeable softening in the stress-strain curve prior to specimen failure. Additionally, the model exhibits excellent in predicting the volumetric changes of the specimens; It is clear that the specimens experience compression for the first three groups with lower S_h, and when S_h = 53.1%, the model can accurately capture the dilatancy observed when axial strain exceeds 4%.

4.4.3 Triaxial test using natural GHBS

In addition to experiments with artificially synthesized HBS using Toyoura sand, Masui et al. (2008) conducted a series of triaxial drained tests on natural HBS specimens obtained in-situ from the Nankai Trough. This study applied the proposed elastoplastic constitutive model to simulate and predict the stress-strain behavior observed in these tests. During the experiments, sediments experienced an initial hydrostatic stress of 1 MPa and a pre-consolidation stress of 3.6 MPa, with porosity ranging from 44% to 50%. The temperature was maintained constant throughout the experiment, with the loading process controlled by axial strain. Detailed experimental conditions are presented in Table 4.8, while the simulated parameters are documented in Table 4.9.

Table 4.8: Detailed experimental conditions (Masui et al. (2008))

Features	Type I	Type II	Type III
Host specimen type	Natural core specimens drilled from eastern Nankai Trough (Sandy sediments)		
Pore pressure	9MPa		
Temperature	5℃		
Effective confining pressure	1MPa		
Hydrate saturation	7.7%	22.5%	37.6%
Porosity	50.8%	49%	44.2%
Test type	CD test		

Table 4.9: Numerical modelling parameters (Masui et al. (2008))

Parameters	Type I	Type II	Type III
κ	0.008	0.008	0.008
λ	0.15	0.15	0.15
e_0	1.033	0.9608	0.791
p_c (MPa)	3.6	3.6	3.6
M	1.37	1.37	1.37
R_0	0.22	0.165	0.08
ν	0.2	0.2	0.2
a	0.9	0.9	0.9
γ	-0.13	-0.13	-0.13
n	0.95	0.95	0.95
η	30	30	30
α_*	5.7	3.2	2.5
S_{h0}	0.077	0.225	0.376
α (MPa)	10	10	21
β	1	1	1
χ_0	1	1	1

μ	8.5	8.5	8.5
ξ	6.32	6.32	6.32

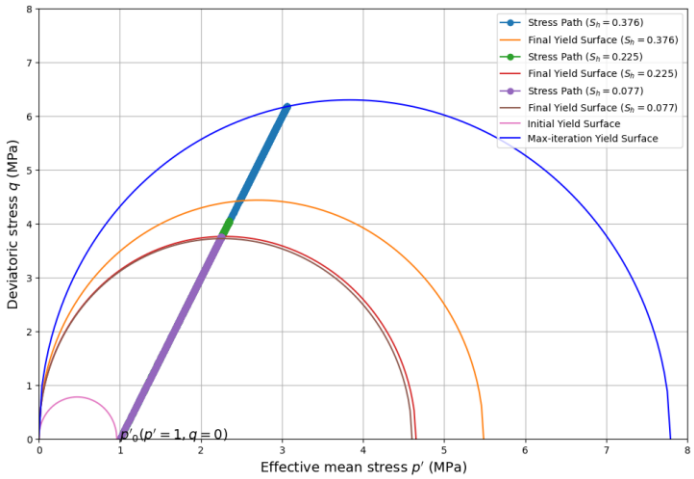

Figure 4.20: Simulations for the stress paths and yield surfaces in natural GHBS

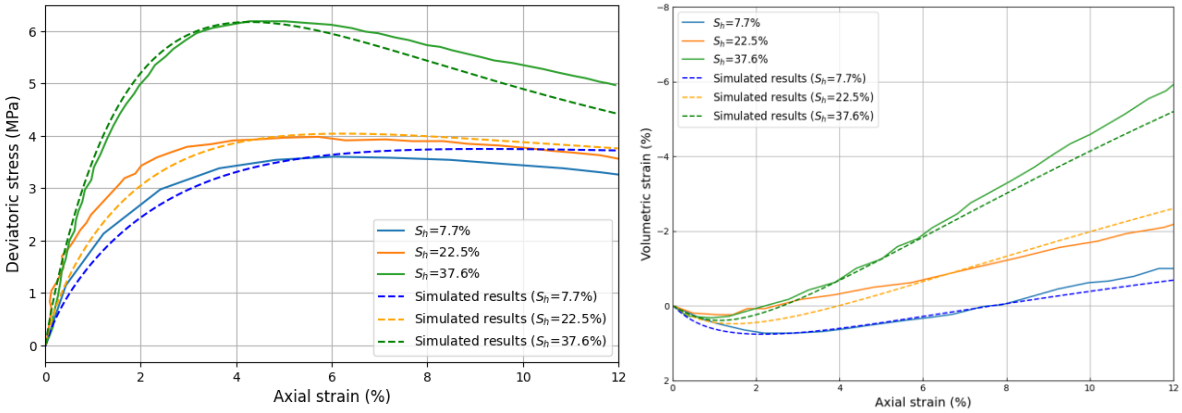

(a) Stress-strain curve (b) Volume change curve

Figure 4.21: Numerical modeling for the mechanical response of GHBS through the comparison between experimental results obtained from Masui et al. (2008)

Fig. 4.20 reflects the development in stress paths and yield surfaces under various S_h. Fig. 4.21 displays the model predictions alongside experimental results for in-situ sandy HBS subjected to triaxial shear tests. It shows a high level of agreement between the modeled and real stress-strain and volumetric behavior. As S_h increases, the stress-strain curves progressively exhibit marked strain-softening phenomena. In the first two sets of test groups with lower S_h, the predictions closely match the experimental results; however, when S_h = 37.6%, the model predicts a lower

softening rate after peak stress compared to the experimental findings. Concerning the volumetric strain, when S_h = 22.5%, the model anticipates a greater amount of compression than observed in the experiments; while S_h = 37.6%, the magnitude of predicted expansion is smaller than those seen in the experimental results.

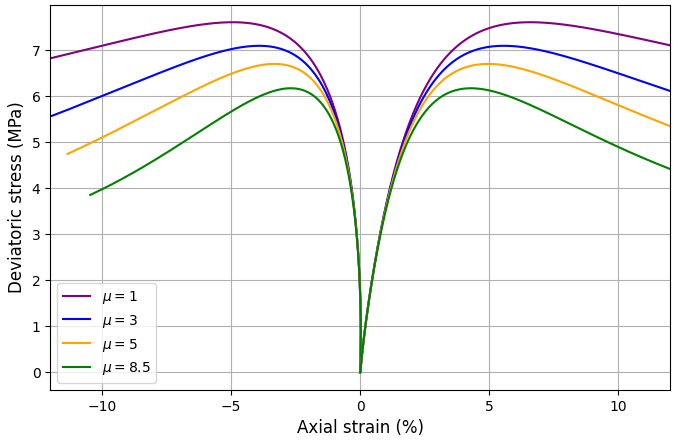

Figure 4.22: The impact of parameter μ on stress responses

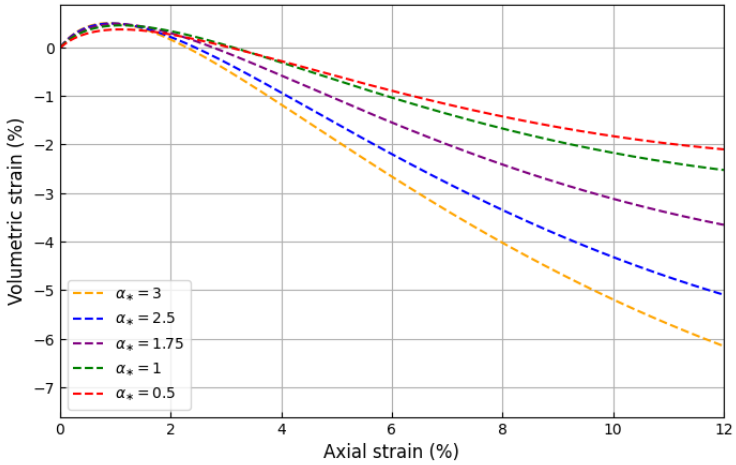

Figure 4.23: The impact of parameter α_* on volume change

Based on experimental data from Masui et al. (2008), we have validated our model through simulations, achieving satisfactory predictive accuracy. To further verify the effectiveness of the model parameters, considering the representativeness of the specimens, natural GHBS with S_h = 0.376. We aimed at maintaining consistency in other parameters, focusing adjustments only on degradation rate parameter μ and anisotropy factor α_*. Fig. 4.22 illustrates the impact of parameter

μ on the stress-strain relationship; a lower μ value implies slower degradation of the hydrate structure, which enables the deviatoric stress to be sustained longer. Consequently, the stress-strain curve reaches a higher peak, suggesting that the material can maintain its load-bearing capacity at a larger axial strain. Conversely, a higher μ value accelerates bonding degradation, leading to a smaller stress peak and faster transition to post-peak softening, displaying a more brittle response. Thus, parameter μ plays a crucial role in predicting the degree of strain softening in GHBS. Fig. 4.23 explores the impact of α_* on volume change. α_* controls the degree of material anisotropy, affecting its deformation behavior upon loading. A higher α_* value results in significant volumetric expansion under axial strain, which indicates that shear-induced expansion dominates in highly anisotropic materials. In contrast, a lower α_* value results in slight volumetric strain, highlighting the typical compaction response of isotropic or weakly anisotropic materials. Thus, α_* has a decisive impact on the dilatancy of GHBS.

Yoneda et al. (2015b) conducted triaxial compression tests on natural GHBS retrieved from the Nankai Trough. These core specimens originated from water depths ranging from 1265.6m to 1315.4m, with overburdens ranging from 266.9m to 316.7m, whose porosities were measured between 40% to 50%. The stress-strain characteristics were analyzed through drained shear tests considering various initial mean stresses and S_h. Detailed experimental conditions are provided in Table 4.10. This study used the proposed elastoplastic constitutive model to simulate the observed behavior, with model parameters outlined in Table 4.11.

Table 4.10: Detailed experimental conditions (Yoneda et al. (2015b))

Features	NO.7	NO.8	NO.9
Host specimen type	Natural core specimens drilled from eastern Nankai Trough (Silty sand)		
Water content	26.4%	23.3%	22.7%
Temperature		10℃	
Pore pressure		13MPa	
Effective confining pressure	1.5MPa	1.6MPa	1.6MPa
Hydrate saturation	38%	70%	79%
Porosity	44.1%	39.6%	39.4%

Test type	CD test

Table 4.11: Numerical modelling parameters (Yoneda et al. (2015b))

Parameters	NO.7	NO.8	NO.9
κ	0.008	0.008	0.008
λ	0.13	0.13	0.13
e_0	0.789	0.656	0.65
p_c (MPa)	12	12	12
M	1.37	1.37	1.37
R_0	0.09	0.04	0.06
v	0.3	0.3	0.3
a	1.5	1.5	1.5
γ	-0.13	-0.13	-0.13
n	0.95	0.95	0.95
η	4.5	10	27
α_*	0.25	0.35	0.35
S_{h0}	0.38	0.7	0.79
α (MPa)	18	50	20
β	1.6	1.6	1.6
χ_0	1	1	1
μ	1	3	3
ξ	17.8	17.8	17.8

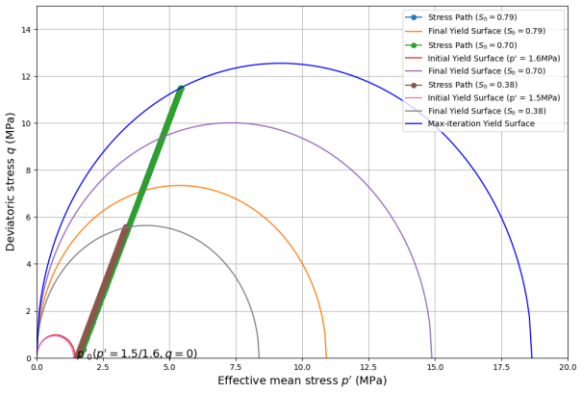

Figure 4.24: Simulations for the stress paths and yield surfaces in core specimens

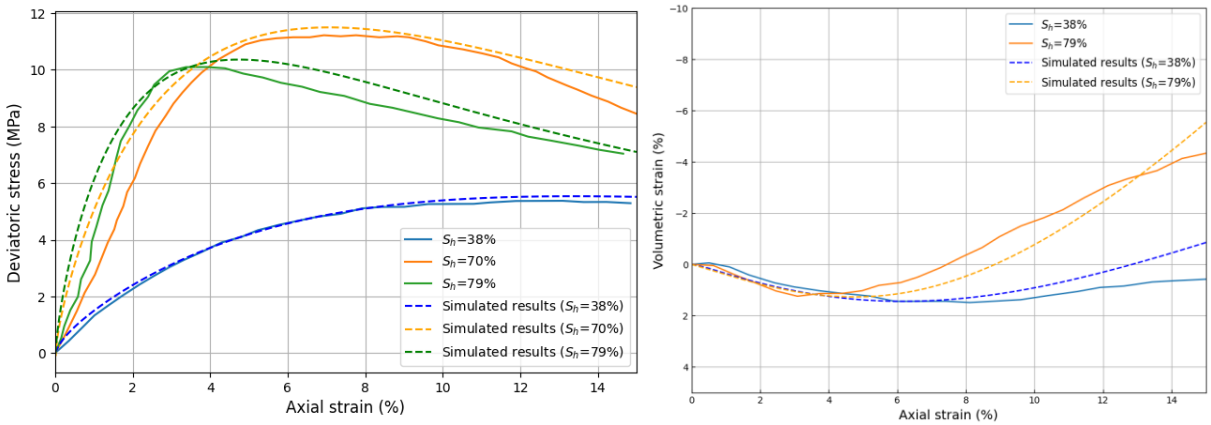

(a) Stress-strain curve (b) Volume change curve

Figure 4.25: Numerical modeling for the mechanical response of GHBS through the comparison between experimental results obtained from Yoneda et al. (2015b)

Fig. 4.24 illustrates the development in stress paths and yield surfaces in core specimens. Fig. 4.25 depicts the predicted and experimental stress-strain response of natural GHBS under triaxial drained test. Overall, the model provides a reasonably good simulation match. Specifically, for the specimens with S_h = 38%, both simulated and experimental results exhibit notable hardening behavior. For the specimens with S_h = 70% and 79%, significant strain softening phenomena are observed; especially for S_h = 79%, the model predicts a more gradual softening phase compared to the experimental outcomes. In terms of volumetric strain curves, when S_h = 38%, the model exhibits slight expansion following initial compression after an increase in axial strain, whereas experimental results indicate a slight rebound during the compression phase. When S_h = 79%, the simulation demonstrates stronger dilatancy compared to the experimental findings.

4.4.4 Simulation for hydrate recovery using depressurization

After validating the effectiveness of the elastoplastic constitutive model for GHBS, it is expected to use this model to simulate the deformation behavior of the HBS layer and the dissociated characteristics of hydrates during depressurization exploitation. Fig. 4.26(a) presents the numerical units and corresponding depressurization path, the depressurization process includes the reduction of pore water pressure and the increase in mean effective stress during drilling operations, which may lead to hydrate decomposition and the risk of reservoir collapse, which may trigger hydrate dissociation and lead to reservoir collapse. To accurately assess the stability of the hydrate layer, this layer can be segmented into multiple units for analysis, each subjected to

varying effective mean stress. According to the phase equilibrium curve of methane hydrates that has been mentioned in Section 1.1.4, this simulation maintains a constant temperature of 285K, and the initial pore water pressure is set at 10 MPa, subsequently decreasing until 0 MPa. Hydrate dissociation initiates when pore water pressure reaches the phase equilibrium boundary point (8.75 MPa). The initial effective confining stress is set as 3MPa, so the evolution of mean effective stress ranges from 3 MPa to 13MPa throughout the recovery process, it is noted that the effect of capillary pressure is not taken into consideration in this simulation.

The initial state of natural HBS in the simulation aligns with those of scenario drawn by Masui et al. (2008), the specimen with the initial hydrate saturation of 37.6% is chosen, with the corresponding model parameters exhibited in Table 4.9. The variation in hydrate concentration and void ratio with respect to the mean effective stress is demonstrated in Fig. 4.26(b). Initially, S_h remains stable, the volume change is only influenced by the consolidation pressure. Because of the cementing effect provided by hydrates, structure stiffness is relatively greater and volume reduction is less evident. However, hydrate dissociation appears as pore water pressure decreases to the phase equilibrium boundary, which is quantified as a decline in S_h, gradually weakening the cementation. This effect leads to decreased resistance to deformation and an increased extent of volume reduction in the sediments. As S_h approaches zero, the volume reduction eventually tends towards a nearly linear trend.

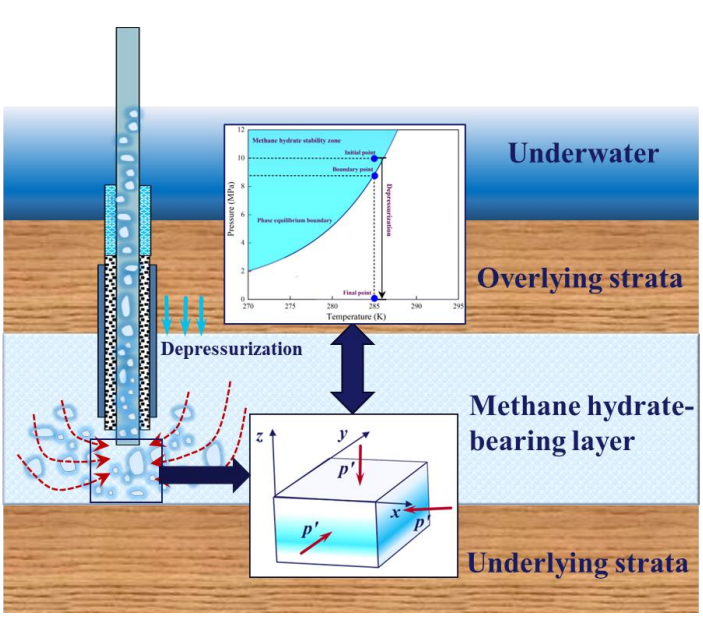

(a) Depressurization modeling

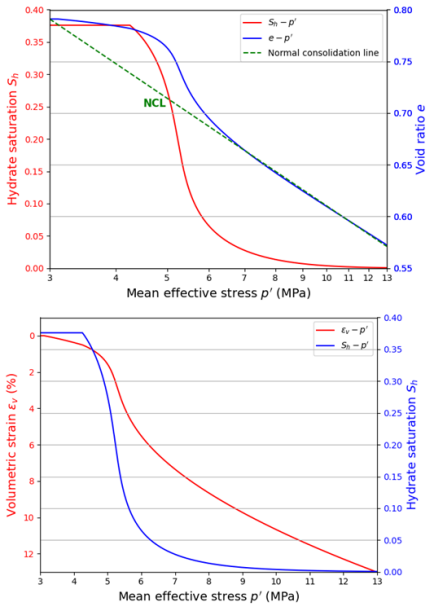

(b) Variation in S_h, e and ε_v

Figure 4.26: Simulation for hydrate recovery using depressurization

Overall, the critical state elastoplastic constitutive model proposed in this study, based on the HISS yield surface theory, offers a more comprehensive characterization of natural GHBS compared to conventional models such as the extended M-C model, D-P model, and modified D-C model. This model effectively captures a wide range of sediment properties including strength, stiffness, dilatancy, volumetric strain, the cementation effects of hydrates, bond degradation, and the material's anisotropy. Consequently, it provides a robust framework for evaluating reservoir stability during hydrate extraction under certain conditions.

4.5 Conclusions

This chapter introduces the modified CCM, which serves as the foundation for integrating the HISS yield surface theory and sub-loading surface theory into the critical state framework. The objective of this integration is to develop an elastoplastic constitutive model tailored for GHBS. This model can describe the strength and stiffness enhancement provided by the cementing effects of hydrates, and capture the volumetric yield of GHBS, as well as considering the features such as bond degradation and cross-anisotropy effect. The model has been validated using experimental data from both synthetic and in-situ specimens, with the findings summarized as follows:

(1) To accommodate different yielding conditions, this model builds upon the MCCM by incorporating the HISS yield surface theory, three shape coefficients a, γ, n are applied to meet varied experimental conditions.

(2) To facilitate a seamless transition from elastic to elastoplastic behavior, sub-loading coefficient R is introduced.

(3) A degradation factor χ is also introduced to describe the concentration dissipation effect of hydrates during shearing. Considering the cementing effect of hydrates and its contribution to structural strength, the model adds a hardening parameter p_d reflecting the strengthening in addition to the existing pre-consolidation stress p_c (hardening parameter) of the MCCM, and quantifies hydrate contribution through the correlation between p_d and S_h. Additionally, a degradation factor is introduced to reflect the concentration dissipation effect of hydrates during shearing.

(4) Considering the reduced overall compressibility induced by hydrate filling the pores, a stiffness coefficient ξ is introduced to represent the stiffness enhancement provided by hydrates. Moreover, the model simplifies the layered distribution of hydrates and their cross-anisotropic properties, employing an anisotropy factor α_* to describe variations in mechanical properties between horizontal and vertical directions.

(5) The model demonstrates robust predictive capabilities in simulating the mechanical responses of GHBS under triaxial drained conditions, which can effectively model the strength, dilatancy, and strain softening phenomena associated with GHBS.

(6) Elastoplastic model is employed to simulate the process of hydrate exploitation using depressurization, indicating that volume deformation is not evident initially due to the hydrate contribution, hydrate decomposition occurs once pore water pressure is lower than the phase equilibrium boundary, which provokes the deterioration in cementation effect, further reducing the void ratio with a larger extent. After S_h decreases to 0, the curve related to the volume change tends to be the normal consolidation line.

Chapter 5. Conclusions and perspectives

5.1 Conclusions

This work is dedicated to developing a constitutive model that can accurately replicate the geo-mechanical behavior of GHBS and then employing numerical methods to assess the mechanical performance under various environmental conditions. Initially, an extensive review of the existing literature on the thermal-hydraulic-mechanical investigations of GHBS conducted in laboratory settings was performed. It is expected to analyze the mechanical responses of host sediments in the presence of hydrates as well as the evolution of their mechanical properties concerning several factors (effective stress, temperature, sediment matrix, loading rate, and porosity) via normalizing the data from the literature. Subsequently, the current state of constitutive modeling for GHBS was reviewed. Models were categorized based on various theoretical frameworks into five types: Mohr-Coulomb criterion-based model, Drucker-Prager criterion-based model, Duncan-Chang model-based model, critical state model, and creep model. The features, limitations, and potential research avenues for each model type were explored, while also discussing the strength, stiffness, and degradation equations involved in the models. Finally, by integrating data captured during the experimental research phase with the theoretical foundations provided in the constitutive theory phase, a new elastoplastic constitutive model was established within the framework of critical state theory, which accounts for volumetric deformation and anisotropic properties and can adapt to different yield conditions. The reliability of the model was validated through the comparison between numerical simulations and experimental results. The main conclusions are driven as follows:

(1) Through the investigation of compressibility of GHBS, it can be found that the presence of hydrates enhances the sediment's ability to resist deformation. Moreover, the comprehensive analysis of the mechanical responses in GHBS according to the literature shows that at lower S_h, GHBS exhibit the stress-strain response analogous to HFS, lacking distinct yield points, alongside strain hardening and volumetric contraction. In contrast, GHBS display strain softening coupled

with volumetric expansion at high S_h. The presence of hydrates provides a great improvement in strength and dilatancy of sediments. The strengthening and dilatancy controlling in HFS and GHBS in pore-filling morphology are governed by particle contact friction. For GHBS in load-bearing type, the cementation strength is less than the shear stress. Conversely, those in cementing type are determined by the cohesive force and tensile strength imparted by hydrates. Strength is also dominated by hydrates for the grain-coating type, with cementation strength exceeding shear stress, and the dilation trend hinges on the orientation of the shear plane.

(2) Factors such as S_h, hydrate dissociation ratio, $\sigma_c^{'}$, T, sediment composition, ϕ, and strain rate have a certain influence on the mechanical properties of GHBS. c exhibits a dependency on particle size concerning S_h, with increasing exponentially for the coarse-grained sediments while linearly for the fine-grained sediments. φ is independent of S_h and determined by host sediment type. v does not show a clear correlation with S_h, but ψ follows a power relationship $\psi = a + b \cdot (S_h)^c$, with related parameters depending on the hydrate pore habit. The strength after hydrate dissociation is proportional to the residual S_h and inversely to the dissociation rate. CO_2 replacement displays the largest residual strength and stiffness compared to other dissociated methods. $\sigma_c^{'}$ curtails the evolution of fractures and augments inter-particle linkages within sediments, thus enhancing the strength and stiffness of GHBS. v decreases parabolically with the increase of $\sigma_c^{'}$, indicating the reduced capability to lateral deformation of GHBS under substantial confinement. Sediments exhibit higher peak strength and strain hardening at lower T, accompanied by the transition from compaction to expansion. GHBS with larger particle size and well-graded distribution contribute to greater deformation resistance. An earlier peak in cementation effect appears and then strengthens GHBS when subjected to a higher strain rate. GHBS with lower porosity restricts the volume deformation due to the enhancement in structural density.

(3) While models based on M-C and D-P criteria offer simplicity and nonlinear relationships, respectively, they fail to capture the strain softening, and volumetric yielding comprehensively. Nonlinear elastic models provide insights into stress-strain behavior but lack robustness in simulating hydrate dissociation and deformation. CSM stands out for its ability to predict volumetric yield and strain softening, though challenges persist in representing diverse yield surfaces, anisotropic behaviors, and thermal effects.

(4) This study developed a critical state model for natural GHBS based on the HISS yield theory and subloading surface theory. The model incorporates a hardening parameter p_d to capture

the strength enhancement contributed by hydrates within the pores and a degradation factor χ to account for the hydrate dissociation during shearing. Another hardening parameter p_c is used to describe the structural characteristics of the host sediment, and cross-anisotropy features displayed in sediments are considered by introducing an anisotropic parameter. Additionally, the model employs a subloading surface ratio R to depict the non-linear elastoplastic behavior of the material before yielding. The developed model integrates the advantages of the critical state model that can simulate the volumetric yielding and strain softening, it also can adapt to different yield conditions and anisotropic characteristics. Numerical simulations building upon the existing triaxial test conducted on GHBS were performed, and the predictive results obtained through modelling were compared with experimental outcomes, which successfully demonstrate the model's effectiveness in reflecting the mechanical properties of sediments under the presence of hydrates.

5.2 Perspectives

NGH, given the abundant reserves and high energy density, are increasingly recognized as a promising clean energy source for the next generation. Before commercial exploitation, it is imperative to examine the geo-mechanical behavior of GHBS comprehensively. Both laboratory investigation and constitutive modeling are the approaches to achieve the recognition of their behavior. Despite significant findings that have been made, numerous technical and theoretical challenges persist. Future research should focus on the following key areas:

- Most laboratory tests assume that hydrates are uniformly distributed within the sediment, with consistent hydrate content between the skeletal structures, which does not align with the heterogeneous distribution found in natural settings. Techniques such as X-ray imaging, nuclear magnetic resonance, and ultrasonic imaging can be utilized to gain real-time insights into the distribution of hydrates. Additionally, advanced experimental methods, such as using stratified sediment samples or microfluidic chips, can simulate the heterogeneous distribution of NGH by controlling local scale variations.
- Most constitutive models for GHBS overlook the impact of thermal-induced phase changes, which is a significant oversight given the high sensitivity of hydrates to temperature variations. Future research should consider the energy required for hydrate dissociation, changes in sediment structure, and subsequent mechanical responses. It is

suggested that models be expanded to include the thermodynamics of phase changes, energy balance equations, and the impact of latent heat on the sediment matrix.

- Existing constitutive models rarely consider the effects of pore fluids. The dynamics of pore fluids not only determine the pore pressure but also significantly impact the mechanical behavior of the host sediments due to interactions between the pore fluids and the sediment matrix. This is particularly relevant in fine-grained sediments, where small pore sizes and large surface areas may exhibit stronger capillary forces Therefore, it is essential that future models address capillary pressure and pore size distribution, focusing on the coupled effects of thermal, mechanical, and flow processes.
- Although this work has established an elastoplastic constitutive model that considers anisotropy and can adapt to various yield conditions, its application has so far been limited to theoretical and numerical calculations. To further validate the practicality of the model, subsequent work should integrate this model into finite element programs to simulate and assess the stability of hydrate reservoirs.

References

Adachi, T. and Oka, F., 1982. Constitutive equations for normally consolidated clay based on elasto-viscoplasticity, Soils Found, 22, 57-70.

Alejano, L.R., Bobet, A., 2012. Drucker–Prager Criterion. Rock Mech Rock Eng 45, 995–999. https://doi.org/10.1007/s00603-012-0278-2

Anderson, G.K., 2004. Enthalpy of dissociation and hydration number of methane hydrate from the Clapeyron equation. The Journal of Chemical Thermodynamics 36, 1119–1127. https://doi.org/10.1016/j.jct.2004.07.005

Antunes, C. de M.M.O., Kakitani, C., Marcelino Neto, M.A., Morales, R.E.M., Sum, A.K., 2018. An Examination of the Prediction of Hydrate Formation Conditions in the Presence of Thermodynamic Inhibitors. Braz. J. Chem. Eng. 35, 265–274. https://doi.org/10.1590/0104-6632.20180351s20160489

Archer, D., 2007. Methane hydrate stability and anthropogenic climate change. Biogeosciences 4, 521–544. https://doi.org/10.5194/bg-4-521-2007

Aregbe, A.G., 2017. Gas Hydrate—Properties, Formation and Benefits. Open Journal of Yangtze Oil and Gas 2, 27–44. https://doi.org/10.4236/ojogas.2017.21003

Aromada, S.A., Kvamme, B., Wei, N., Saeidi, N., 2019. Enthalpies of Hydrate Formation and Dissociation from Residual Thermodynamics. Energies 12, 4726. https://doi.org/10.3390/en12244726

Avlonitis, D., 2005. An investigation of gas hydrates formation energetics. AIChE Journal 51, 1258–1273. https://doi.org/10.1002/aic.10374

Bagherzadeh, S.A., Moudrakovski, I.L., Ripmeester, J.A., Englezos, P., 2011. Magnetic Resonance Imaging of Gas Hydrate Formation in a Bed of Silica Sand Particles. Energy Fuels 25, 3083–3092. https://doi.org/10.1021/ef200399a

Bagherzadeh-Khalkhali, A., Mirghasemi, A.A., 2009. Numerical and experimental direct shear tests for coarse-grained soils. Particuology 7, 83–91. https://doi.org/10.1016/j.partic.2008.11.006

Bavoh, C.B., Lal, B., Khan, M.S., Osei, H., Ayuob, M., 2018. Combined Inhibition Effect of 1-Ethyl-3-methylimidazolium Chloride + Glycine on Methane Hydrate. J. Phys.: Conf. Ser. 1123, 012060. https://doi.org/10.1088/1742-6596/1123/1/012060

Bassiouni, Z., 1994. Theory, measurement, and interpretation of well logs. SPE, Richardson, Texas, Vol. 4, 2-11.

Beauchamp, B., 2004. Natural gas hydrates: myths, facts and issues. Comptes Rendus. Géoscience 336, 751–765. https://doi.org/10.1016/j.crte.2004.04.003

Biswas, R., 2022. Recent Developments in Using Seismic Waves as a Probe for Subsurface Investigations: Theory and Practices. CRC Press.

Booth, J.S., Winters, W.J., Dillon, W.P., Clennell, M.B., Rowe, M.M., 1998. Major occurrences and reservoir concepts of marine clathrate hydrates: implications of field evidence. Geological Society, London, Special Publications 137, 113–127. https://doi.org/10.1144/GSL.SP.1998.137.01.08

Burger, J., Gupta, D., Jacobs, P., Shillinglaw, J., 2003. Overview on Hydrate Coring, Handling and Analysis. Westport Technology Center. https://doi.org/10.2172/908303

Brown, H.E., Holbrook, W.S., Hornbach, M.J., Nealon, J., 2006. Slide structure and role of gas hydrate at the northern boundary of the Storegga Slide, offshore Norway. Marine Geology 229, 179–186. https://doi.org/10.1016/j.margeo.2006.03.011

Brown, O.L.I., 1951. The Clausius-Clapeyron equation. J. Chem. Educ. 28, 428. https://doi.org/10.1021/ed028p428

Broseta, D., Ruffine, L., Desmedt, A., 2017. Gas Hydrates 1: Fundamentals, Characterization and Modeling. John Wiley & Sons.

Britto, A.M., Gunn, M.J., 1987. Critical state soil mechanics via finite elements, Ellis Horwood series in civil engineering. E. Horwood; Halsted Press, Chichester, West Sussex : New York.

Carman, C.P., 1937. Fluid flow through granular beds. Trans. Inst. Chem. Eng. London 15, 150–156. https://doi.org/10.1016/S0263-8762(97)80003-2

Cha, Y., Yun, T.S., Kim, Y.J., Lee, J.Y., Kwon, T.H., 2016. Geomechanical, Hydraulic and Thermal Characteristics of Deep Oceanic Sandy Sediments Recovered during the Second Ulleung Basin Gas Hydrate Expedition. Energies 9, 775. https://doi.org/10.3390/en9100775

Chatterjee, R., Singha, D.K., Ojha, M., Sen, M.K., Sain, K., 2016. Porosity estimation from pre-stack seismic data in gas-hydrate bearing sediments, Krishna-Godavari basin, India. Journal of Natural Gas Science and Engineering 33, 562–572. https://doi.org/10.1016/j.jngse.2016.05.066

Chaturvedi, K.R., Sinha, A.S.K., Nair, V.C., Sharma, T., 2021. Enhanced carbon dioxide sequestration by direct injection of flue gas doped with hydrogen into hydrate reservoir: Possibility of natural gas production. Energy 227, 120521. https://doi.org/10.1016/j.energy.2021.120521

Chazallon, B., Rodriguez, C.T., Ruffine, L., Carpentier, Y., Donval, J.-P., Ker, S., Riboulot, V., 2021. Characterizing the variability of natural gas hydrate composition from a selected site of the Western Black Sea, off Romania. Marine and Petroleum Geology 124, 104785. https://doi.org/10.1016/j.marpetgeo.2020.104785

Chen, B., Yang, M., Zheng, J., Wang, D., Song, Y., 2018. Measurement of water phase permeability in the methane hydrate dissociation process using a new method. International Journal of Heat and Mass Transfer 118, 1316–1324. https://doi.org/10.1016/j.ijheatmasstransfer.2017.11.085

Chen, L., Feng, Y., Okajima, J., Komiya, A., Maruyama, S., 2018. Production behavior and numerical analysis for 2017 methane hydrate extraction test of Shenhu, South China Sea. Journal of Natural Gas Science and Engineering 53, 55–66. https://doi.org/10.1016/j.jngse.2018.02.029

Chen, M., Li, Y., Merey, Ş., Wu, N., Hu, Q., Zhang, Y., Dong, L., Yu, G., Jiang, H., 2022. Review on the Test Methods and Devices for Mechanical Properties of Hydrate-Bearing Sediments. Sustainability 14, 6239. https://doi.org/10.3390/su14106239

Chen, M., Li, Y., Zhang, Y., Qi, M., Wu, N., 2023. Recent advances in creep behaviors characterization for hydrate-bearing sediment. Renewable and Sustainable Energy Reviews 183, 113434. https://doi.org/10.1016/j.rser.2023.113434

Chen, X., Verma, R., Espinoza, D.N., Prodanović, M., 2018. Pore-Scale Determination of Gas Relative Permeability in Hydrate-Bearing Sediments Using X-Ray Computed Micro-Tomography and Lattice Boltzmann Method. Water Resources Research 54, 600–608. https://doi.org/10.1002/2017WR021851

Cheng, F., Wu, Z., Sun, X., Shen, S., Wu, P., Liu, W., Chen, B., Liu, X., Li, Y., 2023. Compression-induced dynamic change in effective permeability of hydrate-bearing sediments during hydrate dissociation by depressurization. Energy 264, 126137. https://doi.org/10.1016/j.energy.2022.126137

Chibura, P.E., Zhang, W., Luo, A., Wang, J., 2022. A review on gas hydrate production feasibility for permafrost and marine hydrates. Journal of Natural Gas Science and Engineering 100, 104441. https://doi.org/10.1016/j.jngse.2022.104441

Choi, J.H., Dai, S., Cha, J.H., Seol, Y., 2014. Laboratory formation of noncementing hydrates in sandy sediments. Geochemistry, Geophysics, Geosystems 15, 1648–1656. https://doi.org/10.1002/2014GC005287

Choi, J.H., Dai, S., Lin, J.S., Seol, Y., 2018. Multistage Triaxial Tests on Laboratory-Formed Methane Hydrate-Bearing Sediments. Journal of Geophysical Research: Solid Earth 123, 3347–3357. https://doi.org/10.1029/2018JB015525

Choi, J.H., Lin, J.S., Dai, S., Lei, L., Seol, Y., 2020. Triaxial compression of hydrate-bearing sediments undergoing hydrate dissociation by depressurization. Geomechanics for Energy and the Environment 23, 100187. https://doi.org/10.1016/j.gete.2020.100187

Chong, Z.R., Yang, S.H.B., Babu, P., Linga, P., Li, X.S., 2016. Review of natural gas hydrates as an energy resource: Prospects and challenges. Applied Energy 162, 1633–1652. https://doi.org/10.1016/j.apenergy.2014.12.061

Christiansen, R.L., Sloan Jr., E.D., 1994. Mechanisms and Kinetics of Hydrate Formation. Annals of the New York Academy of Sciences 715, 283–305. https://doi.org/10.1111/j.1749-6632.1994.tb38841.x

Collett, T.S., Boswell, R.., Lee, M.W., Anderson, B.J., Rose, K., Lewis, K.A., 2012. Evaluation of Long-Term Gas-Hydrate-Production Testing Locations on the Alaska North Slope. SPE Reservoir Evaluation & Engineering 15, 243–264. https://doi.org/10.2118/155504-PA

Collett, T., Johnson, A., Knapp, C., Boswell, R., 2009. Natural Gas Hydrates—Energy Resource Potential and Associated Geologic Hazards. American Association of Petroleum Geologists. https://doi.org/10.1306/M891320

Collett, T.S., Lee, M.W., Agena, W.F., Miller, J.J., Lewis, K.A., Zyrianova, M.V., Boswell, R., Inks, T.L., 2011. Permafrost-associated natural gas hydrate occurrences on the Alaska North Slope. Marine and Petroleum Geology, Thematic Set on Scientific results of the Mount Elbert Gas Hydrate Stratigraphic Test Well, Alaska North Slope 28, 279–294. https://doi.org/10.1016/j.marpetgeo.2009.12.001

Collins, I.F., Hilder, T., 2002. A theoretical framework for constructing elastic/plastic constitutive models of triaxial tests. International Journal for Numerical and Analytical Methods in Geomechanics 26, 1313–1347. https://doi.org/10.1002/nag.247

Colwell, F., Matsumoto, R., Reed, D., 2004. A review of the gas hydrates, geology, and biology of the Nankai Trough. Chemical Geology, Geomicrobiology and Biogeochemistry of Gas Hydrates and Hydrocarbon Seeps 205, 391–404. https://doi.org/10.1016/j.chemgeo.2003.12.023

Cortes, D.D., Martin, A.I., Yun, T.S., Francisca, F.M., Santamarina, J.C., Ruppel, C., 2009. Thermal conductivity of hydrate-bearing sediments. Journal of Geophysical Research: Solid Earth 114. https://doi.org/10.1029/2008JB006235

Cranganu, C., 2009. In-situ thermal stimulation of gas hydrates. Journal of Petroleum Science and Engineering 65, 76–80. https://doi.org/10.1016/j.petrol.2008.12.028

Cui, J., Li, K., Cheng, L., Li, Q., Sun, Z., Xiao, P., Li, X., Chen, G., Sun, C., 2021. Experimental investigation on the spatial differences of hydrate dissociation by depressurization in water-saturated methane hydrate reservoirs. Fuel 292, 120277. https://doi.org/10.1016/j.fuel.2021.120277

Cui, Y., Lu, C., Wu, M., Peng, Y., Yao, Y., Luo, W., 2018. Review of exploration and production technology of natural gas hydrate. Advances in Geo-Energy Research 2. https://doi.org/10.26804/ager.2018.01.05

Dafalias, Y.F., 1986. Bounding Surface Plasticity. I: Mathematical Foundation and Hypoplasticity. Journal of Engineering Mechanics 112, 966–987. https://doi.org/10.1061/(ASCE)0733-9399(1986)112:9(966)

Dai, S., Santamarina, J.C., 2017. Hydrate-Bearing Clayey Sediments: Morphology, Physical Properties, Production and Engineering/Geological Implications (No. DOE-GT-0009897-1). Georgia Institute of Technology, Atlanta, GA (United States). https://doi.org/10.2172/1417303

Dai, S., Seol, Y., 2014. Water permeability in hydrate-bearing sediments: A pore-scale study. Geophysical Research Letters 41, 4176–4184. https://doi.org/10.1002/2014GL060535

Daigle, H., Cook, A., Malinverno, A., 2015. Permeability and porosity of hydrate-bearing sediments in the northern Gulf of Mexico. Marine and Petroleum Geology 68, 551–564. https://doi.org/10.1016/j.marpetgeo.2015.10.004

Dangayach, S., Singh, D.N., Kumar, P., Dewri, S.K., Roy, B., Tandi, C., Singh, J., 2015. Thermal instability of gas hydrate bearing sediments: Some issues. Marine and Petroleum Geology 67, 653–662. https://doi.org/10.1016/j.marpetgeo.2015.05.034

Darcy, H., 1856. Les fontaines publiques de la ville de Dijon: exposition et application des principes à suivre et des formules à employer dans les questions de distribution d'eau. Victor Dalmont.

Davy, H., 1800. On a Combination of Oxymuriatic Gas and Oxygen Gas. [Abstract]. Abstracts of the Papers Printed in the Philosophical Transactions of the Royal Society of London 1, 393–394.

Deaton, W.M. and Frost, E.M., 1946. Gas hydrates and their relation to the operation of natural gas pipe lines. U. S. Bureau of Mines Monograph 8.

Delli, M.L., Grozic, J.L.H., 2014. Experimental determination of permeability of porous media in the presence of gas hydrates. Journal of Petroleum Science and Engineering 120, 1–9. https://doi.org/10.1016/j.petrol.2014.05.011

Delli, M.L., Grozic, J.L.H., 2013. Prediction Performance of Permeability Models in Gas-Hydrate-Bearing Sands. SPE Journal 18, 274–284. https://doi.org/10.2118/149508-PA

Demirbas, A., 2010. Methane hydrates as potential energy resource: Part 1 – Importance, resource and recovery facilities. Energy Conversion and Management 51, 1547–1561. https://doi.org/10.1016/j.enconman.2010.02.013

Demirbas, A., Rehan, M., Al-Sasi, B.O., Nizami, A.S., 2016. Evaluation of natural gas hydrates as a future methane source. Petroleum Science and Technology 34, 1204–1210. https://doi.org/10.1080/10916466.2016.1185442

Dendy Sloan, E., 2003. Clathrate hydrate measurements: microscopic, mesoscopic, and macroscopic. The Journal of Chemical Thermodynamics 35, 41–53. https://doi.org/10.1016/S0021-9614(02)00302-6

Desai, C.S., 1989. SINGLE SURFACE YIELD AND POTENTIAL FUNCTION PLASTICITY. COMPUTERS AND GEOTECHNICS 7.

Desai, C.S., Faruque, M.O., 1984. Constitutive Model for (Geological) Materials. Journal of Engineering Mechanics 110, 1391–1408. https://doi.org/10.1061/(ASCE)0733-9399(1984)110:9(1391)

Desai, C.S., Sharma, K.G., Wathugala, G.W., Rigby, D.B., 1991. Implementation of hierarchical single surface δ0 and δ1 models in finite element procedure. International Journal for Numerical and Analytical Methods in Geomechanics 15, 649–680. https://doi.org/10.1002/nag.1610150904

Desai, C.S., Somasundaram, S., Frantziskonis, G., 1986. A hierarchical approach for constitutive modelling of geologic materials. Num Anal Meth Geomechanics 10, 225–257. https://doi.org/10.1002/nag.1610100302

Desai, C.S., Wathugala, G.W., Sharma, K.G., Woo, L., 1990. Factors affecting reliability of computer solutions with hierarchical single surface constitutive models. Computer Methods in Applied Mechanics and

Engineering, Proceedings of the Workshop on Reliability in Computational Mechanics 82, 115–137. https://doi.org/10.1016/0045-7825(90)90161-E

Deusner, C., Gupta, S., Xie, X.-G., Leung, Y.F., Uchida, S., Kossel, E., Haeckel, M., 2019. Strain Rate-Dependent Hardening-Softening Characteristics of Gas Hydrate-Bearing Sediments. Geochemistry, Geophysics, Geosystems 20, 4885–4905. https://doi.org/10.1029/2019GC008458

Dong, H., Sun, J., Zhu, J., Liu, L., Lin, Z., Golsanami, N., Cui, L., Yan, W., 2019. Developing a new hydrate saturation calculation model for hydrate-bearing sediments. Fuel 248, 27–37. https://doi.org/10.1016/j.fuel.2019.03.038

Dong, L., Li, Y., Liao, H., Liu, C., Chen, Q., Hu, G., Liu, L., Meng, Q., 2020. Strength estimation for hydrate-bearing sediments based on triaxial shearing tests. Journal of Petroleum Science and Engineering 184, 106478. https://doi.org/10.1016/j.petrol.2019.106478

Dong, L., Li, Y., Liu, C., Liao, H., Chen, G., Chen, Q., Liu, L., Hu, G., 2019. Mechanical Properties of Methane Hydrate-Bearing Interlayered Sediments. J. Ocean Univ. China 18, 1344–1350. https://doi.org/10.1007/s11802-019-3929-z

Dong, L., Li, Y., Zhang, Y., Hu, G., Liao, H., Chen, Q., Wu, N., 2024. Deformation Characteristics of Hydrate-Bearing Sediments. J. Ocean Univ. China 23, 149–156. https://doi.org/10.1007/s11802-024-5551-y

Dong, L., Liao, H., Li, Y., Meng, Q., Hu, G., Wang, J., Wu, N., 2022. Analysis of the Mechanical Properties of the Reconstituted Hydrate-Bearing Clayey-Silt Samples from the South China Sea. Journal of Marine Science and Engineering 10, 831. https://doi.org/10.3390/jmse10060831

Dou, X., Wu, Q., Liu, Z., Zhao, Y., Li, Y., Gao, D., Ning, F., 2023. Effects of hydrate distribution heterogeneity on the mechanical properties of hydrate-bearing sediments with consideration of the coalescence phenomenon: Insights from DEM simulations. Computers and Geotechnics 162, 105627. https://doi.org/10.1016/j.compgeo.2023.105627

Drucker, D.C., Prager, W., 1952. Soil mechanics and plastic analysis or limit design. Quartely of Appl.Math. 10, 157–175.

Duncan, J.M., Chang, C.Y., 1970. Nonlinear Analysis of Stress and Strain in Soils. Journal of the Soil Mechanics and Foundations Division 96, 1629–1653. https://doi.org/10.1061/JSFEAQ.0001458

Durham, W.B., Kirby, S.H., Stern, L.A., Zhang, W., 2003. The strength and rheology of methane clathrate hydrate. Journal of Geophysical Research: Solid Earth 108. https://doi.org/10.1029/2002JB001872

Englezos, P., Lee, J.D., 2005. Gas hydrates: A cleaner source of energy and opportunity for innovative technologies. Korean J. Chem. Eng. 22, 671–681. https://doi.org/10.1007/BF02705781

Ersland, G., 2010. Natural Gas Hydrates, in: Potocnik, P. (Ed.), Natural Gas. Sciyo. https://doi.org/10.5772/9838

Fang, H., Shi, K., Yu, Y., 2020. Geomechanical constitutive modelling of gas hydrate-bearing sediments by a state-dependent multishear bounding surface model. Journal of Natural Gas Science and Engineering 75, 103119. https://doi.org/10.1016/j.jngse.2019.103119

Fang, Y., Flemings, P.B., Germaine, J.T., Daigle, H., Phillips, S.C., O'Connell, J., 2022. Compression behavior of hydrate-bearing sediments. AAPG Bulletin 106, 1101–1126. https://doi.org/10.1306/01132221002

Feng, J., Sun, L., Wang, Y., Li, X., 2019. Advances of experimental study on gas production from synthetic hydrate reservoir in China. Chinese Journal of Chemical Engineering, SI: Natural Gas Hydrates 27, 2213–2225. https://doi.org/10.1016/j.cjche.2019.02.036

Fischer, M., Bruzzano, S., Egenolf-Jonkmanns, B., Zeidler-Fandrich, B., Wack, H., Deerberg, G., 2014. Thermal Storage by Thermoreversible Chemical Reaction Systems. Energy Procedia, Proceedings of the 2nd International Conference on Solar Heating and Cooling for Buildings and Industry (SHC 2013) 48, 327–336. https://doi.org/10.1016/j.egypro.2014.02.038

Fujii, T., Takayama, T., Nakamizu, M., Yamamoto, K., Dallimore, S.R., Mwenifumbo, J., Wright, J.F., Kurihara, M., Sato, A., Al-Jubori, A., 2008. WIRE-LINE LOGGING ANALYSIS OF THE 2007 JOGMEC/NRCAN/AURORA MALLIK GAS HYDRATE PRODUCTION TEST WELL [WWW Document]. https://doi.org/10.14288/1.0041108

Gabitto, J.F., Tsouris, C., 2010. Physical Properties of Gas Hydrates: A Review. Journal of Thermodynamics 2010, 1–12. https://doi.org/10.1155/2010/271291

Gai, X., Sánchez, M., 2017. A geomechanical model for gas hydrate-bearing sediments. Environmental Geotechnics 4, 143–156. https://doi.org/10.1680/jenge.15.00050

Ghaedi, H., Ayoub, M., Bhat, A.H., Mahmood, S.M., Akbari, S., Murshid, G., 2016. The effects of salt, particle and pore size on the process of carbon dioxide hydrate formation: A critical review. AIP Conference Proceedings 1787, 060001. https://doi.org/10.1063/1.4968128

Ghiassian, H., Grozic, J.L.H., 2013. Strength behavior of methane hydrate bearing sand in undrained triaxial testing. Marine and Petroleum Geology 43, 310–319. https://doi.org/10.1016/j.marpetgeo.2013.01.007

Gong, G., Guojun Zhao, Pang, W., Yang, M., Chen, B., Zheng, J., 2023. Review of hydrate-bearing sediment permeability for natural gas hydrate exploitation: Measurement and application development. Journal of Petroleum Science and Engineering 220, 111217. https://doi.org/10.1016/j.petrol.2022.111217

Graham, J., Houlsby, G. t., 1983. Anisotropic elasticity of a natural clay. Géotechnique 33, 165–180. https://doi.org/10.1680/geot.1983.33.2.165

Gundersen, A., 2013. Evaluation of Methods for Drilling and Production of Hydrate Formations (Master thesis). 125. Institutt for petroleumsteknologi og anvendt geofysikk.

Guo, W., Li, Y., Jia, R., Wang, Y., Tang, G., Li, X., 2023. Experimental study on mechanical properties of pore-filling and fracture-filling clayey silt hydrate-bearing sediments. Energy 284, 129354. https://doi.org/10.1016/j.energy.2023.129354

Guo, Z., Fang, Q., Nong, M., Ren, X., 2021. A novel Kozeny-Carman-based permeability model for hydrate-bearing sediments. Energy 234, 121203. https://doi.org/10.1016/j.energy.2021.121203

Gupta, A., Lachance, J., Sloan, E.D., Koh, C.A., 2008. Measurements of methane hydrate heat of dissociation using high pressure differential scanning calorimetry. Chemical Engineering Science 63, 5848–5853. https://doi.org/10.1016/j.ces.2008.09.002

Gupta, P., Chandrasekharan Nair, V., Sangwai, J.S., 2018. Phase Equilibrium of Methane Hydrate in the Presence of Aqueous Solutions of Quaternary Ammonium Salts. J. Chem. Eng. Data 63, 2410–2419. https://doi.org/10.1021/acs.jced.7b00976

Hammerschmidt, E.G., 2002. Formation of Gas Hydrates in Natural Gas Transmission Lines [WWW Document]. ACS Publications. https://doi.org/10.1021/ie50296a010

Han, Z.H., Zhang, L.Q., Zhou, J., Wang, S., 2021. Effect of clay mineral grain characteristics on mechanical behaviours of hydrate-bearing sediments. Journal of Engineering Geology 29, 1733–1743. https://doi.org/10.13544/j.cnki.jeg.2021-0052

Handa, Y.P., 1986. Compositions, enthalpies of dissociation, and heat capacities in the range 85 to 270 K for clathrate hydrates of methane, ethane, and propane, and enthalpy of dissociation of isobutane hydrate,

as determined by a heat-flow calorimeter. The Journal of Chemical Thermodynamics 18, 915–921. https://doi.org/10.1016/0021-9614(86)90149-7

Handin J., Hager R.V., Jr, Friedman M., Feather J.N., 1963. Experimental Deformation of Sedimentary Rocks Under Confining Pressure: Pore Pressure Tests. AAPG Bulletin 47, 717–755.

Hashiguchi, K., 1989. Subloading surface model in unconventional plasticity. International journal of solids and structures 25, 917–945.

Hashiguchi, K., Chen, Z.-P., 1998. Elastoplastic constitutive equation of soils with the subloading surface and the rotational hardening. Int. J. Numer. Anal. Meth. Geomech. 22, 197–227. https://doi.org/10.1002/(SICI)1096-9853(199803)22:3<197::AID-NAG914>3.0.CO;2-T

Hashiguchi, K., Okayasu, T., 2000. Time-Dependent Elastoplastic Constitutive Equation Based on the Subloading Surface Model and Its Application to Soils. Soils and Foundations 40, 19–36. https://doi.org/10.3208/sandf.40.4_19

Hashiguchi, K., Ozaki, S., Okayasu, T., 2005. Unconventional friction theory based on the subloading surface concept. International Journal of Solids and Structures 42, 1705–1727. https://doi.org/10.1016/j.ijsolstr.2004.08.006

Hassanpouryouzband, A., Joonaki, E., Farahani, M.V., Takeya, S., Ruppel, C., Yang, J., J. English, N., M. Schicks, J., Edlmann, K., Mehrabian, H., M. Aman, Z., Tohidi, B., 2020. Gas hydrates in sustainable chemistry. Chemical Society Reviews 49, 5225–5309. https://doi.org/10.1039/C8CS00989A

Hauge, L.P., Birkedal, K.A., Ersland, G., Graue, A., 2014. Methane Production from Natural Gas Hydrates by CO2 Replacement – Review of Lab Experiments and Field Trial. Presented at the SPE Bergen One Day Seminar, OnePetro. https://doi.org/10.2118/169198-MS

He, J., Liu, X., Yu, Z., Xie, C., Li, Z., 2013. Factors influencing the porosity of gas hydrate bearing sediments. Sci. China Earth Sci. 56, 557–567. https://doi.org/10.1007/s11430-012-4452-x

He, Z., Feng, Y., Zhang, S., Wang, X., Wu, S., Pan, X., 2018. Oxygenic denitrification for nitrogen removal with less greenhouse gas emissions: Microbiology and potential applications. Science of The Total Environment 621, 453–464. https://doi.org/10.1016/j.scitotenv.2017.11.280

Holder, G.D., Kamath, V.A., Godbole, S.P., 1984. The Potential of Natural Gas Hydrates as an Energy Resource. Annual Review of Energy 9, 427–445. https://doi.org/10.1146/annurev.eg.09.110184.002235

Holland, M., Schultheiss, P., Roberts, J., Druce, M., 2008. OBSERVED GAS HYDRATE MORPHOLOGIES IN MARINE SEDIMENTS [WWW Document]. https://doi.org/10.14288/1.0041062

Hooke, R., 1678. De potentia restitutiva, or of spring. Explaining the power of springing bodies, London.

Hou, X., Qi, S., Huang, X., Guo, S., Zou, Y., Ma, L., Zhang, L., 2022. Hydrate morphology and mechanical behavior of hydrate-bearing sediments: a critical review. Geomech. Geophys. Geo-energ. Geo-resour. 8, 161. https://doi.org/10.1007/s40948-022-00461-8

Huang, B.X., Xue, W.C., Wang, Y.Z., Zhang, T., 2012. Review of Theory and Practice on Natural Gas Hydrate. Advanced Materials Research 361–363, 149–160. https://doi.org/10.4028/www.scientific.net/AMR.361-363.149

Huang, D., Fan, S., 2005. Measuring and modeling thermal conductivity of gas hydrate-bearing sand. Journal of Geophysical Research: Solid Earth 110. https://doi.org/10.1029/2004JB003314

Huang, T., Li, X., Zhang, Y., Wang, Y., Chen, Z., 2020. Experimental study of the drilling process in hydrate-bearing sediments under different circulation rates of drilling fluid. Journal of Petroleum Science and Engineering 189, 107001. https://doi.org/10.1016/j.petrol.2020.107001

Hunter, R.B., Collett, T.S., Boswell, R., Anderson, B.J., Digert, S.A., Pospisil, G., Baker, R., Weeks, M., 2011. Mount Elbert Gas Hydrate Stratigraphic Test Well, Alaska North Slope: Overview of scientific and technical program. Marine and Petroleum Geology, Thematic Set on Scientific results of the Mount Elbert Gas Hydrate Stratigraphic Test Well, Alaska North Slope 28, 295–310. https://doi.org/10.1016/j.marpetgeo.2010.02.015

Hu, Q., Li, Y., Wu, N., Sun, J., Chen, Q., Sun, X., 2023. Study on creep behaviors and nonlinear creep constitutive model for sandy marine hydrate-bearing sediments. Ocean Engineering 286, 115717. https://doi.org/10.1016/j.oceaneng.2023.115717

Hu, Q., Xiao, X., 2023. Formation methods and applications of carbon dioxide hydrate: An overview. Carbon Capture Science & Technology 7, 100113. https://doi.org/10.1016/j.ccst.2023.100113

Hu, W., Ning, F., Liu, Z., Wang, D., Dou, X., Li, Y., Hu, G., Liu, C., 2022. The effect of particle size and hydrate status on dynamic mechanical properties of hydrate-bearing sediments. Energy Science & Engineering 10, 340–354. https://doi.org/10.1002/ese3.1011

Hyndman, R.D., Spence, G.D., 1992. A seismic study of methane hydrate marine bottom simulating reflectors. Journal of Geophysical Research: Solid Earth 97, 6683–6698. https://doi.org/10.1029/92JB00234

Hyodo, M., Li, Y., Yoneda, J., Nakata, Y., Yoshimoto, N., Kajiyama, S., Nishimura, A., Song, Y., 2014a. A comparative analysis of the mechanical behavior of carbon dioxide and methane hydrate-bearing sediments. American Mineralogist 99, 178–183. https://doi.org/10.2138/am.2014.4620

Hyodo, M., Li, Y., Yoneda, J., Nakata, Y., Yoshimoto, N., Nishimura, A., 2014b. Effects of dissociation on the shear strength and deformation behavior of methane hydrate-bearing sediments. Marine and Petroleum Geology 51, 52–62. https://doi.org/10.1016/j.marpetgeo.2013.11.015

Hyodo, M., Li, Y., Yoneda, J., Nakata, Y., Yoshimoto, N., Nishimura, A., Song, Y., 2013a. Mechanical behavior of gas-saturated methane hydrate-bearing sediments. Journal of Geophysical Research: Solid Earth 118, 5185–5194. https://doi.org/10.1002/2013JB010233

Hyodo, M., Nakata, Y., Yoshimoto, N., 2016. Challenge for methane hydrate production by geotechnical engineering. Japanese Geotechnical Society Special Publication 2, 62–75. https://doi.org/10.3208/jgssp.KL-6

Hyodo, M., Nakata, Y., Yoshimoto, N., Ebinuma, T., 2005. BASIC RESEARCH ON THE MECHANICAL BEHAVIOR OF METHANE HYDRATE-SEDIMENTS MIXTURE. Soils and Foundations 45, 75–85. https://doi.org/10.3208/sandf.45.1_75

Hyodo, M., Nishimura, A., Kajiyama, S., 2015. Effect of Fines on Shear Strength of Methane Hydrate Bearing Sand. Presented at the Eleventh Ocean Mining and Gas Hydrates Symposium, OnePetro.

Hyodo, M., Wu, Y., Nakashima, K., Kajiyama, S., Nakata, Y., 2017. Influence of Fines Content on the Mechanical Behavior of Methane Hydrate-Bearing Sediments. Journal of Geophysical Research: Solid Earth 122, 7511–7524. https://doi.org/10.1002/2017JB014154

Hyodo, M., Yoneda, J., Yoshimoto, N., Nakata, Y., 2013b. Mechanical and dissociation properties of methane hydrate-bearing sand in deep seabed. Soils and Foundations 53, 299–314. https://doi.org/10.1016/j.sandf.2013.02.010

İncekara, Ç.Ö., 2021. Global Natural Gas Demand Projections under Fuzzy Logic. EJONS 5, 367–385. https://doi.org/10.38063/ejons.430

Inkong, K., Rangsunvigit, P., Kulprathipanja, S., Linga, P., 2019. Effects of temperature and pressure on the methane hydrate formation with the presence of tetrahydrofuran (THF) as a promoter in an unstirred tank reactor. Fuel 255, 115705. https://doi.org/10.1016/j.fuel.2019.115705

Iwai, H., Kawasaki, T., Zhang, F., 2022. Constitutive model for gas hydrate-bearing soils considering different types of hydrate morphology and prediction of strength-band. Soils and Foundations 62, 101103. https://doi.org/10.1016/j.sandf.2021.101103

Iwai, H., Konishi, Y., Kimoto, S., 2019. Time-Dependent Behavior of CO2-Hydrate-Bearing Sediments and Application of Elasto-Viscoplastic Constitutive Model. Journal of Japan Society of Civil Engineers, Ser. C (Geosphere Engineering) 75, 273–287. https://doi.org/10.2208/jscejge.75.273

Jacobson, L.C., Hujo, W., Molinero, V., 2010. Amorphous Precursors in the Nucleation of Clathrate Hydrates. J. Am. Chem. Soc. 132, 11806–11811. https://doi.org/10.1021/ja1051445

Janbu, N., 1963. Soil compressibility as determined by oedometer and triaxial tests. Proc. European Conf. SMFE, Wiesbaden, 1963 1, 19–25.

Jang, J., Santamarina, J.C., 2016. Hydrate bearing clayey sediments: Formation and gas production concepts. Marine and Petroleum Geology 77, 235–246. https://doi.org/10.1016/j.marpetgeo.2016.06.013

Jiang, M., Peng, D., Ooi, J.Y., 2017. DEM investigation of mechanical behavior and strain localization of methane hydrate bearing sediments with different temperatures and water pressures. Engineering Geology 223, 92–109. https://doi.org/10.1016/j.enggeo.2017.04.011

Jiang, M., Zhu, F., Liu, F., Utili, S., 2014. A bond contact model for methane hydrate-bearing sediments with interparticle cementation. International Journal for Numerical and Analytical Methods in Geomechanics 38, 1823–1854. https://doi.org/10.1002/nag.2283

Jin, Y., Kida, M., Nagao, J., 2013. Structure H (sH) Clathrate Hydrate with New Large Molecule Guest Substances. J. Phys. Chem. C 117, 23469–23475. https://doi.org/10.1021/jp403430z

Joon Shin, H., Lee, Y. J., Im, J.H., Won Han, K., Lee, J.W., Lee, Y., Dong Lee, J., Jang, W.Y., Yoon, J.H., 2009. Thermodynamic stability, spectroscopic identification and cage occupation of binary CO_2 clathrate hydrates. Chemical Engineering Science 64, 5125–5130. https://doi.org/10.1016/j.ces.2009.08.019

Joseph, J., Singh, D.N., Kumar, P., Dewri, S.K., Tandi, C., Singh, J., 2016. State-of-the-Art of Gas Hydrates and Relative Permeability of Hydrate Bearing Sediments. Marine Georesources & Geotechnology 34, 450–464. https://doi.org/10.1080/1064119X.2015.1025929

Jr, E.D.S., Koh, C.A., 2007. Clathrate Hydrates of Natural Gases. CRC Press.

Judd, A.G., 2000. Geological Sources of Methane, in: Khalil, M.A.K. (Ed.), Atmospheric Methane: Its Role in the Global Environment. Springer, Berlin, Heidelberg, pp. 280–303. https://doi.org/10.1007/978-3-662-04145-1_15

Jung, J.W., Espinoza, D.N., Santamarina, J.C., 2010. Properties and phenomena relevant to CH_4-CO_2 replacement in hydrate-bearing sediments. Journal of Geophysical Research: Solid Earth 115. https://doi.org/10.1029/2009JB000812

Jung, J.W., Santamarina, J.C., 2011. Hydrate adhesive and tensile strengths. Geochemistry, Geophysics, Geosystems 12. https://doi.org/10.1029/2010GC003495

Jung, J.W., Santamarina, J.C., 2010. CH_4-CO_2 replacement in hydrate-bearing sediments: A pore-scale study. Geochemistry, Geophysics, Geosystems 11. https://doi.org/10.1029/2010GC003339

Kachanov, L., 1986. Introduction to continuum damage mechanics. Springer Science & Business Media.

Kajiyama, S., Hyodo, M., Nakata, Y., Yoshimoto, N., Wu, Y., Kato, A., 2017a. Shear behaviour of methane hydrate bearing sand with various particle characteristics and fines. Soils and Foundations 57, 176–193. https://doi.org/10.1016/j.sandf.2017.03.002

Kajiyama, S., Wu, Y., Hyodo, M., Nakata, Y., Nakashima, K., Yoshimoto, N., 2017b. Experimental investigation on the mechanical properties of methane hydrate-bearing sand formed with rounded particles. Journal of Natural Gas Science and Engineering 45, 96–107. https://doi.org/10.1016/j.jngse.2017.05.008

Kamath, A., Godbole, S.P., Ostermann, R.D., Collett, T.S., 1987. Evaluation of the stability of gas hydrates in Northern Alaska. Cold Regions Science and Technology 14, 107–119. https://doi.org/10.1016/0165-232X(87)90026-7

Kang, D.H., Yun, T.S., Kim, K.Y., Jang, J., 2016. Effect of hydrate nucleation mechanisms and capillarity on permeability reduction in granular media. Geophysical Research Letters 43, 9018–9025. https://doi.org/10.1002/2016GL070511

Khurana, M., Yin, Z., Linga, P., 2017. A Review of Clathrate Hydrate Nucleation. ACS Sustainable Chem. Eng. 5, 11176–11203. https://doi.org/10.1021/acssuschemeng.7b03238

Kim, H.S., Cho, G.C., 2014. Experimental Study On Compression Indices Of Gas Hydrate-bearing Sediments. Presented at the Offshore Technology Conference, OnePetro. https://doi.org/10.4043/25185-MS

Kim, J., Dai, S., Jang, J., Waite, W.F., Collett, T.S., Kumar, P., 2019. Compressibility and particle crushing of Krishna-Godavari Basin sediments from offshore India: Implications for gas production from deep-water gas hydrate deposits. Marine and Petroleum Geology 108, 697–704. https://doi.org/10.1016/j.marpetgeo.2018.07.012

Kim, K.S., Kang, J.W., Kang, S.P., 2011. Tuning ionic liquids for hydrate inhibition. Chem. Commun. 47, 6341–6343. https://doi.org/10.1039/C0CC05676F

Kim, N.J., Hwan Lee, J., Cho, Y.S., Chun, W., 2010. Formation enhancement of methane hydrate for natural gas transport and storage. Energy, 7th International Conference on Sustainable Energy Technologies 35, 2717–2722. https://doi.org/10.1016/j.energy.2009.07.020

Klar, A., Soga, K., Ng, M., 2010. Coupled deformation–flow analysis for methane hydrate extraction. Geotechnique 60, 765–776.

Kleinberg, R.L., Flaum, C., Collett, T.S., 2005. Magnetic resonance log of JAPEX.JNOC:GSC et al. Mallike 5L-38 gas hydrate produciton research well: gas hydrate saturation, growth habit, and relative permeability. In: Dallimore, S.R., Collett, T.S. (Eds.), Cientific Results from the Mallik 2002 Gas Hydrate Production Research Well Program, Mackenzie Delta, Northwest Territories, Canada. Geological Survey of Canada.

Kleinberg, R.L., Flaum, C., Griffin, D.D., Brewer, P.G., Malby, G.E., Peltzer, E.T., Yesinowski, J.P., 2003. Deep sea NMR: Methane hydrate growth habit in porous media and its relationship to hydraulic permeability, deposit accumulation, and submarine slope stability. Journal of Geophysical Research: Solid Earth 108. https://doi.org/10.1029/2003JB002389

Ko, G., Seo, Y., 2019. SF_6 Hydrate Formation in Various Reaction Media: A Preliminary Study on Hydrate-Based Greenhouse Gas Separation. Environ. Sci. Technol. 53, 12945–12952. https://doi.org/10.1021/acs.est.9b04902

Koh, C.A., 2002. Towards a fundamental understanding of natural gas hydrates. Chem. Soc. Rev. 31, 157–167. https://doi.org/10.1039/b008672j

Koh, C.A., Westacott, R.E., Zhang, W., Hirachand, K., Creek, J.L., Soper, A.K., 2002. Mechanisms of gas hydrate formation and inhibition. Fluid Phase Equilibria, Proceedings of the Ninth International Conference on Properties and Phase Equilibria for Product and Process Design 194–197, 143–151. https://doi.org/10.1016/S0378-3812(01)00660-4

Komatsu, H., Ota, M., Smith, R.L., Inomata, H., 2013. Review of CO_2–CH_4 clathrate hydrate replacement reaction laboratory studies – Properties and kinetics. Journal of the Taiwan Institute of Chemical Engineers 44, 517–537. https://doi.org/10.1016/j.jtice.2013.03.010

Kominz, M.A., Patterson, K., Odette, D., 2011. Lithology Dependence of Porosity In Slope and Deep Marine Sediments. Journal of Sedimentary Research 81, 730–742. https://doi.org/10.2110/jsr.2011.60

Kondner, R.L., 1963. Hyperbolic Stress-Strain Response: Cohesive Soils. Journal of the Soil Mechanics and Foundations Division 89, 115–143. https://doi.org/10.1061/JSFEAQ.0000479

Kondner, R.L., Horner, J.M., 1965. Triaxial Compression of a Cohesive Soil with Effective Octahedral Normal Stress Control. Can. Geotech. J. 2, 40–52. https://doi.org/10.1139/t65-004

Kong, L., Wang, X., Hua, L., Lin, X., 2023. A bounding surface model of gas-hydrate-bearing sediments. Environmental Geotechnics 10, 196–205. https://doi.org/10.1680/jenge.19.00060

Konno, Y., Yoneda, J., Egawa, K., Ito, T., Jin, Y., Kida, M., Suzuki, K., Fujii, T., Nagao, J., 2015. Permeability of sediment cores from methane hydrate deposit in the Eastern Nankai Trough. Marine and Petroleum Geology, Gas hydrate drilling in Eastern Nankai 66, 487–495. https://doi.org/10.1016/j.marpetgeo.2015.02.020

Kozeny, J., 1927. Über kapillare Leitung des Wassers im Boden. Sitzungsberichte der Akademie der Wissenschaften in Wien 136, 271.

Krajcinovic, D., Silva, M.A.G., 1982. Statistical aspects of the continuous damage theory. International Journal of Solids and Structures 18, 551–562. https://doi.org/10.1016/0020-7683(82)90039-7

Kumar, A., Maini, B., P.R. Bishnoi, Clarke, M., Zatsepina, O., Srinivasan, S., 2010. Experimental determination of permeability in the presence of hydrates and its effect on the dissociation characteristics of gas hydrates in porous media. Journal of Petroleum Science and Engineering 70, 114–122. https://doi.org/10.1016/j.petrol.2009.10.005

Kumar, D., Sen, M.K., Bangs, N.L., 2007. Gas hydrate concentration and characteristics within Hydrate Ridge inferred from multicomponent seismic reflection data. Journal of Geophysical Research: Solid Earth 112. https://doi.org/10.1029/2007JB004993

Kumar, P., Turner, D., Sloan, E.D., 2004. Thermal diffusivity measurements of porous methane hydrate and hydrate-sediment mixtures. Journal of Geophysical Research: Solid Earth 109. https://doi.org/10.1029/2003JB002763

Kvalstad, T.J., Andresen, L., Forsberg, C.F., Berg, Kjell, Bryn, Petter, Wangen, M., 2005. The Storegga slide: evaluation of triggering sources and slide mechanics, in: Solheim, A., Bryn, P., Berg, K., Sejrup, H.P., Mienert, J. (Eds.), Ormen Lange–an Integrated Study for Safe Field Development in the Storegga Submarine Area. Elsevier, Oxford, pp. 245–256. https://doi.org/10.1016/B978-0-08-044694-3.50025-1

Kvamme, B., Kuznetsova, T., Jensen, B., Stensholt, S., Bauman, J., Sjøblom, S., Lervik, K.N., 2014. Consequences of CO_2 solubility for hydrate formation from carbon dioxide containing water and other impurities. Phys. Chem. Chem. Phys. 16, 8623–8638. https://doi.org/10.1039/C3CP53858C

Kvamme, B., Wei, N., Zhao, J., Zhou, S., Zhang, L., Sun, W., Saeidi, N., 2022. Alcohols for hydrate inhibition – Different alcohols and different mechanisms. Petroleum 8, 1–16. https://doi.org/10.1016/j.petlm.2021.10.007

Labuz, J.F., Zang, A., 2015. Mohr–Coulomb Failure Criterion, in: Ulusay, R. (Ed.), The ISRM Suggested Methods for Rock Characterization, Testing and Monitoring: 2007-2014. Springer International Publishing, Cham, pp. 227–231. https://doi.org/10.1007/978-3-319-07713-0_19

Le, T.X., Tang, A.M., Aimedieu, P., Bornert, M., Chabot, B., Rodts, S., 2018. Mechanical properties of synthetic methane hydrate-bearing sand.

Lee, J.S., Lee, J.Y., Kim, Y.M., Lee, C., 2013. Stress-dependent and strength properties of gas hydrate-bearing marine sediments from the Ulleung Basin, East Sea, Korea. Marine and Petroleum Geology, Scientific Results of the Second Gas Hydrate Drilling Expedition in the Ulleung Basin (UBGH2), East Sea of Korea 47, 66–76. https://doi.org/10.1016/j.marpetgeo.2013.04.006

Lee, J.Y., Santamarina, J.C., Ruppel, C., 2010. Volume change associated with formation and dissociation of hydrate in sediment. Geochemistry, Geophysics, Geosystems 11. https://doi.org/10.1029/2009GC002667

Lee, J.Y., Yun, T.S., Santamarina, J.C., Ruppel, C., 2007. Observations related to tetrahydrofuran and methane hydrates for laboratory studies of hydrate-bearing sediments. Geochemistry, Geophysics, Geosystems 8. https://doi.org/10.1029/2006GC001531

Lee, M.W., 2008. Models for gas hydrate-bearing sediments inferred from hydrate permeability and elastic velocities. U.S. Geological Survey.

Lee, W., Shin, J.Y., Cha, J.H., Kim, K.S., Kang, S.P., 2016. Inhibition effect of ionic liquids and their mixtures with poly(N-vinylcaprolactam) on methane hydrate formation. Journal of Industrial and Engineering Chemistry 38, 211–216. https://doi.org/10.1016/j.jiec.2016.05.007

Lee, Y., Deusner, C., Kossel, E., Choi, W., Seo, Y., Haeckel, M., 2020. Influence of CH4 hydrate exploitation using depressurization and replacement methods on mechanical strength of hydrate-bearing sediment. Applied Energy 277, 115569. https://doi.org/10.1016/j.apenergy.2020.115569

Lei, L., Gai, X., Seol, Y., 2020. Load-bearing characteristic of methane hydrate within coarse-grained sediments – Insights from isotropic consolidation. Marine and Petroleum Geology 121, 104571. https://doi.org/10.1016/j.marpetgeo.2020.104571

Lei, L., Santamarina, J.C., 2019. Physical properties of fine-grained sediments with segregated hydrate lenses. Marine and Petroleum Geology 109, 899–911. https://doi.org/10.1016/j.marpetgeo.2019.08.053

Lerche, I., Bagirov, E., 1998. Guide to gas hydrate stability in various geological settings. Marine and Petroleum Geology 15, 427–437. https://doi.org/10.1016/S0264-8172(98)00013-0

Li, C.H., Zhao, Q., Xu, H.J., Feng, K., Liu, X.W., 2014. Relation between relative permeability and hydrate saturation in Shenhu area, South China Sea. Appl. Geophys. 11, 207–214. https://doi.org/10.1007/s11770-014-0432-6

Li, D., Wang, Z., Liang, D., Wu, X., 2019. Effect of Clay Content on the Mechanical Properties of Hydrate-Bearing Sediments during Hydrate Production via Depressurization. Energies 12, 2684. https://doi.org/10.3390/en12142684

Li, D., Wu, Q., Wang, Z., Lu, J., Liang, D., Li, X., 2018. Tri-Axial Shear Tests on Hydrate-Bearing Sediments during Hydrate Dissociation with Depressurization. Energies 11, 1819. https://doi.org/10.3390/en11071819

Li, G., Zhan, L., Yun, T., Dai, S., 2020. Pore-Scale Controls on the Gas and Water Transport in Hydrate-Bearing Sediments. Geophysical Research Letters 47, e2020GL086990. https://doi.org/10.1029/2020GL086990

Li, J., Zhang, Y., Lin, L., Zhou, Y., 2023. Study on the shear mechanics of gas hydrate-bearing sand-well interface with different roughness and dissociation. Bull Eng Geol Environ 82, 404. https://doi.org/10.1007/s10064-023-03432-9

Li, M., Wu, P., Zhou, S., Zhang, L., Yang, L., Li, Y., Liu, Y., Zhao, J., Song, Y., 2021. Permeability Analysis of Hydrate-Bearing Sediments during the Hydrate Formation Process. Energy Fuels 35, 19606–19613. https://doi.org/10.1021/acs.energyfuels.1c02913

Li, Q.C., Zhao, D., Yin, J., Zhou, X., Li, Y., Chi, P., Han, Y., Ansari, U., Cheng, Y., 2023. Sediment Instability Caused by Gas Production from Hydrate-bearing Sediment in Northern South China Sea by Horizontal Wellbore: Evolution and Mechanism. Nat Resour Res 32, 1595–1620. https://doi.org/10.1007/s11053-023-10202-7

Li, Q.C., Cheng, Y., Li, Qiang, Zhang, C., Ansari, U., Song, B., 2018. Establishment and evaluation of strength criterion for clayey silt hydrate-bearing sediments. Energy Sources, Part A: Recovery, Utilization, and Environmental Effects 40, 742–750. https://doi.org/10.1080/15567036.2018.1457742

Li, X.S., Dafalias, Y.F., 2000. Dilatancy for cohesionless soils. Géotechnique 50, 449–460. https://doi.org/10.1680/geot.2000.50.4.449

Li, X.S., Dafalias, Y.F., Wang, Z.L., 1999. State-dependant dilatancy in critical-state constitutive modelling of sand. Can. Geotech. J. 36, 599–611. https://doi.org/10.1139/t99-029

Li, X.S., Xu, C.G., Zhang, Y., Ruan, X.K., Li, G., Wang, Y., 2016. Investigation into gas production from natural gas hydrate: A review. Applied Energy 172, 286–322. https://doi.org/10.1016/j.apenergy.2016.03.101

Li, Y., Cheng, Y., Yan, C., Wang, Z., Zhang, Q., Zhou, P., 2021. Stratum Settlement during Depressurization of Horizontal Wells in Gas Hydrate Reservoirs. Energy Fuels 35, 14692–14708. https://doi.org/10.1021/acs.energyfuels.1c02249

Li, Y., Cheng, Y.F., Yan, C.L., Wang, Z.Y., Song, L.F., 2023. Triaxial creep tests and the visco-elastic-plastic constitutive model of hydrate formations. Gas Science and Engineering 115, 205006. https://doi.org/10.1016/j.jgsce.2023.205006

Li, Y., Cheng, Y.F., Yan, C.L., Wang, Z.Y., Song, L.F., 2022. Effects of creep characteristics of natural gas hydrate-bearing sediments on wellbore stability. Petroleum Science 19, 220–233. https://doi.org/10.1016/j.petsci.2021.10.026

Li, Y., Liu, C., Liu, L., Sun, J., Liu, H., Meng, Q., 2018. Experimental study on evolution behaviors of triaxial-shearing parameters for hydrate-bearing intermediate fine sediment. Advances in Geo-Energy Research 2, 43–52. https://doi.org/10.26804/ager.2018.01.04

Li, Y., Liu, L., Jin, Y., Wu, N., 2021. Characterization and development of natural gas hydrate in marine clayey-silt reservoirs: A review and discussion. Advances in Geo-Energy Research 5. https://doi.org/10.46690/ager.2021.01.08

Li, Y., Liu, W., Zhu, Y., Chen, Y., Song, Y., Li, Q., 2016. Mechanical behaviors of permafrost-associated methane hydrate-bearing sediments under different mining methods. Applied Energy 162, 1627–1632. https://doi.org/10.1016/j.apenergy.2015.04.065

Li, Y.C., Jiao, L.J., Yin, X.X., Li, Q., Hua, Z.Z., 2022. Molecular Dynamics Simulation of Thermal Properties of Carbon Dioxide Hydrates with Different Structures. Refrigeration and Air Conditioning, 36, 140-148.

Li, Y.L., Dong, L., Wu, N.Y., Nouri, A., Liao, H.L., Chen, Q., Sun, J.Y., Liu, C.L., 2021. Influences of hydrate layered distribution patterns on triaxial shearing characteristics of hydrate-bearing sediments. Engineering Geology 294, 106375. https://doi.org/10.1016/j.enggeo.2021.106375

Li, Y.H., Li, J.Y., You, Z.S., Wu, P., Qu, Y., Zhang, A., Sun, X., Song, Y.C., 2023. A particle-scale investigation of mechanical behavior of cemented hydrate-bearing sediment using Discrete Element Method. Geomechanics for Energy and the Environment 33, 100436. https://doi.org/10.1016/j.gete.2023.100436

Li, Y.H., Liu, W.G., Song, Y.C., Yang, M.J., Zhao, J.F., 2016. Creep behaviors of methane hydrate coexisting with ice. Journal of Natural Gas Science and Engineering 33, 347–354. https://doi.org/10.1016/j.jngse.2016.05.042

Li, Y.H., Song, Y.C., Liu, W.G., Yu, F., Wang, R., 2013. A new strength criterion and constitutive model of gas hydrate-bearing sediments under high confining pressures. Journal of Petroleum Science and Engineering 109, 45–50. https://doi.org/10.1016/j.petrol.2013.08.010

Li, Y.H., Song, Y.C., Yu, F., Liu, W., Wang, R., 2011a. Effect of confining pressure on mechanical behavior of methane hydrate-bearing sediments. Petroleum Exploration and Development 38, 637–640. https://doi.org/10.1016/S1876-3804(11)60061-X

Li, Y.H., Song, Y.C., Yu, F., Liu, W., Zhao, J., 2011b. Experimental study on mechanical properties of gas hydrate-bearing sediments using kaolin clay. China Ocean Eng 25, 113–122. https://doi.org/10.1007/s13344-011-0009-6

Li, Y.H., Wang, L., Shen, S., Liu, T., Zhao, J., Sun, X., 2021. Triaxial Tests on Water-Saturated Gas Hydrate-Bearing Fine-Grained Samples of the South China Sea under Different Drainage Conditions. Energy Fuels 35, 4118–4126. https://doi.org/10.1021/acs.energyfuels.1c00071

Li, Y., Wang, L., Xie, Y., Wu, P., Liu, T., Huang, L., Zhang, S., Song, Y., 2023. Deformation characteristics of methane hydrate-bearing clayey and sandy sediments during depressurization dissociation. Energy 275, 127527. https://doi.org/10.1016/j.energy.2023.127527

Li, Y.H., Wu, P., Sun, X., Liu, W.G., Song, Y.C., Zhao, J.F., 2019. Creep Behaviors of Methane Hydrate-Bearing Frozen Sediments. Energies 12, 251. https://doi.org/10.3390/en12020251

Li, Y.L., Liu, C.L., Liu, L.L., 2016. Damage statistic constitutive model of hydrate-bearing sediments and the determination method of parameters. Acta Petrolei Sinica 37, 1273. https://doi.org/10.7623/syxb201610007

Liang, J., Meng, M.M., Liang, J.Q., Ren, J.F., He, Y.L., Li, T.W., Xu, M.J., Wang, X.X., 2022. Drilling Cores and Geophysical Characteristics of Gas Hydrate-Bearing Sediments in the Production Test Region in the Shenhu sea, South China sea. Frontiers in Earth Science 10, 911123. https://doi.org/10.3389/feart.2022.911123

Liang, Y., Tan, Y., Luo, Y., Zhang, Y., Li, B., 2020. Progress and challenges on gas production from natural gas hydrate-bearing sediment. Journal of Cleaner Production 261, 121061. https://doi.org/10.1016/j.jclepro.2020.121061

Lijith, K.P., Malagar, Bhini.R.C., Singh, D.N., 2019. A comprehensive review on the geomechanical properties of gas hydrate bearing sediments. Marine and Petroleum Geology 104, 270–285. https://doi.org/10.1016/j.marpetgeo.2019.03.024

Lin, J.S., Seol, Y., Choi, J.H., 2015. An SMP critical state model for methane hydrate-bearing sands. International Journal for Numerical and Analytical Methods in Geomechanics 39, 969–987. https://doi.org/10.1002/nag.2347

Liu, F., Kou, X.Y., Jiang, M.J., Xiong, J.H., Wu, X.F., 2013. Triaxial shear strength of synthetic hydrate-bearing sediments. Chinese Journal of Geotechnical Engineering, 35, 1565-1572.

Liu, H., Mu, L., Liu, B., Zhang, X., Wang, J., Wang, B., Sun, C., Yang, L., Wang, H., Xiao, P., Chen, G., 2013. Experimental Studies of the Separation of C_2 Compounds from CH_4 + C_2H_4 + C_2H_6 + N_2 Gas

Mixtures by an Absorption–Hydration Hybrid Method. Ind. Eng. Chem. Res. 52, 2707–2713. https://doi.org/10.1021/ie3028526

Liu, J.W., Li, X.S., 2021. Recent Advances on Natural Gas Hydrate Exploration and Development in the South China Sea. Energy Fuels 35, 7528–7552. https://doi.org/10.1021/acs.energyfuels.1c00494

Liu, Lin., Yao, Y.P., Zhang, X.H., Lu, X.B., Wang, S.Y., 2020. An elastoplastic constitutive model for gas hydrate-bearing sediments. Chinese Journal of Theoretical and Applied Mechanics 52, 556–566. https://doi.org/10.6052/0459-1879-19-184

Liu, L.L., Zhang, X.H., Li, Y.L., Li, C.L., Lu, X.B., 2017. A Damage-Softening Statistical Constitutive Model of Composite Hydrate-Bearing Sediments.

Liu, S., Liang, Y., Li, B., Wan, Q., Han, X., 2019. Interaction relationship analysis between heat transfer and hydrate decomposition for optimization exploitation. Fuel 256, 115742. https://doi.org/10.1016/j.fuel.2019.115742

Liu, W., Chen, Y., Zhu, Y., Song, Y., Li, Y., Li, Q., Wang, L., 2014. Effects of Different Mining Methods on the Strength Behavior of Gas Hydrate-Bearing Sediments. Energy Procedia, International Conference on Applied Energy, ICAE2014 61, 547–551. https://doi.org/10.1016/j.egypro.2014.11.1167

Liu, W., Luo, T., Li, Y., Song, Y., Zhu, Y., Liu, Y., Zhao, J., Wu, Z., Xu, X., 2016. Experimental study on the mechanical properties of sediments containing CH4 and CO2 hydrate mixtures. Journal of Natural Gas Science and Engineering 32, 20–27. https://doi.org/10.1016/j.jngse.2016.03.012

Liu, W., Zhao, J., Luo, Y., Song, Y., Li, Y., Yang, M., Zhang, Y., Liu, Y., Wang, D., 2013. Experimental measurements of mechanical properties of carbon dioxide hydrate-bearing sediments. Marine and Petroleum Geology 46, 201–209. https://doi.org/10.1016/j.marpetgeo.2013.06.016

Liu, Y., Zhang, L., Yang, L., Dong, H., Zhao, J., Song, Y., 2021. Behaviors of CO_2 Hydrate Formation in the Presence of Acid-Dissolvable Organic Matters. Environ. Sci. Technol. 55, 6206–6213. https://doi.org/10.1021/acs.est.0c06407

Liu, Y., Zheng, Y., 2019. Plastic Mechanics of Geomaterial, Springer Geophysics. Springer, Singapore. https://doi.org/10.1007/978-981-13-3753-6

Liu, Z., Dai, S., Ning, F., Peng, L., Wei, H., Wei, C., 2018. Strength Estimation for Hydrate-Bearing Sediments From Direct Shear Tests of Hydrate-Bearing Sand and Silt. Geophysical Research Letters 45, 715–723. https://doi.org/10.1002/2017GL076374

Liu, Z., Lu, Y., Cheng, J., Han, Q., Hu, Z., Wang, L., 2019. Geomechanics involved in gas hydrate recovery. Chinese Journal of Chemical Engineering, SI: Natural Gas Hydrates 27, 2099–2106. https://doi.org/10.1016/j.cjche.2019.02.015

Lodge, A.S., 1955. THE TRANSFORMATION TO ISOTROPIC FORM OF THE EQUILIBRIUM EQUATIONS FOR A CLASS OF ANISOTROPIC ELASTIC SOLIDS. The Quarterly Journal of Mechanics and Applied Mathematics 8, 211–225. https://doi.org/10.1093/qjmam/8.2.211

Long, Z., Zhou, X., He, Y., Li, D., Liang, D., 2018. Performance of mixture of ethylene glycol and glycine in inhibiting methane hydrate formation. Journal of Natural Gas Science and Engineering 56, 134–140. https://doi.org/10.1016/j.jngse.2018.05.034

Long, Z., Zhou, X., Shen, X., Li, D., Liang, D., 2015. Phase Equilibria and Dissociation Enthalpies of Methane Hydrate in Imidazolium Ionic Liquid Aqueous Solutions. Ind. Eng. Chem. Res. 54, 11701–11708. https://doi.org/10.1021/acs.iecr.5b03480

Lu, S., Ren, T., Gong, Y., Horton, R., 2007. An Improved Model for Predicting Soil Thermal Conductivity from Water Content at Room Temperature. Soil Science Society of America Journal 71, 8–14. https://doi.org/10.2136/sssaj2006.0041

Lu, X., Zhang, X., Sun, F., Wang, S., Liu, L., Liu, C., 2021. Experimental Study on the Shear Band of Methane Hydrate-Bearing Sediment. Journal of Marine Science and Engineering 9, 1158. https://doi.org/10.3390/jmse9111158

Lu, X.B., Zhang, X.H., Wang, S.Y., 2013. Advances in study of mechanical properties of gas hydrate-bearing sediments. Open Ocean Engineering Journal, 6, 26-40. https://doi.org/10.2174/1874835X01306010026

Lubliner, J., 2008, Plasticity Theory. Courier Dover Publications.

Lucazeau, F., Armitage, J., Kabongo, É.K., 2015. Thermal Regime and Evolution of the Congo Basin as an Intracratonic Basin, in: de Wit, M.J., Guillocheau, F., de Wit, M.C.J. (Eds.), Geology and Resource Potential of the Congo Basin. Springer, Berlin, Heidelberg, pp. 229–244. https://doi.org/10.1007/978-3-642-29482-2_12

Luo, T., Li, Y., Liu, W., Sun, X., Shen, S., 2017. Experimental Study on the Mechanical Properties of CH_4 and CO_2 Hydrate Remodeling Cores in Qilian Mountain. Energies 10, 2078. https://doi.org/10.3390/en10122078

Luo, T., Li, Y., Madhusudhan, B.N., Sun, X., Song, Y., 2020a. Deformation behaviors of hydrate-bearing silty sediment induced by depressurization and thermal recovery. Applied Energy 276, 115468. https://doi.org/10.1016/j.apenergy.2020.115468

Luo, T., Li, Y., Madhusudhan, B.N., Zhao, J., Song, Y., 2020b. Comparative analysis of the consolidation and shear behaviors of CH_4 and CO_2 hydrate-bearing silty sediments. Journal of Natural Gas Science and Engineering 75, 103157. https://doi.org/10.1016/j.jngse.2020.103157

Luo, T., Li, Y., Sun, X., Shen, S., Wu, P., 2018. Effect of sediment particle size on the mechanical properties of CH4 hydrate-bearing sediments. Journal of Petroleum Science and Engineering 171, 302–314. https://doi.org/10.1016/j.petrol.2018.07.054

Luo, T., Zou, D., Zhao, X., Zhang, C., Han, T., Song, Y., 2022. Strength behaviours of methane hydrate-bearing marine sediments in the South China Sea. Journal of Natural Gas Science and Engineering 100, 104476. https://doi.org/10.1016/j.jngse.2022.104476

Lv, J., Zhao, J., Jiang, L., Liu, Y., Mu, H., 2020. A review of micro computed tomography studies on the gas hydrate pore habits and seepage properties in hydrate bearing sediments. Journal of Natural Gas Science and Engineering 83, 103555. https://doi.org/10.1016/j.jngse.2020.103555

Ma, L., Xu, X., 2021. Mechanical behavior and constitutive model of methane hydrate bearing sediments. Geomech. Geophys. Geo-energ. Geo-resour. 7, 76. https://doi.org/10.1007/s40948-021-00275-0

Madhusudhan, B.N., Clayton, C.R.I., Priest, J.A., 2019. The Effects of Hydrate on the Strength and Stiffness of Some Sands. Journal of Geophysical Research: Solid Earth 124, 65–75. https://doi.org/10.1029/2018JB015880

Mahabadi, N., Dai, S., Seol, Y., Jang, J., 2019. Impact of hydrate saturation on water permeability in hydrate-bearing sediments. Journal of Petroleum Science and Engineering 174, 696–703. https://doi.org/10.1016/j.petrol.2018.11.084

Majorowicz, J.A., Osadetz, K.G., 2001. Gas hydrate distribution and volume in Canada. AAPG Bulletin 85, 1211–1230.

Makogon, Y.F., 2010. Natural gas hydrates – A promising source of energy. Journal of Natural Gas Science and Engineering 2, 49–59. https://doi.org/10.1016/j.jngse.2009.12.004

Makogon, Y., Holditch, S., Makogon, T.Y., 2005. Russian field illustrates gas-hydrate production. Oil and Gas Journal 103, 43–47.

Makogon, Y.F., Holditch, S.A., Makogon, T.Y., 2007. Natural gas-hydrates — A potential energy source for the 21st Century. Journal of Petroleum Science and Engineering, Natural Gas Hydrate / Clathrate 56, 14–31. https://doi.org/10.1016/j.petrol.2005.10.009

Malagar, B.R.C., Lijith, K.P., Singh, D.N., 2019. Formation & dissociation of methane gas hydrates in sediments: A critical review. Journal of Natural Gas Science and Engineering 65, 168–184. https://doi.org/10.1016/j.jngse.2019.03.005

Manzari, M.T., Dafalias, Y.F., 1997. A critical state two-surface plasticity model for sands. Géotechnique 47, 255–272. https://doi.org/10.1680/geot.1997.47.2.255

Mao, W.L., Mao, H., Goncharov, A.F., Struzhkin, V.V., Guo, Q., Hu, J., Shu, J., Hemley, R.J., Somayazulu, M., Zhao, Y., 2002. Hydrogen Clusters in Clathrate Hydrate. Science 297, 2247–2249. https://doi.org/10.1126/science.1075394

Masuda, Y., 2002. A field-scale simulation study on gas productivity of formations containing gas hydrates. Proceedings, 4th International Conference on Gas Hydrates, May 19-23, Yokohama, Japan, 2002 40–46.

Masui, A., Haneda, H., Ogata, Y., Aoki, K., 2007. Mechanical Properties of Sandy Sediment Containing Marine Gas Hydrates In Deep Sea Offshore Japan. Presented at the Seventh ISOPE Ocean Mining Symposium, p. ISOPE-M-07-015.

Masui, A., Haneda, H., Ogata, Y., Aoki, K., 2006. Triaxial Compression test on submarine sediment containing methane hydrate in deep sea off the coast off Japan. Presented at the 41st Annual Conference, Japanese Geotechnical Society.

Masui, Akira, Haneda, H., Ogata, Y., Aoki, K., 2005. Effects of Methane Hydrate Formation On Shear Strength of Synthetic Methane Hydrate Sediments. Presented at the The Fifteenth International Offshore and Polar Engineering Conference, p. ISOPE-I-05-056.

Masui, A, Haneda, H., Ogata, Y., Aoki, K., 2005. The effect of saturation degree of methane hydrate on the shear strength of synthetic methane hydrate sediments.

Masui, A., Miyazaki, K., Haneda, H., Ogata, Y., Aoki, K., 2008. Mechanical Properties of Natural Gas Hydrate Bearing Sediments Retrieved from Eastern Nankai Trough. Presented at the Offshore Technology Conference, OnePetro. https://doi.org/10.4043/19277-MS

Matyka, M., Khalili, A., Koza, Z., 2008. Tortuosity-porosity relation in porous media flow. Phys. Rev. E 78, 026306. https://doi.org/10.1103/PhysRevE.78.026306

Max, M.D., 2003. Natural Gas Hydrate in Oceanic and Permafrost Environments. Springer Science & Business Media.

Mayne, P.W., Coop, M.R., Springman, S.M., Huang, A.B., Zornberg, J.G., 2009. Geomaterial behavior and testing, in: Proceedings of the 17th International Conference on Soil Mechanics and Geotechnical Engineering (Volumes 1, 2, 3 and 4). IOS Press, pp. 2777–2872. https://doi.org/10.3233/978-1-60750-031-5-2777

Mienert, J., Vanneste, M., Bünz, S., Andreassen, K., Haflidason, H., Sejrup, H.P., 2005. Ocean warming and gas hydrate stability on the mid-Norwegian margin at the Storegga Slide. Marine and Petroleum Geology, Ormen Lange - an integrated study for the safe development of a deep-water gas field within the Storegga Slide Complex, NE Atlantic continental margin 22, 233–244. https://doi.org/10.1016/j.marpetgeo.2004.10.018

Milkov, A.V., 2004. Global estimates of hydrate-bound gas in marine sediments: how much is really out there? Earth-Science Reviews 66, 183–197. https://doi.org/10.1016/j.earscirev.2003.11.002

Milkov, A.V., Sassen, R., 2001. Estimate of gas hydrate resource, northwestern Gulf of Mexico continental slope. Marine Geology 179, 71–83. https://doi.org/10.1016/S0025-3227(01)00192-X

Minshull, T.A., Marín-Moreno, H., Betlem, P., Bialas, J., Bünz, S., Burwicz, E., Cameselle, A.L., Cifci, G., Giustiniani, M., Hillman, J.I.T., Hölz, S., Hopper, J.R., Ion, G., León, R., Magalhaes, V., Makovsky, Y., Mata, M.-P., Max, M.D., Nielsen, T., Okay, S., Ostrovsky, I., O'Neill, N., Pinheiro, L.M., Plaza-Faverola, A.A., Rey, D., Roy, S., Schwalenberg, K., Senger, K., Vadakkepuliyambatta, S., Vasilev, A., Vázquez, J.-T., 2020. Hydrate occurrence in Europe: A review of available evidence. Marine and Petroleum Geology 111, 735–764. https://doi.org/10.1016/j.marpetgeo.2019.08.014

Misyura, S.Y., 2020. Developing the environmentally friendly technologies of combustion of gas hydrates. Reducing harmful emissions during combustion. Environmental Pollution 265, 114871. https://doi.org/10.1016/j.envpol.2020.114871

Miyazaki, K., Masui, A., Aoki, K., Sakamoto, Y., Yamaguchi, T., Okubo, S., 2010. Strain-Rate Dependence of Triaxial Compressive Strength of Artificial Methane-Hydrate-Bearing Sediment. International Journal of Offshore and Polar Engineering 20.

Miyazaki, K., Masui, A., Sakamoto, Y., Aoki, K., Tenma, N., Yamaguchi, T., 2011. Triaxial compressive properties of artificial methane-hydrate-bearing sediment. Journal of Geophysical Research: Solid Earth 116. https://doi.org/10.1029/2010JB008049

Miyazaki, K., Masui, A., Sakamoto, Y., Tenma, N., Yamaguchi, T., 2010. Effect of Confining Pressure on Triaxial Compressive Properties of Artificial Methane Hydrate Bearing Sediments. Presented at the Offshore Technology Conference, OnePetro. https://doi.org/10.4043/20721-MS

Miyazaki, K., Masui, A., Yamamoto, Y., Ogata, Y., Aoki, K., Yamaguchi, T., 2009. Investigation of Deformation Mechanism For Methane Hydrate Sediment Based Upon Mechanical Properties In Unloading And Reloading Process Under Triaxial Compression. Presented at the Eighth ISOPE Ocean Mining Symposium, OnePetro.

Miyazaki, K., Oikawa, Y., Haneda, H., Yamaguchi, T., 2016. Triaxial Compressive Property of Artificial CO2-Hydrate Sand. International Journal of Offshore and Polar Engineering 26, 315–320. https://doi.org/10.17736/ijope.2016.jc631

Miyazaki, K., Tenma, N., Aoki, K., Yamaguchi, T., 2012. A Nonlinear Elastic Model for Triaxial Compressive Properties of Artificial Methane-Hydrate-Bearing Sediment Samples. Energies 5, 4057–4075. https://doi.org/10.3390/en5104057

Miyazaki, K., Tenma, N., Yamaguchi, T., 2017. Relationship between Creep Property and Loading-Rate Dependence of Strength of Artificial Methane-Hydrate-Bearing Toyoura Sand under Triaxial Compression. Energies 10, 1466. https://doi.org/10.3390/en10101466

Moridis, G., Apps, J., Pruess, K., Myer, L., 1998. EOSHYDR: A TOUGH2 Module for CH4-Hydrate Release and Flow in theSubsurface (No. LBNL-42386). Lawrence Berkeley National Lab. (LBNL), Berkeley, CA (United States).

Moridis, G.J., Collett, T.S., Boswell, R., Kurihara, M., Reagan, M.T., Koh, C., Sloan, E.D., 2008. Toward Production From Gas Hydrates: Current Status, Assessment of Resources, and Model-Based Evaluation of Technology and Potential. Presented at the SPE Unconventional Reservoirs Conference, OnePetro. https://doi.org/10.2118/114163-MS

Moridis, G.J., Collett, T.S., Dallimore, S.R., Satoh, T., Hancock, S., Weatherill, B., 2004. Numerical studies of gas production from several CH4 hydrate zones at the Mallik site, Mackenzie Delta, Canada. Journal of Petroleum Science and Engineering 43, 219–238. https://doi.org/10.1016/j.petrol.2004.02.015

Moridis, G.J., Collett, T.S., Pooladi-Darvish, M., Hancock, S., Santamarina, C., Boswell, R., Kneafsey, T., Rutqvist, J., Kowalsky, M.B., Reagan, M.T., Sloan, E.D., Sum, A.K., Koh, C.A., 2011. Challenges, Uncertainties, and Issues Facing Gas Production From Gas-Hydrate Deposits. SPE Reservoir Evaluation & Engineering 14, 76–112. https://doi.org/10.2118/131792-PA

Muraoka, M., Ohtake, M., Susuki, N., Morita, H., Oshima, M., Yamamoto, Y., 2019. Thermal properties of highly saturated methane hydrate-bearing sediments recovered from the Krishna–Godavari Basin. Marine and Petroleum Geology, Marine Gas Hydrate Reservoir Systems Along the Eastern Continental Margin of India: Results of the National Gas Hydrate Program Expedition 02 108, 321–331. https://doi.org/10.1016/j.marpetgeo.2018.10.037

Nakagawa, R., Hachikubo, A., Shoji, H., 2008. Dissociation and specific heats of gas hydrate under submarine and sublacustrine environments.

Nakai, T., Matsuoka, H., 1983. Shear Behaviors of Sand and Clay Under Three-Dimensional Stress Condition. Soils and Foundations 23, 26–42. https://doi.org/10.3208/sandf1972.23.2_26

Nakashima, K., Nakata, Y., Hyodo, M., Yoshimoto, N., Hiraoka, S., Kajiyama, S., 2021. Compressive characteristics of methane hydrate-bearing sands under isotropic consolidation. Soils and Foundations 61, 506–519. https://doi.org/10.1016/j.sandf.2021.01.011

Narasimhan, T.N., 1999. Fourier's heat conduction equation: History, influence, and connections. Reviews of Geophysics 37, 151–172. https://doi.org/10.1029/1998RG900006

Nasir, Q., Suleman, H., Elsheikh, Y.A., 2020. A review on the role and impact of various additives as promoters/ inhibitors for gas hydrate formation. Journal of Natural Gas Science and Engineering 76, 103211. https://doi.org/10.1016/j.jngse.2020.103211

Ng, C.W.W., Baghbanrezvan, S., Kadlicek, T., Zhou, C., 2020. A state-dependent constitutive model for methane hydrate-bearing sediments inside the stability region. Géotechnique 70, 1094–1108. https://doi.org/10.1680/jgeot.18.P.143

Nishihara, M., 1952. Creep of shale and sandy-shale. The Journal of the Geological Society of Japan 58, 373–377. https://doi.org/10.5575/geosoc.58.373

Noguchi, S., Shimoda, N., Takano, O., Oikawa, N., Inamori, T., Saeki, T., Fujii, T., 2011. 3-D internal architecture of methane hydrate-bearing turbidite channels in the eastern Nankai Trough, Japan. Marine and Petroleum Geology, Occurrence and exploration of gas hydrate in the marginal seas and continental margin of the Asia, India and Oceania region 28, 1817–1828. https://doi.org/10.1016/j.marpetgeo.2011.02.004

Nova, R., 2004. Development of Elastoplastic Strain Hardening Models of Soil Behaviour, in: Darve, F., Vardoulakis, I. (Eds.), Degradations and Instabilities in Geomaterials, International Centre for Mechanical Sciences. Springer, Vienna, pp. 35–76. https://doi.org/10.1007/978-3-7091-2768-1_2

Pang, X.-Q., Chen, Z.-H., Jia, C.-Z., Wang, E.-Z., Shi, H.-S., Wu, Z.-Y., Hu, T., Liu, K.-Y., Zhao, Z.-F., Pang, B., Wang, T., 2021. Evaluation and re-understanding of the global natural gas hydrate resources. Pet. Sci. 18, 323–338. https://doi.org/10.1007/s12182-021-00568-9

Park, J., Castro, G.M., Carlos Santamarina, J., 2018. Closure to "Revised Soil Classification System for Coarse-Fine Mixtures" by Junghee Park and J. Carlos Santamarina. Journal of Geotechnical and Geoenvironmental Engineering 144, 07018019. https://doi.org/10.1061/(ASCE)GT.1943-5606.0001908

Partoon, B., Malik, S.N.A., Azemi, M.H., Sabil, K.M., 2013. Experimental investigations on the potential of SDS as low-dosage promoter for carbon dioxide hydrate formation. Asia-Pacific Journal of Chemical Engineering 8, 916–921. https://doi.org/10.1002/apj.1736

Pecher, I.A., Holbrook, W.S., 2003. Seismic Methods for Detecting and Quantifying Marine Methane Hydrate/Free Gas Reservoirs, in: Max, M.D. (Ed.), Natural Gas Hydrate: In Oceanic and Permafrost Environments. Springer Netherlands, Dordrecht, pp. 275–294. https://doi.org/10.1007/978-94-011-4387-5_22

Pegah, E., Liu, H., 2020. Evaluating the overconsolidation ratios and peak friction angles of granular soil deposits using noninvasive seismic surveying. Acta Geotech. 15, 3193–3209. https://doi.org/10.1007/s11440-020-00953-5

Pei, J., Wei, N., Zhang, B., Zhao, J., Kvamme, B., Coffin, R.B., Li, H., Bai, R., 2022. Imitating the effects of drilling fluid invasion on the strength behaviors of hydrate-bearing sediments: An experimental study. Frontiers in Earth Science 10, 994602. https://doi.org/10.3389/feart.2022.994602

Perzyna, P., 1963. The constitutive equations for work-hardening and rate sensitive plastic materials. Proc. Vibrational Problems 4, 281–290.

Perzyna, P., 1966. Fundamental Problems in Viscoplasticity, in: Chernyi, G.G., Dryden, H.L., Germain, P., Howarth, L., Olszak, W., Prager, W., Probstein, R.F., Ziegler, H. (Eds.), Advances in Applied Mechanics. Elsevier, pp. 243–377. https://doi.org/10.1016/S0065-2156(08)70009-7

Pinkert, S., 2017. Rowe's Stress-Dilatancy Theory for Hydrate-Bearing Sand. International Journal of Geomechanics 17, 06016008. https://doi.org/10.1061/(ASCE)GM.1943-5622.0000682

Pinkert, S., Grozic, J.L.H., 2015. Failure Mechanisms in Cemented Hydrate-Bearing Sands. J. Chem. Eng. Data 60, 376–382. https://doi.org/10.1021/je500638c

Pinkert, S., Grozic, J.L.H., 2014. Prediction of the mechanical response of hydrate-bearing sands. Journal of Geophysical Research: Solid Earth 119, 4695–4707. https://doi.org/10.1002/2013JB010920

Pinkert, S., Grozic, J.L.H., Priest, J.A., 2015. Strain-Softening Model for Hydrate-Bearing Sands. Int. J. Geomech. 15, 04015007. https://doi.org/10.1061/(ASCE)GM.1943-5622.0000477

Phillips, O.M., 1991. Flow and Reactions in Permeable Rocks. Cambridge University Press.

Pinkert, S., Grozic, J.L.H., 2014. Prediction of the mechanical response of hydrate-bearing sands. Journal of Geophysical Research: Solid Earth 119, 4695–4707. https://doi.org/10.1002/2013JB010920

Poirier, J.P., 1985. Creep of Crystals: High-Temperature Deformation Processes in Metals, Ceramics and Minerals. Cambridge University Press.

Poorooshasb, H.B., Holubec, I., Sherbourne, A.N., 1966. Yielding and Flow of Sand in Triaxial Compression: Part I. Can. Geotech. J. 3, 179–190. https://doi.org/10.1139/t66-023

Prashant, J., Yang, J., Jadhawar, J., Tohidi, B., 2005. PRELIMINARY EXPERIMENTAL INVESTIGATION ON REPLACING METHANE IN HYDRATE STRUCTURE WITH CARBON DIOXIDE IN POROUS MEDIA.

Pribnow, D., Umsonst, T., 1993. Estimation of thermal conductivity from the mineral composition: Influence of fabric and anisotropy. Geophysical Research Letters 20, 2199–2202. https://doi.org/10.1029/93GL02135

Priest, J.A., Hayley, J.L., 2019. Strength of Laboratory Synthesized Hydrate-Bearing Sands and Their Relationship to Natural Hydrate-Bearing Sediments. Journal of Geophysical Research: Solid Earth 124, 12556–12575. https://doi.org/10.1029/2019JB018324

Priest, J.A., Rees, E.V.L., Clayton, C.R.I., 2009. Influence of gas hydrate morphology on the seismic velocities of sands. Journal of Geophysical Research: Solid Earth 114. https://doi.org/10.1029/2009JB006284

Qin, Y., Pan, Z., Liu, Z., Shang, L., Zhou, L., 2021. Influence of the Particle Size of Porous Media on the Formation of Natural Gas Hydrate: A Review. Energy Fuels 35, 11640–11664. https://doi.org/10.1021/acs.energyfuels.1c00936

Quadrelli, R., Peterson, S., 2007. The energy–climate challenge: Recent trends in CO2 emissions from fuel combustion. Energy Policy 35, 5938–5952. https://doi.org/10.1016/j.enpol.2007.07.001

Radhakrishnan, R., Trout, B.L., 2002. A new approach for studying nucleation phenomena using molecular simulations: Application to CO2 hydrate clathrates. The Journal of Chemical Physics 117, 1786–1796. https://doi.org/10.1063/1.1485962

Rake, L., Pinkert, S., 2021. The 'excess gas' method for laboratory formation of methane hydrate-bearing sand: geotechnical application. Sci Rep 11, 22068. https://doi.org/10.1038/s41598-021-00777-7

Ren, X., Guo, Z., Ning, F., Ma, S., 2020. Permeability of hydrate-bearing sediments. Earth-Science Reviews 202, 103100. https://doi.org/10.1016/j.earscirev.2020.103100

Richard, A.R., Adidharma, H., 2013. The performance of ionic liquids and their mixtures in inhibiting methane hydrate formation. Chemical Engineering Science 87, 270–276. https://doi.org/10.1016/j.ces.2012.10.021

Ripmeester, J.A., 2000. Hydrate Research-From Correlations to a Knowledge-based Discipline: The Importance of Structure. Annals of the New York Academy of Sciences 912, 1–16. https://doi.org/10.1111/j.1749-6632.2000.tb06754.x

Rojas, Y., Lou, X., 2010. Instrumental analysis of gas hydrates properties. Asia-Pacific Journal of Chemical Engineering 5, 310–323. https://doi.org/10.1002/apj.293

Roostaie, M., Leonenko, Y., 2020. Analytical modeling of methane hydrate dissociation under thermal stimulation. Journal of Petroleum Science and Engineering 184, 106505. https://doi.org/10.1016/j.petrol.2019.106505

Roscoe, K., Burland, J., 1968. On the generalized stress-strain behaviour of wet clay.

Roscoe, K., Schofield, A., 1972. Mechanical Behaviour of an idealised Wet-Clay.

Roscoe, K.H., Schofield, An., Wroth, C P., 1958. On the yielding of soils. Geotechnique 8, 22–53.

Roscoe, K.H., Schofield, A., Thurairajah, A., 1964 An evaluation of test data for selecting a yield criterion for soils. West Conshohocken: ASTM International.

Rowe, P.W., Taylor, G.I., 1962. The stress-dilatancy relation for static equilibrium of an assembly of particles in contact. Proceedings of the Royal Society of London. Series A. Mathematical and Physical Sciences 269, 500–527. https://doi.org/10.1098/rspa.1962.0193

Ruppel, C.D., Kessler, J.D., 2017. The interaction of climate change and methane hydrates. Reviews of Geophysics 55, 126–168. https://doi.org/10.1002/2016RG000534

Rydzy, M.B., Schicks, J.M., Naumann, R., Erzinger, J., 2007. Dissociation Enthalpies of Synthesized Multicomponent Gas Hydrates with Respect to the Guest Composition and Cage Occupancy. J. Phys. Chem. B 111, 9539–9545. https://doi.org/10.1021/jp0712755

Sahoo, S.K., Best, A.I., 2021. The Influence of Gas Hydrate Morphology on Reservoir Permeability and Geophysical Shear Wave Remote Sensing. Journal of Geophysical Research: Solid Earth 126, e2021JB022206. https://doi.org/10.1029/2021JB022206

Sahu, C., Kumar, R., Sangwai, J.S., 2020. Comprehensive Review on Exploration and Drilling Techniques for Natural Gas Hydrate Reservoirs. Energy Fuels 34, 11813–11839. https://doi.org/10.1021/acs.energyfuels.0c02202

Sánchez, M., Gai, X., Santamarina, J.C., 2017. A constitutive mechanical model for gas hydrate bearing sediments incorporating inelastic mechanisms. Computers and Geotechnics 84, 28–46. https://doi.org/10.1016/j.compgeo.2016.11.012

Santamarina, J.C., Dai, S., Terzariol, M., Jang, J., Waite, W.F., Winters, W.J., Nagao, J., Yoneda, J., Konno, Y., Fujii, T., Suzuki, K., 2015. Hydro-bio-geomechanical properties of hydrate-bearing sediments from Nankai Trough. Marine and Petroleum Geology, Gas hydrate drilling in Eastern Nankai 66, 434–450. https://doi.org/10.1016/j.marpetgeo.2015.02.033

Santamarina, J.C., Ruppel, C., 2010. The Impact of Hydrate Saturation on the Mechanical, Electrical, and Thermal Properties of Hydrate-Bearing Sand, Silts, and Clay, in: Geophysical Characterization of Gas Hydrates, Geophysical Developments Series. Society of Exploration Geophysicists, pp. 373–384. https://doi.org/10.1190/1.9781560802197.ch26

Santamarina, J.C., Shin, H., 2009. Friction in Granular Media. Meso-scale Shear Physics in Earthquake and Landslide Mechanics. CRC Press, London, 2009 157-188.

Schicks, J.M., Luzi-Helbing, M., 2015. Kinetic and Thermodynamic Aspects of Clathrate Hydrate Nucleation and Growth. J. Chem. Eng. Data 60, 269–277. https://doi.org/10.1021/je5005593

Schicks, J.M., 2022. Gas hydrates in nature and in the laboratory: necessary requirements for formation and properties of the resulting hydrate phase. ChemTexts 8, 13. https://doi.org/10.1007/s40828-022-00164-3

Schwalenberg, K., Gehrmann, R.A.S., Bialas, J., Rippe, D., 2020. Analysis of marine controlled source electromagnetic data for the assessment of gas hydrates in the Danube deep-sea fan, Black Sea. Marine and Petroleum Geology 122, 104650. https://doi.org/10.1016/j.marpetgeo.2020.104650

Seol, Y., Lei, L., Choi, J.-H., Jarvis, K., Hill, D., 2019. Integration of triaxial testing and pore-scale visualization of methane hydrate bearing sediments. Review of Scientific Instruments 90, 124504. https://doi.org/10.1063/1.5125445

Shahnazar, S., Hasan, N., 2014. Gas hydrate formation condition: Review on experimental and modeling approaches. Fluid Phase Equilibria 379, 72–85. https://doi.org/10.1016/j.fluid.2014.07.012

Shan, W., Chen, H., Yuan, Y., Ma, Y., 2022. Effectiveness of excess gas method for the preparation of hydrate-bearing sediments: Influence and mechanism of moisture content. Journal of Cleaner Production 366, 132889. https://doi.org/10.1016/j.jclepro.2022.132889

Shen, J., Chiu, A.C.F., Ng, C.W.W., 2022. Modeling the Mechanical Behavior of Methane Hydrate-Bearing Sand Using the Equivalent Granular Void Ratio. Journal of Marine Science and Engineering 10, 1040. https://doi.org/10.3390/jmse10081040

Shen, J., Chiu, C.F., Ng, C.W.W., Lei, G.H., Xu, J., 2016. A state-dependent critical state model for methane hydrate-bearing sand. Computers and Geotechnics 75, 1–11. https://doi.org/10.1016/j.compgeo.2016.01.013

Shen, P., Li, G., Li, B., Li, X., 2020. Coupling effect of porosity and hydrate saturation on the permeability of methane hydrate-bearing sediments. Fuel 269, 117425. https://doi.org/10.1016/j.fuel.2020.117425

Shen, S., Li, Y., Sun, X., Wang, L., Song, Y., 2022. Stress behavior of hydrate-bearing sands with changing temperature and hydrate saturation. Journal of Natural Gas Science and Engineering 98, 104389. https://doi.org/10.1016/j.jngse.2021.104389

Shen, S., Li, Y., Sun, X., Wang, L., Song, Y., 2020. Experimental study on the permeability of methane hydrate-bearing sediments during triaxial loading. Journal of Natural Gas Science and Engineering 82, 103510. https://doi.org/10.1016/j.jngse.2020.103510

Shen, S., Sun, X., Wang, L., Song, Y., Li, Y., 2021. Effect of Temperature on the Mechanical Properties of Hydrate-Bearing Sand under Different Confining Pressures. Energy Fuels 35, 4106–4117. https://doi.org/10.1021/acs.energyfuels.1c00052

Sheng, D.C., Fredlund, D.G., 2008. Elasto-plastic Modelling of Unsaturated Soils: an Overview. Keynote lecture, 12th Int conf int assoc computer methods & advances in geomechanics (IACMAG). 2008 1-6.

Sloan, E.D., 1998. Gas Hydrates: Review of Physical/Chemical Properties. Energy Fuels 12, 191–196. https://doi.org/10.1021/ef970164+

Sloan, E.D., 2003. Fundamental principles and applications of natural gas hydrates. Nature 426, 353–359. https://doi.org/10.1038/nature02135

Sloan, E.D., Fleyfel, F., 1992. Hydrate dissociation enthalpy and guest size. Fluid Phase Equilibria 76, 123–140. https://doi.org/10.1016/0378-3812(92)85082-J

Stow, D., Brackenridge, R., Patel, U., Toulmin, S., 2012. Geohazards and Ocean Hazards in Deepwater: Overview and Methods of Assessment. Presented at the Offshore Technology Conference, OnePetro. https://doi.org/10.4043/23697-MS

Soga, K., Lee, S., Ng, M., Klar, A., 2006. Characterisation and engineering properties of methane hydrate soils. Characterisation and engineering properties of natural soils 4, 2591–1642.

Soga, K., O'sullivan, C., 2010. Modeling of Geomaterials Behavior. Soils and Foundations 50, 861–875. https://doi.org/10.3208/sandf.50.861

Solanki, C., Desai, M., 2008. Preconsolidation Pressure from Soil Index and Plasticity Properties. 12th International Conference on Computer Methods and Advances in Geomechanics 2008 2.

Song, Y., Luo, T., Madhusudhan, B.N., Sun, X., Liu, Y., Kong, X., Li, Y., 2019. Strength behaviors of CH4 hydrate-bearing silty sediments during thermal decomposition. Journal of Natural Gas Science and Engineering 72, 103031. https://doi.org/10.1016/j.jngse.2019.103031

Song, Y., Zhu, Y., Liu, W., Li, Y., Lu, Y., Shen, Z., 2016. The effects of methane hydrate dissociation at different temperatures on the stability of porous sediments. Journal of Petroleum Science and Engineering 147, 77–86. https://doi.org/10.1016/j.petrol.2016.05.009

Song, Y., Zhu, Y., Liu, W., Zhao, J., Li, Y., Chen, Y., Shen, Z., Lu, Y., Ji, C., 2014. Experimental research on the mechanical properties of methane hydrate-bearing sediments during hydrate dissociation. Marine and Petroleum Geology 51, 70–78. https://doi.org/10.1016/j.marpetgeo.2013.11.017

Spangenberg, E., 2001. Modeling of the influence of gas hydrate content on the electrical properties of porous sediments. Journal of Geophysical Research: Solid Earth 106, 6535–6548. https://doi.org/10.1029/2000JB900434

Stern, L.A., Kirby, S.H., Durham, W.B., 1998. Polycrystalline Methane Hydrate: Synthesis from Superheated Ice, and Low-Temperature Mechanical Properties. Energy Fuels 12, 201–211. https://doi.org/10.1021/ef970167m

Sukkarak, R., Pramthawee, P., Jongpradist, P., 2017. A modified elasto-plastic model with double yield surfaces and considering particle breakage for the settlement analysis of high rockfill dams. KSCE J Civ Eng 21, 734–745. https://doi.org/10.1007/s12205-016-0867-9

Sultan, N., Cochonat, P., Foucher, J.P., Mienert, J., 2004. Effect of gas hydrates melting on seafloor slope instability. Marine Geology, COSTA - Continental Slope Stability 213, 379–401. https://doi.org/10.1016/j.margeo.2004.10.015

Sun, J., Hao, X., Li, C., Wu, N., Chen, Q., Liu, C., Li, Y., Meng, Q., Huang, L., Bu, Q., 2022. Experimental Study on the Distribution Characteristics of CO_2 in Methane Hydrate-Bearing Sediment during CH4/CO2 Replacement. Energies 15, 5634. https://doi.org/10.3390/en15155634

Sun, X., Guo, X., Shao, L., Li, Y., 2016. Drucker-Prager elasto-plastic constitutive model for methane hydrate-bearing sediment. Trans. Tianjin Univ. 22, 441–450. https://doi.org/10.1007/s12209-016-2728-5

Sun, X., Guo, X., Shao, L., Tang, H., 2015. A thermodynamics-based critical state constitutive model for methane hydrate bearing sediment. Journal of Natural Gas Science and Engineering 27, 1024–1034. https://doi.org/10.1016/j.jngse.2015.09.048

Sun, X., Wang, L., Luo, H., Song, Y., Li, Y., 2019. Numerical modeling for the mechanical behavior of marine gas hydrate-bearing sediments during hydrate production by depressurization. Journal of Petroleum Science and Engineering 177, 971–982. https://doi.org/10.1016/j.petrol.2019.03.012

Sun, X., Zhang, G., Zhao, Y., Song, J., Wang, S., Zhou, G., Lu, G., 2022. Effects of Alcohol Chain Length on Methane Hydrate Dissociation: Insights from Molecular Dynamics Simulations, in: Lin, J. (Ed.),

Proceedings of the International Field Exploration and Development Conference. Springer Nature, Singapore, pp. 2146–2158. https://doi.org/10.1007/978-981-99-1964-2_183

Sun, Y., Zhang, Y., Liu, L., Lu, J., Tian, S., Li, G., 2023. Strength Behaviors and Constitutive Model of Gas-Saturated Methane Hydrate-Bearing Sediment in Gas-Rich Phase Environment. JMSE 11, 142. https://doi.org/10.3390/jmse11010142

Sun, Z.G., Sun, L., 2010. Equilibrium Conditions of Semi-Clathrate Hydrate Dissociation for Methane + Tetra-n-butyl Ammonium Bromide. J. Chem. Eng. Data 55, 3538–3541. https://doi.org/10.1021/je100183s

Sun, Z.M., Zhang, J., Liu, C.L., Zhao, S.J., Ye, Y.G., 2013. Experimental Study on the In Situ Mechanical Properties of Methane Hydrate-Bearing Sediments. Applied Mechanics and Materials 275–277, 326–331. https://doi.org/10.4028/www.scientific.net/AMM.275-277.326

Tan, B.B., 2004. Geotechnical Characterization of Sediments from Hydrate Ridge, Cascadia Continental Margin. Massachusetts Institute of Technology, 2004.

Tanaka, H., Yagasaki, T., Matsumoto, M., 2020. On the Occurrence of Clathrate Hydrates in Extreme Conditions: Dissociation Pressures and Occupancies at Cryogenic Temperatures with Application to Planetary Systems. The Planetary Science Journal, 80. https://doi.org/10.3847/PSJ/abc3c0

Tang, B., Zhu, C., Qiu, N., Cui, Y., Guo, S., Luo, X., Zhang, B., Li, K., Li, W., Fu, X., 2021. Analyzing and Estimating Thermal Conductivity of Sedimentary Rocks from Mineral Composition and Pore Property. Geofluids 2021, 6665027. https://doi.org/10.1155/2021/6665027

Teerawattanasuk, C., Voottipruex, P., 2014. Influence of Clay and Silt Proportions on Cement-Treated Fine-Grained Soil. Journal of Materials in Civil Engineering 26, 420–428. https://doi.org/10.1061/(ASCE)MT.1943-5533.0000813

Teixeira Parente, M., Mattis, S., Gupta, S., Deusner, C., Wohlmuth, B., 2019. Efficient parameter estimation for a methane hydrate model with active subspaces. Comput Geosci 23, 355–372. https://doi.org/10.1007/s10596-018-9769-x

Terzariol, M., Park, J., Castro, G.M., Santamarina, J.C., 2020. Methane hydrate-bearing sediments: Pore habit and implications. Marine and Petroleum Geology 116, 104302. https://doi.org/10.1016/j.marpetgeo.2020.104302

Torré, J. P., Haillot, D., Rigal, S., de Souza Lima, R., Dicharry, C., Bedecarrats, J.P., 2015. 1,3 Dioxolane versus tetrahydrofuran as promoters for CO2-hydrate formation: Thermodynamics properties, and kinetics

in presence of sodium dodecyl sulfate. Chemical Engineering Science 126, 688–697. https://doi.org/10.1016/j.ces.2015.01.018

Tse, J.S., 2015. Computational Techniques in the Study of the Properties of Clathrate Hydrates, in: Reviews in Computational Chemistry Volume 28. John Wiley & Sons, Ltd, pp. 315–389. https://doi.org/10.1002/9781118889886.ch7

Uchida, S., Soga, K., Yamamoto, K., 2012. Critical state soil constitutive model for methane hydrate soil. Journal of Geophysical Research: Solid Earth 117. https://doi.org/10.1029/2011JB008661

Uchida, S., Xie, X.-G., Leung, Y.F., 2016. Role of critical state framework in understanding geomechanical behavior of methane hydrate-bearing sediments. Journal of Geophysical Research: Solid Earth 121, 5580–5595. https://doi.org/10.1002/2016JB012967

Vafaei, N., Fakharian, K., Sadrekarimi, A., 2021. Sand-sand and sand-steel interface grain-scale behavior under shearing. Transportation Geotechnics 30, 100636. https://doi.org/10.1016/j.trgeo.2021.100636

Vargas, W.L., McCarthy, J.J., 2001. Heat conduction in granular materials. AIChE Journal 47, 1052–1059. https://doi.org/10.1002/aic.690470511

Vlahakis, J.J., 1972. The Growth Rate of Ice Crystals : The Properties of carbon dioxide hydrate a review of properties of 51 gas hydrates. Office of Water 830, 56–86.

Viriyakul, C., Jeenmuang, K., Inkong, K., Kulprathipanja, S., Rangsunvigit, P., 2021. A detailed morphology investigation on the effects of mixed anionic and nonionic surfactants on methane hydrate formation and dissociation. Journal of Natural Gas Science and Engineering 90, 103904. https://doi.org/10.1016/j.jngse.2021.103904

Vosteen, H.-D., Schellschmidt, R., 2003. Influence of temperature on thermal conductivity, thermal capacity and thermal diffusivity for different types of rock. Physics and Chemistry of the Earth, Parts A/B/C, Heat Flow and the Structure of the Lithosphere 28, 499–509. https://doi.org/10.1016/S1474-7065(03)00069-X

v. Stackelberg, M., Müller, H.R., 1954. Feste Gashydrate II. Struktur und Raumchemie. Zeitschrift für Elektrochemie, Berichte der Bunsengesellschaft für physikalische Chemie 58, 25–39. https://doi.org/10.1002/bbpc.19540580105

Waite, W.F., Kneafsey, T.J., Winters, W.J., Mason, D.H., 2008. Physical property changes in hydrate-bearing sediment due to depressurization and subsequent repressurization. Journal of Geophysical Research: Solid Earth 113. https://doi.org/10.1029/2007JB005351

Waite, W.F., Santamarina, J.C., Cortes, D.D., Dugan, B., Espinoza, D.N., Germaine, J., Jang, J., Jung, J., Kneafsey, T.J., Shin, H., others, 2009. Physical properties of hydrate-bearing sediments. Reviews of geophysics 47. https://doi.org/10.1029/2008RG000279

Waite, W.F., Stern, L.A., Kirby, S.H., Winters, W.J., Mason, D.H., 2007. Simultaneous determination of thermal conductivity, thermal diffusivity and specific heat in sI methane hydrate. Geophysical Journal International 169, 767–774. https://doi.org/10.1111/j.1365-246X.2007.03382.x

Wang, B., Dong, H., Liu, Yanzhen, Lv, X., Liu, Yu, Zhao, J., Song, Y., 2018. Evaluation of thermal stimulation on gas production from depressurized methane hydrate deposits☆. Applied Energy, Transformative Innovations for a Sustainable Future – Part III 227, 710–718. https://doi.org/10.1016/j.apenergy.2017.08.005

Wan, R.G., Guo, P.J., 1998. A simple constitutive model for granular soils: Modified stress-dilatancy approach. Computers and Geotechnics 22, 109–133. https://doi.org/10.1016/S0266-352X(98)00004-4

Wang, K., Chang, Y., Chen, G., Sun, B., Sun, H., Li, H., Dai, Y., 2022. Three-dimensional mechanical behaviors of casing during gas production from marine hydrate reservoirs using depressurization. Energy 247, 123526. https://doi.org/10.1016/j.energy.2022.123526

Wang, L., Li, Y., Shen, S., Liu, W., Sun, X., Liu, Y., Zhao, J., 2022. Mechanical behaviours of gas-hydrate-bearing clayey sediments of the South China Sea. Environmental Geotechnics 9, 210–222. https://doi.org/10.1680/jenge.19.00048

Wang, L., Liu, W., Li, Y., Wu, P., Shen, S., 2019. Mechanical Behaviors of Methane Hydrate-Bearing Sediments Using Montmorillonite Clay. Energy Procedia, Innovative Solutions for Energy Transitions 158, 5281–5286. https://doi.org/10.1016/j.egypro.2019.01.648

Wang, L., Sun, X., Shen, S., Wu, P., Liu, T., Liu, W., Zhao, J., Li, Y., 2021. Undrained triaxial tests on water-saturated methane hydrate–bearing clayey-silty sediments of the South China Sea. Can. Geotech. J. 58, 351–366. https://doi.org/10.1139/cgj-2019-0711

Wang, L.Y., Zhang, Y.J., Xie, H.L., Lu, X.R., Wen, X.L., Liu, Z., Zhou, H.J., Liu, Z.J., Xu, Y.L., 2022. Effect of voltage and initial temperature on thermodynamics and kinetics of CO_2 hydrate formation in an electrostatic spraying reactor. Energy 239, 122384. https://doi.org/10.1016/j.energy.2021.122384

Wang, L., Zhao, J., Sun, X., Wu, P., Shen, S., Liu, T., Li, Y., 2021. Comprehensive review of geomechanical constitutive models of gas hydrate-bearing sediments. Journal of Natural Gas Science and Engineering 88, 103755. https://doi.org/10.1016/j.jngse.2020.103755

Wang, M.Q., Yang, J., 2014. IMPLEMENTATION, VERIFICATION AND APPLICATION OF THREE DIMENSIONAL HISS MODEL IN ABAQUS. ENGINEERING MECHANICS 31, 160-165.

Wang, R., Liu, W., Li, Y., Yu, F., Nie, X., Song, Y., 2012. Effects of Porosity on the Creep Behavior of Hydrate-Bearing Sediments, in: Volume 6: Materials Technology; Polar and Arctic Sciences and Technology; Petroleum Technology Symposium. Presented at the ASME 2012 31st International Conference on Ocean, Offshore and Arctic Engineering, American Society of Mechanical Engineers, Rio de Janeiro, Brazil, pp. 703–708. https://doi.org/10.1115/OMAE2012-84080

Wang, S., Cheng, Z.C., Liu, Q.B., Lv, P.F., Lv, J.C., Jiang, L.L., Song, Y.C., 2021. Microscope insights into gas hydrate formation and dissociation in sediments by using microfluidics. Chemical Engineering Journal 425, 130633. https://doi.org/10.1016/j.cej.2021.130633

Wang, S., Qi, J., Yin, Z., Zhang, J., Ma, W., 2014. A simple rheological element based creep model for frozen soils. Cold Regions Science and Technology 106–107, 47–54. https://doi.org/10.1016/j.coldregions.2014.06.007

Wang, X., Wu, S., Lee, M., Guo, Y., Yang, S., Liang, J., 2011. Gas hydrate saturation from acoustic impedance and resistivity logs in the Shenhu area, South China Sea. Marine and Petroleum Geology 28, 1625–1633. https://doi.org/10.1016/j.marpetgeo.2011.07.002

Wang, X., Xu, M., 2021. DEM investigation of the creep behavior of methane hydrate-bearing sand. IOP Conf. Ser.: Earth Environ. Sci. 861, 072133. https://doi.org/10.1088/1755-1315/861/7/072133

Wang, Y., Kou, X., Feng, J.C., Li, X.S., Zhang, Y., 2020. Sediment deformation and strain evaluation during methane hydrate dissociation in a novel experimental apparatus. Applied Energy 262, 114397. https://doi.org/10.1016/j.apenergy.2019.114397

Wang, Z., Qi, C., Yu, H., Zhao, F., Luo, Y., 2022. Elastoplastic constitutive model for gas hydrate bearing sediments considering hydrate occurrence habits. Geomech. Geophys. Geo-energ. Geo-resour. 8, 190. https://doi.org/10.1007/s40948-022-00494-z

Warrier, P., Khan, M.N., Srivastava, V., Maupin, C.M., Koh, C.A., 2016. Overview: Nucleation of clathrate hydrates. The Journal of Chemical Physics 145, 211705. https://doi.org/10.1063/1.4968590

Wei, J., Cheng, Y., Yan, C., Li, Q., Han, S., Ansari, U., 2019. Decomposition prevention through thermal sensitivity of hydrate formations around wellbore. Applied Thermal Engineering 159, 113921. https://doi.org/10.1016/j.applthermaleng.2019.113921

Wei, J., Fang, Y., Lu, Hailong, Lu, Hongfeng, Lu, J., Liang, J., Yang, S., 2018. Distribution and characteristics of natural gas hydrates in the Shenhu Sea Area, South China Sea. Marine and Petroleum Geology 98, 622–628. https://doi.org/10.1016/j.marpetgeo.2018.07.028

Wei, N., Bai, R., Zhao, J., Zhang, Y., Xue, J., 2021. The prospect of natural gas hydrate (NGH) under the vision of Peak Carbon Dioxide Emissions in China. Petroleum, Safe & Efficient Use of Natural Gas Hydrate 7, 357–363. https://doi.org/10.1016/j.petlm.2021.11.001

Wei, N., Pei, J., Li, H., Zhou, S., Zhao, J., Kvamme, B., Coffin, R.B., Zhang, L., Zhang, Y., Xue, J., 2024. Classification of natural gas hydrate resources: Review, application and prospect. Gas Science and Engineering 124, 205269. https://doi.org/10.1016/j.jgsce.2024.205269

White, M.D., Wurstner, S.K., McGrail, B.P., 2011. Numerical studies of methane production from Class 1 gas hydrate accumulations enhanced with carbon dioxide injection. Marine and Petroleum Geology, Thematic Set on Scientific results of the Mount Elbert Gas Hydrate Stratigraphic Test Well, Alaska North Slope 28, 546–560. https://doi.org/10.1016/j.marpetgeo.2009.06.008

Winters, W.J., Waite, W.F., Mason, D.H., Gilbert, L.Y., Pecher, I.A., 2007. Methane gas hydrate effect on sediment acoustic and strength properties. Journal of Petroleum Science and Engineering, Natural Gas Hydrate / Clathrate 56, 127–135. https://doi.org/10.1016/j.petrol.2006.02.003

Wu, D.M., Li, G., Li, X.S., Lv, X., 2017. Experimental investigation of permeability characteristics under different hydrate saturation. Chemical Industry and Engineering Progress, 36, 2916-2923

Wu, J., Ning, F., Trinh, T.T., Kjelstrup, S., Vlugt, T.J.H., He, J., Skallerud, B.H., Zhang, Z., 2015. Mechanical instability of monocrystalline and polycrystalline methane hydrates. Nat Commun 6, 8743. https://doi.org/10.1038/ncomms9743

Wu, N., Liu, C., Hao, X., 2018. Experimental simulations and methods for natural gas hydrate analysis in China. China Geology 1, 61–71. https://doi.org/10.31035/cg2018008

Wu, P., Li, Y., Liu, W., Liu, Y., Wang, D., Song, Y., 2020a. Microstructure Evolution of Hydrate-Bearing Sands During Thermal Dissociation and Ensued Impacts on the Mechanical and Seepage Characteristics. Journal of Geophysical Research: Solid Earth 125, e2019JB019103. https://doi.org/10.1029/2019JB019103

Wu, P., Li, Y., Liu, W., Sun, X., Kong, X., Song, Y., 2020b. Cementation Failure Behavior of Consolidated Gas Hydrate-Bearing Sand. Journal of Geophysical Research: Solid Earth 125, e2019JB018623. https://doi.org/10.1029/2019JB018623

Wu, P., Li, Y., Sun, X., Liu, W., Song, Y., 2021. Mechanical Characteristics of Hydrate-Bearing Sediment: A Review. Energy Fuels 35, 1041–1057. https://doi.org/10.1021/acs.energyfuels.0c03995

Wu, P., Li, Y., Wang, L., Sun, X., Wu, D., He, Y., Li, Q., Song, Y., 2022. Hydrate-bearing sediment of the South China Sea: Microstructure and mechanical characteristics. Engineering Geology 307, 106782. https://doi.org/10.1016/j.enggeo.2022.106782

Wu, Q., Zhao, Y., Yoshimoto, N., Guan, J., Nakata, Y., Kajiyama, S., Hyodo, M., 2023. Strain Rate-Dependent Mechanical Response of Hydrate-Bearing Sediments under Plane Strain Condition. Journal of Marine Science and Engineering 11, 1161. https://doi.org/10.3390/jmse11061161

Wu, Y., Li, N., Hyodo, M., Gu, M., Cui, J., Spencer, B.F., 2019. Modeling the mechanical response of gas hydrate reservoirs in triaxial stress space. International Journal of Hydrogen Energy 44, 26698–26710. https://doi.org/10.1016/j.ijhydene.2019.08.119

Wu, Y., Liao, J., Zhang, W., Cui, J., 2021. Characterization of stress–dilatancy behavior for methane hydrate-bearing sediments. Journal of Natural Gas Science and Engineering 92, 104000. https://doi.org/10.1016/j.jngse.2021.104000

Wu, Y., Tahmasebi, P., Liu, K., Lin, C., Kamrava, S., Liu, S., Fagbemi, S., Liu, C., Chai, R., An, S., 2023. Modeling the physical properties of hydrate-bearing sediments: Considering the effects of occurrence patterns. Energy 278, 127674. https://doi.org/10.1016/j.energy.2023.127674

Xie, X.G., 2019. Geomechanical behavior of methane hydrate bearing sediments: from laboratory to field scale.

Xie, Y., Li, R., Wang, X.-H., Zheng, T., Cui, J.-L., Yuan, Q., Qin, H.-B., Sun, C.-Y., Chen, G.-J., 2020. Review on the accumulation behavior of natural gas hydrates in porous sediments. Journal of Natural Gas Science and Engineering 83, 103520. https://doi.org/10.1016/j.jngse.2020.103520

Xu, J., Xu, C., Huang, L., Hyodo, M., 2023. Strength estimation and stress–dilatancy characteristics of natural gas hydrate-bearing sediments under high effective confining pressure. Acta Geotech. 18, 811–827. https://doi.org/10.1007/s11440-022-01620-7

Xu, J., Xu, C., Wang, R., Jiang, C., Jiao, S., Hyodo, M., 2022a. Microscopic mechanism analysis of influence of high effective confining pressure on mechanical properties of hydrate-bearing sediments. Computers and Geotechnics 152, 105011. https://doi.org/10.1016/j.compgeo.2022.105011

Xu, J., Xu, C., Yoshimoto, N., Hyodo, M., Kajiyama, S., Huang, L., 2022b. Compression and Deformation Characteristics of Hydrate-Bearing Sediments under High Effective Confining Pressure. International Journal of Geomechanics 22, 04022067. https://doi.org/10.1061/(ASCE)GM.1943-5622.0002382

Xu, J., Xu, C., Yoshimoto, N., Hyodo, M., Kajiyama, S., Huang, L., 2022c. Experimental Investigation of the Mechanical Properties of Methane Hydrate–Bearing Sediments under High Effective Confining Pressure. Journal of Geotechnical and Geoenvironmental Engineering 148, 04021190. https://doi.org/10.1061/(ASCE)GT.1943-5606.0002728

Xu, M., Wang, X., 2023. DEM simulations of the creep behavior of cemented methane hydrate-bearing sand. Gas Science and Engineering 110, 204881. https://doi.org/10.1016/j.jgsce.2023.204881

Yakushev, V.S., Chuvilin, E.M., 2000. Natural gas and gas hydrate accumulations within permafrost in Russia. Cold Regions Science and Technology 31, 189–197. https://doi.org/10.1016/S0165-232X(00)00012-4

Yamamoto, K., 2015. Overview and introduction: Pressure core-sampling and analyses in the 2012–2013 MH21 offshore test of gas production from methane hydrates in the eastern Nankai Trough. Marine and Petroleum Geology, Gas hydrate drilling in Eastern Nankai 66, 296–309. https://doi.org/10.1016/j.marpetgeo.2015.02.024

Yan, C., Cheng, Y., Li, M., Han, Z., Zhang, H., Li, Q., Teng, F., Ding, J., 2017. Mechanical experiments and constitutive model of natural gas hydrate reservoirs. International Journal of Hydrogen Energy 42, 19810–19818. https://doi.org/10.1016/j.ijhydene.2017.06.135

Yan, C., Li, Y., Yan, X., Cheng, Y., Han, Z., Tian, W., Ren, X., 2019. Wellbore shrinkage during drilling in methane hydrate reservoirs. Energy Science & Engineering 7, 930–942. https://doi.org/10.1002/ese3.323

Yan, C., Ren, X., Cheng, Y., Song, B., Li, Y., Tian, W., 2020. Geomechanical issues in the exploitation of natural gas hydrate. Gondwana Research 81, 403–422. https://doi.org/10.1016/j.gr.2019.11.014

Yan, M., Yan, R., Yu, H., 2021. Strain-Softening Characteristics of Hydrate-Bearing Sediments and Modified Duncan–Chang Model. Advances in Materials Science and Engineering 2021, 1–15. https://doi.org/10.1155/2021/2809370

Yan, R., Yu, H., Yang, D., Tang, H., Zhang, Q., 2023. Shear strength and pore pressure characteristics of methane hydrate-bearing soil under undrained condition. International Journal of Hydrogen Energy 48, 12240–12256. https://doi.org/10.1016/j.ijhydene.2022.12.038

Yan, R.T., Wei, C.F., Wei, H.Z., Tian, H.H., Wu, E.L., 2012. Effect of hydrate formation on mechanical strength of hydrate-bearing sand. Chinese Journal of Geotechnical Engineering 34, 1234–1240.

Yang, D., Yan, R., Yan, M., Lu, D., Wei, C., 2023. Geomechanical properties of artificial methane hydrate-bearing fine-grained sediments. Gas Science and Engineering 109, 104852. https://doi.org/10.1016/j.jngse.2022.104852

Yang, J., Tohidi, B., Chapoy, A., 2008. IMPACT OF SEDIMENTARY MINERALOGY ON GEOPHYSICAL AND GEOMECHANICAL PROPERTIES OF HYDRATE-BEARING SEDIMENTS. Sixth International Conference on Gas Hydrates, Sponsor, Vancouver, BC, Canada, p. 6-10.

Yang, L., Zhao, J., Liu, W., Li, Y., Yang, M., Song, Y., 2015. Microstructure Observations of Natural Gas Hydrate Occurrence in Porous Media Using Microfocus X-ray Computed Tomography. Energy Fuels 29, 4835–4841. https://doi.org/10.1021/acs.energyfuels.5b00881

Yang, M., Jing, W., Wang, P., Jiang, L., Song, Y., 2015. Effects of an additive mixture (THF+TBAB) on CO_2 hydrate phase equilibrium. Fluid Phase Equilibria 401, 27–33. https://doi.org/10.1016/j.fluid.2015.05.007

Yang, M., Zhao, J., Zheng, J., Song, Y., 2019. Hydrate reformation characteristics in natural gas hydrate dissociation process: A review. Applied Energy 256, 113878. https://doi.org/10.1016/j.apenergy.2019.113878

Yang, Z.J., Zhou, J.Z., Chen, Q., Wan, Y.Z., Wei, C.F., Meng, X.C., 2020. Triaxial Test and Constitutive Model for Hydrate-bearing Clayey Sand. Journal of Yangtze River Scientific Research Institute 37, 139. https://doi.org/10.11988/ckyyb.20190935

Yao, Y.P., Hou, W., Zhou, A.N., 2009. UH model: three-dimensional unified hardening model for overconsolidated clays. Géotechnique 59, 451–469. https://doi.org/10.1680/geot.2007.00029

Yao, Y.P., Liu, L., Luo, T., Tian, Y., Zhang, J.M., 2019. Unified hardening (UH) model for clays and sands. Computers and Geotechnics 110, 326–343. https://doi.org/10.1016/j.compgeo.2019.02.024

Yiallourides, C., Partain, R.A., 2019. Offshore Methane Hydrates in Japan: Prospects, Challenges and the Law. https://doi.org/10.2139/ssrn.3601849

Yin, Z., Linga, P., 2019. Methane hydrates: A future clean energy resource. Chinese Journal of Chemical Engineering, SI: Natural Gas Hydrates 27, 2026–2036. https://doi.org/10.1016/j.cjche.2019.01.005

Yoneda, J., Jin, Y., Katagiri, J., Tenma, N., 2016. Strengthening mechanism of cemented hydrate-bearing sand at microscales. Geophysical Research Letters 43, 7442–7450. https://doi.org/10.1002/2016GL069951

Yoneda, J., Jin, Y., Muraoka, M., Oshima, M., Suzuki, K., Walker, M., Otsuki, S., Kumagai, K., Collett, T.S., Boswell, R., Okinaka, N., 2021. Multiple physical properties of gas hydrate-bearing sediments recovered from Alaska North Slope 2018 Hydrate-01 Stratigraphic Test Well. Marine and Petroleum Geology 123, 104748. https://doi.org/10.1016/j.marpetgeo.2020.104748

Yoneda, J., Masui, A., Konno, Y., Jin, Y., Egawa, K., Kida, M., Ito, T., Nagao, J., Tenma, N., 2015a. Mechanical behavior of hydrate-bearing pressure-core sediments visualized under triaxial compression. Marine and Petroleum Geology, Gas hydrate drilling in Eastern Nankai 66, 451–459. https://doi.org/10.1016/j.marpetgeo.2015.02.028

Yoneda, J., Masui, A., Konno, Y., Jin, Y., Egawa, K., Kida, M., Ito, T., Nagao, J., Tenma, N., 2015b. Mechanical properties of hydrate-bearing turbidite reservoir in the first gas production test site of the Eastern Nankai Trough. Marine and Petroleum Geology, Gas hydrate drilling in Eastern Nankai 66, 471–486. https://doi.org/10.1016/j.marpetgeo.2015.02.029

Yoneda, J., Masui, A., Konno, Y., Jin, Y., Kida, M., Katagiri, J., Nagao, J., Tenma, N., 2017. Pressure-core-based reservoir characterization for geomechanics: Insights from gas hydrate drilling during 2012–

2013 at the eastern Nankai Trough. Marine and Petroleum Geology 86, 1–16. https://doi.org/10.1016/j.marpetgeo.2017.05.024

Yoneda, J., Masui, A., Tenma, N., Nagao, J., 2013. Triaxial testing system for pressure core analysis using image processing technique. Review of Scientific Instruments 84, 114503. https://doi.org/10.1063/1.4831799

Yoneda, J., Oshima, M., Kida, M., Kato, A., Konno, Y., Jin, Y., Tenma, N., 2019. Consolidation and hardening behavior of hydrate-bearing pressure-core sediments recovered from the Krishna–Godavari Basin, offshore India. Marine and Petroleum Geology, Marine Gas Hydrate Reservoir Systems Along the Eastern Continental Margin of India: Results of the National Gas Hydrate Program Expedition 02 108, 512–523. https://doi.org/10.1016/j.marpetgeo.2018.09.021

Yoneda, J., Oshima, M., Kida, M., Kato, A., Konno, Y., Jin, Y., Jang, J., Waite, W.F., Kumar, P., Tenma, N., 2019. Pressure core based onshore laboratory analysis on mechanical properties of hydrate-bearing sediments recovered during India's National Gas Hydrate Program Expedition (NGHP) 02. Marine and Petroleum Geology, Marine Gas Hydrate Reservoir Systems Along the Eastern Continental Margin of India: Results of the National Gas Hydrate Program Expedition 02 108, 482–501. https://doi.org/10.1016/j.marpetgeo.2018.09.005

Yoshimoto, M., Kimoto, S., 2022. Undrained creep behavior of CO2 hydrate-bearing sand and its constitutive modeling considering the cementing effect of hydrates. Soils and Foundations 62, 101095. https://doi.org/10.1016/j.sandf.2021.101095

Yoshimoto, N., Wu, Q., Fujita, K., Kajiyama, S., Nakata, Y., Hyodo, M., 2023. Hydrate dissociation and mechanical properties of hydrate-bearing sediments under local thermal stimulation conditions. Gas Science and Engineering 116, 205045. https://doi.org/10.1016/j.jgsce.2023.205045

You, K., Flemings, P. B., Malinverno, A., Collett, T. s., Darnell, K., 2019. Mechanisms of Methane Hydrate Formation in Geological Systems. Reviews of Geophysics 57, 1146–1196. https://doi.org/10.1029/2018RG000638

You, Z., Hao, Y., Hu, W., Shen, S., Wu, P., Li, Y., 2023. Strength analysis of hydrate-bearing sandy sediments in excess gas and excess water based on drained triaxial compression tests. Engineering Geology 325, 107292. https://doi.org/10.1016/j.enggeo.2023.107292

You, Z., Wu, P., Sun, X., Liu, Y., Li, T., Li, Y., 2022. Effect of Hydrate Distribution on the Mechanical Response of Hydrate-Bearing Sand: Discrete Element Method Simulation. Energy Fuels 36, 3802–3815. https://doi.org/10.1021/acs.energyfuels.2c00122

Yu, C., Chen, L., Sun, B., 2019. Experimental characterization of guest molecular occupancy in clathrate hydrate cages: A review. Chinese Journal of Chemical Engineering, SI: Natural Gas Hydrates 27, 2189–2206. https://doi.org/10.1016/j.cjche.2019.03.026

Yu, F., Song, Y., Liu, W., Li, Y., Lam, W., 2011. Analyses of stress strain behavior and constitutive model of artificial methane hydrate. Journal of Petroleum Science and Engineering 77, 183–188. https://doi.org/10.1016/j.petrol.2011.03.004

Yu, Y.-S., Zhang, X., Liu, J.-W., Lee, Y., Li, X.-S., 2021. Natural gas hydrate resources and hydrate technologies: a review and analysis of the associated energy and global warming challenges. Energy Environ. Sci. 14, 5611–5668. https://doi.org/10.1039/D1EE02093E

Yuan, Q., Kong, L., Xu, R., Zhao, Y., 2020. A State-Dependent Constitutive Model for Gas Hydrate-Bearing Sediments Considering Cementing Effect. JMSE 8, 621. https://doi.org/10.3390/jmse8080621

Yun, T.S., Santamarina, J.C., 2008. Fundamental study of thermal conduction in dry soils. Granular Matter 10, 197–207. https://doi.org/10.1007/s10035-007-0051-5

Yun, T.S., Santamarina, J.C., Ruppel, C., 2007. Mechanical properties of sand, silt, and clay containing tetrahydrofuran hydrate. Journal of Geophysical Research: Solid Earth 112. https://doi.org/10.1029/2006JB004484

Zeng, Z., Kong, L., Zhao, Y., Sang, S., Niu, G., Liu, J., Wang, N., 2023. Mechanical Properties of Gas Hydrate-Bearing Sediments Influenced by Multiple Factors: A Comprehensive Review of Triaxial Tests. Energy Fuels. https://doi.org/10.1021/acs.energyfuels.3c02623

Zhai, C., Sun, K.M., Xin, L.W., Tian, S., 2015. Experimental study of permeability of sand soil bearing sediments containing methane hydrates. Journal of WuHan University of Technology, 37, 78-82.

Zhang, H., Luo, X., Bi, J., He, G., Guo, Z., 2019. Submarine slope stability analysis during natural gas hydrate dissociation. Marine Georesources & Geotechnology 37, 467–476. https://doi.org/10.1080/1064119X.2018.1452997

Zhang, J., Yin, Z., Li, Q., Li, S., Wang, Y., Li, X.S., 2023. Comparison of fluid production between excess-gas and excess-water hydrate-bearing sediments under depressurization and its implication on energy recovery. Energy 282, 128315. https://doi.org/10.1016/j.energy.2023.128315

Zhang, Q., Shen, X., Zhou, X., Liang, D., 2017. Inhibition Effect Study of Carboxyl-Terminated Polyvinyl Caprolactam on Methane Hydrate Formation. Energy Fuels 31, 839–846. https://doi.org/10.1021/acs.energyfuels.6b02603

Zhang, W., Ma, Q., Wang, R., Ren, S., 2011. An experimental study of shear strength of gas-hydrate-bearing core samples. Pet. Sci. 8, 177–182. https://doi.org/10.1007/s12182-011-0132-2

Zhang, X., Lin, J., Lu, X., Liu, L., Liu, C., Li, M., Su, Y., 2018. A hypoplastic model for gas hydrate-bearing sandy sediments. International Journal for Numerical and Analytical Methods in Geomechanics 42, 931–942. https://doi.org/10.1002/nag.2772

Zhang, X.H., Lu, X.B., Shi, Y.H., Xia, Z., 2015. Study on the mechanical properties of hydrate-bearing silty clay. Marine and Petroleum Geology 67, 72–80. https://doi.org/10.1016/j.marpetgeo.2015.04.019

Zhang, X.H., Lu, X.B., Zhang, L.M., Wang, S.Y., Li, Q.P., 2012. Experimental study on mechanical properties of methane-hydrate-bearing sediments. Acta Mech Sin 28, 1356–1366. https://doi.org/10.1007/s10409-012-0142-3

Zhang, X.H., Luo, D.S., Lu, X.B., Liu, L.L., Liu, C.L., 2018. Mechanical properties of gas hydrate-bearing sediments during hydrate dissociation. Acta Mech. Sin. 34, 266–274. https://doi.org/10.1007/s10409-017-0699-y

Zhang, Y., Hou, Z., Li, J., Cheng, Z., Li, D., 2023. Experimental and model study on the weakening of gas hydrate-bearing sand considering dissociation. Geomech. Geophys. Geo-energ. Geo-resour. 9, 59. https://doi.org/10.1007/s40948-023-00608-1

Zhang, Y., Li, X.S., Chen, Z.Y., Wang, Y., Ruan, X.K., 2015. Effect of Hydrate Saturation on the Methane Hydrate Dissociation by Depressurization in Sediments in a Cubic Hydrate Simulator. Ind. Eng. Chem. Res. 54, 2627–2637. https://doi.org/10.1021/ie5042885

Zhao, J., Sun, S., Liu, C., Meng, Q., 2018. Thermal conductivity and thermal diffusivity of methane hydrate formed from compacted granular ice. Heat Mass Transfer 54, 3287–3295. https://doi.org/10.1007/s00231-018-2342-2

Zhao, J., Wang, J., Liu, W., Song, Y., 2015a. Analysis of heat transfer effects on gas production from methane hydrate by thermal stimulation. International Journal of Heat and Mass Transfer 87, 145–150. https://doi.org/10.1016/j.ijheatmasstransfer.2015.04.007

Zhao, J., Xiang, X., Zhao, Jinzhou, Li, H., Guo, P., Zhang, L., Zhou, S., Wei, N., Li, Q., Pang, W., 2019. An experimental analysis on the elastic mechanical parameters of weakly-consolidated non-diagenetic gas hydrate sediments. Natural Gas Industry B 6, 317–322. https://doi.org/10.1016/j.ngib.2018.12.001

Zhao, J., Zhu, Z., Song, Y., Liu, W., Zhang, Y., Wang, D., 2015b. Analyzing the process of gas production for natural gas hydrate using depressurization. Applied Energy 142, 125–134. https://doi.org/10.1016/j.apenergy.2014.12.071

Zhou, B., Sanchez, M., Oldecop, L., Santamarina, J.C., 2022. A Geomechanical Model for Gas Hydrate Bearing Sediments Incorporating High Dilatancy, Temperature, and Rate Effects. Energies 15, 4280. https://doi.org/10.3390/en15124280

Zhou, J., Yang, Z., Wei, C., Chen, P., Yan, R., 2021. Mechanical behavior of hydrate-bearing sands with fine particles under isotropic and triaxial compression. Journal of Natural Gas Science and Engineering 92, 103991. https://doi.org/10.1016/j.jngse.2021.103991

Zhou, M., Soga, K., Yamamoto, K., 2018. Upscaled Anisotropic Methane Hydrate Critical State Model for Turbidite Hydrate-Bearing Sediments at East Nankai Trough. Journal of Geophysical Research: Solid Earth 123, 6277–6298. https://doi.org/10.1029/2018JB015653

Zhou, M., Soga, K., Yamamoto, K., Huang, H., 2020. Geomechanical responses during depressurization of hydrate-bearing sediment formation over a long methane gas production period. Geomechanics for Energy and the Environment, Challenges of gas production from hydrate-bearing sediments 23, 100111. https://doi.org/10.1016/j.gete.2018.12.002

Zhou, Y., Zhou, J., Chen, P., Wei, C., 2023. Shear strength degradation of gas hydrate-bearing sediment due to partial hydrate dissociation. Journal of Rock Mechanics and Geotechnical Engineering. https://doi.org/10.1016/j.jrmge.2023.10.002

Zhu, Y., Chen, C., Luo, T., Song, Y., Li, Y., 2022. Creep behaviours of methane hydrate-bearing sediments. Environmental Geotechnics 9, 199–209. https://doi.org/10.1680/jenge.18.00196

Zhu, Y., Li, Y., Liu, W., Song, Y., Luo, T., Wu, Z., 2015. Dynamic strength characteristics of methane hydrate-bearing sediments under seismic load. Journal of Natural Gas Science and Engineering 26, 608–616. https://doi.org/10.1016/j.jngse.2015.06.055

Zhu, Y., Wang, H., Chen, C., Luo, T., 2020. Effects of sand contents on mechanical characteristics of methane hydrate-bearing sediments in the permafrost. Journal of Natural Gas Science and Engineering 75, 103129. https://doi.org/10.1016/j.jngse.2019.103129

Achievements obtained during PhD

Zhang, H. L.*, Qi, S. X., Bian, H. B., Wang, J.J., Xu, S. X., Wu, B. (2025)
A Nonlinear Viscoelastic-Plastic Creep Model for Silty Mudstone Considering Critical Damage State. *Results in Engineering*, 26, 2025, 104988. https://doi.org/10.1016/j.rineng.2025.104988 (Published)

Zhang, H. L.*, Qi, S. X., Bian, H. B., Wang, J.J., Xu, S. X., Wu, B. (2025)
Creep-failure pattern and micromorphological evolution of simulated silty mudstone under multistaged loading. *Mechanics of Time-Dependent Materials*, 29, 10 (2025). https://doi.org/10.1007/s11043-024-09742-z (Published)

Zhang, H. L.*, Bian, H. B., Qi, S. X., Wang, J. J. (2024)
A comprehensive analysis of formation conditions, intrinsic properties, and mechanical responses of gas hydrate-bearing sediments, *Rock Mechanics Bulletin* (14 March 2024), https://doi.org/10.1016/j.rockmb.2024.100114 (Published)

Xu, S. X., Wu, B, **Zhang, H.L.***, Qi, S.X., Wang, J. J., Bian, H.B. (2024)
Study on crack propagation mechanism and charge structure optimization of tunnel shaped charge hydraulic blasting, *Case Studies in Construction Materials*, Volume 21, 2024, e03805, https://doi.org/10.1016/j.cscm.2024.e03805. (Published)

Xu, S. X., Wu, B, **Zhang, H.L.***, Qi, S.X., Bian, H.B, Wang, J. J. (2025)
Directional crack propagation and optimization strategies for multi-hole shaped charge blasting in tunnel construction, *Structures*, Volume 72, 2025, 108268, https://doi.org/10.1016/j.istruc.2025.108268 (Published)

Qi, S. X., **Zhang, H. L.***, Bian, H. B., Wang, J.J., Xu, S. X., Wu, B. (2024)
Damage Characteristics and Degradation Mechanism of Silty Mudstone Under Wet–Dry Cycling. *Geotechnical and Geological Engineering*, 42, 6095–6112 (2024). https://doi.org/10.1007/s10706-024-02877-3 (Published)

Liu, J., **Zhang, H.L.**, Bian, H. B., Wen W., Zeng, L.* (2024)

Uniaxial Mechanical Properties and Failure Characteristics of Fractured Silty Mudstone, *KSCE Journal of Civil Engineering*, Volume 28, pages 139–154, (2024) https://doi.org/10.1007/s12205-023-0200-3 (Published)

Wang, J.J., **Zhang, H.L.***, Qi, S.X., Bian, H.B., Duan, X.B., Long, B. (2023)
Study on the Micro Mechanism of Damage Caused by Unloading Confining Pressure of Silty Mudstone, *Case Studies in Construction Materials*, 2023: e02580, https://doi.org/10.1016/j.cscm.2023.e02580 (Published)

Wang, J.J., **Zhang, H.L.***, Qi, S.X., Bian, H.B., Long, B, Duan, X.B. (2023)
Study on the Strength and Failure Characteristics of Silty Mudstone Using Different Unloading Paths, *Materials*, 16(14):5155, https://doi.org/10.3390/ma16145155 (Published)

Zhang, H. L.*, Qi, S. X., Bian, H. B., Wang, J.J. (2025)
Fracture-Induced Variations in Mechanical Properties of Silty Mudstone Under Triaxial Stress, *Environmental Earth Sciences*. (Accepted)

Zhang, H. L.*, Bian, H. B., Qi, S. X., Wang, J.J. (2025)
Advances in Geomechanical Characterization of Gas Hydrate-Bearing Sediments: A Synthesis of Experimental Insights and Constitutive Modeling, *Geoenergy Science and Engineering*. (Under review)